Title
Integrating Green Manufacturing in Sustainable Life Cycle Design: A Case Study on PEM Fuel Cells

Author
Chien, Joshua

Publication Date
2013

Peer reviewed|Thesis/dissertation

Integrating Green Manufacturing in Sustainable Life Cycle Design: A Case Study on PEM Fuel Cells

by

Joshua Michael Chien

A dissertation submitted in partial satisfaction of the
requirements for the degree of
Doctor of Philosophy

in

Engineering - Mechanical Engineering

in the

Graduate Division

of the

University of California, Berkeley

Committee in charge:

Professor David A. Dornfeld, Chair
Professor Tarek Zohdi
Professor Arpad Horvath

Fall 2013

Integrating Green Manufacturing in Sustainable Life Cycle Design: A Case Study on PEM Fuel Cells

Abstract

Integrating Green Manufacturing in Sustainable Life Cycle Design: A Case Study on PEM Fuel Cells

by

Joshua Michael Chien

Doctor of Philosophy in Engineering - Mechanical Engineering

University of California, Berkeley

Professor David A. Dornfeld, Chair

Global resource consumption and anthropogenic carbon emissions are increasing at an unsustainable rate, causing noticeably adverse changes to our ecosystem and jeopardizing the ability for future generations to thrive. This realization has brought together designers and engineers to holistically incorporate all aspects of sustainability in the product's entire life cycle using principles such as green engineering and design for environment (DFE) and eco-design tools such as life cycle assessment (LCA). However, to properly assess and facilitate designs and technologies that are indeed more environmentally benign, changes are needed to shift from the conventional serial LCA to a more coupled and integrated sustainable life cycle design (iSLCD) approach that resonates the three pillars of sustainability. A unique concept of the Product Life Cycle Zodiac (PLCZ) is introduced that reveals the complete holistic product life cycle from Earth to landfill and enables the information flow of the different life cycle phases to be fed back or looped for product development and process planning. In addition, the precision of the iSLCD approach can be vastly improved by the leveraging of green manufacturing, such as the scales of green manufacturing (SGM), where changes at the manufacturing process level can propagate throughout all downstream stages.

A case study reflecting the influence of design and manufacturing using the iSLCD framework is considered. A potential proxy for large carbon emission reductions is the electrification of the automotive industry, which has promised to provide a renewable and cleaner alternative to the conventional internal combustion engine (ICE). Alternative energy vehicles such as the Polymer Electrolyte Membrane (PEM) fuel cell vehicle utilizes compressed hydrogen to offer zero emissions during the operational use phase. However, despite being commercially available for over a decade, current annual production volumes are more than several orders of magnitude lower than todays conventional ICEs. At current low production volumes the processes for PEM fuel cell manufacturing are burdened with large inefficiencies such as low throughput batch processing (as compared to continuous roll-to-roll processing), high equipment idle times, low material utilization and processing yields. These inefficiencies contribute to an increase of the specific energy consumption (SEC) and hence the environ-

mental impact of the fuel cells to a point where the benefits of zero emissions may potentially be outweighed by the emissions during the manufacture of the fuel cell. Furthermore, the low production volumes and the use of exotic materials such as platinum catalysts impedes the adoption of the technology due to prohibitively high cost. Therefore, it is of interest to analyze in, parallel with the environmental impacts, the cost implications and where identify area of potential cost reductions.

The case study investigates the environmental and economical performance of PEM fuel cell manufacturing for automotive applications. The research is in part a collaborative effort with Daimler-Benz in attempts to assess and improve the current state-of-the-art manufacturing practices by leveraging the SGM. Detailed unit processes are modeled in terms of energy consumption as a function of manufacturing inputs and are integrated into a facility scale HVAC energy consumption model. The life cycle phases included in the model follow the product life cycle zodiac (PLCZ) from raw material extraction to product distribution and the various end-of-life pathways. The economical aspect is investigated using a design for manufacturing and assembly (DFMA) technique in conjunction with the environmental analysis. A thorough analysis of the results and the breakdown of the component contributions and sensitivity analysis of the model is conducted. The sensitivity analysis provides insights to not only the the fuel cell manufacturing, but also highlights the importance of integrating the SGM. Lastly, the influence of data uncertainty is incorporated using a stochastic Monte Carlo technique.

I dedicate this dissertation to family, especially my mother, Barbara, my father, Steve, my sister, Christine, my aunt Amy, and to my uncle Ron. I would also like to dedicate this dissertation to my ancestors as well as to the future engineers who will strive for a sustainable tomorrow...

Contents

List of Figures

List of Tables

Acknowledgments

There are several acknowledgments that are in need of recognition. First and foremost is my advisor Professor David Dornfeld who enabled me to pursue the path of a graduate career and help make this dissertation possible. I am extremely grateful for his care, hospitality, plethora of advice, and providing the necessary resources to succeed. I would also like to acknowledge my committee members Professor Zohdi and Professor Horvath, both of which have been very valuable in terms of my research and intellect the classroom. Last, but not least, I would like to acknowledge Daimler-Benz for their contribution to my research, in particular, Klaus Berger and Christian Wulff. Special appreciation for Mr. Berger for giving me the invaluable opportunity to work with Daimler's fuel cell team and allowing me to visit both the production facility in Vancouver and R&D facility in Stuttgart, Germany. Also, much appreciation for Mr. Wulff for providing me the guidance and the necessary information to complete my dissertation. Thank you to all.

Part I

Sustainable Design

Chapter 1

Introduction

Consider this, at the end of 2012 there was an unprecedented estimate of 6.8 billion mobile cellular subscribers, a number that has doubled since 2007, and total mobile devices in use is predicted to overcome the global population by 2017 [110][111][320]. Apple's mobile device line, the iPhone®, alone has already sold over 350 million units [109] since introduced just six years ago. The resulting carbon emissions from mobile devices are responsible for roughly 2% of the total annual global greenhouse gas emissions, a staggering magnitude considering the influence of a single product sector [102]. The consumer mobile market is just one of many examples of increased product consumption, effectively leading to unsustainable consumption levels of natural resources and energy, and ultimately impacting climate change.

What is causing this rapid increase in consumption? In part, it is due to increase in global wealth where the global GDP per capita in the last century has increased by a factor of more than five, and will continue to increase especially in poorer countries [157]. Furthermore, the number of people in the world has dramatically increase over the decades. From the end of the the industrial revolution to the end of World War II, the global population doubled, reaching a population of 2.5 billion. Since then, the global population has nearly tripled to today's 7.2 billion and is forecasted to reach 9.6 billion by 2050 [101]. That factor of three increase population led to nearly a ten-fold increase in material consumption [115]. Lastly, perhaps arguably the greatest the contributor is the exponential growth in technological development. For instance, since the early 1970's, the electronics industry has closely followed Moore's Law, which states that the number of transistors on an integrated circuit will double every 18 months. The list of reasons could go on, but the emphasis lies in the combination of wealth, population, and technological development. If remains unaddressed, serious consequences in the environmental impact due to human consumption will arise, causing detrimental and potentially irreversible damage to our ecosystem well-being.

1.1 Environmental Impact

The relationship between environmental impact and human activities has been extensively studied and talked about for the past several decades. In the early 1970's, Ehrlich and Holdren [86] attributed the impact of human activities as the product of population and per capita consumption, which in itself was a function of population. Around the same time, Commoner [47] argued that the recent evidence showed that environmental degradation was due to technological displacements and transformation. Together they developed what is known as the $IPAT$ identity, which evolved into a simple yet powerful equation that relates technological innovation with anthropogenic impact. Mathematically, the impact (I) can be expressed as the product of three variants: population (P), affluence (A), and technology (T), and is expressed in Equation 1.1 below:

$$\textbf{I}\text{mpact} = \textbf{P}\text{opulation} \times \textbf{A}\text{ffluence} \times \textbf{T}\text{echnology} \tag{1.1}$$

Where

- **Impact**: total impact, typically represented as emitted pollution (i.e.,, carbon emissions) or consumed energy (units of joules) per year
- **Population**: Number of people in a given country or globally for the given year
- **Affluence**: Population wealth, typically expressed as GDP ($) per capita per year or energy (units of joules) per capita per year
- **Technology**: Impact intensity arising from technological growth in units of either pollution (i.e.,, carbon emissions) per energy (joules) or energy (joules) per GDP ($)

Data on population and affluence are well documented and easily accessible (albeit less so in developing countries). While the technology variant is more difficult to obtain, a few major industrial sectors such as energy and agriculture are typically well documented. Ehrlich and Holdren also stressed that the three variants are not independent and in fact are coupled with one being a function of the other [86][47].

A key component missing, and what was subjected to criticism as a major flaw of the $IPAT$ identity, was the idea of consumption intensity or "intensity of use". The technology variant associates an economic value to pollution and environmental impact, but can be ambiguous on how the association is made. Therefore, an attempt was made to disaggregate the technology variant, shifting from one degree-of-freedom to two degrees: consumption intensity such as energy per GDP and technology efficiency such as emissions per energy [334]. This formulation with four parameters is generally known as the $ImPACT$ identity, as shown in Equation 1.2 below, and is referred to as the *Kaya* identity specifically for carbon emissions and energy consumption [334][143]:

$$\textbf{Im}\text{pact} = \textbf{P}\text{opulation} \times \textbf{A}\text{ffluence} \times \textbf{C}\text{onsumption} \times \textbf{T}\text{echnology} \tag{1.2}$$

Where

- **Population** and **Affluence** are defined as the same in $IPAT$
- **Consumption**: Consumption intensity due to consumer behavior, defined as some tangible quantity, such as energy (joule), per GDP ($)
- **Technology**: Technological efficiency of a industrial sector or product, defined as the ratio of environmental impact to goods demanded and produced (e.g., grams of carbon dioxide per joule)

Although similar in mathematical formulation, the advantage of the $ImPACT$ identity is apparent. With the additional degree-of-freedom, environmental impact can be reduced by both rethinking consumer expenditures, for example by increasing the life of a product, and by improving material/resource utilization and energy efficiency in manufacturing through innovation. If all else remains constant or "business-as-usual" (BAU), manufacturers can still strive for higher efficiencies, independent of population, affluence, and consumption growth, leading to additional cost benefits.

The validity of the $ImPACT$ identity has not been proven per sè, but is closely monitored and studied, particularly by the Intergovernmental Panel on Climate Change (IPCC), an organization founded between a joint venture of the United Nations Environment Programme (UNEP) and the World Meteorological Organization (WMO). Since its establishment in 1988, the IPCC has released four assessment reports (the fifth due in 2014) that examine the current state on climate change. Through collaborative efforts on scientific, technical, and socio-economical research, the assessment reports provide a thorough analysis on the causes, potential impacts, and mitigation strategies regarding climate change [156]. The outcome of the findings implicitly supports the relationship of the $ImPACT$ identity. Significant evidence starting from the Second Assessment Report (SAR), released in 1995, shows that the large majority of environmental impact is due to anthropogenic activity. The Third Assessment Report (TAR), released in 2001, concluded that majority of global temperature increase in the last 50 years is likely (over 66% probability) due to human activities. The Fourth Assessment Report (AR4), released in 2007, concluded that human activities (with over 90% probability) are the main source of global temperature increase, and from a social perspective, the increase will most strongly and quickly impact the global poor and marginalized [155].

The strong confidence for associating the environmental impact to anthropogenic activity is due to the fact that current data and models showing global temperature change with only natural forcing, such as volcanic activity and solar variations, do not match observations [155]. For instance, Figure 1.1 shows the flow and interactions of the global carbon cycle with land, sea, and air. As seen in the figure in solid arrows, natural carbon sources and sinks are generally in equilibrium with volcanic activity contributing to an insignificant amount (<0.1GtC/year).[1] Land plants and biomass offset their respiratory emissions with

[1] GtC = giga-tons of atomic carbon

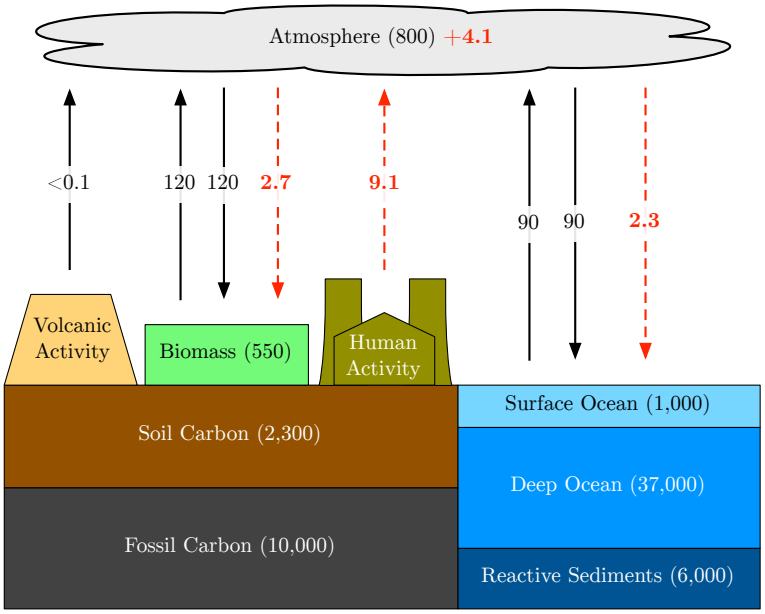

Figure 1.1: Earth's current carbon cycle in GtC. Dashed arrows indicate anthropogenic emissions. Values in parenthesis refer to stored carbon. Reproduced from [75].

photosynthesis and the same activity occurs in oceans with the release and absorption from bio-activity [75]. Disturbance in the the natural carbon cycle is shown in the dashed arrows for the years 2000-2008. Anthropogenic emissions in terms of fossil fuel, cement production, and land change are distributed with roughly 50% (4.1GtC of the 9.1GtC) of the emissions absorbed by the atmosphere [129]. It is important to highlight that even though the ocean and land mass acts as a carbon sink, the current rate of anthropogenic emissions overtakes the rate of sequestration. In fact the mean global carbon emission from 1990-2000 to 2000-2008 increased by roughly 20% while land and ocean sequestration only increased by roughly 4%, leaving the excess carbon to be absorbed by the atmosphere (an approximate increase of 30%) [129].

1.2 Trends and Projections

A recent press release by the International Energy Agency (IEA) revealed that the new estimates for energy-related carbon dioxide emissions in 2012 reached a record high of 31.6GtC, a number that has over doubled since 1973 [149]. Historically, the global carbon emissions trend has followed the $ImPACT$, or rather the Kaya identity, very closely. Figure 1.2 plots the total energy related carbon emissions from 1965 to 2010 along with global development (top plot) in terms of the Kaya identity variants: population, GDP per capita, total fuel consumption per GDP, and carbon dioxide (CO_2) per all fuel types. In addition, the lower figure plots the total global fuel consumption by fuel type in billion tonnes of oil equivalent

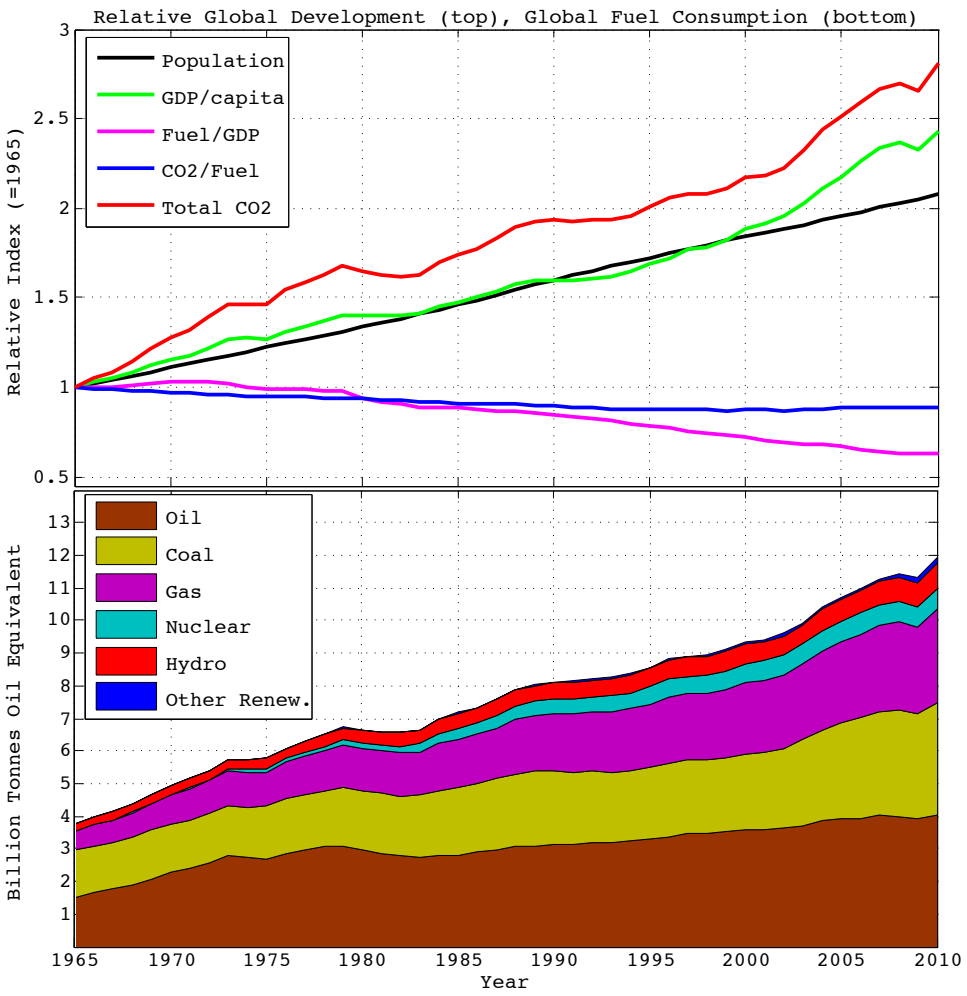

Figure 1.2: Global development and emissions relative to 1965 (top) and global energy consumption by fuel (bottom). Data from [254].

(BTOE). As seen in the figure, global wealth (GDP/capita) has steadily increased over the past several decades reaching 2.5× the value in 1965.[2] In addition, during the same time period, fuel costs (fuel per GDP) decreased in value by roughly 40%.[3] As a result, fuel consumption increased three-fold, with the largest increases from natural gas and nuclear. Despite the three-fold increases in fuel consumption, total carbon emission only increased 2.75×. This is primarily due to the increasingly larger contribution of renewable and non-fossil fuel energy where the fuel carbon intensity is much lower.

As a consequence of increasing anthropogenic carbon emissions and the Earth's inability

[2]World values of GDP have been scaled to the equivalent purchasing power of the 1990 U.S. dollar [254].

[3]The decrease in value is primarily due to inflation where 1 USD in 2010 has the same purchasing power as 0.6 USD in 1990 [184].

to sequester carbon at a similar rate, the total concentration of CO_2,[4] in terms of parts-per-million (PPM), has increased dramatically. Figure 1.3a plots the atmospheric CO_2 concentration from 1880 to 2010. The influence of human development to CO_2 concentration is evident with concentration increases of roughly 7% and 30% from 1880 to the end of WWII and from the end of WWII to 2010, respectively.

The direct effects of increase carbon concentration in the atmosphere have contributed to an increase in the effective radiative forcing as shown in Figure 1.3b. The fluctuations in forcing are due to spikes in stratospheric aerosols (e.g., natural occurrences such as volcanic activity) and variations in solar irradiance [280]. However, the mean trend is primarily caused by carbon dioxide, or more precisely gases that increase the Earth's effective radiative forcing, categorized as greenhouse gases (GHGs). Significant empirical evidence correlates the magnitude of radiative energy re-absorbed by the Earth's surface to greenhouse gases such as CO_2 and methane [155]. This phenomenon is due the fact that greenhouse gases have absorption spectrums with peak intensities in the infrared regime. Infrared or outgoing longwave radiation (OLR) is emitted from the Earth's surface in the form of heat and is absorbed by greenhouse gases and re-emitted back to Earth and into space [262]. The radiative forcing cycle is illustrated in Figure 1.4. Extraterrestrial solar radiant flux enters the upper atmosphere with an average of 1367W/m^2, and having a maximum of 1412W/m^2 and minimum of 1322W/m^2 depending on the time of year [13]. The solar flux, known as the solar constant, can be further averaged over the entire Earth's surface area, yielding an average solar radiation of 342W/m^2.[5] Of that average, roughly 20% is absorbed by the atmosphere, while the remaining 80% is either reflected back into space via surface and cloud albedo or absorbed by the Earth. On the Earth's surface, 50% of the heat released (from surface radiation, thermal heat, and evaporation) is emitted back out to space and the remaining 50% is absorbed by the atmosphere [155]. Coupled with the radiation absorbed from the sun, the greenhouse gases re-emit the collective radiation back to the Earth's surface, and hence the term greenhouse effect.

From an energy balance perspective the additional burden of radiative forcing causes an increase in the Earth's surface temperature, or what is ubiquitously known as global warming. Data plotted in Figure 1.3c from the NASA's Goddard Institute for Space Studies show that the global mean surface temperature from land, air, and sea has continued to rise, particularly within the last several decades [108]. The data also shows that in the last 130 years global temperature increased by an average of 0.8°C with 0.6°C occurring only within the last 40 years. In fact the past 12 years (2001-2012) rank among the top 14 warmest ever to be recorded since global standardized recordings began in 1850 [43].

The global increase in temperature and carbon absorption have serious detrimental effects on the Earth's ecosystem. As a result of warmer air and sea temperatures, sea levels have risen due to the melting of the Arctic ice and thermal volumetric expansion of the ocean.

[4]Here CO_2 and carbon are synonymous since each CO_2 molecule contains exactly one carbon atom

[5]Incoming solar flux is projected onto the Earth with an area of πr^2, whereas the surface area is $4\pi r^2$ giving $1367\text{W/m}^2 \div 4 = 342\text{W/m}^2$

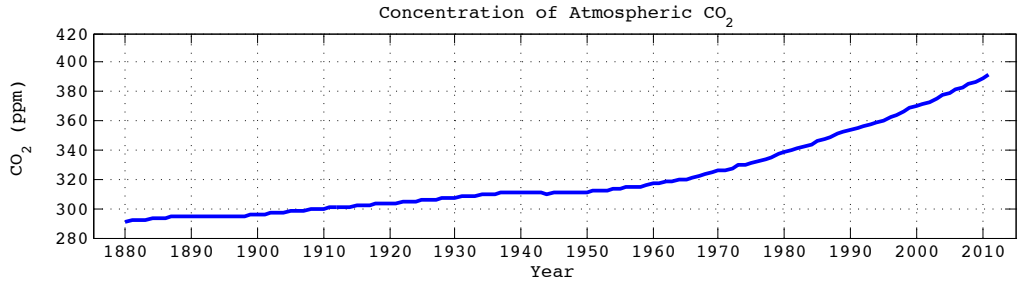

(a)

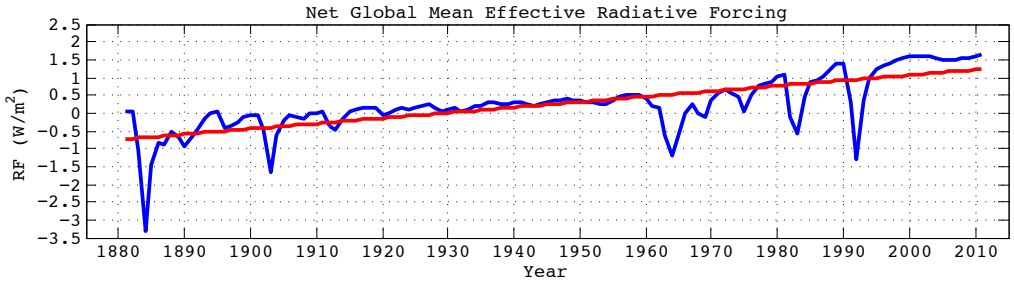

(b)

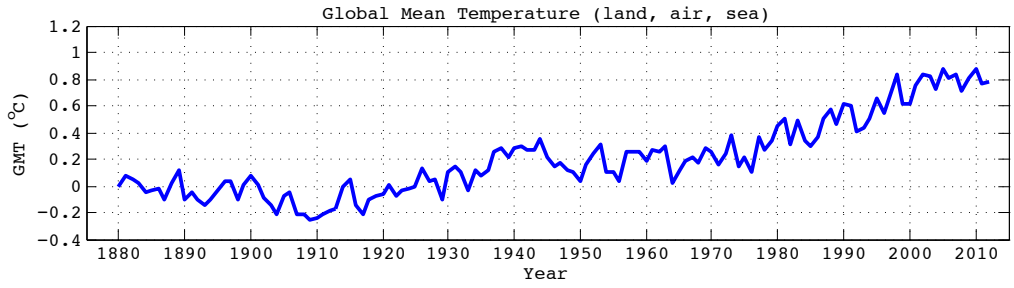

(c)

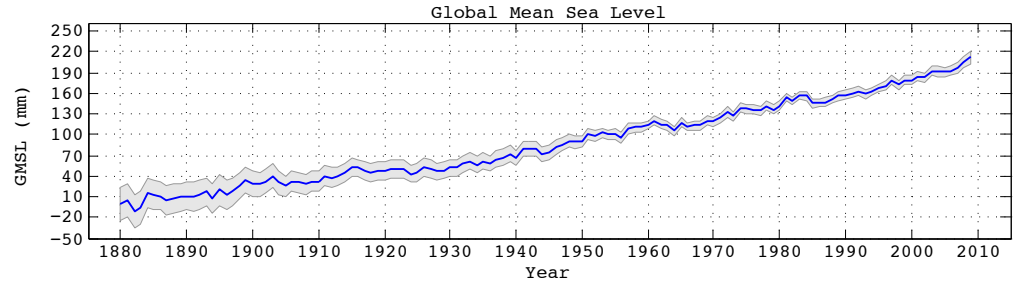

(d)

Figure 1.3: Global levels from 1880-2010 of a) atmospheric CO_2 (PPM), b) effective radiative forcing (W/m^2), c) mean temperature (°C), d) mean sea rise (mm). Data obtained from [108].

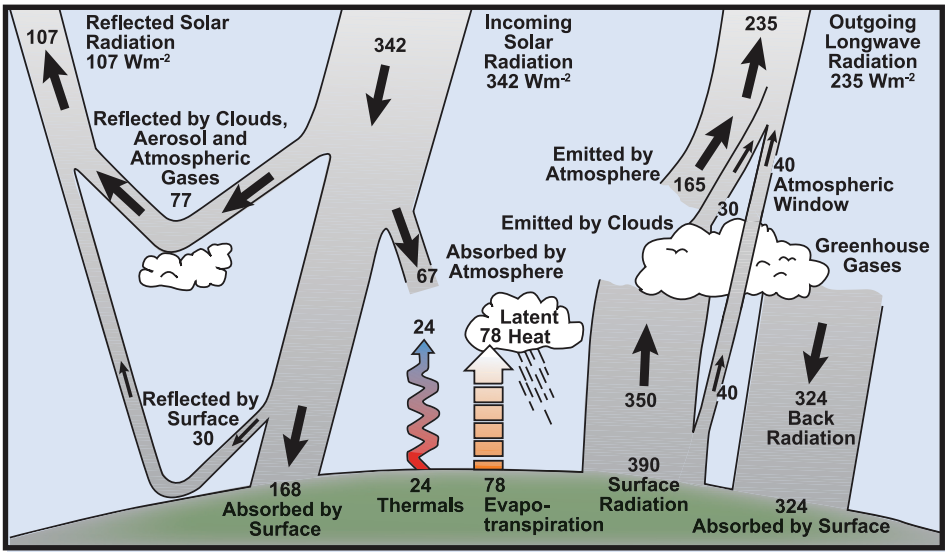

Figure 1.4: Earth's radiative forcing cycle. Image from [155].

As seen Figure 1.3d, sea levels on average have steadily risen over 20cm since 1880. Current projections by the IPCC have sea levels rising an additional 50% by 2050 with sea level rates doubling during the next century [155]. Furthermore, the projections on rising sea level rates exclude the rapid changes to the ice sheets such as the Greenland and West Antarctic Ice Sheets, which contain an equivalent sea level rise of 6m and 5m, respectively [199]. Rising sea levels have major implications in loss of inhabitable land area. Simulations from the geographic information system (GIS) reveal a global sea level rise of 1 meter creates potentially an inundated area of 1,055,000km^2, a 0.7% decrease in total land area and an impact to 1.7% of the world's population. Results from the same simulation also show that a sea rise of up to 6m yields an inundated area of 2,192,000km^2, a 1.5% decrease in total land area and an impact to 6.8% of the world's population[199]. Moreover, recent findings of large methane deposits in the Arctic ice exacerbate the situation. Scientists claim that the thawing permafrost in the Arctic ice could release enough methane to shift forward the 2°C global temperature increase mark by 15 to 35 years [212]!

Besides the potential inundated land and methane "time bomb," other devastating effects of increasing global temperature may arise. For instance, with severe increases in temperature (>3°C), food crops begin to fail, water becomes more scarce, coral and aqua life is threatened due to increased pH levels, and more heat waves and forest fires [26]. Figure 1.5 below summarizes some of these detrimental effects to the ecosystem and society.

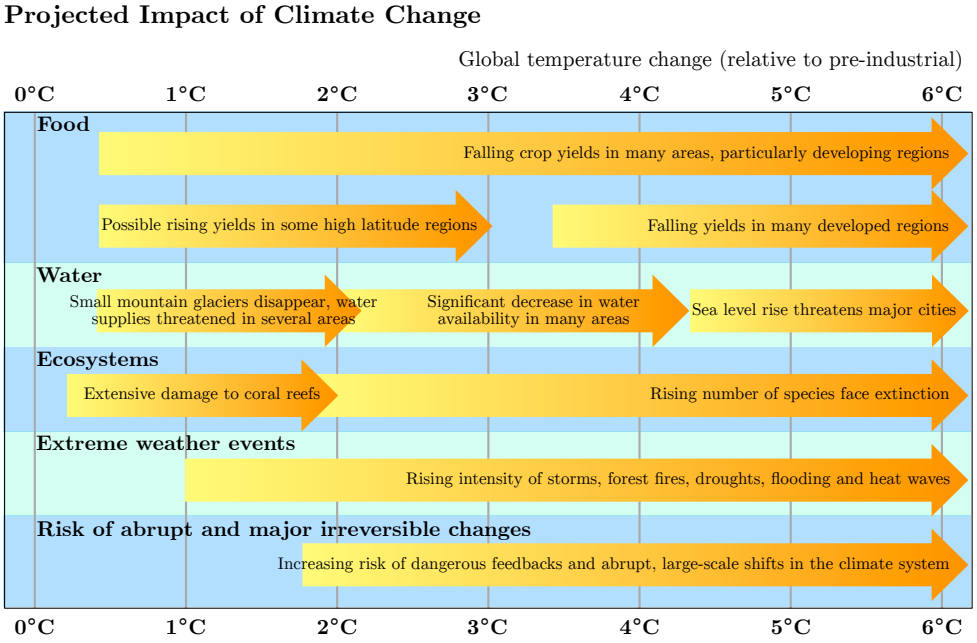

Figure 1.5: Project impacts versus increased global temperatures. Reproduced from [26].

1.3 Stabilization Scenarios

It is now understood that there exists a strong relationship between anthropogenic carbon emissions and global climate change. To develop mitigation strategies, numerous scenario pathways have been formulated to accurate model the *ImPACT* identity. Mapped out in Figure 1.6, the pathways provide an assessment of the impact for policymakers to facilitate the decision making process. The scenario pathways are not a prediction of the future, but simply provide a "what-if" input (i.e., socio-economical inputs) into climate change models that are inherently coupled and contain a high degree of uncertainty. The scenarios themselves attempt to portray realistic situations in the economy, population, and technology energy mix, which heavily influence the outcome of the models.

Beginning with the FAR, the IPCC has released numerous scenario pathways with S(A-D)90 in 1990, which was shortly followed by IS92(a-f) in 1992 used in the SAR. Most recently, the Specials Report on Emission Scenarios by the TAR focuses on four categories or "families": economic and environmental and two spatial scales: regional and global, yielding six scenarios: A1FI, A1T, A1B, A2, B1, and B2. Each scenario represents a different demographic, social, economic, technological, and environmental developments [157].

- **A1**: scenario with new and more efficient technologies, population peaking at mid-century and decreasing thereafter, and very rapid economic growth with more evenly distributed wealth and global interaction. The A1 scenario can be broken down into three energy technological pathways:

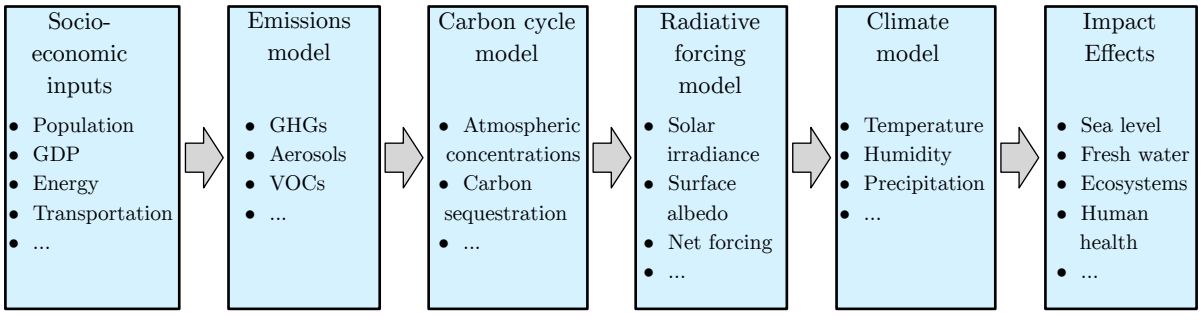

Figure 1.6: Sequential model approach for climate change. Adopted from [227].

  - **A1FI**: fossil intensive - decline in energy intensity (joules/$) at a slow pace, share of coal consumption remains relatively constant, modest increase in share of renewable energy
  - **A1T**: non-fossil intensive - decline in energy intensity (joules/$) at a fast pace, share of coal consumption decreases exponentially, rapid adoption in renewable energy
  - **A1B**: balanced energy mix - decline in energy intensity (joules/$) at an intermediate pace, share of coal consumption decreases linearly, intermediate adoption in renewable energy

- **A2**: scenario that is more regional and local focused with increasing global population and dispersed economic and technological growth that is slower than other scenarios.

- **B1**: scenario similar to A1 except economic growth structures more towards a service and information based economy with reduced material consumption and more clean and resource-efficient technologies, emphasis on improving global triple bottom-line: economic, social, and environmental sustainability, without any additional climate initiatives.

- **B2**: scenario with emphasis on regional and local triple bottom-line, population growth rate is lower than A2 with intermediate levels of economic development, technological change at less rapid and more diverse pace than A1 and B1.

A new set of scenario pathways are currently being developed that will be release in the Fifth Assessment Report (AR5). These new pathways are a radical change to the existing ones where now each individual model (e.g., radiative forcing, economic development, etc.) is in parallel development with each other. This allows a more integrated and robust approach where inconsistencies due to information delays are minimized [227]. Various outcomes have resulted in the scenario assessments including the findings from the FAR which led to the adoption of the Kyoto Protocol [155].

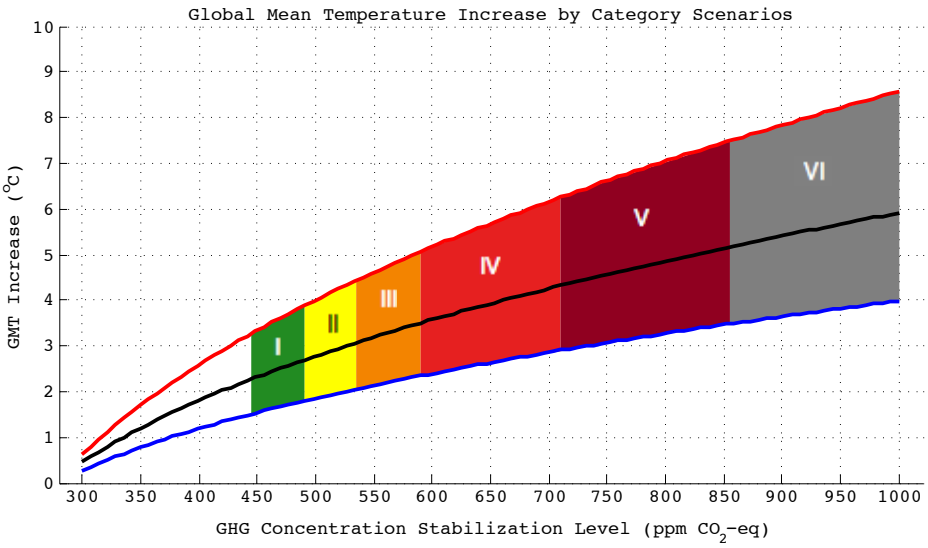

Figure 1.7: Global mean temperature increase (from pre-industrial levels) versus stabilization scenario category. Reproduced from [154].

Due to the level of uncertainty, each individual scenario modeled, for example with Monte Carlo techniques, will yield multiple results that can be mapped onto some sort of distribution. Using the most recent IPCC scenarios, which are denoted as post-TAR, the simulation results are divided into six CO_2 concentration categories ranging from 350PPM to 790PPM. Plotting the simulations results, seen in Figure 1.7 and tabulated in Table 1.1, shows the global mean temperature (relative to pre-industrial levels) increasing with greenhouse gas concentration with the center line representing best estimates and upper and lower lines representing the 85^{th} and 15^{th} percentile, respectively. The trend has a power-law relationship with $0 < n < 1$, which translates to less than double the temperature increase when the concentration level is doubled. However, the current PPM levels in the atmosphere have already reached the beginning of category II[6] and is projected to reach category V in the next 50 years assuming business-as-usual [154].

One key takeaway from all IPCC scenarios, particularly from the original S(A-d)90 and IS92(a-f), is that in order to achieve category I or II stabilization levels immediate reductions in global carbon emissions are necessary. However, in 1996, Wigley, Richels, and Edmonds [346] published an updated version of the IS92 scenarios that factored in economic (i.e., costs) implications in choosing the preferred scenario. The updated profiles, known as the WRE scenarios, follows the BAU trajectory initially for the first 10-30 years depending on the stabilization level. Wigley et al. argued that it was more economical (i.e., higher return-on-investment) to front the investment in stabilization technologies as early as possible despite having an initially higher carbon emissions rate. By doing so, the anthropogenic carbon emissions profile drops significantly after the initial surge due to the early investment of

[6]GHG PPM is approximately 100PPM greater than CO_2 PPM

Table 1.1: Summary of stabilization scenarios from the post-TAR simulations. Ranges correspond to the 15th to 85th percentile [154].

Category	**CO_2 concentration** (ppm)	**CO_2-eq concentration** (ppm)	**Radiative Forcing** (W/m^2)	**Global mean temperature increase above pre-industrial** (°C)	**Peaking year for CO_2 emissions**	**Change in global CO_2 emissions in 2050** (±% of 2000 emissions)
I	350-400	445-490	2.5-3.0	2.0-2.4	2000-2015	-85 to -50
II	400-440	490-535	3.0-3.5	2.4-2.8	2000-2020	-60 to -30
III	440-485	535-590	3.5-4.0	2.8-3.2	2010-2030	-30 to 5
IV	485-570	590-710	4.0-5.0	3.2-4.0	2020-2060	10 to 60
V	570-660	710-855	5.0-6.0	4.0-4.9	2050-2080	25 to 85
VI	660-790	855-1130	6.0-7.5	4.9-6.1	2060-2090	90 to 140

cleaner technologies, yet yielding the same net cumulative carbon content (at a time scale of three centuries) as the IS92(a-f) pathways [346]. Figure 1.8 plots five WRE scenario profiles (350, 450, 550, 650, 750PPM) along with the original IS92a, "business-as-usual" curve, and actual global anthropogenic emissions from 1975 to 2010. There are several revelations that can be extracted. First, all WRE scenarios peak within the next 50 years and decrease thereafter. Even at WRE750, which from Table 1.1 translates to roughly 5-6°C increase in temperature, requires decreasing emission rates after 50 years. Second, current anthropogenic emissions already exceed the WRE350, a level which is considered by many researchers and scientists to be the upper sustainable limit. Obtaining the 350PPM limit is not infeasible, however, it would require immense collective emission reduction efforts at a rate that shifts forward the zero emissions point currently set at the year 2080. In addition, achieving zero and net negative anthropogenic emissions at that stage would require early adoption and commercialization of technologies that sequester and consume carbon such as artificial photosynthesis, which is being developed by researchers from UC Berkeley, Cal Tech, and LBNL.

There doesn't exist a "holy grail" or silver bullet technology that will allow us to reach sustainable concentration levels in a reasonable time period (within the next century). Instead, a portfolio of technologies is required with each contributing to some degree to incrementally lower the PPM curve back to a sustainable level. A paper published in *Science* by Pacala and Socolow [246] explains the idea of stabilization or technology wedges where a virtual triangle or wedge can be drawn to represent the pathway transition from BAU to a sustainable level. A near infinite number of smaller triangles within the original wedge can then be drawn to represent the various carbon reducing technologies and strategies. Figure 1.9 shows the representation of the wedges where each wedge plays a crucial role in lowering the emissions curve. The actual number of wedges highly depends on the targeted concentration level and

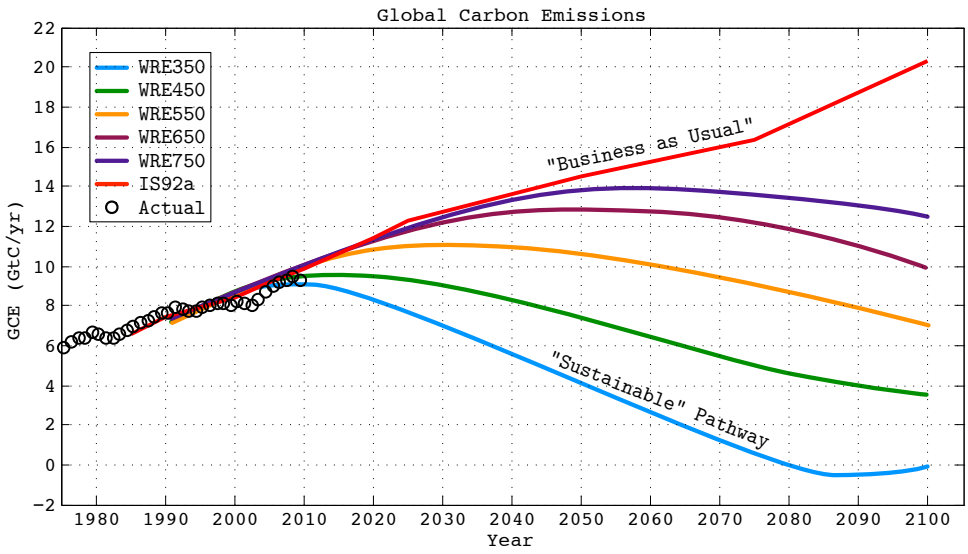

Figure 1.8: WRE scenarios plotted with IS92a (BAU) and actual annual carbon emissions from 1975-2010. WRE curves from [346] and actual data from [107].

the current rate of carbon emissions. At the time when the paper was published in 2004, the carbon emissions growth rate was at 1.5%/year, yielding seven arbitrary equally sized wedges of existing technologies in a 50 year reduction period for stabilization at 500PPM [246]. Their solution made the climate change problem seem manageable and even somewhat trivial. However, their solution was very optimistic and required the immediately deployment of such technologies irrespective of cost.

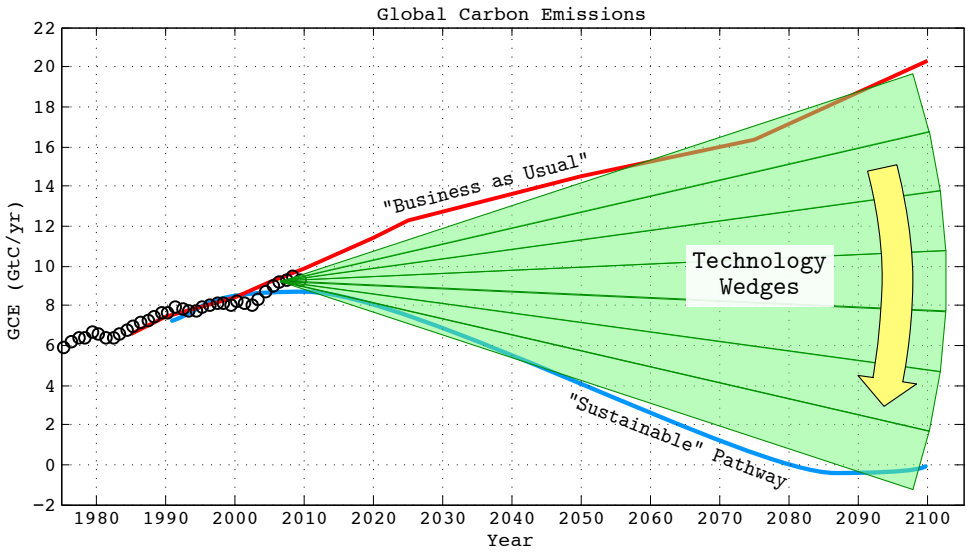

Figure 1.9: Stabilization or technologies wedges to achieve sustainable WRE levels as described in [246].

1.4 Technology Wedges

In their paper, Pacala and Socolow proposed 15 potential wedges to reduce total anthropogenic carbon emission by 25GtC from 2004 to 2054 that were already being deployed at the industrial scale. Their mitigation solution was divided into three categories: efficiency and conservation, decarbonization of electricity and fuels, and natural sinks. For example, an entire wedge can be achieved in the transportation sector by improving the fuel economy of the internal combustion engine (ICE) from 30PMG to 60MPG by 2054[7]. However, most if not all wedges are coupled with each other such that improvements made downstream have less of an impact by the improvements made upstream. Full details of all 15 wedges can be found in [246], which partially resonates from an early paper by Hoffert et al. [142].

A major criticism to Pacala and Socolow's solutions was that they explicitly did not account for costs required to deploy and implement the wedges. Fast forward to nearly a decade later we find that our carbon emissions problem has grown at an accelerated rate and although the slow adoption of technology wedges can not be attributed to costs alone, it is undeniable that economic factors have played a large role. A recent paper by Davis et al. [60] revisited Pacala and Socolow's original assertion of needing seven wedges with the most current data and determined the original seven stabilization wedges would only reach 567PPM. They recalculated that nine stabilization wedges were need to achieve the 500PPM level within the next 50 years. In fact, assuming the SRES A2 scenario to be BAU, as many as 31 wedges would be required to completely phase out carbon emissions [60].

[7]We are heading in the right direction, new CAFE standards approved by the Obama Administration have set fuel economy for cars and light-duty trucks at an equivalent 54.5MPG by 2025[234]

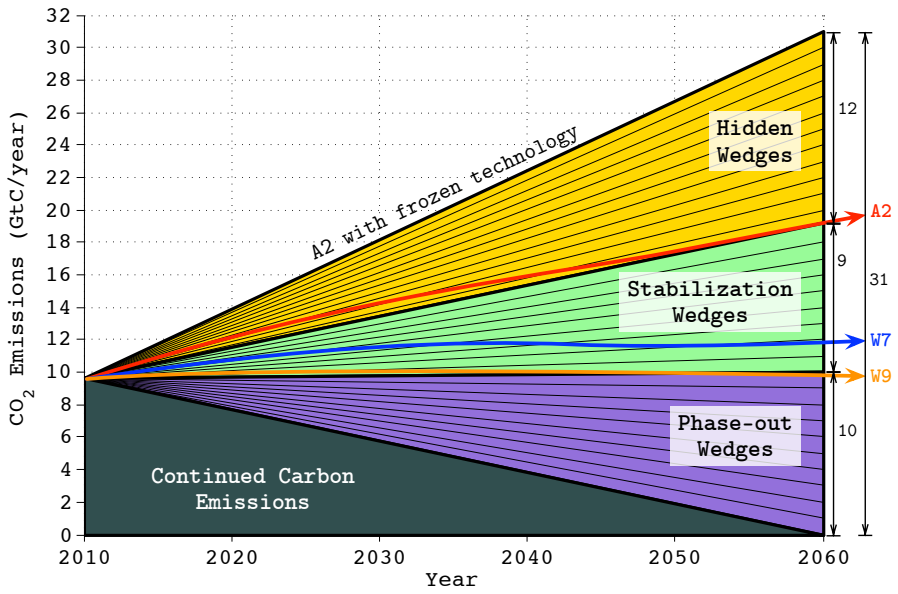

Figure 1.10: Revision of stabilization wedges under the SRES A2 scenario for the years 2010 to 2060. A total of 31 wedges broken down to 12 hidden, 9 stabilization, and 10 phase-out wedges. Reproduced from [60]

Figure 1.10 shows the additional wedges required to achieve Pacala and Socolow's 500PPM level and beyond. The 31 wedges are divided and categorized into three sections: 12 hidden, 9 stabilization, and 10 phase-out wedges. The 12 hidden wedges represent the continued global decarbonization (i.e., reduction in carbon intensity) that is already planned or implemented today regardless of any additional mitigation efforts. The hidden wedges reflect the true "business-as-usual" scenario in which our current level of efforts will simply converge to the SRES A2 scenario by 2060. If by some unfortunate chance that these hidden wedges are are halted (i.e., freezing today's technology) then global carbon emissions would increase an additional 12GtC by 2060. The 9 stabilization wedges represent additional efforts required beyond today's technological progress and the 10 phase-out wedges represent the complete transition to a carbon-free economy (e.g., 100% renewable energy, ceased deforestation, etc.). In all, an average of 22 terawatts (TW) of sustaining carbon-free or fossil fuel equivalent energy is needed to reach WRE500 by 2060 [60], which equates to more than today's total global power demand![8]

Electrifying Transportation

It is evident that the consumption and burning of fossil fuels is a major contributor for global warming. Drastic, if not complete overhaul, shifts to carbon-free energy technologies in the next 50 to 100 years is required to achieve the aforementioned stabilization levels.

[8]Recent world power consumption is estimated to be 18TW [300]

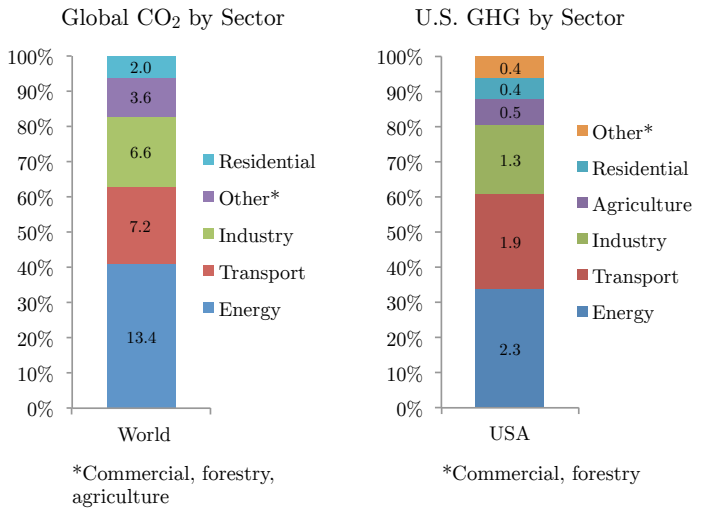

Figure 1.11: Breakdown of the global carbon emissions and U.S. greenhouse gases by sector for 2010 [87][148][254]

A large part of that shift will come from the transportation sector where current efforts are to reduce and eventually eliminate tailpipe emissions through higher efficiencies, light weight materials, and new propulsion technologies such as battery power and fuel cells. As shown in Figure 1.11, for the year 2010 the transportation sector in the U.S. was the second highest contributor to greenhouse gases (second to energy for electricity and heat generation), accounting for $1.9GtCO_2eq$ or 28% of the total greenhouse gases. Globally for that same year, the transportation sector accounted for $7.2GtCO_2$ or 22% of the total CO_2 emissions and the numbers are expected to grow, particularly in developing countries where population and wealth are growing at an accerlated rate. In fact globally, the number of vehicles[9] in operation exceeded the 1 billion mark in 2010, up 3.6% from the previous year, with China seeing a dramatic increase of 27.5% in vehicle registrations [299].

Addressing the global transportation sector alone will not solve our carbon emissions problem, however, it does potentially give us a reduction of at least 2 wedges.[10] Breaking down the transportation sector, as shown in Figure 1.12a, roughly 75% of transportation emissions is attributed to road type vehicles, which translates to 1.5 of the 2 wedges. In the U.S., 60% of transportation or equivalently 75% of road vehicles can be classified as light-duty vehicles (LDV) as shown in Figure 1.12b. If assuming that the rest of the world has a similar breakdown[11], converting LDVs to carbon-free fuels would have the potential impact of an entire wedge.

The technology to transition from fossil fuels to carbon-free already exists in emerging technologies such as electric vehicles (EV) powered by either electro-chemical cells (i.e.,

[9]Excludes off-road and heavy-duty vehicles

[10]For 2010, $7.2GtCO_2 = 1.96GtC$ and that number is expected to grow

[11]China in 2005 had 85% road emissions with 60% being LDV [176]

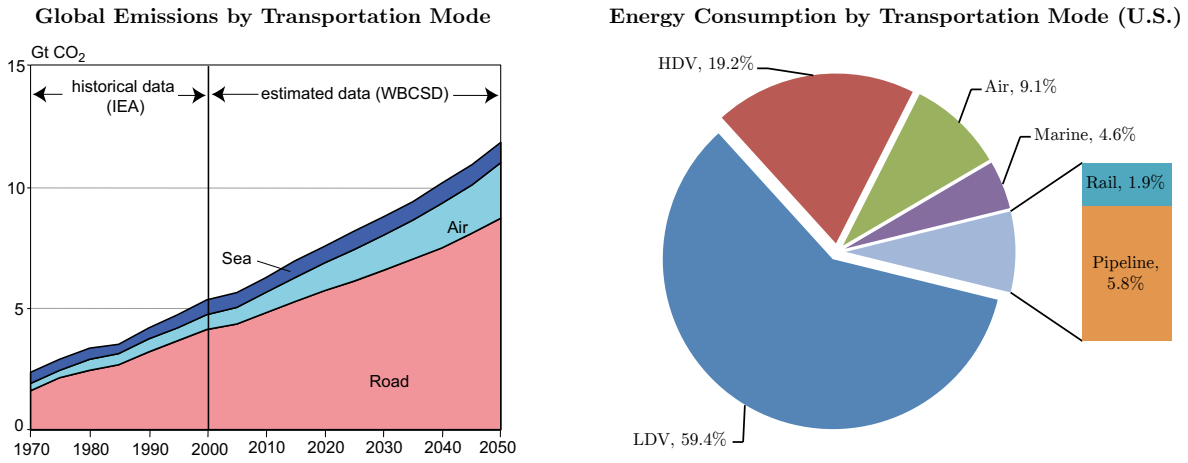

Figure 1.12: Transportation sector breakdown by mode of a) global emission [154], and b) energy consumption in the U.S. [87].

battery) or fuel cells using hydrogen gas as the fuel. Emerging may be slightly misleading because in fact battery powered EVs (BEV) were invented in the 19th century and had success up until the early 20th century when rendered obsolete due to the mass production of the ICE and falling oil prices [271]. It is not until recently EVs began to gain back traction with virtually every automobile manufacturer having some degree of hybrid (gasoline plus battery) option and companies like Tesla Motors and Nissan offering all-electric EVs. Although current EV sales pale against ICEs (0.02% of the global market share in 2012 [206]), EV adoption has accelerated over the years with decreasing costs and improving battery technologies. Figure 1.13 shows the forecast of EV adoption compared to gasoline ICE and hybrids in the U.S., where by 2030 over 50% of new vehicle sales are expected to consist of EVs.

In addition to BEVs, fuel cell vehicles (FCV) are another viable option for carbon-free transportation. For example, the bus fleet from the 2010 Winter Olympic games in Whistler, BC, Canada were powered by Ballard's FCvelocity-HD6 power module, which provide a 62% reduction in greenhouse gas emissions compared to diesel buses [275]. Historically, the concept of hydrogen fuel cells was demonstrated back around the same time as the electro-chemical cell, however, it wasn't until the mid-20th century when fuel cell systems were first developed and eventually used in space applications. From the 1960's and on various fuel cell technologies were investigated for their applicability in transportation, but suffered from high costs and durability issues [104]. Despite their early presence, fuel cell technology for automotive application is still considered in the infant stages. It wasn't until the start this century that FCVs began to be commercialized and as recent as 2007 that they became commercially available to end-users. Current costs are still relatively high and production volumes are low even by EV standards with global sales in 2011 reaching 1600 units (buses

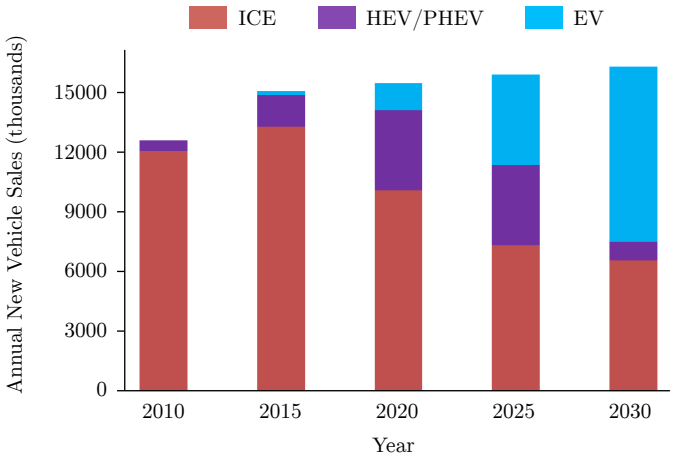

Figure 1.13: Forecast of new vehicles sales in the U.S. by technology to 2035. Reproduced from [22]

included), but are expected to increase to 3000 units in 2012 [105].

The advantage with BEVs and FCVs is that the use or operation phase emits zero emissions, hence carbon-free technologies. However, like gasoline, the fuel, whether it is hydrogen gas or electricity, must be produced or generated upstream and the method to do so is not necessarily carbon-free (in fact it is far from it). Figure 1.14 traces the fuel pathways for various vehicles types including BEVs and FCVs. For BEVs, the primary fuel is electricity, which is generated off the grid from potentially numerous carbon (e.g., coal) and carbon-free (e.g., wind) sources. Operating a BEV in U.S. will have a different carbon emissions than say China or Canada where the average electricity grid mix is 50% coal, 70% coal, and 80% hydro electric for the U.S., China, and Canada, respectively. The same can be said with FCVs where electricity is required for the electrolysis of hydrogen gas or direct conversion using natural gas. Figure 1.15 compares the estimated well-to-wheel (WTW)[12] greenhouse gas emissions for various vehicle technology types in the year 2035 [233]. It is not surprising to see that gasoline powered ICEs lead the way in emissions. However, depending on how the fuel is being produced or generated, "carbon-free" BEVs and FCVs could potentially have even higher emissions as in the case of hydrogen production from distributed natural gas. Furthermore, there doesn't exist an option (at least by 2035) in which the WTW emissions are completely carbon-free. Even with renewable electricity (BEVs) or wind powered electrolysis (FCVs) there are still some levels of carbon emissions along the value stream between generation and distribution. In summary, EVs have the potential to be completely carbon-free due to zero emissions during use, but other aspects in the technology such as the fuel cycle needs to be considered in order to determine if EVs are indeed a pathway to mitigating carbon emissions.

[12]Well-to-wheel is a term to denote all the phases of the fuel cycle from extraction and production (Well) to distribution to fuel consumption during use (Wheel)

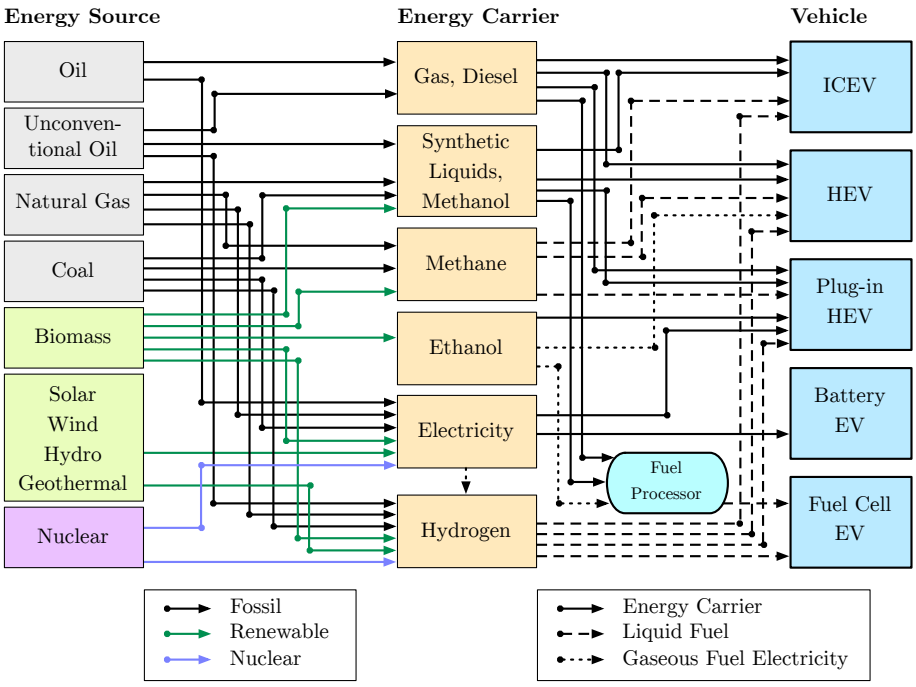

Figure 1.14: Fuel source pathways for various vehicle technologies. Reproduced from [307].

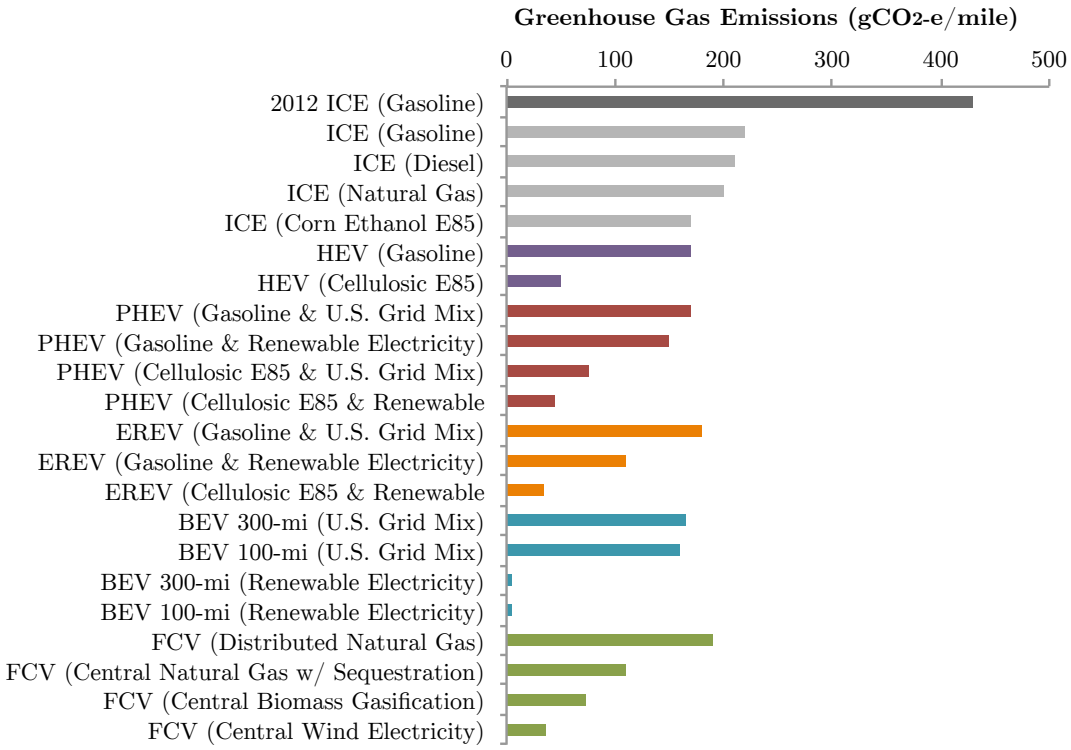

Figure 1.15: Well-to-Wheel greenhouse gases for a mid-size car in 2035 (unless otherwise noted) [233].

1.5 Sustainable Life Cycle Design

As explained in previous section, EVs have the potential to greatly reduce carbon emission due to zero emissions during operation. However, the operation of the vehicle is just one of many aspects or phases that will influence the effective size of the technology wedge. It was already shown in Figure 1.15 that how the fuel or electricity is produced plays a large role in determining the efficacy of the technology. For instance, a FCV fueled by hydrogen produced by central natural gas may potentially yield a net zero or negative wedge despite having zero emissions during use. In fact, it is not only how the fuel is produced that contributes to impact, but other aspects in the EV life cycle that requires consideration such as how and where the vehicle is manufactured, what materials are being used, and how the vehicle is disposed of? These questions allude to the need to holistically view EVs or the displacing technology in all phases of the life cycle, from design conception to end-of-life, and across all levels of the supply chain.

Accounting for the impacts from a holistic perspective is by no means trivial. Take a metallic fork for example, energy and fuel is required to mine the shafts, drill the rocks, extract the ore, crush and smelt the ore, refine the metal minerals, ship the metals to the manufacturer, forge and stamp the metal to form the fork, distribute to the end-user, and finally disposed of at its end-of-life [115]. Then there are the subprocesses for each of the process stages described that are required for proper operation such as process water cooling (PCW) and thermal management (e.g., facility HVAC system) during manufacturing. This example illustrates the hidden complexity of the energy required throughout the product's life cycle even for a common kitchen utensil much less for an EV with thousands of parts and exotic materials.

Despite the complexity, the holistic view of the product's life cycle and the level of precision necessary is imperative for properly assessing the environmental impact. Tools and methodologies have been developed over the years to help designers integrate environmental aspects for sustainable product design and allow manufacturers to assess the environmental performance of their products. One methodological tool that has gained immense popularity over the years in assessing environmental impacts is *life cycle assessment* (LCA). LCA can be defined as [115]:

> "The life-cycle assessment is an objective process to evaluate the environmental burdens associated with a product, process, or activity by identifying and quantifying energy and material usage and environmental releases, to assess the impact of those energy and material uses and releases on the environment, and to evaluate and implement opportunities to effect environmental improvements."

The general LCA framework is shown in Figure 1.16a where four stages are defined: 1) defining the goal and scope (e.g., EVs replacing ICEs), 2) conduct a detailed life cycle inventory (LCI) analysis on both energy and resource flows throughout the life cycle (e.g., a set for EVs and another for ICEs), 3) assessing the potential impacts (e.g., effective carbon

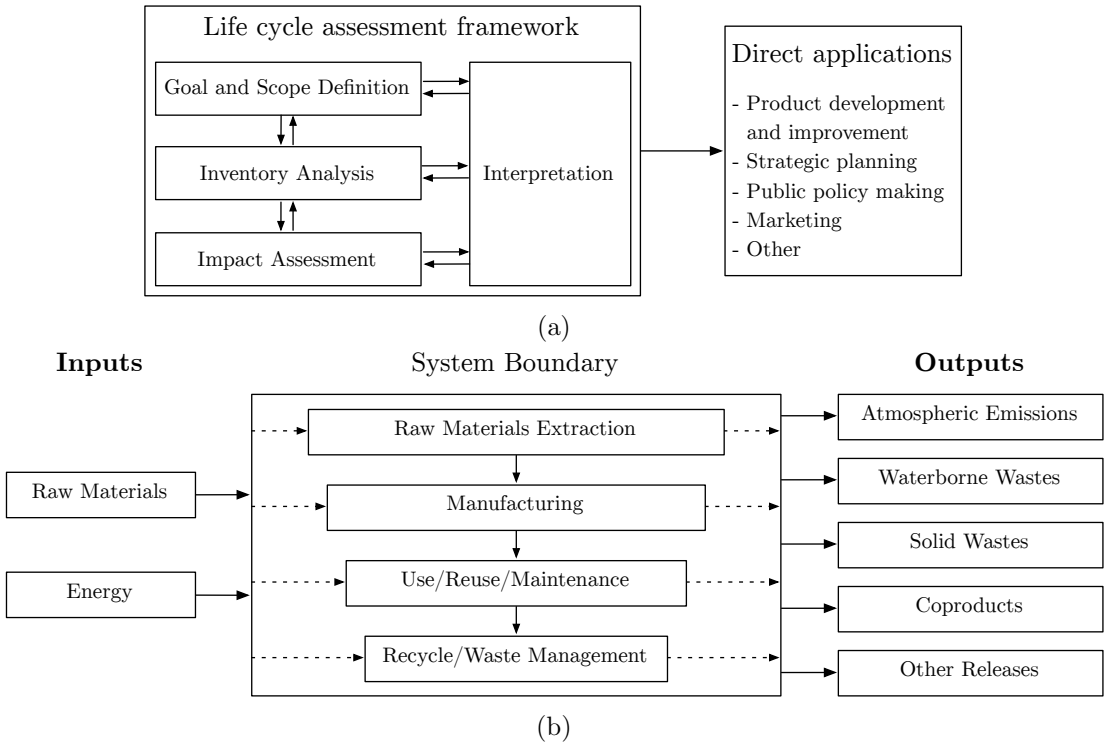

Figure 1.16: a) ISO14000 framework for life cycle assessment [158] b) Inputs and outputs of the life cycle stages [58]

emissions per mile), and 4) interpreting and comparing results (e.g., FCVs manufactured using process A, B, C, and using hydrogen generated from wind has a lower impact than conventional ICEs). The framework can be formulated into a methodology and used as a tool as shown in Figure 1.16b. Much like the fork example, raw materials and energy is required at every stage of the product life cycle, which is defined by a predefined system boundary.[13] The life cycle stages reflect a "cradle-to-grave" type analysis where the product materializes (cradle) to eventually end-of-life or disposal (grave). If the product or parts of the product can be re-materialized at its end-of-life such as being reused or recycled then the analysis is considered to be "cradle-to-cradle." The resulting output flows are traced throughout the entire life cycle and used to evaluate the environmental impact and performance.

LCA can be a powerful tool for designers to holistically assess the environment impacts of a technology or product, however, LCA it is inherently not design oriented [263]. LCA-based tools are advantageous when analyzing existing technologies and products where the materials and manufacturing processes are already established. For new products and emerging technologies where designs are not finalized and the materials and manufacturing processes are not known *a priori*, it becomes very difficult for designers to conduct a comprehensive

[13]Without the system boundary the assessment would be continuous in an infinite loop!

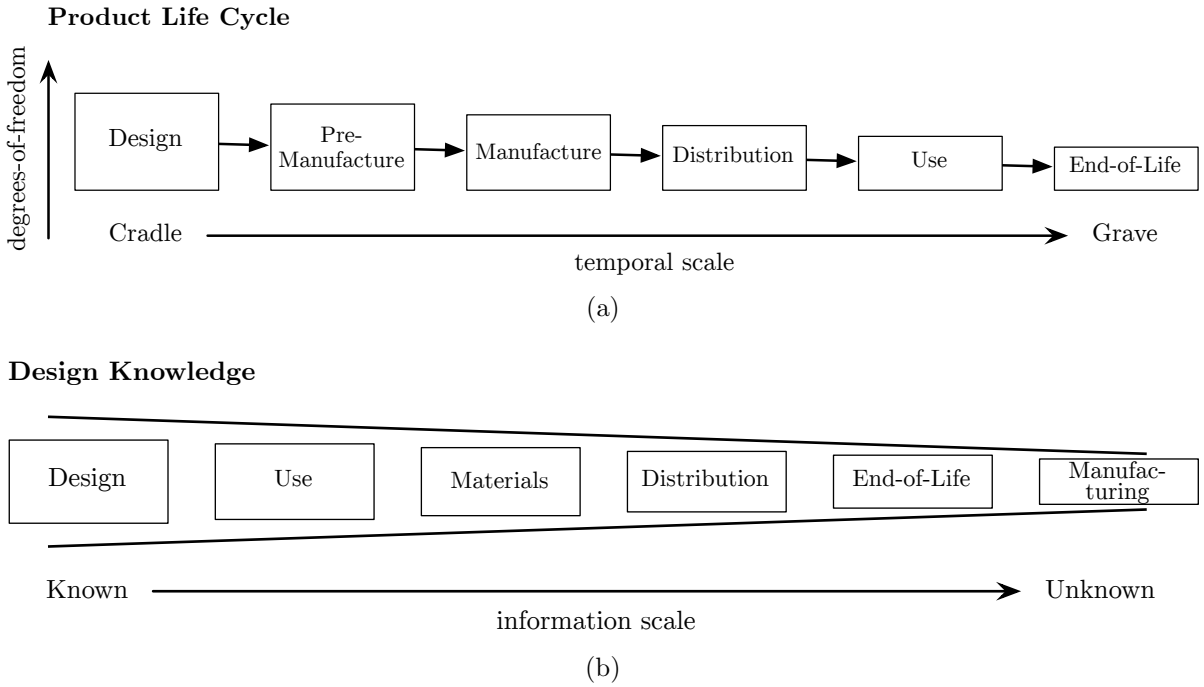

Figure 1.17: a) Level of influence for each stage in the product life cycle, b) Design knowledge of the product life cycle *a priori*

LCA to the level of detail necessary for making environmental conscious decisions. To illustrate, Figure 1.17a shows the typical life cycle of a product from cradle grave. At the cradle, the design phase yields the highest influence or degrees-of-freedom (DOF) over the entire the product life cycle and each stage thereafter has less flexibility than the one before it. Therefore, changes made in the design stage will propagate throughout all stages in the life cycle. For an existing product, the propagation and flows can be traced since each stage in the temporal view, as in conventional LCA, is visible. However, for new products, the temporal view does not exist and the designer designs the product based on the product information scale as shown in Figure 1.17b. While the order of the stages after design is arguable and will depend on the nature of the product, the decreasing level of information after design remains consistent. What the designer is most knowledgeable is the design itself (e.g., shape, appearance) and functionality, represented by the use phase. The designer may also have some knowledge regarding the material selection depending on the nature of the product, although, the exact choice is usually unknown due to the intimate relationship with manufacturing. From the material level and on the scope narrows dramatically with manufacturing potentially being the the least known due to the number of processes and subprocesses involved.

This is where the discontinuity lies in sustainable product design. The designer, who has the most influence on the product, has insufficient knowledge on environmental trade-offs

between the various potential pathways and intricacies to materialize the product. Especially when designing a complex product such as an EV the number of design DOFs may reach tens of thousands of possible combinations in terms of material selection, manufacturing processes, and supply chain considerations. Simultaneously between environmental trade-off, cost considerations, using life cycle costing assessment (LCCA), for each design change and corresponding implications need to be taking account. One of the key takeaways from Pacala and Socolow's proposed sustainable wedges and later by Davis et al. is that in today's economy the adoption rate of a new sustainable technology is highly dependent on cost. A prime example is the adoption of EVs, particularly FCVs where current estimated automotive fuel cell system cost is around \$200/kW [14] [160] compared to around \$36/kW [257] for an equivalent gasoline fueled ICE. Understanding the holistic trade-offs is crucial for a sustainable, in both environmental and cost, design and once a design path is chosen it is typically irreversible, or at the very least extremely difficult to make correctional changes due to costs, time constraints, and so forth.

The aim of this dissertation is to therefore propose a framework followed by various models that expands on the existing linear LCA and LCCA and tools to create an integrated sustainable life cycle design (iSLCD) model that parameterizes all phases in the product life cycle to design, particularly material selection and manufacturing processes. The iSLCD concept is depicted in Figure 1.18 at a high level perspective emphasizing the three pillars in the triple bottom-line. A true sustainable solution will take into account environmental, economical, and social impacts, which is revolved around all phases of the product life cycle and ultimately intimately integrated with design.

[14] At a production volume of 1000 units per year. Current production volumes are roughly a magnitude lower.

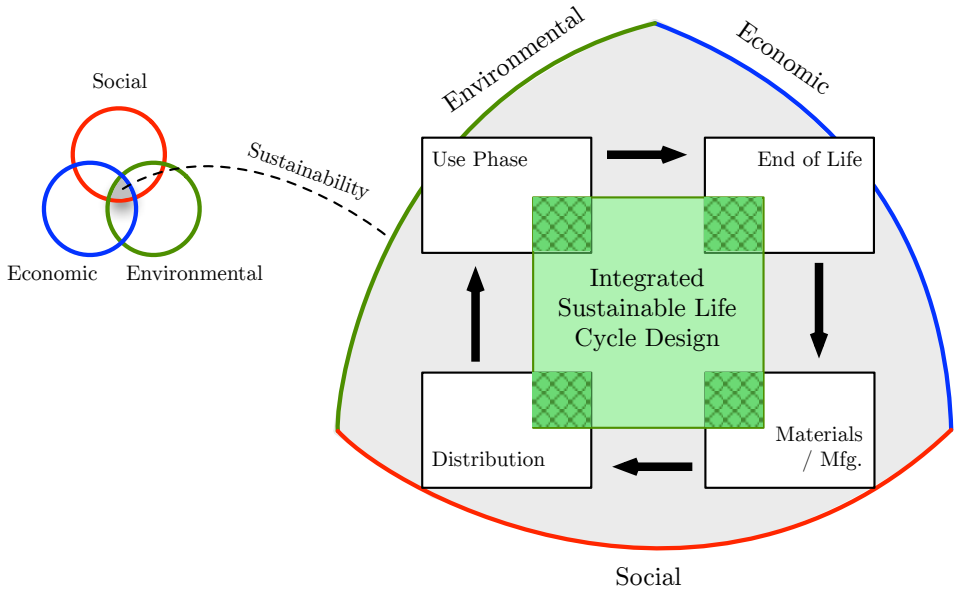

Figure 1.18: Novel integrated sustainable life cycle design framework

The accuracy of the iSLCD model will highly depend on the completeness and level of detail of the manufacturing phase model. The material selection with influence the appropriate manufacturing processes, which will then determine the machine tools and conditions (e.g., manufacturing line, facility requirements, etc.) for production. Cost will play a large role in the supply chain and will influence the production location and distribution network. Ultimately, the iSLCD model will allow the designer to obtain the most optimal pathway (depending on the trade-offs) or help make more informed decisions for a solution that contributes to a net positive sustainable wedge.

1.6 Dissertation Structure

The remaining structure of this dissertation is broken down into two parts: Part 1 (includes this chapter) focuses on the iSLCD framework and relevant manufacturing models, and Part 2 applies the iSLCD framework and model as a case study on polymer electrolyte membrane (PEM) fuel cells with the assistance from Daimler-Benz AG. A more detailed description is as follows:

- Chapter 2 will cover a review on sustainable life cycle design with a large emphasis on LCA, the current LCA framework, and touching on existing LCA tools. The focus then shifts to the manufacturing phase model where an introduction and overview of green

manufacturing is given. The modeling aspect of green manufacturing is divided into five levels referred to as the scales of green manufacturing (SGM): process, machine tool, production line, facility, and enterprise. The chapter concludes with the framework on integrating the SGM with LCA and LCCA.

- Chapter 3 focuses on the key levels within the SGM using unit process modeling. An introduction and overview of unit process modeling is given along with the analysis of several manufacturing processes that are pertinent for the fuel cell case study in Part 2. In addition, the facility model is proposed that models the energy consumption of a HVAC system for a given heat load. The chapter concludes with an overview and methodology for uncertainty analysis for stochastic modeling of the iSLCD.

- Part 2 begins with Chapter 4 where the focus shifts specifically to PEM fuel cells for automotive applications. An introduction of the history, various fuel cells technologies, and components is given. The focus narrows to PEM fuel cells and an overview of the relevant components and design practices. In addition, a brief literature review on the environmental and cost impacts for PEM fuel cells is given.

- Chapter 5 covers the current state-of-the-art practices for PEM fuel cell manufacturing that is publicly available. Detailed explanations of the materials and manufacturing processes are covered.

- Chapter 6 specifically focuses on modeling the manufacturing of Daimler's PEM fuel cells with the emphasis on environmental impact and cost. The iSLCD framework from Chapter 2 is formulated followed by setting up the appropriate unit process models and listing out the input design parameters and assumptions.

- Chapter 7 goes over the results from the iSLCD model accompanied by a thorough discussion. The results include data uncertainty, which is modeled using a Monte Carlo technique. Furthermore, a sensitivity analysis is conducted specifically focusing on the design attributes and influence of design to the SGM. Key parameters are identified that show the greatest influence and where further research improvements should be made.

- Chapter 8 concludes the dissertation and highlights recommendation to improving the design and manufacture of Daimler's PEM fuel cell.

- The last chapter is the appendix, which will consists of all the data, background calculations, and assumptions used in the modeling. The appendix specifically contains information for chapters 2, 3, 5, and data for 6 and 7.

Chapter 2

The iSLCD Framework

Recall from the last chapter the conclusion that the environmental impacts of a product should be holistically assessed over the product's entire life cycle. It was also highlighted that the design phase in the product life cycle carries the greatest influence in controlling the environmental impacts and that economical considerations for each design change should simultaneously be addressed. Building on the notion of a holistic product life cycle, a novel framework, integrated sustainable life cycle design (iSLCD), was introduced that aimed at incorporating design at every life cycle phase while harmonizing the three pillars sustainability.

To further explore the idea of an iSLCD, the framework can be partitioned into three core areas: sustainability, life cycle design, and integration. The definition of sustainability or sustainable development is best described by the Brundtland Commission's report as [18]:

> *"development which meets the needs of current generations without compromising the ability of future generations to meet their own needs"*

Brundtland's definition is concise yet ambiguous, and gives two criteria for sustainable development - to "meet our current needs" and "meet our future needs." The ambiguity comes from determining what exactly is "meeting needs," which can be very subjective. For some it could mean economic prosperity, or preserving the environment, or social justice and equality. Collectively, however, "meeting needs" pertains to all-of-the-above. The idea that sustainable development in fact encompasses the importance of having strong economic and social development while preserving natural resources and the environment throughout all time horizons.

Achieving sustainable development is not trivial and requires re-thinking on how products and services are developed. The first step to implement a sustainable design framework is to recognize that design needs to embody and aim to balance the three pillars of sustainability - economical, environmental, and social, or commonly referred to as the triple bottom line (TBL). To illustrate, Figure 2.1 shows a Venn diagram of the TBL and the potential key design considerations for each of the three pillars. Each pillar has its own set of elements for

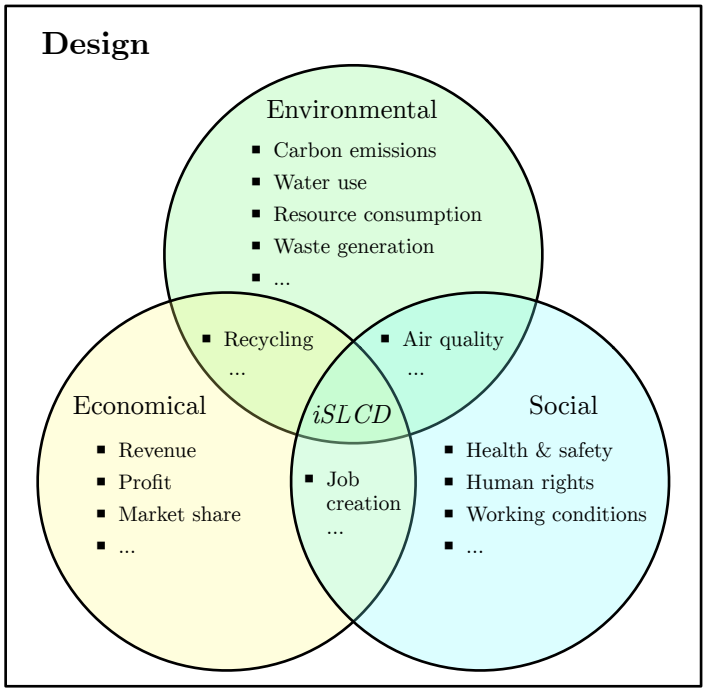

Figure 2.1: Design elements embodying triple bottom line. Adopted from [338]

satisfying the needs of that pillar. However, addressing the elements that intersect multiple pillars, such as recycling, can be more effective and yield greater benefits and balance. Likewise, implementing the iSLCD framework, which intersects all three pillars, provides the most effective means to achieve sustainable development.

In practice, implementing the sustainable development framework using the TBL can be very challenging and complex due to the potentially large degrees-of-freedom and consisting of metrics in different domains. The conventional and current practice approach is to treat each pillar of activities separately as a portfolio [124]. The reason being is that each element in TBL is optimized separately due to lack of systematic framework or methodology to track, categorize, and evaluate the sustainability performance [338]. To address these shortcomings, there have been several attempts to develop an intuitive sustainable product design framework or methodology. Hacking and Guthrie [127] proposed a new hybrid framework that integrates existing frameworks - Integrated Assessment, Triple Bottom Line Assessment, and Sustainability Assessment, in a three-dimensional framework with the focus on "strategicness", "comprehensiveness", and "integratedness." Wang and Lin [338] proposed a TBL framework that links the each pillar with a sustainable management system, life cycle analysis, and reverse logistics. They developed a "sustainability index" system that assigns an index to each of the TBL pillars (seven total including the intersections). The index is meant as a metric for evaluating the contribution of the total value-added and total cost of the whole system. To obtain the final overall sustainability index a multi-objective analysis (MOA)

optimization technique was suggested. A similar TBL framework was proposed by Hoffenson et al. [141] where several objective functions representing the product design parameters (e.g., material cost, yield, injury rate) were optimized for each of the three pillars. A MOA approach was taken using a weighted scheme technique where the results highly depended on the choice of weights. Along the lines of MOA, Zhang and Haapala [361] emphasized the importance of the TBL in manufacturing and how multi-criteria decision making (MCDM) can act as a feedback loop to influence the operations during manufacturing.

Building upon previously proposed frameworks and methodologies of the aforementioned studies and tailoring towards the iSLCD framework, a novel methodology for sustainable product design is proposed. Shown in Figure 2.2, the sustainable design is an iterative process that begins with the generation of design concepts from the pre-design phase where information gathering takes place such as addressing user needs, understanding market trends, and incorporating regulations. The set of design parameters are simultaneously fed into the three core modules: environmental life cycle assessment (ELCA), or LCA, economic life cycle cost assessment (LCCA), and social life cycle assessment (SLCA). Each module has its own separate analysis and corresponding metrics. However, each module stems from the same product life cycle flow, which enables the integration. A forth module is included to conduct the sensitivity and scenario analysis to account for the uncertainty in both the product life cycle flow and in the data. The sensitivity analysis is an integral part of the design iteration and facilitates in pinpointing certain aspects in design that carry more influence. The output of the modules are further evaluated using a multi-criteria decision making (MCDM) technique, similar to what has been previously proposed in literature.

The efficacy of the iSLCD methodology is highly dependent on the construction and formulation of the product life cycle (PLC). As previously detailed, the iSLCD framework captures the holistic view of product design from raw material extraction to end-of-life and links each phase back to design. However, the existing holistic view only covers what is called the temporal scale of the PLC, where the occurrence of the next phase is dependent on the previous phase (e.g., raw material extraction comes before manufacturing). The temporal scale allows identification of the phases that should be considered, however, it does not provide information on how the phase is constructed. Therefore, a second orthogonal dimension, the spatial scale, is introduced that defines how each of the phases are constructed. The necessity of the spatial scale is more obvious in phases such as raw materials and manufacturing. For example, defining the mass of the material needed for the product resides on the temporal scale whereas the source or location of the material origins lies on the spatial scale. The inclusion of the spatial scale to the materials and manufacturing phases is the basis of what will be covered in a later section as green manufacturing. The added spatial dimension also provides another view of the intricacies involved in the PLC and allows more degrees-of-freedom for the module integration.

The integration of all three assessment modules forms the ideal methodology for the iSLCD. However, in its current state, the implementation of all the modules is simply not feasible. The infeasibility attests more to the fact that SLCA is considered to be a relatively upcoming and nascent field in sustainability where models have not been fully developed

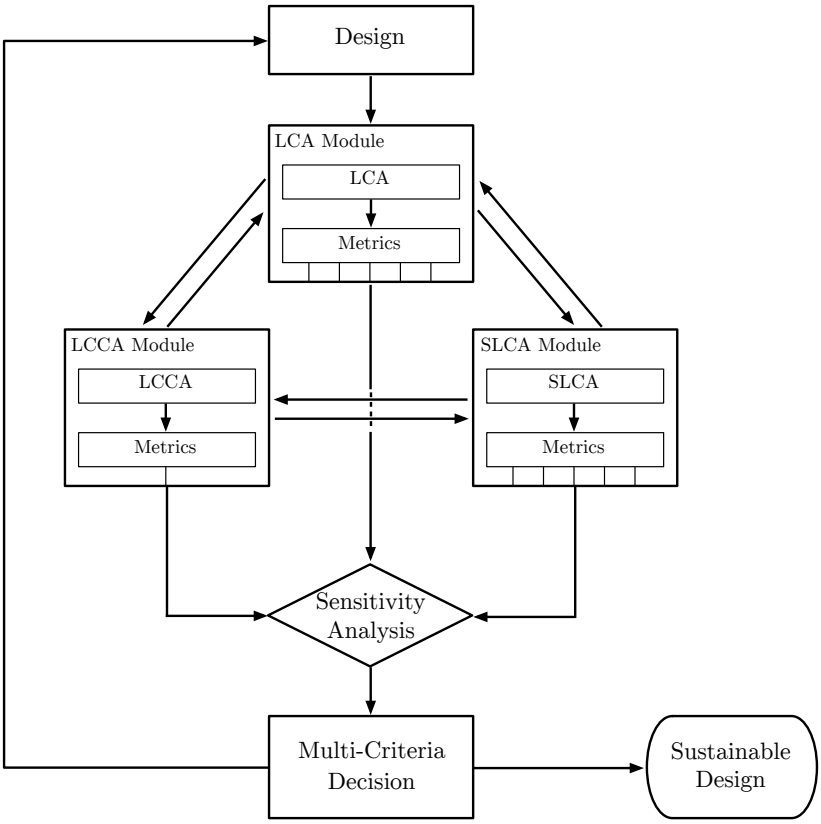

Figure 2.2: The iSLCD methodology flow chart

or well defined. Current developments on SLCA show a similar framework as conventional LCA. However, there has not been a consensus on metrics, impact categories, how to measure the metrics, and what to include in the framework. The perception of social impacts is very variable with different research institutions and corporations providing a unique definition and metrics. For these reasons, SLCA will not be considered in this dissertation although it is recognized as an equally important pillar for sustainability. More details on the SLCA framework and metrics can be found in [168][78][24].

The remaining sections of this chapter will specifically focus on the LCA and LCCA modules, the holistic temporal/spatial scales of PLC, and the complete integration. The MCDM phase will not be covered explicitly, but is considered in the case study. The lack of emphasis is due to the fact that most common MCDM and MOA techniques involve a weighting scheme or designer's preference such as multi-attribute utility theory (see [39] and [321]), which tends to be highly subjective. As a substitute, a trade-off analysis will be employed in the case study.

2.1 LCA Background and Tools

The notion of life cycle assessment (LCA) was first introduced in the previous chapter. The intention of this section is to provide a deeper understanding of the LCA framework and acknowledge the various types of tools and methods for practitioners. From a historical perspective, early signs of LCA have dated as far back as the late 1960's and early 1970's with studies on resource and energy efficiency, pollution control, and solid waste [119]. LCA became particularly useful in the context of comparing alternative designs or technologies such as paper versus plastic grocery bags and plastic versus glass bottles as classical examples. In these instances it was recognized that the environmental burden extended further beyond the scope of the use phase with major contributions coming from the production, transportation, end-of-life phases. Despite the early presence, LCA to some is still considered to be a young and evolving application [265]. It was not until the 1990's where LCA started to see a rapid growth in adoption. With the creation of the ISO-14000 family standards, which supported environmental management and practice. Shortly thereafter the ISO-1404X standard on LCA was established, which included ISO-14040: LCA-principles and framework that was first introduced in 1997, and ISO-14044: LCA-requirements and guidelines, in 2006 [119].

LCA Framework

LCA is a technique for assessing the cradle-to-grave environmental impacts of a product, process, or service, and to enable environmentally conscious decisions [158]. From here on, products, processes, and services will simply be referred to as products. From the ISO14040 standard, the LCA framework is broken down into four stages: 1) goal and scope definition, 2) inventory analysis, 3) impact assessment, and 4) interpretation. This section provides a brief overview of each of the four categories. For more in depth explanation can be found in the EPA report "Life Cycle Assessment: Principles and Practice" [58].

Goal and Scope Definition:

The LCA framework begins with defining the goals and scope of the assessment that pertain to incorporating life cycle environmental impacts into the decision-making process. Doing so involves defining the applicable methodology and metrics as well as determining the type of information needed to add value, the necessary accuracy of the results needed to add value, and how the results should be interpreted and portrayed. The scope of the methodology should include the four phases of a product or process life cycle: raw material extraction, manufacturing, use/reuse/maintenance, and recycle/waste management. In addition, the following items are to be addressed or identified:

- **Functional Unit**: a product system may have a number of possible functions in which the functional unit is the measure of performance of a particular function. It is classified a normative parameter for which all analyses and comparisons are referenced

to [158]. For instance, the functional unit of a beverage container could be the volume of the contained liquid.

- **System Boundary**: primarily pertaining to process based LCA, the system boundaries dictate the cut-off criteria in the LCA model. The system boundaries should be chosen such that inputs and outputs at the boundaries are elementary flows[1][158] and that, ideally, further expansion of the boundaries will yield insignificant changes to the results [94].
- **Data Quality**: the quality of the data will depend on the intended audience to whom the final results are reflected to. The intended audience, whether internal or external, will influence the overall cost and time involved to perform the LCA. Generally speaking, data quality should address: time related coverage, geographical coverage, technological coverage, precision/completeness and representativeness of the data, consistency and reproducibility of the methods used throughout, sources of the data and their representativeness, and uncertainty of the information [158].
- **Attributional vs. Consequential**: attributional and consequential LCA are contrasting goals aimed to answer two different questions. In an attributional LCA, the goal is to attempt to answer the magnitude of the environmental impact and is often used to compare different products and services with the same functional unit. In a consequential LCA, the goal is to determine the change in environmental impact for a given product or service as a consequence of a decision made upstream.

Inventory Analysis:

Inventory analysis or life cycle inventory (LCI) can be considered as the heart of the LCA framework. All relevant data collection and calculation procedures are determined in the LCI for quantifying the inputs and outputs of the assessment. Depending on the goals and scope of the project, a LCI may include material and energy flows (similar to material flow analysis [305]), atmospheric, waterborne, and soil emissions, solid wastes, and other releases pertaining to the entire life cycle of a product. The accuracy and precision of the LCI will depend on the the data quality and comprehensiveness of the model. The following are key attributes of the LCI:

- **Unit Process**: the building blocks of the LCI model and is the most elementary portion of a product system in which data are collected [158]. Unit processes are bounded by the system boundaries and link together in a systematic fashion to form the compete life cycle.
- **Allocation**: is the technique of partitioning and allocating the raw materials, resources, and energy input flows of a unit process to the corresponding output product systems [158].

[1] An elementary flow is the basic unit of material or energy entering or exiting the system under study

- **Process-based LCI**: a methodology that takes the conventional approach of assessing the material and energy flows required to build and run a specified system. Process based LCI has the potential to be very accuracy and precise (depending on the system boundaries), however, at the cost of being overly complicated and time consuming, with some instances involving infinite iterations [266]. To avoid the situation of an infinite iteration, sensitivity analysis should be preformed to determine the boundary at which further iterations will not significantly alter the output results.
- **Economic Input-Output (EIO) LCI**: an alternative methodology that takes advantage of a country's economy activity in terms of monetary transactions from one industrial sector of the economy to another. The economic activity is represented by a square input-output (IO) table or matrix consisting of all the distinct industrial sectors where the input (per dollar invested) to one sector (row) correlates to the output (per dollar returned) of all the remain sectors inclusively (columns). The square economic IO matrix is multiplied by an array of environmental outputs corresponding to each industrial sector. The final output is an impact (e.g., carbon emissions, energy consumption, toxicity) per unit dollar input for a given sector. The advantage of the EIO methodology is the avoidance of the infinite boundary iteration problem by covering the entire economy. However, its main disadvantage is the level precision due to aggregated sectors and data. Furthermore, EIO tables typically take years to compile (e.g., typically around 5 years for the U.S.), which potentially reduces the representativeness quality of the data. For more information on EIO LCA see [136].
- **Hybrid LCI**: takes advantage of the strengths in both process and EIO based LCI. The limitations of time and data for process based LCI and lack of granularity for EIO-based LCI are thereby mitigated. Generally, there are two approaches for conducting a hybrid LCI: bottom-up approach where process data is supplemented by EIO data, or top-down where specific EIO data is enhanced by process data [266]. For more information on hybrid LCI approaches see [55][304].

Impact Assessment:

Impact assessment or life cycle impact assessment (LCIA) is the phase that systematically associates the output of the LCI analysis to environmental impact, human health, and impact to the ecosystem such as resource depletion. A key attribute of the LCIA is the formulation of stressors. Stressors are a set of conditions that provides the linkage to an environmental impact. For instance, carbon emissions leading to global warming.

In a LCIA, the degree of stressor is divided into two methodologies - midpoints and endpoints. Endpoint LCIA models are the end consequences, typically categorized as human health, ecosystem impacts, and resource depletion, due to the physical impacts from the LCI analysis. However, the modeling between the physical impacts and endpoints can be highly complex leading to high degrees of uncertainty. Therefore, a common simplification is to model midpoints, which reflects the relative potency of the stressors. For instance, damage

to the ecosystem endpoint can be linked to greenhouse gases or the global warming potential midpoint and hence reducing the global warming potential has a high probability of reducing the damage to the ecosystem. Common midpoints include global warming potential, acidification, eutrophication, and human toxicity. The following points list out the methodology required for conducting a LCIA:

- **Impact Categories**: the first step in a LCIA is to select and define the relevant impact categories corresponding to the goals and scope of the project (e.g., global warming, acidification, eutrophication).
- **Classification**: assigning and possibly combining the LCI results to the impact categories and partition the LCI results if necessary (e.g., assigning carbon dioxide emissions to the global warming category).
- **Characterization**: converting and combining the classified LCI results into their representative indictors using science-based conversion factors for direct comparison (e.g., converting the potential impact of carbon dioxide and methane into an equivalent global warming potential). Table 2.1 gives an overview of possible impact categories and corresponding classifications and characterizations.
- **Normalization**: an optional step according to ISO [49], normalization is a technique where different characterized impact scores are normalized to a common reference in order to be compared.
- **Grouping/Weighting**: an optional step according to the ISO [49], the impact categories are sorted and ranked according to the priorities defined in the goal and scope. A weighting scheme can be applied to the different impact categories to obtain a single indicator score. This is an optional step due to the high subjectivity of ranking and determination of the weights.

In practice, numerous of LCIA methodologies have already been created by various organizations that span multiple countries. Each LCIA methodology is unique with different classification and characterization factors focused either midpoints, endpoints, or both. For the same LCI, LCIA results may differ depending on the choice of methodology. For instance, indicator results between the Danish EDIP1997 and the Dutch CML2001 were found to be, in some cases, two orders of magnitude different for the impact categories under human toxicity and ecosystems [79]. There is no widely accepted standard or universal methodology that associates LCI data with specific environmental impacts with consistency and accuracy. The selection of the appropriate methodology becomes highly subjective and should be chosen on the basis of the goals and scope of the project [158]. An overview of some of the major LCIA methodologies is found in Table 2.2.

Interpretation:

Table 2.1: Various Impact Categories with corresponding Classification and Characterization factors [58]

Impact Category	**Scale**	**LCI Data (i.e., Classification)**	**Possible Characterization Factor**
Global Warming	Global	Carbon Dioxide (CO_2) Nitrogen Dioxide (NO_2) Methane (CH_4) CFCs	Global Warming Potential
Stratospheric Ozone Depletion	Global	CFCs HCFCs Halons	Ozone Depleting Potential
Acidification	Regional Local	Sulfur Oxides (SO_x) Nitrogen Oxides (NO_x) Ammonia (NH_4)	Acidification Potential
Eutrophication	Local	Phosphate (PO_4) Nitrogen Oxide (NO) Nitrogen Dioxide (NO_2) Nitrates	Eutrophication Potential
Human Health	Global Regional Local	Total releases to air, water, and soil	LC_{50}
Resource Depletion	Global Regional Local	Quantity of minerals used Quantity of fossil fuels used	Resource Depletion Potential
Water Use	Regional Local	Water used or consumed	Water Shortage Potential

Life cycle interpretation is the final stage of the LCA framework. The purpose of the interpretation is to present the findings of the LCI and LCIA and provide conclusions and recommendations in a transparent and effective manner. Results of the LCI and LCIA are evaluated in regards to completeness and consistency, and should factor uncertainty and sensitivity analysis [158]. In addition, any limitations and assumptions should be clearly laid out.

LCA Limitations

Life cycle assessment has become the most objective tool for assessing the environmental impacts of a product. However, despite the resourcefulness, LCA does have its drawbacks and limitations. The first and foremost is simply that the inherent intent of LCA is to reflect environmental impacts, thus leaving out economic and social considerations for sustainability [119]. In addition, LCA can be extremely time and resource intensive, highly subjective in

Table 2.2: Summary of the major LCIA methodologies [49]

	Developer	Climate change	Ozone depletion	Respiratory in-organics	Human toxicity	Ionizing radiation	Eco-toxicity	Ozone formation	Acidification	Terrest. eutrophication	Aquatic eutrophication	Land use	Resource consumption
CML2002	CML	O	O	n/a	M	O	O	M	M	M	M	O	M
Eco-indicator99	PRe	E	E	E	O	O	n/a	E	E	E	n/a	E	E
EDIP1997/ 2003	DTU	O	M	O	M	O	M	M	M	M	M	n/a	M
EPS2000	IVL	E	E	E	E	O	E	E	O	O	O	E	E
Impact2002+	EPFL	O	O	E	M,E	O	M,E	E	M,E	n/a	M,E	O	E
LIME	AIST	E	E	M	E	n/a	O	M,E	M,E	n/a	M,E	O	E
MEEuP	VhK	O	O	M	M	n/a	M	M	M	M	M	n/a	O
ReCiPe	RUN+PRe+ CML+RIVM	M,E	E	M,E	M,E	O	M,E	M,E	M,E	O	M,E	M,E	E
Swiss Ecoscarcity07	E2	O	O	O	O	M,E	M	O	O	O	O	M,E	O
TRACI	US EPA	O	O	M	M	n/a	M	M	M	O	M	n/a	O

O: Available in the methodology
M: Midpoint model available
E: Endpoint model available

terms of the scope (e.g., system boundaries), and LCIA methodologies with poor spatial resolution (e.g., treat local and global information and effects the same way) [25]. There is also the discrepancy between actual versus potential effects, for instance, climate change from carbon dioxide versus the global warming potential of methane.

Arguably the greatest limitation is the lack of completeness and representativeness of the LCI models. Conventional inventory models are generally static and steady-state comprising of a number of processes that have linear input-output relationships [25][128]. Therefore, there is a need to improve the temporal resolution during modeling and incorporate the effects of non-linearity. For instance, changes in the environmental impact with product demand. Furthermore, generic or aggregate data may mask technologies that are more environmentally burdensome. The limitations in the LCI models may potentially create large uncertainties and thereby undermining the efficacy of the environmental impact assessment.

LCA Tools

In the last decade or so, numerous environmental assessment methodologies and tools have been proposed and developed. The number has been steadily increasing and is suggested that over 30 various eco-tools have been developed [263]. The type of tool also varies widely from qualitative intensive to more quantitative and data intensive. In general, the tools can be classified into the following three categories: checklist based, LCA based, and green quality function deployment (QFD) based.

Checklist based tools are the most trivial and provide qualitative "rule-of-thumb" for green design. A good example is the '12 principles of green engineering' [8], which recommends the use of non-hazardous materials, reduce waste, use renewable materials and energy, and so forth.

LCA based tools are the most diverse in terms of methodology, scope, and precision. On one end of the spectrum there are qualitative and semi-qualitative LCA tools such as the somewhat simplistic streamlined LCA (s-LCA) method where stages in the product life cycle are ordinal ranked (typically an integer from 0 to 4 where higher number is preferable) based on several environmental indicators (e.g., energy use, resource consumption) [115]. On the other end of the spectrum, there are fully comprehensive process based LCA tools commercially packaged in a PC software such as the GaBi Software by PE International. Although more time intensive and costly (can cost tens-of-thousands of dollars), tools such as GaBi provides a graphical interface for process flow diagrams with thousands of available processes and numerous LCIA methodologies and the ability to conduct parametric sensitively and uncertain analysis using stochastic techniques. There are other types of LCA based tools in between such as the Economic Input-Output LCA (EIOLCA) web based tool developed by Carnegie Mellon University [153]. Despite the drawbacks of EIO assessments, the EIOLCA tool is particularly attractive because it offers comprehensive sector information for several different countries and for several impact categories such as greenhouse gases and toxic releases, at free of cost.

There are also industry specific LCA tools. For example, the Greenhouse Gases Regulated Emissions and Energy Use in Transportation (GREET) Model by Argonne National Laboratory provides a well-to-wheel life cycle for various transportation fuels [9]. Other example is the Building for Environmental and Economic Sustainability (BEES) tool developed by the NIST that combines a partial LCA and life cycle costing for the buildings and construction industry [112]. A non-exhaustive list of various LCA based tools are summarized in Table 2.3.

Green QFD based tools incorporate environmental impacts of a product as part of the customer needs. Data for both customer needs and environmental needs are collected and correlation functions are developed to identify hot spots from both quality of the product and environmental concerns. A major drawback of the QFD-based tools is the subjectivity of the correlation, which is typically developed by those with lack of life cycle considerations [263].

Table 2.3: Various commercially available LCA tools and software

Tool	Developer	Interface	Type	Precision	No. Methodologies	Cradle-Grave?	Uncertainty Analysis?	Cost
GaBi	PE International	PC software	Process	*****	12[1]	Yes	Yes	$$$$$
Simapro	PRé	PC software	Hybrid	****	18[2]	Yes	Yes	$$$
Umberto	ifu Hamburg	PC software	Process	***	6[3]	Yes	Yes	$$
CES Selector	Granta Designs	PC software	Process	***	LCI	Yes	No	$$
Sustainable Minds	Sustainable Minds	Web	Process	**	1[4]	Limited	No	$
EIOLCA	Carnegie Mellon	Web	Input-Output	*	LCI	Yes	No	Free

[1] Version 6.2
[2] Version 7.3
[3] Version 5.5
[4] Uses TRACI 2.1 for version 2013

2.2 Life Cycle Costing

Life cycle costing assessment (LCCA) is a technique for estimating the total-cost-of-ownership (TOC) of a product, and is a crucial step in determining the product's economic viability. The TOC concept draws many parallels to cradle-to-grave LCA analysis where included costs span from inception to disposal. For every design decision that influences the environmental impact will also influence the costs along with additional cost externalities such as general and administrative (G&A) and profit margin. A brief overview on LCCA is covered with more detailed explanations can be found in [19][114][186].

The concept of TOC involves every costs that is required to acquire, sustain, and dispose or decommission. The appropriate LCCA model highly depends on the situation, however, the framework remains the same. Figure 2.3 shows the basic cost trees for acquisition costs (Figure 2.3a) and sustaining costs (Figure 2.3b) [19]. The acquisition costs are the initial and recurring investments for design and development (e.g., R&D), procurement (e.g., equipment, facility, etc.), and process improvements (e.g., upgrading to higher efficiency pump). Sustaining costs are essentially the behind-the-scene or supporting costs required to maintain operations and ensures from the delivery of the product all the way to the disposal.

In practice for a designer, obtaining data for every component of the acquisition and sustaining costs may be impractical or simply not feasible. There are numerous external factors that are often out of the designer's control such as forecasting and gather information on the

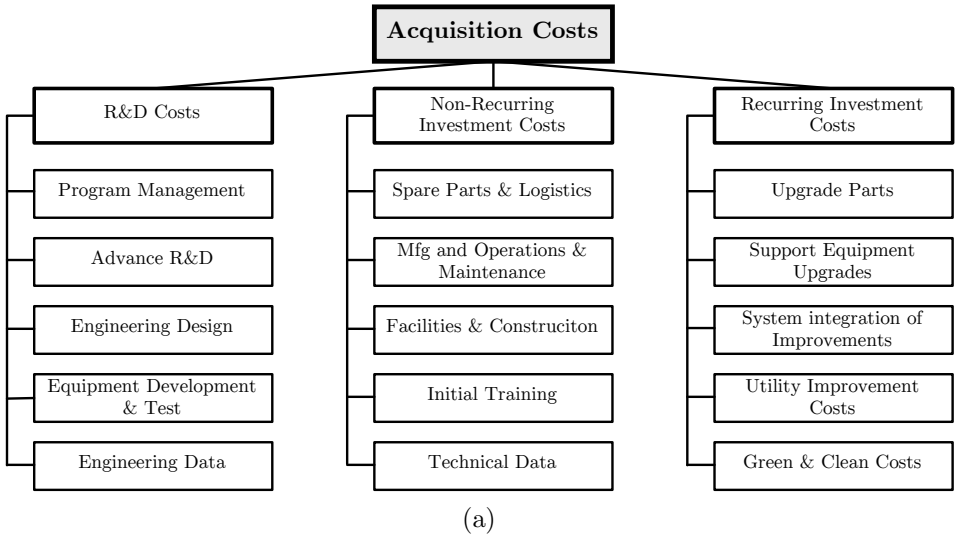

(a)

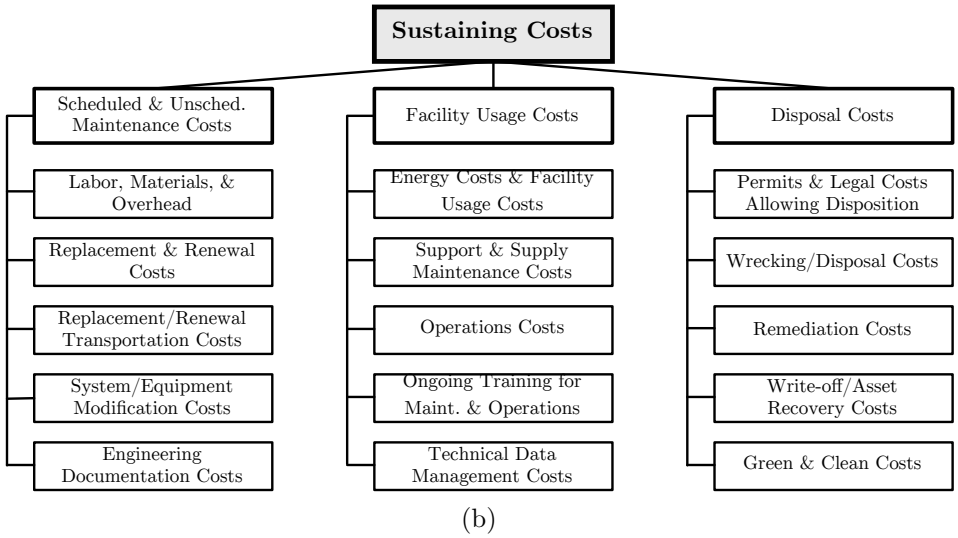

(b)

Figure 2.3: Cost tree for a) acquisition costs, and b) sustaining costs [19]

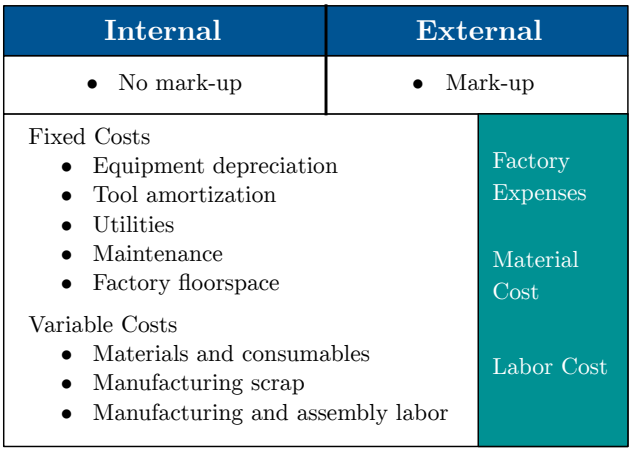

Figure 2.4: Factors included in the DFMA. Adopted from [162]

economy, market, competition, profit margins, and so on. Therefore, it makes more sense to take a design-for-manufacturing and assembly (DFMA) approach that focuses particularly on understanding the cost components for the manufacture of the product. Pioneered by Geoffrey Boothroyd and Peter Dewhurst in the early 1980's, DFMA is considered a subset of LCCA that quantifies loosely used terms such as "manufacturability" and "producibility" by emphasizing on the design for ease of manufacture of the collection of parts and the ease of assembling those parts into the final product [32]. The DFMA technique is heavily used by OEMs, primarily as a tool for simplifying design and benchmarking competitors and suppliers. Furthermore, the DFMA can be integrated with a LCA analysis by linking to an EIO database.

DFMA

This dissertation herein uses a hybrid version of DFMA and LCCA, which will be simply referred to as DFMA, as a benchmarking tool for understanding the economic impact as a result of a change in design or scenario. Hence, the DFMA herein excludes certain overhead such as internal profit margin, general and administrative (G&A), and research development and engineering (RD&E) expenses. The factors included in the DFMA can be broken down into three categories: factory expense, material costs, labor costs. Factory expenses include machine tool cost, factory floor space, utilities, etc. Figure 2.4 list the cost components included in the DFMA. For more information on DFMA see [32].

From the manufacturers perspective, the total annualized cost to manufacture a product is given by the economic cost model (modified from [126] and [161]). The formulation of the DFMA cost equation is as follows:

$$C_y = m \cdot (C_c + C_r + C_{oc} + C_p + C_{fs} + C_M - C_s) \tag{2.1}$$

Where

C_y: total annualized cost in constant dollars

C_c: amortized capital/system investment with interest

C_r: replacement or disposal cost

C_{oc}: operating cost (including material, labor, and maintenace)

C_p: property tax

C_{fs}: facility floor space cost

C_M: end-of-life salvage value

C_s: tool depreciation deduction

m: mark-up factor to reflect non-direct manufacturing costs

Other components not incorporated include income tax deduction, warranty, and insurance. The total annualized cost, C_y, represents the equivalent annual payment throughout the lifetime of the capital (e.g., machine tool) and is calculated using the capital recovery factor (CRF). The cost components in Equation 2.1 can be grouped into two categories - fixed costs, which consists of C_c, C_r, C_p, C_{fs}, C_s, and variable costs which are the operating costs, C_{oc}, such as utilities, material and consumables, labor, and maintenance. The equations for each component in Equation 2.1 can be found in section A2 of the Appendix.

Capital Recovery Factor

The amortized capital or system cost denotes the effective series of annual payment reflecting compounding interest or discount. The compounding future cost must be adjusted to the present value for fair comparison. The effective annual payment is given by the Capital Recovery Factor (CRF), which is commonly used term in economics to represent the effective uniform loan payments at a periodic interval [126] and is the ratio of the periodic payment to the total loan sum. The CRF is a function of the time interval (e.g., machine tool lifetime), t, and compounding interest rate per the time interval, i:

$$CRF(i,t) = \frac{i(1+i)^t}{[(1+i)^t - 1]} \tag{2.2}$$

Discount Rate

The discount rate, often used synonymous with the real interest rate, reflects the absolute interest rate at which money is borrowed or lent and is used to normalize cash flows of different time scales to a common time for equivalent comparisons [186]. The idea stems from the principle that, generally, people prefer to received goods and services now rather than later and thereby associating a "penalty" (i.e., interest) for extended periods. All future costs are converted to their equivalent present day cost such that the amount of money needed to be invested in the present day at an some interest/discount rate would equal the value of the future costs at the future time of occurrence. In the trivial case when the discount rate is zero, the influence of timing does not matter and the future value is only dependent on inflation.

Depreciation

Depreciation stems from the idea that things tends to lose value or worth over time and use. Determining the depreciation of a commodity is a very complex and depend many external factors that can be highly subjective. For the purpose of the DFMA, the depreciation specifically focuses on the manufacturing capital: factory infrastructure and industrial equipment. There are numerous methods of modeling depreciation, each with varying complexity, and the most straightforward is to use the straight line (uniform) method due to difficulty in evaluating the salvage value and depreciation profile *a priori* [114]. The straight line method is modeled by linear interpolation of the initial to salvage value over a given period of time. Other modeling methods include sum-of-years digits, declining balance, and multi-straight line. The depreciation rate can then be expressed as:

$$D_k = \frac{C_{cap} - C_{salv}}{t_{life}} \tag{2.3}$$

Where C_{cap} is the initial capital cost at time, $t = 0$, C_{salv} is the final salvage value or worth at the end-of-life time, and t_{life} is the time period, typically the lifetime of the captial.

Mark-Up

Mark-up is the fraction of the OEM cost that represents the overhead including profit, G&A, and R&D. The actual mark-up percentage varies from one manufacturer to the next and will depend on the externalities such as product maturity, the specific market, and competition from similar products. Typically, the mark-up rates will vary with the production volume or factory capacity utilization [161][160]. At low volumes, or more specifically low utilization, of production the mark-up is generally very high to account for the invested risk and engineering efforts. At high volume and high utilization, the margin for overhead exclusive of profit is very small and the resulting mark-up is simply equal to the profit margin. The proposed DFMA only takes mark-up into account for commodities that are external to the manufacturer such as a purchased part from a supplier (as shown in Figure 2.4).

Inflation

The purchasing power of a currency is influenced by the inflation rate (or deflation rate) and it accounts for the rise in cost of a commodity over time [126]. General practice is to exclude inflation in LCCA provided the assumption that inflation covers all costs equally [186]. However, although inflation is not explicitly part of the DFMA, it does factor in determining the effective discount rate:

$$i' = \frac{1 + i_d}{1 + j} \tag{2.4}$$

Where i' is the effective discount rate, i_d is the discount rate, and j is the current inflation rate for a given country. For consistency, all monetary values are adjusted to the equivalent purchasing power of the 2013 U.S. dollar using the CPI Inflation Calculator provided by the U.S. Bureau of Labor Statistics [184]. Non-U.S. currency will be converted to the U.S. dollar equivalent for that year before adjusting for inflation. The lone exception is using the EIOLCA database, which then will be scaled to the 2002 U.S. dollar (the year of the most recent EIO database).

2.3 Green Manufacturing

It has become clear that among the product life cycle stages, materials and manufacturing play a crucial role in influencing the triple bottom line in terms of environmental impact and cost. For the LCA, materials and manufacturing dominate the LCI and for the LCCA, materials and manufacturing is the core of the DFMA. Although it is ubiquitously known that the design stages carries the great influence in determining the outcome of the product, it is the materials and manufacturing stage that enables the design leverage. The reason being is that essentially what is being modeled in DFMA and a large majority of LCA are the materials and manufacturing flows and the realization that, in some capacity, the remaining life cycle stages can be influence by the materials and manufacturing. For example, the selection of suitable materials for enabling lower power consumption or higher performance such as the transition from aluminum to copper wiring in integrated circuits. Another example would be the improvement of automotive drivetrain performance (or alternatively increased fuel economy) by increasing manufacturing precision to achieve lower gear surface roughness [134]. There are also economic implications, for example, Hewlett Packard in the mid-1980's was able to reduce manufacturing costs by five-fold by using DFMA and concurrent engineering through collaborative efforts with design engineers working alongside manufacturing engineers [32]. Furthermore, the manufacturing phase can be considered to have the largest degrees-of-freedom in terms independent control variables, or knobs that can be adjusted without changing the functional outcome of the product. Examples of such knobs include: process technology, machine tool type, mold die design, line balancing, and tool utilization. Hence, placing the emphasis on manufacturing can potentially allow greater insight to the optimal design.

Cognitive awareness linking manufacturing to TBL has lead to a paradigm shift towards sustainable manufacturing, a relatively new field that places emphasizes on the three pillars of sustainability pertaining to manufacturing. A subset of sustainable manufacturing that deals specifically in the realm of environmental sustainability is the area of green manufacturing, which is often considered as the first step towards sustainable production [77]. The term green manufacturing herein will be inclusive of materials (i.e., materials and manufacturing) and covers anywhere from environmentally benign material selection, to process optimization (e.g., reduce scrape/waste, minimize energy consumption), to intelligent machine tool design, and up to facility layout and construction and supply chain effects. Each aspect of green manufacturing will have some, if not large, implications in the environmental impact and cost. In addition, there are externalities that should be taken into consideration such pressure from the government in terms of regulations, penalties, and tax benefits/incentives, scarcity of resources and risk such as exotic and rare materials, pressure from society/consumers/customers/competitors, marketing strategy (the perceived value of being environmentally friendly), and so on [77].

Implementing a green manufacturing strategy can be quite challenging due to the complexity and intricacy of manufacturing processes, particularly on the front of simply where to begin. Modeling such sophisticated systems can be difficult considering the level of precision necessary to make impactful environmental and economical conscious decisions. It was recognized that there was a need to parse these complex systems in a way where manufacturing elements are separately analyzed. A suitable framework, shown in Figure 2.5, was proposed that classified the manufacturing elements into manufacturing "levels of study" consisting of two orthogonal frameworks - spatial (organizational) and temporal levels [266].

Each cell in Figure 2.5 represents an integrated view of the manufacturing design levels. On the spatial axis there are levels that describe all activities in the manufacturing system, which consists of: 1) product feature, 2) machine/device, 3) facility/line/cell, and 4) supply-chain. On the orthogonal axis, the temporal view describes all levels pertaining to the design and manufacturing life cycle: 1) product design, 2) process design, 3) process adjustments, and 4) post-processing [266]. Using the manufacturing design level matrix as part of the green manufacturing framework requires the identification each cell, how they are connected, and the flow of information from one cell to another.

Another intriguing representation of the various manufacturing levels is the so called "Google Earth view" of manufacturing, which expands on the spatial level in the sense of combining both the spatial and temporal scales. Coined by Dornfeld et al. [77], this "Google Earth view" of manufacturing takes the perspective of the entire enterprise (consisting of all internal and external operations) and "zooms" in to the level where product features are defined. The "Google Earth view" will be referred from here on as the scales of green manufacturing (SGM), and comprises of the following scales:

- **Process:** Work is directly applied to the part to shape, form, treat, coat, etc. The design and materials also dictates the machine tool type. The process scale includes

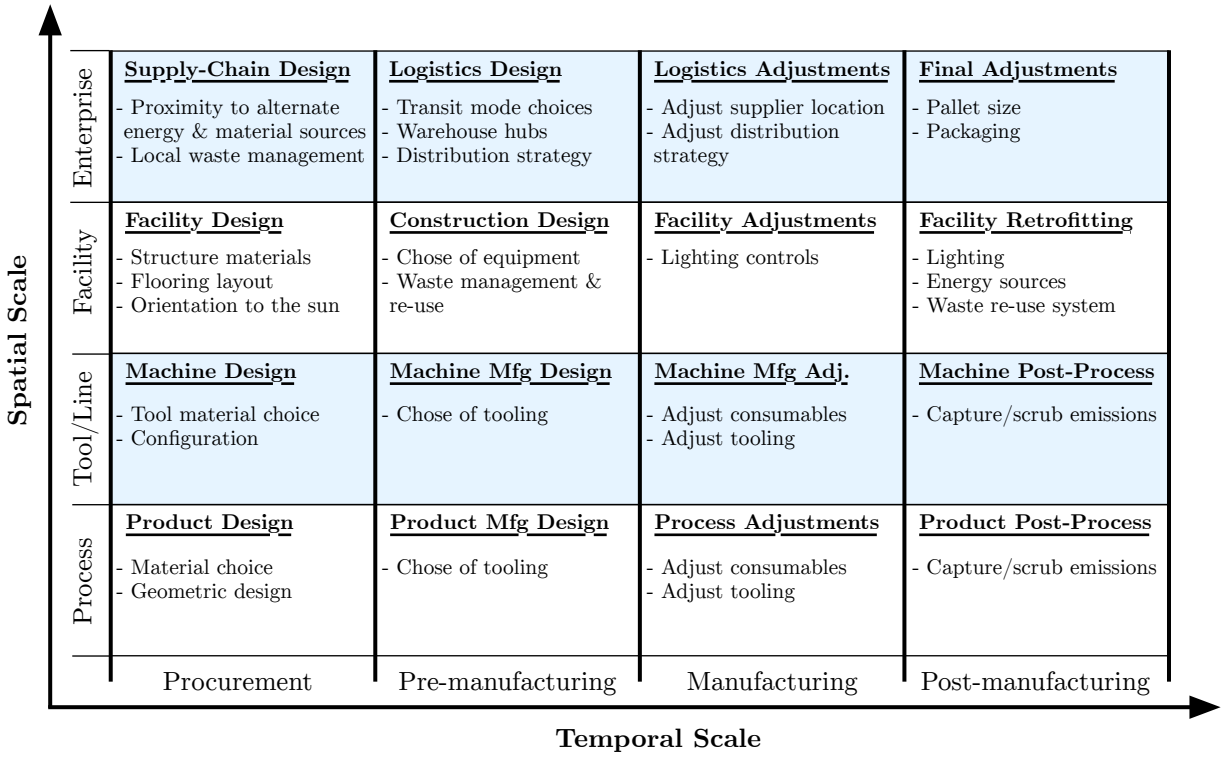

Figure 2.5: Temporal versus Scale of manufacturing. Reproduced from [266]

process energy, processing time, water, materials, consumables, compressed air, and scrap and waste.

- **Machine Tool:** Selection of the machine tool influences power consumption, consumables and resources, cycle time (e.g., tool setup, part removal), die mold and tooling, and will dictate the how the production line is set up including any ancillary equipment to support the machine tool (e.g., chillers).

- **Production Line:** Process flow, the addition of non-value added process steps (i.e., clean, inspection), line utilization/balancing, ancillary equipment for supporting the line, external machines such as robots, cycle time by transfer stations, dictate facility requirements.

- **Facility:** facility resources (e.g., DI water), thermal management (e.g., HVAC), line size influences the facility size, organization of multiple lines, overhead

- **Enterprise:** supply-chain, location of the facility, how energy is produced, local government regulations, how far to ship items, environmental regulations, availability of materials and resources, economy/cost-of-living, and consumer behavior.

The concept of the SGM has also been brought up by similar works in literature, notably by Herrmann et al. [140], where three layers, instead of five scales, were proposed - process/machine, factory building, and national/international supply chain. However, the SGM provides a higher spatial resolution for an integrated model and incorporates the effects of the enterprise.

It is important to point out that each scale is not mutual exclusive and is in fact a function of the other. Changes made from the process scale will have the most leverage and will percolate through all scales of manufacturing. Take an injected molded cup as an example. The material, size, and thickness of the cup wall will dictate the injection molding process heat to melt the polymer and mold pressure to form the cup. The cup size and mold pressure will then dictate the type and size of the injection molding machine (IMM) tool. The size of the IMM tool and process (e.g., cooling time) will dictate the cycle-time thereby influencing the production line scheduling. The heat released from the production line due to the process and IMM will influence the heat loading on the HVAC system. Finally, at the enterprise level, where that cup is manufactured will influence the carbon emissions released from the local power generation utility and the magnitude of which will be proportional to the total energy consumption from the process, tool, line, and facility.

Literature Review

In the context of green manufacturing, numerous researchers have investigated or at least considered one or more scales in their analysis on environmental impact or cost. Some, such as Niggeschmidt et al. [235], have proposed a green manufacturing framework for measuring, characterizing, and optimizing process level data. Others, such as Reich-Weiser et al., have stressed the shortcomings of strictly focusing on the process scale for process-based LCA where overwhelming amounts data can make the modeling and extrapolation to the other scales extremely difficult and often infeasible. Figure 2.6 categories several notable papers in green manufacturing in terms of emphasis for each scale.

As seen in the figure, the majority of studies surveyed have focused on the process and tool/line scales to some degree. This does not come as a surprise since some of the earlier research in the field of green manufacturing have primarily focused at the process scale. Mattis et al. [209] was one the first to investigate the energy consumption of the injection molding process at the process and machine tool level. Theoretical models were constructed for modeling the energy consumption during polymer plasticizing in addition to energy require for machine operations such as clamping and part ejection. The models were used to identifying the tool operations that consume the most amounts of energy. Akbari et al. [5] proposed, at the time, a novel concept to evaluate the environmental impact of machine tools by including the impacts of the part itself and the entire production line. It was concluded that potentially more energy could be saved with processes and materials that make the product last longer or have higher quality despite an increase in energy during manufacturing. Along those similar lines, Kordonowy [183] examined the breakdown of power consumption for various machine tools and found significant non-valued added

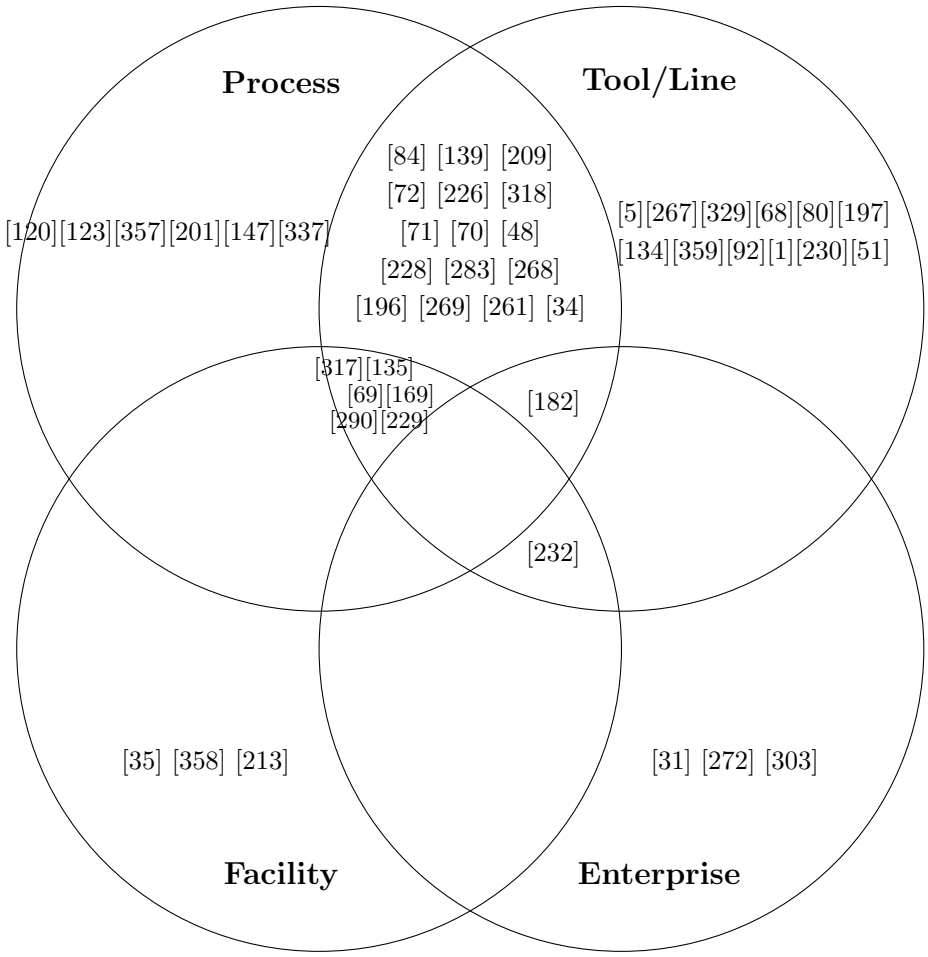

Figure 2.6: Overview of various works in the areas of SGM.

process energy that is required to idle the machine tool and that there was a large discrepancy between the theoretical minimum and actual energy consumption. Building on Kordonowy's work, Gutowski et al. [121] published a paper that looked at a wide variety of machine tool processes and compared the processing energy density (energy per volume) as a function of the processing rate (e.g., material removal rate). The analysis showed that processes with lower processing rate relative to processing precision (e.g., nano-manufacturing) had higher energy densities. A more recent study by Reinhart et al. [268] compared the material and energy efficiency of two different slot surface hardening process technology flows for the same product feature. The results showed that it was more efficient to replace induction hardening with grind-hardening due to a shallower depth-of-cut milling operation that could be simultaneously finish and surface harden with grind-hardening.

Fewer studies have included the impacts at the facility and enterprise scales. However, there is increasing awareness to include these scales as part of the manufacturing system. Kara et al. [169] stressed the need to measure and monitor energy consumption data at

all scales within the factory and the factory itself in order to development an appropriate strategy to reduce the energy consumption. The framework focused on the methodology to collect energy data on the machine tool, for the entire line and ancillary equipment, and at the facility main power line, as wells as suggesting the required sampling interval for each scale. Using a similar framework, Diaz et al. [69] conducted a LCA analysis on a milling process under different working environment scenarios. Power consumption data was collected from a CNC milling machine tool during milling of an AISI 1018 steel part. A LCI analysis was performed on the machine tool and factory HVAC and lighting energy was included in the analysis. However, the facility level analysis was subject to large uncertainty due to the use of aggregate HVAC data found in literature. Studies that have linked the enterprise scale with manufacturing have been scarce. Reich-Weiser et al. [267] developed an eco-tool using an EIO-based LCA for the manufacture and transportation of photo-voltaic (PV) cells. The study investigated the environmental impacts during the manufacture of the PV cells with consideration of production (i.e., facility) location, which yielded different environmental impacts depending on the local energy grid mix. The study also looked at the transportation network and carbon emissions associated for various production to installation locations. A more comprehensive study on the facility and enterprise scale was the work by Ng et al. [232], which took a streamlined algorithmic approach to determine the material and energy consumption of a sheet metal stamping plant. The study took into account material consumption, machine tool power, indirect energy consumption such as HVAC, lighting, fans, etc., and transportation emissions by part mass and distance travelled. The accuracy was further reduced by using machine tool power consumption data that was based on the tool power rating rather than actual or even modeled power data. Although the study did include the major aspects of the manufacturing scales, the analysis was overly simplified where each scale was static and treated as mutually exclusive.

Perhaps the most comprehensive or complete study found in terms of integration was the work by Thiede et al. [317]. The study was built upon the manufacturing systems framework proposed by Herrmann et al. [140] and created a model simulation to visualize the energy flows. The model was applied to a couple case studies where measured process level parameters were used to measure and model the energy consumption of the machine tool and facility support systems (e.g., compressed air, cooling water) energy consumption as a function of production volume. Perhaps the main drawback of the model was the lack of consideration for the HVAC energy consumption and impacts at the enterprise scale.

There were no studies were found that included all the scales of green manufacturing. The closest by Herrman et al. and Thiede et al. were very comprehensive, however, did not include the complete integration and coupling and only focused on one or two metrics such as energy consumption.

2.4 The Integration

In this chapter, an overview of the LCA framework was given including a discussion on tools available and the limitations of the framework, emphasizing the need for more comprehensive LCI models. Also presented was an overview of LCCA with the focus on DFMA and how the cost analysis can be integrated to create a more comprehensive EIO LCI model. An introduction to green manufacturing was given, highlighting the importance of the spatial scale in the product life cycle with the idea of integrating the scales of green manufacturing as an added dimension to the conventional linear and temporal product life cycle. This section aims to detail the final core area in which the aforementioned frameworks and methodologies are integrated to form the iSLCD framework.

As currently presented, the iSLCD framework primarily focuses in the domain of the temporal scale. By integrating the spatial scale of the SGM to the iSLCD framework and expanding the temporal scale of the product life cycles phases, a more comprehensive iSLCD framework is created. Shown in Figure 2.7, this enhanced iSLCD framework incorporates the full cradle-to-grave product life cycle zodiac (PLCZ)- 12 primary life cycle phases that undergoes beginning-of-life to end-of-life. The PLCZ is also vertically symmetrical in the sense that every beginning-of-life phase has a parallel end-of-life phase. The closed-looped PLCZ surrounds the five scales of green manufacturing, which can be thought as residing in the dimension orthogonal (i.e., through plane) to the temporal scale. The design phase in the conventional product life cycle is removed to a separate cloud similar to the original iSLCD framework. Again, the idea is that design encompasses every life cycle stage at both the temporal and spatial scales as opposed to limiting to individual phases such as design-for-use, design-for-manufacturing, design-for-recyclability, and so on. The dedicated design phase is replaced with an Earth phase for recognizing that all product flows for the raw material and extraction phases initiates and terminates with the Earth.

The phase flows (arrows) on the PLCZ represent the primary flows of the product. Embodied in every phase are the additional secondary product and material flows (e.g., fuel, consumables, replacement parts) as well as energy flows, waste streams, and transportation flows. In the case for secondary products, a collaborative effort between every enterprise connected to the same supply chain is required. In addition, the separate iSLCD frameworks for each sub-product should be carried out in parallel with the primary product.

The idea that every product life cycle phase embodies the SCM is quite unique. In each phase there is a corresponding enterprise and value chain, which could be the same enterprise as the product manufacturer or an enterprise along the supply chain. Phases containing the SGM such as raw material extraction and product manufacture are more pronounced and straightforward. The SGM for other phases have the applicability of the scales to a varying degree. For instance, a delivery service enterprise is associated to the product distribution, or a maintenance/service enterprise is associated to product use, or an enterprise that handles recycling. Each of those enterprises will have scales analogous to the SGM. Using the repair and refurbish phase as an example, processes involved can be related to manually disassembly (e.g, unscrewing, disconnecting parts) and the machine tool could be represented by manual

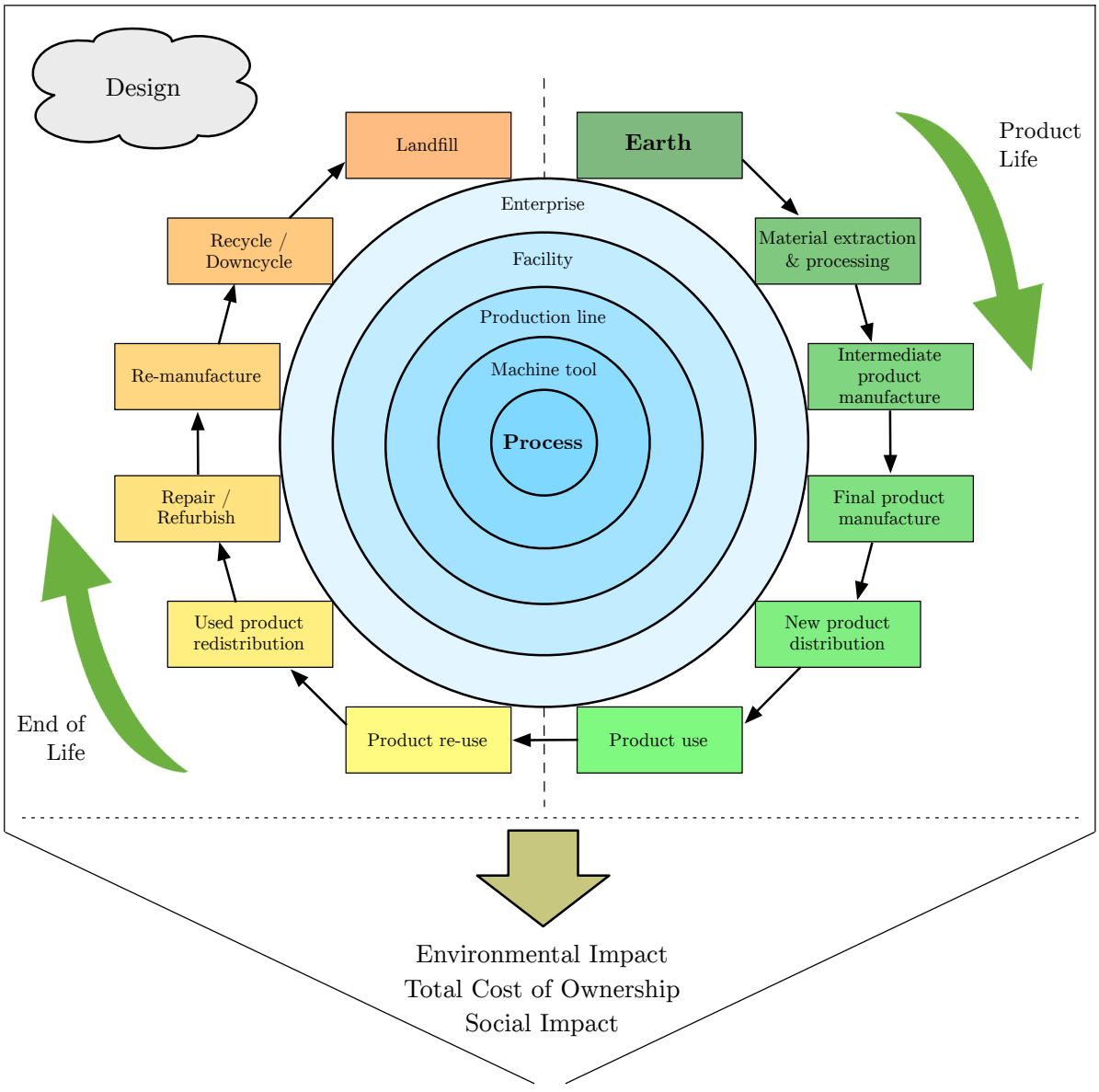

Figure 2.7: Holistic product life cycle zodiac with integrated SGM

labor. Although more ambiguous, the Earth and landfill phases involve natural processes such as photosynthesis and decomposition, respectively.

The inclusion of the SGM allows modeling of the iSLCD more intuitive and consistent. Figure 2.8 shows the spatial representation of each scale and the flows (e.g., energy, materials) that interlink one scale to another. As shown in the figure, the primary flows enter and exit at the highest scale, i.e., the enterprise scale, and along the temporal direction. On the spatial axis (peering into the SGM), the sub-flows link each of the scales from the facility down to the process scale and back up. For example, electricity from the facility's main power transformer is distributed to each production line, which is then further distributed to each machine tool and delivered to the process. At the same token, heat generated from the process and combined at the machine tool and production line scales is absorbed by the facility HVAC system.

The visual illustration provides a better understanding on how to model the SGM. The foundation of the SGM builds upon the process scale where the number of processes may reach on the order of thousands (machine tool scale with numbers reaching on the order of hundreds, production lines on the order of tens, and typically several facilities with one enterprise). Much in the way LCI models are built, the SGM model can be built using unit processes, which are considered to be the fundamental building blocks of manufacturing [327]. In its simplest form, value-added unit processes can be envisioned as black boxes where inputs are elementary flows such as energy and raw materials and the output is the part or semi-finished part that has been treated or transformed (e.g., heat treated, material removal) in some manner. Machine tools and production line ancillary equipment can also be modeled as a combination of value-added unit processes and non-value-added unit processes that characterize the behavior of the machine tool. For comprehensive integration, the black box that encompasses the unit process is replaced with a controllable or parametric box that contain independent design variables that allow changes at the feature level. At the facility scale, energy consumption from the HVAC can be modeled using thermodynamic principles, factoring in the thermal balance between internal heat generation from the processes and machine tools and external heat sources such as solar radiation. Detailed explanation of the unit process models are covered in the subsequent chapter. Additionally, a robust HVAC energy consumption model is proposed that enables integration of the unit processes.

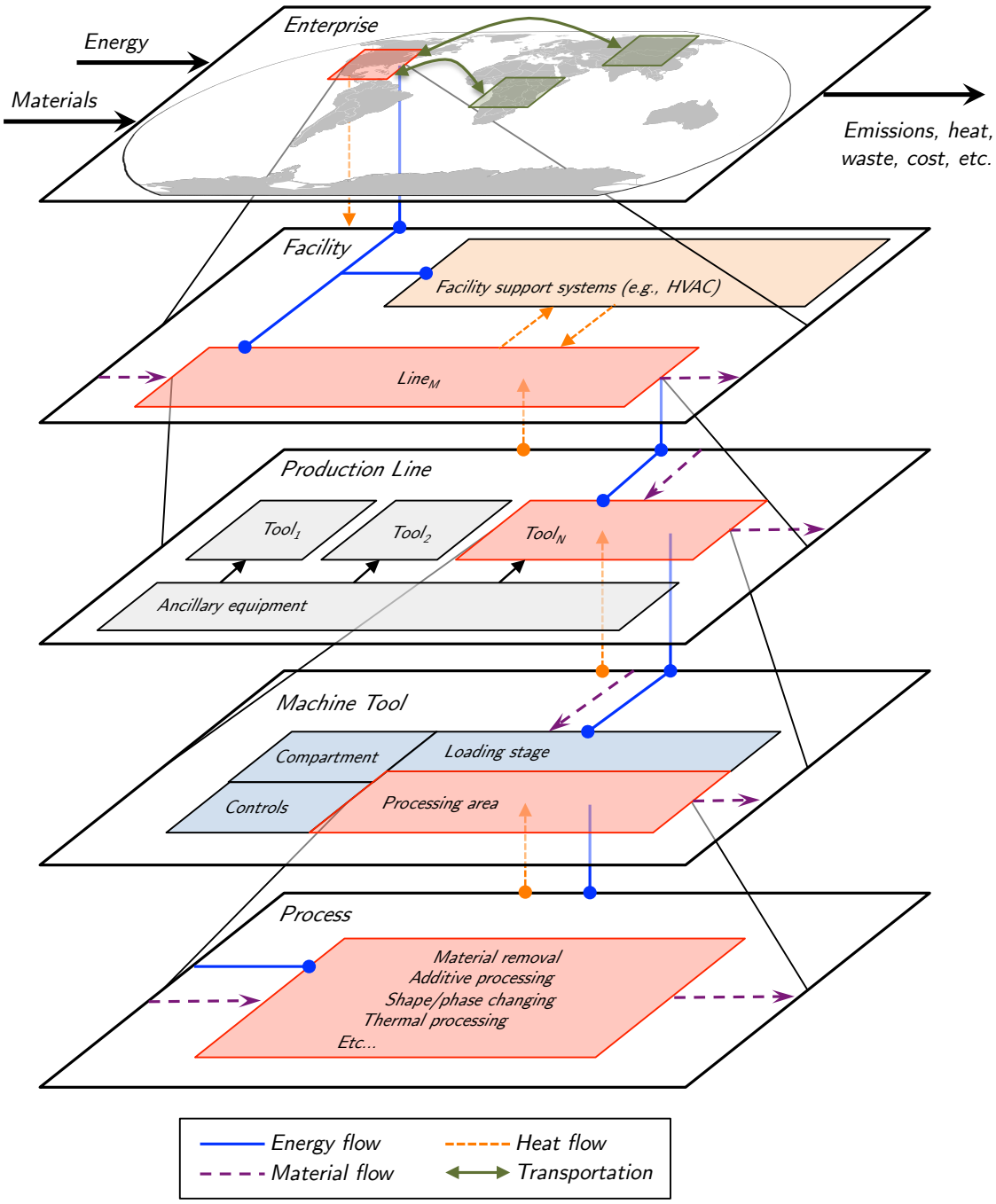

Figure 2.8: Integration corresponding flows of each scale in the SGM

Chapter 3

Scales of Green Manufacturing Models

The development of the iSLCD model resides in the quality and comprehensiveness of the product life cycle and the SGM models, which can be constructed using unit process models. Organizations in several countries have begun to measure and model unit processes and categorize them in LCI databases that are well-document, transparent, and consistent. The most mature and widely used LCI database is Ecoinvent[1] by Ecoinvent Centre [172]. Originating in the early 1990's, the Ecoinvent databases provides thousands of industrial LCI datasets primarily valid for Swiss and Western European environment [85]. In the U.S., The Department of Energy initiated the U.S. LCI Database project in 2001, which provided datasets for U.S. based activities [239]. These datasets, although growing, are still considered quite limited in terms of unique processes with the heavy emphasis on conventional processes such has milling, drilling, forming, and so on. A limited scope on non-conventional processes such as electrical discharge machining (EDM) and rapid prototyping (RPT) may be included, however, are often incomplete and/or reduced to theoretical results [172]. Furthermore, the lack of a global standardized database leads to differences in the functional unit (e.g., per kg, per m^3) and system boundaries as well as being country specific [263]. Other forms of LCI data exist such as input-output databases, which are not available for all countries, but are well-documented. However, the drawback with input-output databases for LCA is that the unit processes are aggregated and the impact of individual processes cannot be extracted [172].

Perhaps the greatest disadvantage with existing LCI datasets is that current process-based and input-output databases are tailored for product evaluation and not product design. A large majority of the datasets available treat the unit processes as pure black-boxes [263], which do not provide any correlation or ability to factor process parameters and design variations such as shape and thickness. In addition, the lack of parametric ability eliminates design optimization opportunities. These limitations have been acknowledged among the

[1] Version 3 released in 2013 [85]

academic organizations within the manufacturing community and as a result formed the Cooperative Effort on Process Emissions in Manufacturing or CO2PE!-Initiative, a joint collaboration between various Universities and Institutes across the world. The Initiative aims to document and analyze the environmental impacts of a representative sample of current and emerging manufacturing processes [172]. The Initiative recognized that all products and manufacturing processes stemmed from a finite set of individual unit processes and that the number of unique unit processes was relatively small (between 100 and 200). In other words, the 90:10 rule of information could be applied by creating the taxonomy of manufacturing processes (roughly 120 unit processes) to represent tens of thousands of manufacturing plants from different industries [244].

Building the taxonomy required to further define and accurately model the unit process under the framework shown in Figure 3.1. This approach isolates the unit process with inputs consisting only of the unfinished product from the prior unit process and materials and energy (from the facility) require to sustain the process. The outputs includes the unfinished (or finished if final unit process) product for the subsequent unit process as well as any direct waste and immediate emissions and heat. The unit process itself may consist of a family of sub-units such as controllers, pumps, and fans, which can be further modeled. The system boundaries are drawn in such a way that only the operating or use phase is included. Hence, the life cycle impacts of the raw materials, waste, and machine tool itself are disregarded at the unit process level [172].

The quantitative model based on the unit process framework is provided by the CO2PE!-Initiative, which lays out a two-level methodological approach to establish parametric process models [172]. The two approaches, screening approach and in-depth approach, comprises of different levels of detail. The screening approach builds upon theoretical calculations by including representative industrial data (e.g., from equipment specification data sheets) for energy consumption and material loss. The screening approach provides an initial insight of the unit process and outputs a set of approximate LCI data. The in-depth approach takes the analysis one step further by utilizing a semi-empirical model involving time, power consumption, consumables, and emissions studies, which leads to more accurate LCI data [171]. However, the drawback is that empirical machine tool data is required, which is not necessarily feasible or practical to obtain. More details on both approaches can be found in [172] and [171].

Although both approaches tend to be more resource intensive than conventional theoretical analysis, they are preferred in terms of parametric energy consumption modeling. The reason being is that for a large majority of manufacturing processes, there is a considerable amount of energy required to sustain the machine tool that is very difficult to capture with theoretical analysis alone. This includes components such as the controllers, drives, fans, pumps, coolant handling, all of which contributes to the machine tool's *fixed* energy. During processing, additional, or *variable*, energy is required for the primary processing or the actual value-added processing. The disparity between fixed and variable energy and power has been well studied and characterized [5][183][122], particularly for machining processes [71][59]. For instance, Figure 3.2a shows a typical breakdown of the power consumption dur-

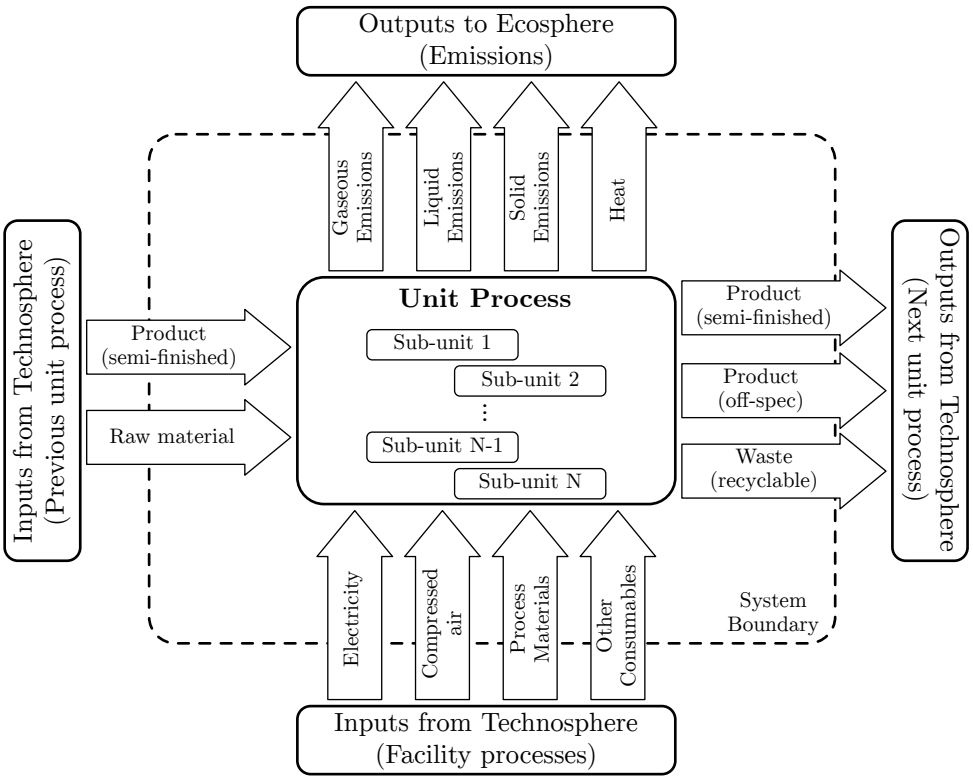

Figure 3.1: Framework of the unit process model [172]

ing a milling machining process. The breakdown shows that only half of the total power consumed goes into processing (machining) of the part. The remaining half is distributed to the constant (i.e., fixed) power components such as tool change and coolant flow that do not contribute directly to the processing of the part, but are necessary for tool operation. Performing a theoretical analysis would have captured the variable power thus yielding only half of the actual power consumption. This underestimation has been found to be consistent with other manufacturing processes to varying degrees with some cases off by up to two orders of magnitude [81].

Whenever possible, the in-depth approach is preferred over the screening approach due to opportunity for process optimization from identifying potential resource and energy efficiency improvements [172]. The opportunity arises the inclusion of time variant as a process variable. In a production setting, the machine tool will experience several production states, each depending on the availability and utilization of the machine tool. The main machine tool states are as follows:

- **Power-off**: machine tool shut off at a) main power switch, b) circuit breaker level, or c) unplugged

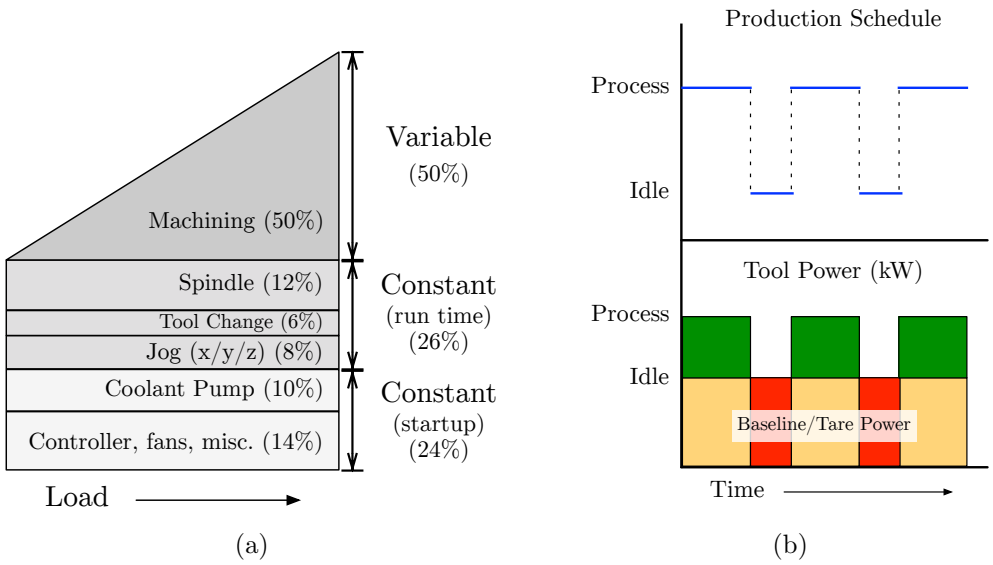

Figure 3.2: a) Machine tool power consumption breakdown. Based on [59], b) Production line scheduling between process and idle states.

- **Standby**: lowest possible 'ON' state (typically powering a portion of the controllers), tool may require a short warm-up prior to operation
- **Idle**: ready for operation with no or very short warm up, typically representative of the machine tool's fixed power, may have different degrees of idling depending on machine tool and manufacturer (also referred to as the baseline or tare power)
- **Nominal Processing**: actual tool power consumption during processing, can vary widely depending on the process parameters and throughput. Note, the difference between nominal and idle is the variable power.
- **Max Power**: special case of Nominal processing in which the machine tool is operating at 100% duty cycle (DC), typically engaged during initial phase or start-up of processing. The power equates to the product of the supplied voltage and maximum current (an additional 1.73 factor is added for three-phase power).

The time variant gives the unit process another dimension, the production states, which not shown in Figure 3.1. During the standby and idle states, energy (and possibly consumables) is continuously consumed despite not being utilized. In a typical production setting, the tool will fluctuate between its different power states, as illustrated in Figure 3.2b. The energy consumption of a part is the sum of the processing energy (value added) and the machine tool idle state (non-value added) energy. With higher tool utilization and more efficient production scheduling, the amount of non-value-added time and thus energy can be reduced.

The remainder of this chapter will divulge into the SGM models in regards to the case study. The unit process modeling covers the process and machine tool scale. An overview of roll-to-roll (R2R) processing is given in regards to the parameters for production line modeling. A detailed facility HVAC energy consumption model is proposed. The last section covers uncertainty analysis pertaining to LCA (arguably the largest source of uncertainty), and is imperative for understanding and evaluating the uncertainty in the data and the behavior of the iSLCD models.

3.1 Processes and Machine Tools

A widely used metric for the modeling of unit processes is the specific energy or specific energy consumption (SEC) of a material for a specific process [123]. The functional unit of the SEC is given in energy consumed per mass of the control volume. The control volume will depend on the type of process. For a removal process the control volume is the mass of material removed whereas for a forming process the control volume is mass of the formed part. The SEC also enables a consistent trade-off comparison among like processes [170].

The formulation of the unit process models will take an in-depth approach when possible, otherwise the screening approach is used. For the in-depth approach each model is comprised of two modeling techniques - theoretical analysis and empirical analysis, which combined form a semi-empirical model. The intention of this approach is to accurately capture process level detail using fundamentally sound engineering principles. For machine tool characterization, an empirical analysis, in the form of regression analysis, is the most effective method for capturing non-process machine tool behavior. A caveat for the empirical analysis is that first hand data (i.e., self measured) is not incorporated. Instead, a meta-study is conducted to survey various works in literature that have studied and measured the primary machine tool energy consumption. The meta-study enables a more robust model by capturing a broader range of data in terms of different machine tools from various sizes and manufactures. However, the uncertainty in the data quality also increases and needs to be taken into account. For of consistency of combining the two modeling methods, the unit process models are constructed in terms of the SEC.

The point of performing the analysis for the unit process models is to understand the methodology and the engineering components involved. Considering that there are literally hundreds of unique processes in manufacturing, covering all or even a majority is simply not feasible. Instead, the unit processes modeled are taken from the set of processes used for the case study in Chapter 4. The processes detailed are: polymer injection molding, polymer compression molding, and sheet metal stamping. All three are conventional processes that exist in LCI databases, however, are usually static and limited in terms of linear relationships. Therefore, the goal is to create a more robust and multi-parameter model to integrate with the SGM. Furthermore, the materials involved in the case study deal with unique polymer composites, which are not available in today's LCI databases.

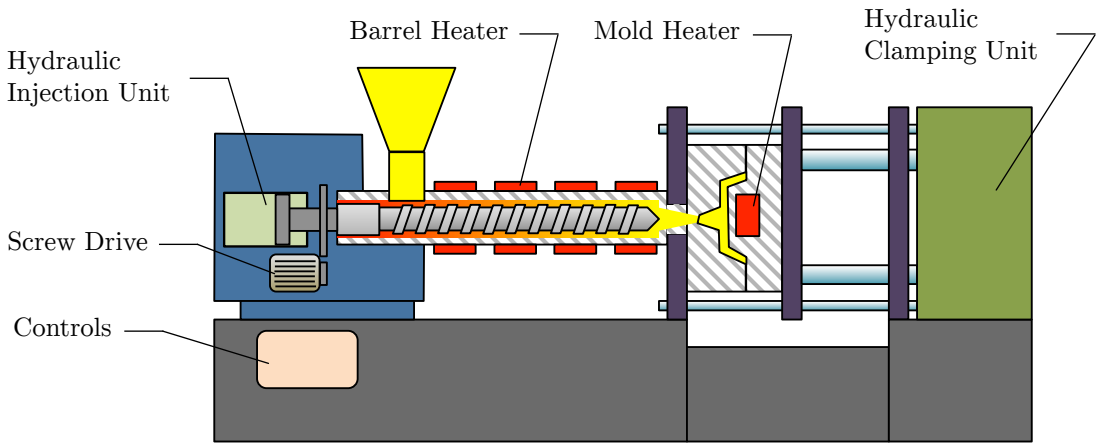

Figure 3.3: Diagram of a typical hybrid injection molding machine

Injection Molding

Polymer injection molding is a mass conserving process in which liquified polymeric material (e.g., thermoplastics, thermosets, elastomers) is pressure forced into a mold cavity to form a desired shape. Injection molding is very widely used industry for the advantage of being a robust process capable of handling a variety of polymeric materials with part sizes from several grams to over 25kg and clamp forces from several tons to over several thousand tons [48].

Different variations of the injection molding machine (IMM) tool are available and can be classified into three categories: hydraulics, all-electric, and hybrids. Hydraulic IMMs, consider to be the most mature technology type, utilize pressurized hydraulic cylinders from one or two electric hydraulic pumps to actuate the injection unit and mold clamping. The hydraulic configuration allows for large part sizes and very high clamp forces. All-electric IMMs replaces the hydraulic units in a hydraulic IMM with electric servo motors. Considered to be a relatively new and upcoming technology, all-electric IMMs offer lower power consumption and faster cycle times, however, at the expense of high costs and limited clamping forces. Hybrid IMMs takes advantage of both technology types by utilizing a hydraulic clamp and servo motor screw drive to plasticize the polymer in the barrel [48]. Figure 3.3 shows a typical configuration of a hybrid IMM with hydraulic injection and clamping units and an electric servo motor screw drive. Note that the majority of the components - controls, drive, injection unit, barrel and mold heater, and clamping unit, are consistent with all IMM configurations and the difference is in the technology of actuation. All three technology types are used in industry, however, there has been a transition towards hybrid IMMs for lower power consumption and higher clamping forces compared to hydraulics and all-electrics, respectively. Therefore, the hybrid IMM will be the focus for modeling the injection molding unit process.

Due to the limit literature and industrial data on injection molding polymer composite

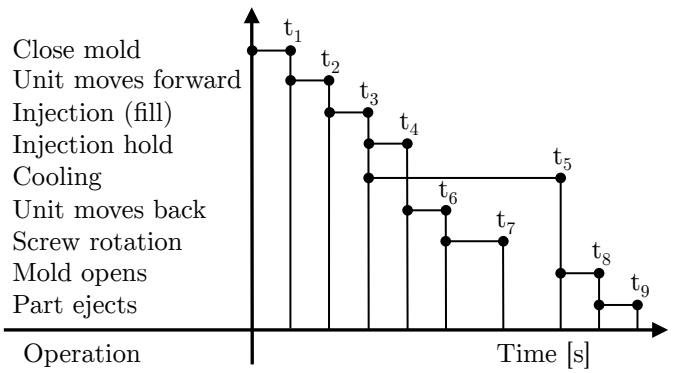

Figure 3.4: Gate-to-gate injection molding cycle time profile [48]

material, an in-depth approach is taken to account for the non-Newtonian visco-elastic nature of the polymer melt. Recall that the in-depth approach is divided into four modules - time, power, consumables, and an emissions study. Only the time and power studies are of interests in terms of energy consumption. Consumables such as the die mold release agent (typically a silicone type material) can be represented as a multiplicative factor in terms of mass (of consumable) per mass of part or per number of cycle. Direct emissions, other than heat, from the injection molding process are considered negligible and will not be considered. In addition, the injection molding unit process only encapsulates the IMM. Optional ancillary equipment such as the chiller and hopper mixer and dryer are not included in this analysis.

Forming a unit process modeled based on the SEC requires a detailed understanding of the time and power events that occur during the injection molding process. As shown in Figure 3.4, the process involves events that occur in series such as mold closing and injection, as well as in parallel such as cooling and plasticizing. The events that contribute to a significant portion of the total cycle time are mold opening and close, mold filling and holding (to maintain pressure within the mold before solidifying), and plasticizing. Note, although the cycle time for cooling of the part is typically the longest, there is no addition power required for cooling since most mold systems are passively cooled.

In terms of power consumption, Figure 3.5 shows the events during start-up and processing that require additional power above baseline. Power to the barrel and mold heaters results in an initial surge followed by a lower constant state of power consumption. During processing, power is fed to the unload motors, which are responsible for opening and closing the mold, moving the injection unit to and from the mold, and rotating the screw. In parallel, significant amounts of power is delivered to the injection and clamping/holding units. The cycle ends with the relatively small addition of power to eject the part from the mold. Each event can be classified as either process dependent or non-process dependent. Events that are process dependent are dictated by the properties of the material such as the viscosity and melt temperature and by design such as the size of the part. Non-process dependent events are dictated by the IMM and are independent of material type and design.

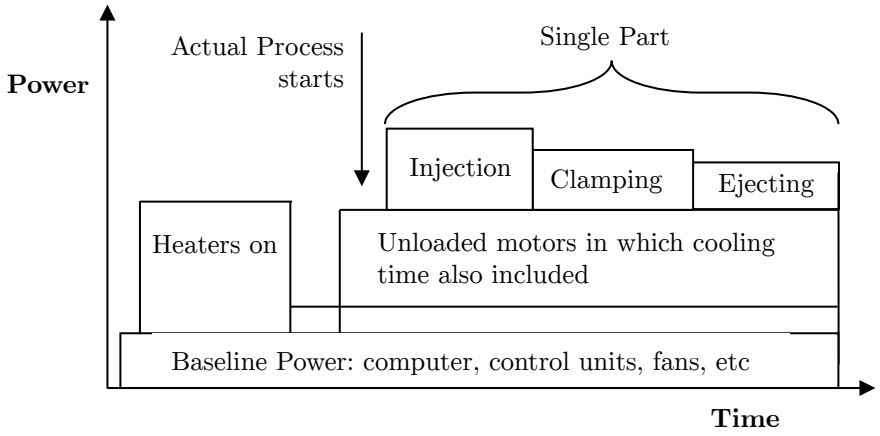

Figure 3.5: Power characteristics of the injection molding cycle [48]

For instance, the size of the IMM (i.e., clamp force) will determine the baseline power, barrel and mold heater idle power, clamp force power (assumed to be always at the rated clamp force), and the speed and power of the mold movement.

Based off the operations highlighted in both Figure 3.4 and 3.5, the equation to model the injection molding unit process can be formulated. Represented as the SEC, the equation for the total input energy per given part mass is given by:

$$SEC = \frac{E_{inj} + E_{hold} + E_{plas} + E_{moc} + E_{base}}{TPT \cdot t_{cycle}} \tag{3.1}$$

Where E_{inj}, E_{hold}, E_{plas}, E_{moc}, and E_{base} are the injection, clamp hold, plasticizing, mold open and close, and baseline energies, respectively. The denominator denotes the mass of the part, which is the product of the throughput, TPT, and the total cycle time, t_{cycle}. The addition energy for moving the injection unit as well as part ejection are assumed to be negligible. Equation 3.1 can be further expanded to include the respective individual cycle time and power consumption:

$$SEC = \frac{(Pt)_{inj} + (Pt)_{hold} + (Pt)_{scw} + (Pt)_{moc} + (P_{base} + P_{heat})\, t_{cycle} + E_{melt}}{m_{part}} \tag{3.2}$$

Where P and t are the respective power consumption and cycle time for the events: injection, clamp hold, and mold open and close. The plasticizing energy is further broken down into a mechanical and thermal component. Mechanically, the plasticizing involves the energy to rotate the barrel screw, which is denoted as $(Pt)_{scw}$. Additional thermal energy is required to assist in transforming the polymeric material from the solid to the full molten state, which is denoted by the E_{melt} term. It is assumed that process is in the post start-up state where the baseline power, P_{base}, and steady-state barrel and mold heater power, P_{heat}, are constant. The non-process dependent components of Equation 3.2: injection, screw

rotation, polymer melting, can be determined using thermo-mechanical principles, while the remaining non-process dependent components are determined empirically. The subsequent sub-sections provides further in-depth analysis on each component.

Thermo-Mechanical Power Model

The power required to inject the molten polymer and fill the mold can be approximated by determining the hydraulic pressure loss through the mold system at a given volumetric flow rate [311]. Assuming a constant flow rate, the injection power in terms of electrical power can be written as:

$$P_{inj} = Q\frac{dP_{tot}(Q)}{\eta_{mot}\eta_{hyd}} \tag{3.3}$$

Where Q is the volumetric flow rate of the molten polymer, dP_t is the total pressure loss through the mold system, and η_{mot} and η_{hyd} are the efficiency losses of the electric motor and hydraulic system (pump and cylinder), respectively. It is assumed that the flow rate is independent of the pressure loss and can be obtained by manufacturer specification data sheets for the IMM. Likewise, the efficiency of the electric motor can be approximated using National Electrical Manufacturers Association (NEMA) efficiency standards for a given motor rating and the hydraulic efficiency can be found in literature [273].

The pressure loss through the mold system is dependent on the viscosity of the molten polymer and the design of the part and mold system. Figure 3.6 shows the schematic view of a typical mold system. As the molten polymer is injected into the mold it first passes through a conical channel called the *sprue* and is distributed by the *runner* to the *gate* and finally to the mold cavity. Therefore, the mechanisms of pressure loss are through the sprue, runner, and mold cavity (gate assumed to be negligible):

$$dP_{tot} = dP_{sprue} + dP_{runner} + dP_{mold} \tag{3.4}$$

Each pressure loss term in Equation 3.4 depends on both the geometry of the channel and the flow rate. Assuming that the sprue, runner, and mold cavity are conical, cylindrical, and rectangular, respectively, the equations for the pressure loss terms, for non-Newtonian flow, are [311]:

$$dP_{sprue} = \frac{2mL_{sprue}}{\bar{R}_{sprue}}\left[\frac{Q\left(\frac{1}{n}+3\right)}{\pi\bar{R}^3_{sprue}}\right]^n \tag{3.5}$$

$$dP_{runner} = \frac{2mL_{runner}}{R_{runner}}\left[\frac{Q\left(\frac{1}{n}+3\right)}{\pi R^3_{runner}}\right]^n \tag{3.6}$$

$$dP_{mold} = \frac{mL_{mold}}{H_{mold}}\left[\frac{2Q\left(\frac{1}{n}+2\right)}{W_{mold}H^2_{mold}}\right]^n \tag{3.7}$$

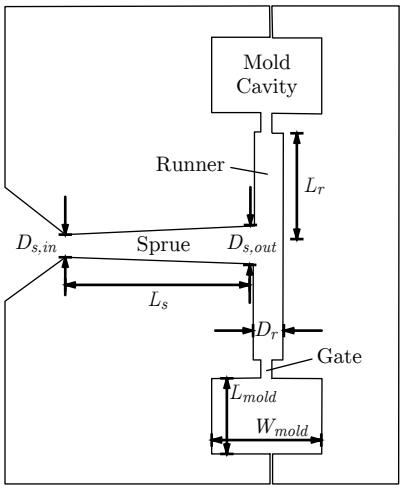

Figure 3.6: Schematic of sprue, runner, and mold die-cavity system

Where the geometric parameters, L_{sprue}, L_{runner}, L_{mold}, R_{runner}, and W_{mold} are shown in Figure 3.6. The average sprue radius is denoted by $\bar{R}_{sprue}$ and mold cavity thickness (not shown in the figure) is denoted by H_{mold}. The parameters, m and n, represent the coefficients of the Power-Law equation used to model non-Newtonian viscosity. [2] Note that Equations 3.5 - 3.7 assume that the flow within the channels and mold are in the laminar flow regime[3], which is a safe assumption due to the relatively high viscosity of the molten polymer [311]. Therefore, the influence of the channel surface roughness can be assumed to be negligible.

The power required to plasticize and mix the polymer pellets to the molten state is broken down to the power delivered to the servo motor for screw rotation and power to the barrel heaters. The screw power is highly dependent on the screw design, size, rotational speed, and the viscosity of the molten polymer [48]. Figure 3.7 shows the schematic of the screw barrel and the critical geometric parameters of the screw. During the metering section of the screw, the channel height (gap between the base of the screw to the barrel surface) decreases, creating large shear stresses between the screw and barrel surface. The electrical power required to create the shear stresses large enough to plasticize the polymer can be expressed as [311]:

$$P_{scw} = \bar{\mu}(\dot{\gamma}, T)\frac{\pi^2 N^2 D_b^2 W_{ch} L_{scw} \alpha_{mtr}}{\sin\left(\bar{\theta}\right) H_{ch} \eta_{mot}} \left(4 - 3\cos^2\theta_b \frac{Q_{ex}}{Q_d}\right) \tag{3.8}$$

Where D_b, W_{ch}, L_{scw}, α_{mtr}, H_{ch}, $\bar{\theta}$, and θ_b are geometric parameters that are tool dependent representing the barrel diameter, channel (flight-to-flight) width, screw length, fraction of the metering section to the length, channel height, mean flight helix angle, and helix angle at the barrel surface, respectively. Also tool dependent are the Q_{ex} and η_{mot} terms, which

[2] Will be covered in the viscosity model at the end this section

[3] Reynolds Number less than 2300

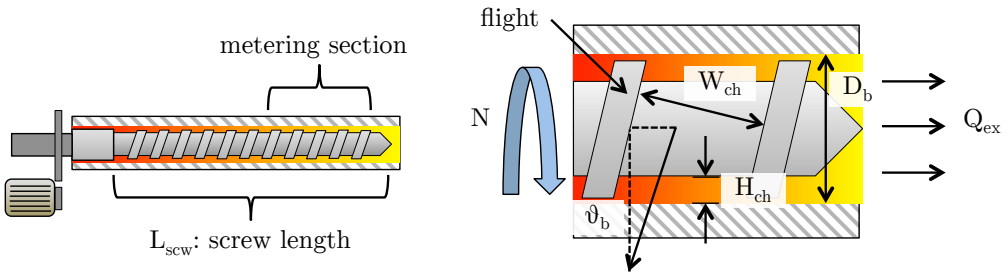

Figure 3.7: Schematic of screw

represent the plasticizing or net flow rate (obtained from manufacturer's specification data sheet) and the electrical efficiency of the servo motor, respectively. Process dependent parameters include the screw rotation speed, N, and the shear-rate and temperature dependent average viscosity, $\bar{\mu}(\dot{\gamma}, T)$. The shear-rate within the screw channel is given by [311]:

$$\dot{\gamma} = \frac{\pi D_b^2 N^2 W_{ch} \cos(\theta_b)}{3Q_{ex}} \tag{3.9}$$

Where D_b, N^2, W_{ch}, θ_b, and Q_{ex} are the same parameters from Equation 3.8

The expression on the right side of Equation 3.8 includes the drag flow term, Q_d, which is the material back flow relative to the axial screw direction. The drag flow term is expressed as [311]:

$$Q_d = 1.28 D_b^2 N H_{op} \tag{3.10}$$

Where H_{op} is the optimal channel height to achieve the given plasticizing flow rate, Q_{ex}. For simplicity and considering the level of uncertainty of the screw design, the channel height is set to equal the optimal channel height [311]:

$$H_{op} = H_{srw} = \frac{3Q_{ex}}{\pi N W D_b \cos\theta_b} \tag{3.11}$$

Furthermore, Equation 3.10 assumes that the helix angle, θ_b, in Equation 3.11 is that of a square-pitched screw. Therefore, $\theta_b = \tan^{-1}(1/\pi)$ or 17.65° [311].

Several comments regarding Equation 3.8. The electrical power consumption only refers to the power consumed in the screw channel. Additional power is consumed in the narrow gap between the screw flights and barrel surface, which may not be negligible [311], but is not considered due complexity of the flow and the uncertainty of the flight design. The screw power is maximized when the net plasticizing flow is zero (i.e., $Q_{ex} = 0$) as in the case when the shot capacity is reached. Conversely, the screw power is minimized when the net and drag flow are equal (i.e., $Q_{ex} = Q_d$) as in the case of open flow such as an open ended barrel (e.g., extruder).

While the shear stress induced by the screw will generate some heat, addition thermal energy by means of the barrel heaters are required to fully melt the polymer to reach the

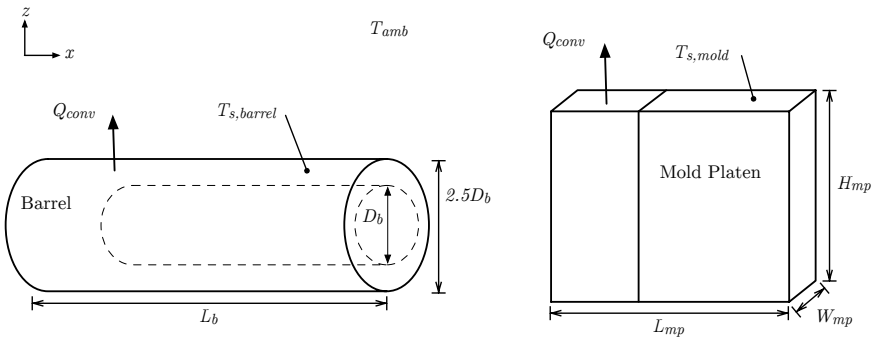

Figure 3.8: Schematic of heat loss

proper injection temperature. The theoretical thermal energy required to reach the injection temperature is a function of the material's heat capacity and enthalpy of fusion [318]:

$$E_{melt} = m_{shot}\left[c_p(T_{inj} - T_{amb}) + \lambda H_f^o\right] \tag{3.12}$$

Where m_{shot} is the injection shot size, c_p is the heat capacity of the polymer, T_{inj} is the process injection temperature, T_{amb} is the ambient temperature (assumed to be the temperature of the hopper), λ is the mean degree of crystallinity[4], and H_f^o is the enthalpy of fusion at 100% crystallinity. For amorphous polymers, λ is set to zero. Note, the injection shot size is equal to the sum of the part, runner, and sprue masses.

The thermal energy denotes the theoretical minimum energy required for melting, however, addition energy needs to be accounted for due to efficiency losses through the injection molding system. Heat from the barrel is transferred via conduction, convection, and radiation to the ambient surroundings. Additional heat is lost if mold heating is used through the mold platens (two-halves). A full transient thermal balance and heat transfer study during the injection molding process is not feasible simply due to uncertainties in the machine size, configuration, build materials, and surrounding environment conditions. However, in steady-state, it can be assumed that the dominate mechanism of heat dissipation is via convection. The components of heat loss is given by:

$$P_{heat} = \alpha_{heat}\left(P_{heat,barrel} + P_{heat,mold}\right) \tag{3.13}$$

Where $P_{heat,barrel}$ and $P_{heat,mold}$ are the convective heat loss for the barrel and mold, respectively. The α_{heat} factor is intended as a correction factor to accommodate for the conductive and radiative heat losses. The convective heat loss equations of both the barrel and mold platens are mathematically identical with the exception of different geometry, as illustrated schematically in Figure 3.8. The equation for the convective heat loss for both the barrel and mold platen can be written as:

[4]Assumed to be independent of temperature

$$P_{loss} = hA_s(T_s - T_{amb}) \tag{3.14}$$

Where h is the heat transfer coefficient, A_s is the surface area, T_s and T_{amb} are the surface and ambient temperatures, respectively. The surface area for both barrel and mold platen are easily determined based on Figure 3.8 while the surface temperatures are assumed to be at the injection and mold processing temperatures. The heat transfer coefficient is a strong function of the heat transfer medium (i.e., air) and the geometry of fluid flow. Using standard textbook definitions, the heat transfer coefficient is defined as [151]:

$$h \equiv \frac{\mathrm{Nu}_x k_f}{x} \tag{3.15}$$

Where Nu_x is the Nusselt number, k_f is the thermal conductivity of the fluid, and x is the characteristic length. The characteristic length, which is a measure of flow effectiveness, is equivalent to the hydraulic diameter and is equal to the diameter for cylindrical geometries and $4 \times (Area \div Perimeter)$ for non-circular geometries [151]. Assuming the convective heat flow is in the $+\hat{z}$-direction, the characteristic length for the barrel is equal to the outer barrel diameter, $2.5D_b$, and is equal to $2L_{mp}W_{mp}/(L_{mp} + W_{mp})$ for the mold platen. The Nusselt number is defined as the ratio of convective to conductive heat transfer, and is dependent on the convection type- free (natural) or forced convection, and the flow type- laminar or turbulent. The Nusselt number is typically determined empirically and closed form equations can be found in standard heat transfer textbooks. For the case of laminar free convection across a cylinder, where the forced flow in the $-\hat{x}$-direction is zero or relatively small, the Nusselt number can be expressed as [151]:

$$\mathrm{Nu}_D = C\mathrm{Ra}_D^n \tag{3.16}$$

Where Ra_D is the Rayleigh number and C and n are empirical constants given in Table 3.1. The Rayleigh number, which is defined as the ratio of free convective flow to the thermal diffusivity of the fluid medium, and is equal to the product of the Grashof and Prandtl numbers. For a cylindrical geometry, the Rayleigh number is expressed as [151]:

$$\mathrm{Ra}_D = \mathrm{Gr}_D\mathrm{Pr} = \frac{g\beta\left(T_s - T_{amb}\right)D^3}{\nu\alpha} \tag{3.17}$$

Where g is the gravitational acceleration (i.e., $9.81 m/s^2$), β is the coefficient of volume expansion and is equal to the inverse mean temperature for an ideal gas, D is the diameter of the cylinder, and ν and α are the kinematic viscosity and thermal diffusivity of air at mean temperature, respectively. Similar expressions to Equation 3.16 can also be found for non-cylindrical geometries, forced convection, and turbulent flows.

Empirical Power Model

As previously stated, the non-process, machine tool dependent components to the power consumption involve a detailed understanding of the design of the IMM down to the circuit

Table 3.1: Constants for Nusselt number equation [151]

Ra_D	C	n
10^{-10} - 10^{-2}	0.675	0.058
10^{-2} - 10^{2}	1.02	0.148
10^{2} - 10^{4}	0.850	0.188
10^{4} - 10^{7}	0.480	0.250
10^{7} - 10^{12}	0.125	0.333

board level. Knowledge of the wattage rating and control logic of the controllers and electrical components is needed to model the baseline power. Further knowledge on the design and mass of the mold platens is required for determining the electrical clamp force power and platen actuation power. Such knowledge is rarely available and therefore an empirical approach, via meta-study, is considered that utilizes actual measured power consumption data. It was observed that the power profile data was most strongly correlated to the size (i.e., clamp force rating) of the IMM. Intuitively this makes sense because higher clamping forces require larger pumps and motors and thus higher wattage controllers. Additionally, higher clamping forces typically lead to larger mold platens to accommodate for larger part sizes. From the data, a functional relationship can determined to create a least-squares curve fit model using standard statistical analysis techniques.

From meta-analysis study, nine power consumption profiles were obtained, with IMM sizes ranging from 15 tons to 550 tons. Figure 3.9 shows a typical time-series power consumption profile with injection molding and machine tool events labeled [261]. The extracted time averaged mean power data of each event- baseline, hold, mold open and close, was meticulously approximated. In some instances, the distinction between separate events was not apparent, in which the best approximation was made or simply excluded from the analysis. The level of error introduced is not significant, however, will be factored in the data uncertainty. The results of the meta-study extraction of the data points can be found in the Appendix.

Curve fitting the data was performed using linear regression. It was deemed that a first order (i.e., linear) fit would be sufficient and an exponential fit[5] could be used where appropriate. For a linear fit, the objective is to determine a function of the form:

$$\hat{y} = mx + C \tag{3.18}$$

Where $\hat{y}$ is the predicted value, x is the dependent variable, m and C are the linear fit parameters representing the slope and y-intercept, respectfully. The fit parameters, m and C are chosen in such a way that the deviation or error between the predicted and actual

[5]An exponential fit was preferred over a second-degree polynomial to avoid a global minimum or maximum.

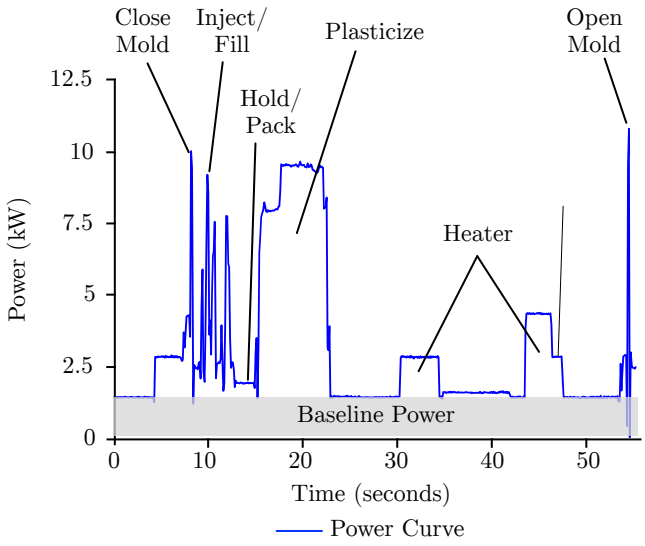

Figure 3.9: Example of an injection molding power profile obtained from the meta-study [261]

value at each x is minimized. Therefore, the goal is to find m and C such that the sum of the squared error[6] (SSE) is zero. Mathematically, the SSE is expressed as:

$$SSE = \sum_{i=1}^{N} e_i^2 = \sum_{i=1}^{N} (y_i - \hat{y}_i)^2 \tag{3.19}$$

Where e_i is the error at each data point, y_i is the actual data, and N is the number of data points. Ideally, the SSE would equal zero indicating a perfect fit, however, such cases are extremely rare. Instead, the goal is to find the fit parameters that yield the minimum error:

$$\min{:}SSE = \frac{\partial SSE}{\partial \bar{X}} = 0 \tag{3.20}$$

Where the SSE is differentiated respect to the set, $\bar{X}$, of fit parameters and set equal to zero.[7] The linear fit parameters are solved by differentiating with respect to m and C and equating the resulting expression to zero. Substituting $\hat{y}_i$ and x_i for the power consumption, P_i, and the machine clamp force, F_i, respectively, yields the final (linear-fit) expressions:

$$m_{lin} = \frac{N \sum_{i=1}^{N} (F_i P_i) - \sum_{i=1}^{N} F_i \sum_{i=1}^{N} P_i}{N \sum_{i=1}^{N} (F_i^2) - \left(\sum_{i=1}^{N} F_i \right)^2} \tag{3.21}$$

[6]The error is squared to keep in positive domain.

[7]This indicates the minimum and not maximum because the maximum is unbounded.

$$C_{lin} = \frac{\sum_{i=1}^{N} P_i - m_{lin} \sum_{i=1}^{N} F_i}{N} \tag{3.22}$$

In the case for an exponential fit, similar calculations are carried out. The curve fit is represented in the form:

$$\hat{y} = Ae^{bx} + C \tag{3.23}$$

Where A, b, and C are the fit parameters. The equation can be further simplified by assuming $C = 0$, which is valid because at zero clamp force the power consumption should also be zero. To take advantage of linear regression, Equation 3.23 can be linearized by taking the natural logarithm of the left and right-hand expressions. The error can therefore be expressed as:

$$e_i = y_i - \hat{y}_i = \ln A + bx_i - \ln y_i \tag{3.24}$$

Where the unknown fit parameters become b and $\ln A$, which can be solved by substituting Equation 3.24 into Equation 3.19 and following the same procedures. The final expression, in matrix form with the appropriate variables, becomes:

$$\begin{bmatrix} N & \sum_{i=1}^{N} F_i \\ \sum_{i=1}^{N} F_i & \sum_{i=1}^{N} (F_i^2) \end{bmatrix} \begin{pmatrix} \ln A \\ b \end{pmatrix} = \begin{pmatrix} \sum_{i=1}^{N} \ln P_i \\ \sum_{i=1}^{N} (F_i \ln P_i) \end{pmatrix} \tag{3.25}$$

Where Equation 3.25 is solved via matrix inversion and the fit parameter, A, is obtained by taking the exponential of $\ln A$.

The resulting curve fits from the meta analysis are plotted in Figure 3.10 and summarized in Table 3.2. Note that some of the data points were excluded due to being indistinguishable. Overall the data was well represented by the linear and exponential fits with a goodness-of-fit (R^2) of at least 0.98 for all three cases. Several comments regarding the fitted models. The clamp hold power had the highest goodness-of-fit, which intuitively makes sense because of its direct correlation with the clamp force. The mold platen open and close power is directly proportional to the mass and thereby the volume of the mold platens. As the tool size increases, the mold platen size increase in all three principle directions thus given an exponential like curve.

Cycle Times

The remaining stage of the in-depth analysis for the SEC involves determining the total part cycle time and the individual cycle times for each event. As previously mentioned, the cooling of the part occurs simultaneously with the injection hold step and the plasticizing for the next cycle, as shown in Figure 3.4. To avoid double counting, the equation for the total cycle time depends on the cooling time relative to the hold and plasticizing times. The total cycle time (in seconds) is therefore computed as:

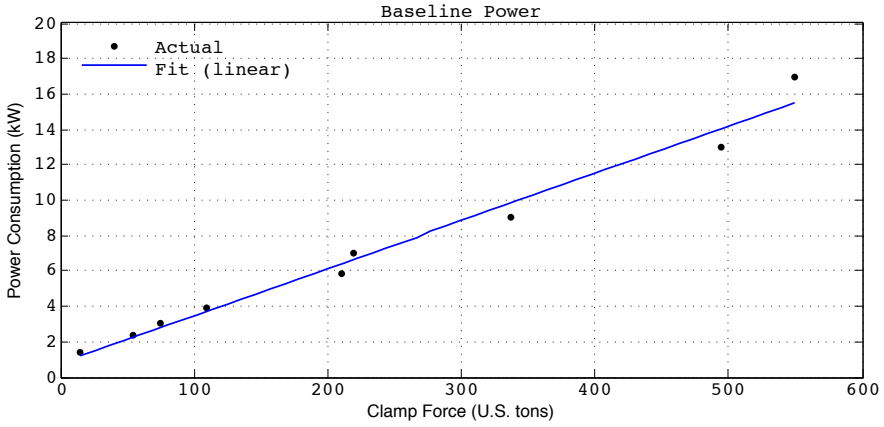

(a)

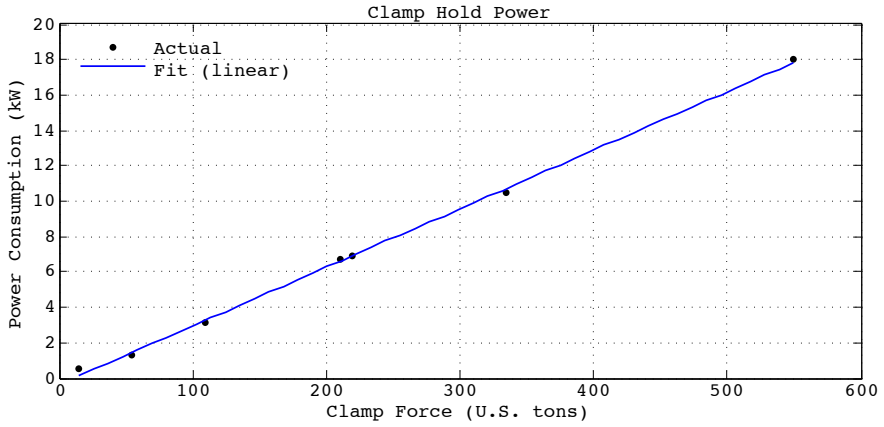

(b)

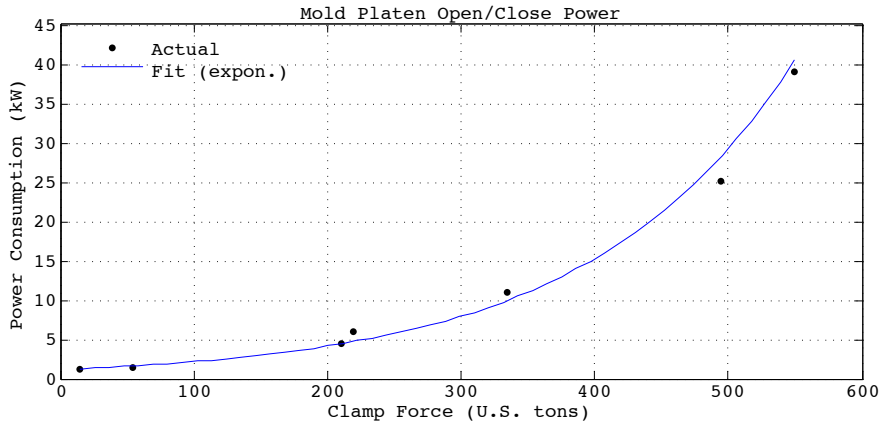

(c)

Figure 3.10: Empirical model for a) baseline power (linear fit), b) clamp hold power (linear fit), c) mold polaten open and close power (exponential fit)

Table 3.2: Regression coefficients for empirical models (power in kW)

	Baseline Power	**Hold Power**	**Mold O/C Power**
Form:	$P_{base} = mF + C$	$P_{hold} = mF + C$	$P_{moc} = Ae^{bF}$
m:	0.0269	0.0328	n.a.
C:	0.782	0	n.a.
A:	n.a.	n.a.	1.115
b:	n.a.	n.a.	0.0066
R^2:	0.98	>0.99	0.99

$$t_{cycle} = \begin{cases} t_{inj} + t_{moc} + t_{cool} & t_{cool} > t_{hold} + t_{scw} \\ t_{inj} + t_{hold} + t_{scw} + t_{moc} & \text{otherwise} \end{cases} \tag{3.26}$$

Where t_{inj}, t_{hold}, t_{scw}, t_{moc}, and t_{cool} are the injection, hold, screw rotation, mold open and close, and cooling times, respectively. The injection time can be approximated assuming constant flow through the sprue, runner, and mold:

$$t_{inj} = 2V_{tot}\frac{dP_{tot}}{P_{inj}} \tag{3.27}$$

Where V_{tot} is the total shot volume and the dQ_t/P_{inj} term is simply the injection flow rate from Equation 3.3. The total shot volume is simply taken as the product of the shot mass and molten polymer density.

The hold time is essentially the amount of time required for the orifice of the sprue to solidify in order to prevent back flow from the pressurized mold when the injection unit is retracted. The solidification time can be approximated under the assumption that the radial temperature difference at the sprue orifice is negligible, which implies that the lumped capacitance method can be used. The solution to the 1-D lumped capacitance heat conduction equation for the hold time is [32]:

$$t_{hold} = \frac{2R_{s,in}^2}{3\pi^2\alpha}\ln\left[\frac{4(T_{inj} - T_{mold})}{T_{melt} - T_{mold}}\right] \tag{3.28}$$

Where $R_{s,in}$ is the radius of the sprue orifice, α is the mean thermal diffusivity of the polymer, T_{inj}, T_{melt}, and T_{mold} are the injection, melt (of the polymer), and mold temperatures, respectively.

The plasticizing time is equal to the duration of the screw rotation, which is dictated by the residence time or plasticizing flow rate from the tool manufacturer. Assuming that the plasticizing rate is known, the theoretical duration for the screw rotation is [342]:

$$t_{scw} = \frac{H_{ch}W_{ch}L_{scw}\alpha_{mtr}}{\sin\left(\bar{\theta}\right)Q_{ex}} \tag{3.29}$$

Where the parameters H_{ch}, W_{ch}, L_{scw}, α_{mtr}, $th\bar{e}ta$, and Q_{ex} are the same as those in Equation 3.8.

The mold open and closing times is primarily dependent on the part design and mold system. For mold opening, sufficient time is required for the part, including runner and sprue, to separate from the mold platens and eject from the tool (typically by free fall). An equation that approximates the open and close time has be proposed by [32]:

$$t_{moc} = 1.75 t_d \left(\frac{2D_{mold} + 0.05}{L_{stroke}} \right)^{0.5} \tag{3.30}$$

Where t_d is the dry cycle time, D_{mold} is the part (including runner and sprue) depth, and L_{stroke} is the maximum opening stroke of the mold platens for a given machine. The dry cycle time is typically specified by the manufacturer and it is defined as the amount of time required to for tool operation with no material and at maximum mold stroke. Note that t_d is in unit of seconds and both D_{mold} and L_{stroke} are in units of centimeters.

The final cycle time component is the cooling time, which is the time required for the part to reach a specific solidification temperature called the ejection temperature. The ejection temperature is typically higher than the mold temperature, but well below the melting point to ensure structural rigidity during ejection. Likewise with the hold time, the dominating mechanism for cooling is assumed to be via heat conduction. For rectangular parts, the cooling time is approximated as [32]:

$$t_{cool} = \frac{h_{max}^2}{\pi^2 \alpha} \ln \left[\frac{4(T_{inj} - T_{mold})}{T_x - T_{mold}} \right] \tag{3.31}$$

Where h_{max} is the maximum mold wall thickness and T_x is the recommended ejection temperature. For cylindrical parts, Equation 3.28 can be used with the melting temperature replaced by the ejection temperature. For parts with very thin wall moldings, Equation 3.31 underestimates the cooling time in which for such instances the thickness of the runner or sprue is used [32].

Viscosity Model

Equations 3.5 - 3.8 take into account the rheological viscoelastic behavior of polymer melts. Newtonian fluids exhibit a constant viscosity where the shear stress varies linearly with the shear rate. However, polymer melts are considered non-Newtonian, which undergo a phenomenon called *shear thinning* where the viscosity decreases with increasing shear rate. One of the simplest models representing non-Newtonian fluids is the two-parameter empirical Power Law model [311]:

$$\eta(\dot{\gamma}) = m\dot{\gamma}^{n-1} \tag{3.32}$$

Where $\dot{\gamma}$ is the shear rate, and m and n are commonly called the consistency (units in $[Ns^n/m^2]$) and Power Law index, respectively. The Power Law index is a dimensionless parameter with $n < 1$ for shear-thinning. The m parameter is quite complex and is a sensitive

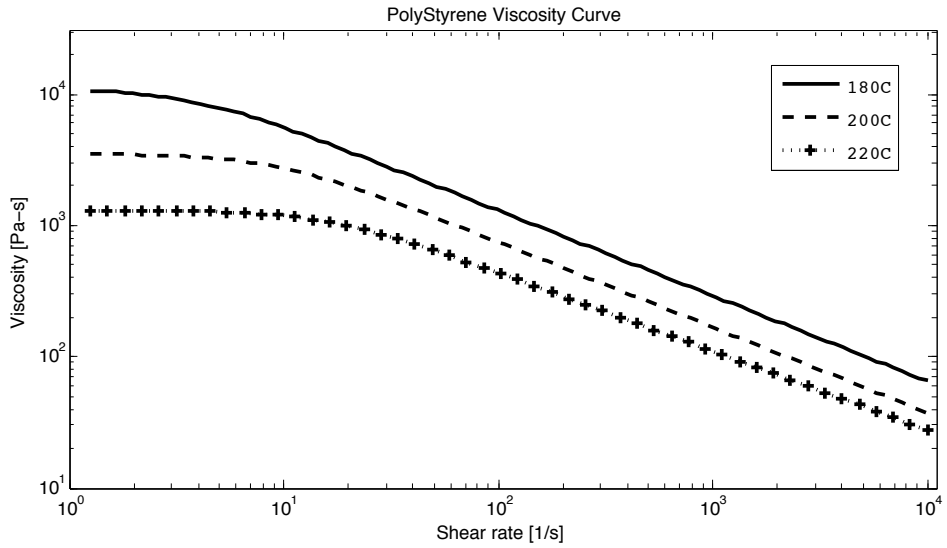

Figure 3.11: Non-Newtonian shear-viscosity curve for polystyrene, data from [311]

function of temperature and, to a lesser extent, pressure. The temperature dependency follows an Arrhenius-type relationship where an increase in temperature dramatically decreases the viscosity [311].

A drawback to the Power Low model is that it tends to overestimate the viscosity at low shear rates. Taking the limit as the shear rate approaches zero results in an infinity viscosity, which intuitively should instead approach the Newtonian regime. More detailed models exist that better account for lower shear rates. One of those models is a four-parameter model called the Carreau model [311]:

$$\frac{\mu\left(\dot{\gamma},T\right)-\eta_{\infty}}{\eta_{o}(T)-\eta_{\infty}}=\frac{1}{\left\{1+\left[\tau(T)\dot{\gamma}\right]^{2}\right\}^{\frac{1-n(T)}{2}}} \tag{3.33}$$

Where $\eta_o(T)$ is the zero shear (i.e., Newtonian) viscosity at a given temperature, η_∞ is the infinite shear-rate viscosity (assumed to be zero), $\tau(T)$ is the relation time (units of time) at a given temperature, and $n(T)$ is a dimensionless parameter that has the same influence as the Power Law index. The Carreau model more accurately reflects the viscoelastic nature of the polymer melt where at low shear rates the denominator term, $1+\left[\tau(T)\dot{\gamma}\right]^2$ approaches unity and hence to the value of the zero-shear viscosity. At high shear rates the model behaviors closer the to Power Law model. An example of the Carreau model for polystyrene is shown in Figure 3.11. As clearly seen in the figure, at low shear rates the viscosity plateaus into the Newtonian regime. Furthermore, the Newtonian region extends as the temperature increases and transitions to the non-Newtonian regime dictated by the relaxation time parameter, τ.

Using the Carreau model provides a more accurate calculation of viscosity, however, Equations 3.5 - 3.7 are in terms of the Power Law model parameters, particularly m. A conversion to determine m from the Carreau can be made by noting that at high shear

rates, the denominator term in Equation 3.33 simplifies to $\tau(T)^{1-n(T)}\dot{\gamma}^{1-n(T)}$. Therefore, the parameter, m, from Equation 3.32 can be calculated to be:

$$m(T) = \eta_o(T)\tau(T)^{n-1} \tag{3.34}$$

Compression Molding

Compression molding is one of the oldest polymer processing techniques. Having said to be developed around the mid-19$^{\text{th}}$ century [316], compression molding is a straightforward process in which moldable polymeric material is placed in a heated die-mold cavity and plastically conformed to the cavity shape via compression pressure between the die halves. The selection of polymeric materials for compression molding is generally the same as injection molding. However, for homogeneous thermoplastics and thermoset sets, injection molding offers the distinct advantage of material handling and ease of automation leading to potentially lower cycle times. Compression molding on the other hand often excels with filled or reinforced polymers due to the relatively low flow and shear stress during compression [325]. The binder material for reinforced polymers is typically thermoplastic or partially polymerized thermoset and mixed with filler(s) such as glass fibers and ceramic particulates. Other materials include sheet molding compound (SMC), which consists of a reinforcing layer such as carbon or glass fibers sandwiched between thermoplastic or thermoset layers, and bulking mold compound (BMC), which comes in the shape of a billet [316]. Due to handling and mixing requirements, compression molding is generally more manufacturable for thermosets with molding pressures ranging 13.8-20.7MPa, process temperatures ranging 150-190C, and cure times depending on the material and design for the polymer undergo complete polymerization [316].

The compression molding process is also advantageous in terms of processing with in very little material waste (lack of sprue and runner), usually lower equipment cost than injection molding, uniform shrinkage due to uniform flow, and no degradation of fibers during flow [316], good for large parts. However, potentially long curing times, uneven parting line, difficult to produce with tight tolerance and intricate designs with deep undercuts [311].

Despite the maturity of the technology, compression molding has not gained a great deal of attention at the fundamental level [325]. Modern day polymer processing, compression molding only accounts for approximately 3% of U.S. and worldwide polymer processing [274]. Even more lacking are analyses on the process and machine tool inefficiencies and unit process level energy consumption. For a comprehensive analysis, it is important to first identify the key components of the compression molding tool, particularly the components that impact the energy consumption. Figure 3.12 shows a schematic drawing of a generic hydraulic compression molding machine (CMM). Highlighted in blue lines are the major components that contribute to energy loss in some form of heat. Energy losses arise from the electrical motor, hydraulic pump, conduit system, and the hydraulic cylinder. Additional heat is lost from the upper and lower heated press platens that house the die-molds.

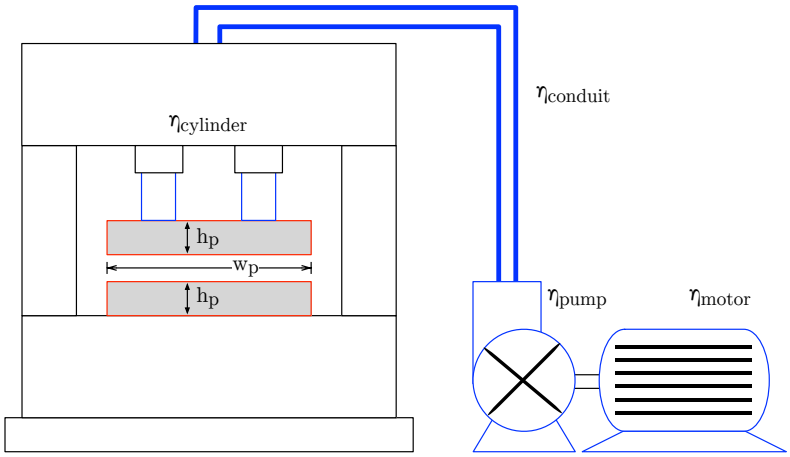

Figure 3.12: Hydraulic compression molding machine

The energy consumption per molded part is the energy required for each molding operation plus the baseline energy. The mold operations are broken down to individual molding cycle (shown in Figure 3.13): 1) load molding compound or prepreg into the mold, 2) top platen lowers to close the mold and initial flow initiates, 3) polymer flows until mold is full and is held to maintain pressure, 4) in mold curing under pressure for complete or near complete polymerization, 5) removal of molded part either manually or with a robotic arm. Steps 1 and 2 are not considered machine tool operations and therefore only factor during the idling of the tool. In terms of energy consumption the SEC can be as:

$$SEC = \frac{E_{mold} + (Pt)_{hold} + (Pt)_{moc} + (P_{base} + P_{heat})\, t_{cycle} + E_{cure}}{m_{part}} \tag{3.35}$$

Where P and t are the respective power consumption and cycle time for the operations: compression, mold hold, and mold open and close. Additional thermal energy is required to assist in softening and curing the polymer, which is denoted by the E_{cure} term. It is also assumed that process is in the post start-up where the baseline power, P_{base} and mold heater power, P_{heat}, are in steady-state. The material dependent components of Equation 3.35 - compression, mold hold, and curing - can be determined using thermo-mechanical principles. The remaining non-process dependent components are determined empirically with the exception of mold heat loss, which is determined on a theoretical basis. The subsequent sub-sections provides further in-depth analysis on each component. Note, there is a high level of uncertainty due to lack of data and representativeness for compression molding.

Theoretical Analysis

A schematic of the molding process in a mold cavity is shown in Figure 3.14. An axial compression force is applied to the mold die, from the pre-mold height until the desired

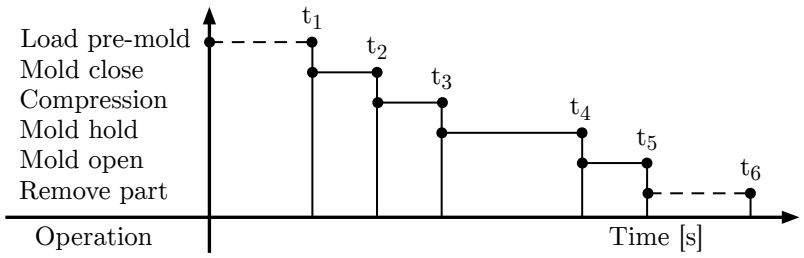

Figure 3.13: Cycle times for compression molding (dotted lines represent operator activity)

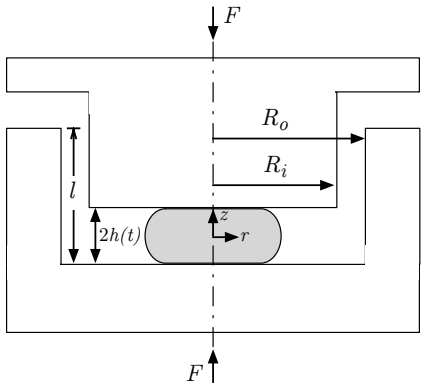

Figure 3.14: Geometry for molding. Adopted from [311]

cavity volume is filled (an annular shape in this case). The theoretical energy to compression mold a polymeric material can be approximated by using the energy equation:

$$E_{mold} = \int_0^h \eta_{sys} n_{cav} A_{cav} dP(h) dh \tag{3.36}$$

Where η_{sys} is the overall efficiency of the compression molding system, n_{cav} and A_{cav} are the number of mold cavities and mold area per cavity, respectively, and $dP(h)$ is the mold pressure as a function of mold displacement (in the molding direction), from the initial pre-mold height (initialized to 0) to the final mold displacement, h. The mold pressure for an annulus and non-Newtonian viscosity can be found in [311]. Modified with an additional shape factor term to approximate a generic mold die shape, the expression for the non-Newtonian die-mold pressure:

$$dP(h) = \frac{2 f_o m l}{R_o^{3n+1}} \frac{\left[2(s+2)\bar{R}\Delta R \dot{l}(h)\right]^n}{(1-\kappa)^{2n+1} F(n,\kappa)} \tag{3.37}$$

Where m, n, and s (recall $s = 1/n$) are the parameters to the non-Newtonian Power Law equation, R_o this the outer annular radius, $\bar{R}$ and ΔR are the average annular radii

and annular space, respectively, f_o is the mold die shape factor (see Appendix A3), κ is the annular shape factor ($\kappa = R_i/R_o$), $F(n, \kappa)$ is a shear and geometry-dependent function for non-Newtonian flow in an annular region (see Appendix A3), and $\dot{l}(h)$ is the increase in annular length as a function of the mold displacement ($\dot{l}(h) = \dot{h}\left(\frac{\bar{R}}{2\Delta R}\right)$).

Determining the energy required to hold the molded part in place immediately post compression for curing is complex and depends on the cavity pressure, curing dynamics of the polymer, and inherent design of the compression tool. A meta-study would have been preformed for modeling the hold power in a similar manner as the injection molding case. However, due to lack of data publicly available, the empirical approach was not possible. For simplification, it is assumed that the power consumption to hold the mold is equal to a fraction of the power consumption for molding. Therefore, the hold energy can be written as the product of the hold power and hold time, which is equal to the set cure time:

$$E_{hold} = \alpha t_{hold} \frac{E_{mold}}{t_{mold}} \tag{3.38}$$

Where α is the fraction of molding power to hold power, $t_{hold} = t_{cure}$ is the hold cycle time, and E_{mold} and t_mold are the molding energy and cycle time, respectively. The cure time is material dependent and will vary from one material manufacturer to another, hence, cure time is set by the manufacturer's recommendations. This simplification leads to added uncertainty, which is taken into consideration.

The remaining theoretical energy analysis involves determining the energy for curing and the thermal energy lost from the mold heaters. The thermal loss mechanisms and assumptions are the exactly the same type of calculations performed in the injection molding section. For curing energy Equation 3.12 is used by replacing T_{inj} with the curing temperature, T_{cure}, and the shot mass replaced with the molded part mass. Additionally, Equations 3.13 to 3.17 can be used to determine the heat loss from the mold platens.

Empirical Analysis

The empirical analysis proved to be much more challenging due to lack of compression molding energy measurement studies in literature. As a proxy, power consumption data for hydraulic press-brake machines (PBM)[8] were obtain from various sources [279][68]. From the machine tool perspective, hydraulic press-braking and hydraulic compression molding are nearly. Initial attempts to correlate press force data with baseline power consumption were unsuccessful. However, a strong correlation was found between the power rating of the hydraulic motor and the actual tool power consumption. Using this correlation, the baseline power consumption of any sized CMM tool could be determined by knowing the tool motor power rating. The Wabash Vantage series CMM was used as a reference tool due to availability of comprehensive specifications such as tool size (U.S. tons), motor rating (kW), heater rating (kW), platen dimensions (meters), and mold stroke (meters) [333]. Using the

[8]Press-braking is process for bending sheet metal

Table 3.3: Regression coefficient for CMM empirical model

	CMM Motor Rating	**PBM Baseline Power**	**CMM Mold Stroke**
Form:	$M_{rating} = Ae^{bF}$	$P_{press} = Ae^{bM}$	$L_{stroke} = Ae^{bF}$
A:	0.3722	0.5911	0.062
b:	0.0389	1.7503	0.3097
R^2:	>0.99	0.74	0.95

same linear regression technique performed in the injection molding section, fitted equations were obtained for the compression molding machine motor rating as a function of tool size and baseline power of the press-brake machine as a function of motor rating. Therefore, the baseline power consumption for a compression molding machine for a given press size can be expressed as:

$$P_{base} = P_{press}\left(M_{rating}\left(F\right)\right) \tag{3.39}$$

Where P_{press} and M_{rating} are the empirical fitted equations for the PBM baseline power (kW) and CMM motor rating (kW), respectively, and F is the CMM compression force rating (U.S. tons). The two fitted equations and corresponding coefficients are shown in the first two columns of Table 3.3. Both equations follow as power law fit with very strong correlational fit to the data as denoted by the R^2 values in the Table and shown in Figure 3.15.

Missing from the analysis is the power consumption attributed to the lowering and raising the mold platen. Unfortunately, the resolution in the data found was not high enough to accurately isolate the platen lower and raise power consumption. Intuitively, the power consumption should be proportional to the lower and raise speed as well as to the rating of the hydraulic motor. Assuming a time averaged lower and raise duty cycle of 50% (high uncertainty), the motor power consumption is be equal to the motor power rating divided by the efficiency of the motor and hydraulic system. The additional energy consumption associated to lowering and raising the platen is proportional to the travel time, which is a function of the mold platen stroke (i.e., travel distance). From the Wabash technical specification sheet, a correlation function was formulated to attribute the mold stroke length to the machine size. The fitted equation and corresponding parameters are shown in the last column of Table 3.3 and in Figure 3.15.

As part of the final SEC calculation, the total cycle time for a given part mass is calculating with the expression:

$$t_{cycle} = \frac{h}{v_{mold}} + \frac{L_{stroke}}{v_{moc}} + t_{cure} \tag{3.40}$$

Where h is the molding displacement during compression, v_{mold} is the molding speed set by the the manufacturer, L_{stroke} is the mold platen open and close stroke, v_{moc} is the mold

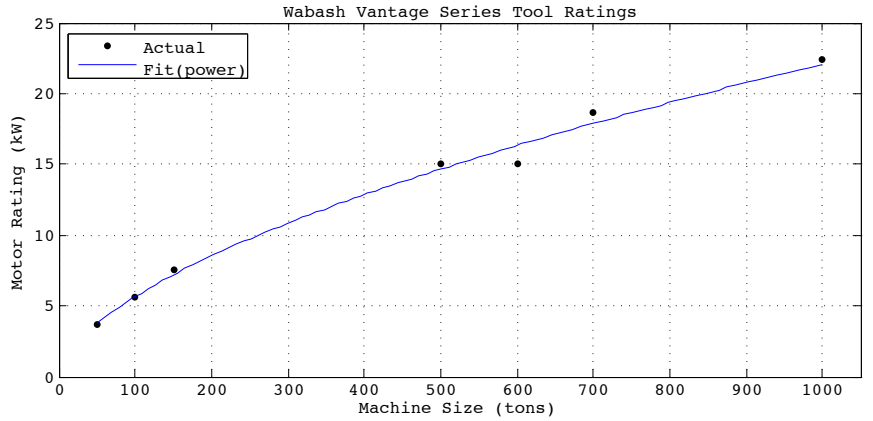

(a)

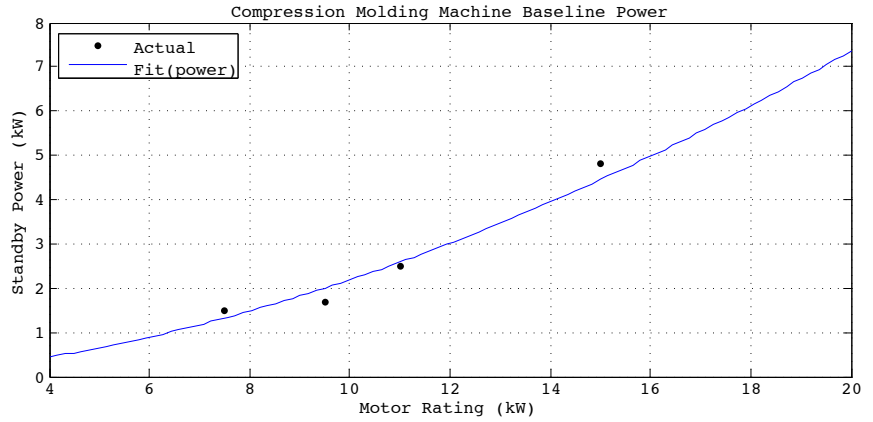

(b)

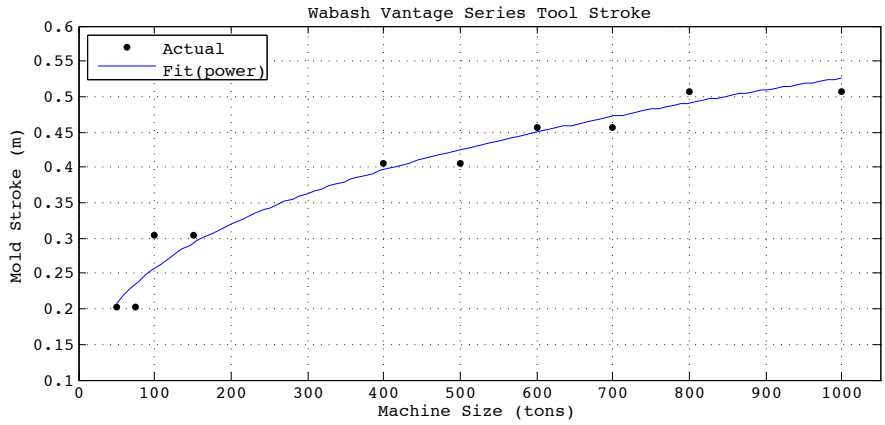

(c)

Figure 3.15: a) Wabash CMM motor rating (kW), b) PBM baseline power (kW) c) Wabash CMM mold stroke (m)

platen open and close speed set by the manufacturer, and t_{cure} is the cure time.

Sheet Metal Stamping

The last unit process of interest is sheet metal forming. Sheet metal forming is a very mature metal forming technique dating back to 5000 B.C., and where today is used to manufacture a wide variety of products ranging from beverage cans to appliances and automobiles [328]. In theory, any sheet metal material with high formability, which is the ability to undergo shape change without failure by necking, can be successfully formed, with common materials consisting of aluminum, low-carbon steel, and titanium. The definition of a sheet metal can be slightly ambiguous, but is typically taken as being less than an eighth of an inch thick and any greater is considered a plate [295].

Within the field of sheet metal forming there are numerous forming process technologies. Some common examples are: punching, blanking, stamping, embossing, bending, parting, roll forming, deep drawing, and a variety of other processes [328]. For each of these forming processes there are also a variety of machine tool technologies. Such machine tools include: hydraulic stamper (high force, low speed), progressive die stamper (low force, high speed), hydro-forming (closed die cavity backed by pressurized fluid [210]), turret press (high speed localized forming and punching), explosive forming, impact forming (high velocity die impact), and press break form (bending operations). For analysis of the SEC, only progressive die stamping process is considered, and while the other processes will not be covered a majority of the fundamental principles still apply.

Progressive die stamping is a vertical multi-station stamping process where multiple dies are fabricated onto a single press. Each press stroke may consist of multiple punching, bending , and forming dies where the sheet metal is progressed forward after each stroke either manually or automatically fed from a coil [32]. The advantage with progressive die stamping over conventional hydraulic stamping is higher throughput for relatively low profile parts where press speeds of over 100 strokes per minute are possible. To achieve these high speeds the hydraulic system is replaced with all-electric servo-motor drives, which have a much faster response and lower energy consumption. However, the drawback is a reduction in the maximum force that can be generated with the servo drives while maintaining high speeds. This sets a limitation on the sheet metal material and gage (i.e., thickness) and part complexity (e.g., limited to shallow trenches) [32].

At the unit process level the stamping operations that will be focused on for energy analysis are shallow trench/channel forming and punching/blanking. The process for punching and blanking are near identical. In punching the punched material is discard whereas in blanking the punched material is the part itself. The progressive die stamping operation is relative simple with typically one press speed and no external heating involved. The specific energy consumption can be written as:

$$SEC = \frac{E_{stamp} + P_{oc}t_{oc} + P_{base}t_{cycle}}{m_{part}} \tag{3.41}$$

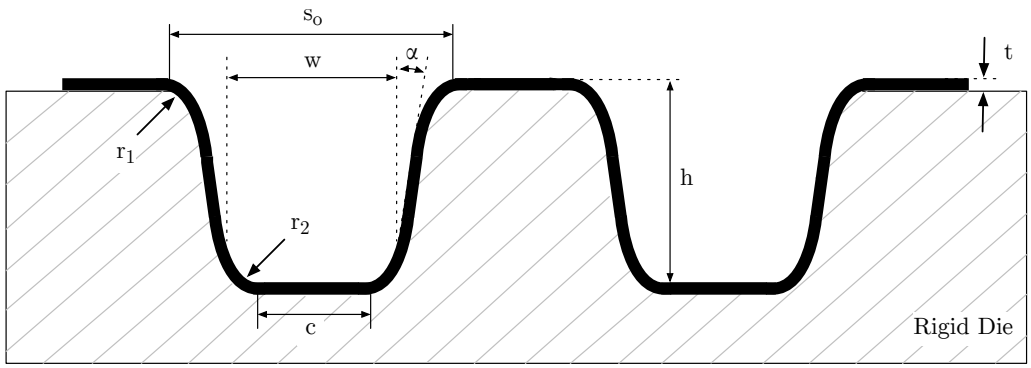

Figure 3.16: Schematic of a formed sheet metal in a rigid die

Where E_{stamp} is the energy required to form the channels and shearing (punching), P_{oc} and t_{oc} are the press lower/raise power consumption and cycle time, respectively, P_{base} is the baseline/idle power consumption, t_{cycle} is the process cycle time and is entirely dictated by the press speed (which is recommended by the manufacturer), and m_{part} is the mass of the finished stamped part. As with injection and compression molding, the energy analysis is broken into a theoretical analysis for the forming energy and empirical analysis for the baseline and platen lower/raise power.

Theoretical Analysis

A schematic of a channel formed sheeted metal in a rigid die is shown in Figure 3.16. The sheet metal is initially loaded as a flat sheet onto the a rigid die female base. A complementary rigid male upper die (not shown) with slightly smaller features is lowered and plastically forms the sheet metal to the contour spacing between the dies. The corners of die channels are rounded to a minimum curvature of radius of three times the sheet metal thickness to reduce the concentration of stress that can lead to rupture and cracking [328].

The theoretical energy required to stretch and form the channels is equal to the elastic and plastic deformed energy, which is equal to the strain energy. The strain energy can be expressed as the product of the strain energy density (energy per unit volume) and the deformed volume. The strain energy density is computed by integrating the material stress-strain curve as a function of the strain. Assuming uni-directional in-plane strain and starting from the unstrained state, the strain energy density is:

$$U_o = \int_0^{\epsilon_f} \sigma(\epsilon) \mathrm{d}\epsilon \tag{3.42}$$

Where U_o is the strain energy density, ϵ_f is the final true strain, and $\sigma(\epsilon)$ is the stress-strain function of the material. The assumption of uni-directional in-plain strain assumes that the strain in the thickness direction (through-plane) and the strain in the direction

perpendicular to the forming (die displacement) direction is relatively negligible. Therefore, the final uni-directional true strain can be express as:

$$\epsilon_f = \ln \frac{s_f}{s_o} \tag{3.43}$$

Where s_f is the final elongated channel length and s_o is the initial projected channel width. The final elongated length can be approximated based on geometry of the channel:

$$s_f = 2\left[(r_1 + r_2)(90 - \alpha) + \frac{h - (r_1 + r_2)(1 - \sin\alpha)}{\cos\alpha}\right] + c \tag{3.44}$$

Where the first and second terms calculates the arc lengths of the upper and lower die corners and the wall slope, respectfully. Generally, the die parameters α, r_1, r_2, h, and c are determined by the designer. The stress-strain function in the strain energy density equation can be modeled using the Ramberg-Osgood expression for most nonlinear metals such as aluminum and steel . However, studies showed that the Ramberg-Osgood expression varied significantly from experimental at stresses higher than the 0.2% proof stress ($\sigma_{0.2}$), which is the industry standard practice to be equivalent to the yield stress [264]. Therefore, a modification was made to include the full stress-strain curve, and assuming the elastic deformation energy is negligible:

$$\sigma(\epsilon) = \begin{cases} \sigma_{0.2}\left(\dfrac{\epsilon}{0.002}\right)^{\frac{1}{n}} & \text{for} \quad \epsilon \leq \epsilon_{0.2} \\ \sigma_{0.2} + (\sigma_u - \sigma_{0.2})\left(\dfrac{\epsilon - 0.002}{\epsilon_u}\right)^{\frac{1}{m}} & \text{for} \quad \epsilon > \epsilon_{0.2} \end{cases} \tag{3.45}$$

Where $\sigma_{0.2}$ is the 0.2% proof stress, σ_u is the ultimate tensile strength, $\epsilon_{0.2}$ is the 0.2% total strain, ϵ_u is the strain at σ_u, n is a parameter that determines the sharpness of the knee in the stress-strain curve, and m is an empirically determined fitting parameter and is highly material dependent (i.e., σ_u). The 0.2% total strain accounts for strains exceeding the 0.2% proof stress and is express as [264]:

$$\epsilon_{0.2} = \frac{\sigma_{0.2}}{E_o} + 0.002 \tag{3.46}$$

Where E_o is the material Young's modulus. Furthermore, an expression for the fitting parameter, m, was experimentally determined [264]:

$$m = 1 + 3.5\frac{\sigma_{0.2}}{\sigma_u} \tag{3.47}$$

A table of the parameters from Equations 3.45 to 3.47 for various stainless steels can be found in Appendix. The final strain energy can be determined by analytical or numerical integration of Equation 3.45 with the true strain, Equation 3.43, and multiplying by the deformed volume. Note, that the actual energy consumption will also depend on the servo-motor drive efficiency and any frictional losses from die arm movement and from the die and sheet metal during forming.

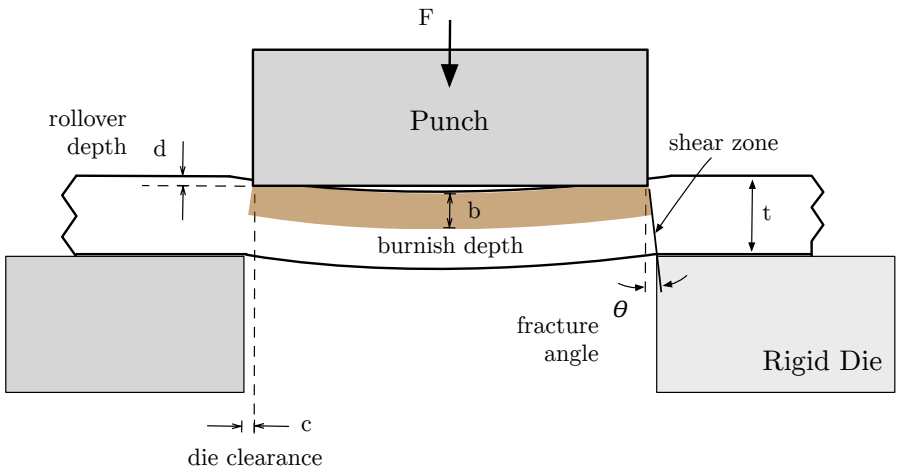

Figure 3.17: Schematic of punching with a rigid die

The punching energy consumption is a function of the concentrated shear stresses at the die edges. Schematically shown in Figure 3.17, the shear stress zone occurs between the point contact from the edges of the lower and upper die. As the punch force increases, the punch ram elastically deforms the sheet material at the punch and die edge, denoted as the rollover depth. The rollover depth is directly proportional to the size of the punch clearance. Once the punch penetrates and plastically deforms the the material a burnish region is created. The size of the burnish region is equal to the depth of the plastic deformation region with the shaper the punch the wider the burnish region [295]. Immediately after the burnish region is formed, fracture occurs at the shear zone and the scrap sheet material is punched out.

The energy dissipated due to punching is equal to the applied force that causes the shear fracture and the penetration depth of the punch into the sheet metal. An expression to approximate the theoretical energy dissipation can be written as [295]:

$$U_{punch} = \sigma_{UTS} p L_p t^2 \tag{3.48}$$

Where σ_{UTS} is the ultimate tensile strength of the sheet metal, p is the penetration depth, which is the sum of the rollover and burnish depth, L_p is the perimeter contact length between the punch and die, and t is the sheet metal thickness.

Empirical Analysis

The meta-analysis for progressive die stamping and proxy technologies yielded very limited results. Only two studies were collected that had enough detail to distinguish both baseline and drive (lower/raise) power. A third proxy technology was found that had power consumption data for an electric servo drive press-braking machine. Although intended for different processes (stamping versus bending) the core of the machine tool itself (e.g., servo-motor drives, controls, operation) is near identical. The collection of data was plotted and fitted

Table 3.4: Regression coefficient for PSM empirical model

	PSM Baseline Power	**PSM Drive Power**
Form:	$P_{base} = AF + b$	$P_{drive} = AF + b$
A:	0.0113	0.0159
b:	0.3725	1.517
R^2:	>0.99	>0.99

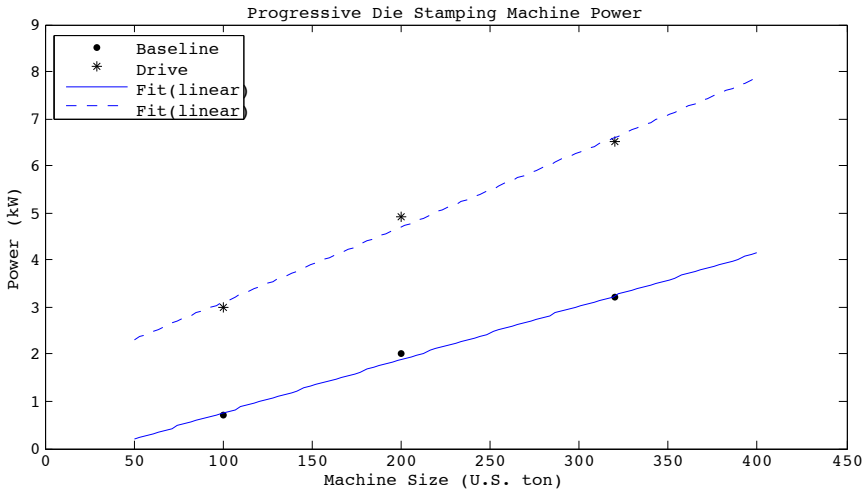

Figure 3.18: Empirical model fits for baseline and drive power

in relation to the machine size (U.S. ton) using linear regression. The results of the fitting are tabulated in Table 3.4 and plotted in Figure 3.18.

The power consumption for both baseline and drive power showed a very strong linear dependence with the machine tool size. The linear correlation may be influenced by the fact that servo-motors are relatively efficient and mainly draw power on demand. For instance, one of the studies collected showed the total tool power consumption varying linearly with press speed from 40SPM to 70SPM[9] for a 200-ton progressive stamping machine [290]. However, there is still potentially a high level of uncertainty due to lack of representative data. The uncertainty becomes even greater for extrapolating to larger machine sizes.

3.2 Roll-to-Roll Processing Line

The modeling of the production line scale in the SGM is dependent on many external and internal factors. The primary external factor is the product demand, which dictates the production volume and therefore the production line size (machine tool type and size) and the

[9]SPM = strokes per minute

number of simultaneous production lines (internal factors). A very interesting production line technology is roll-to-roll (R2R) processing, which is a continuous (usually fully automated) processing technique where the product is in the form of a web (continuous sheet) or conveyed on a web. R2R processing has existed since the beginning of the 19$^{\text{th}}$ century originating in the paper industry and now spans textiles to liquid coating applications, and more recently thin-film electronics and solar cells [289]. For products that can be processed using a R2R technique the advantage is clear. Higher production volumes and rates can be achieved through reduced setup time, transfer time, and parallel production by simply increasing the width of the web. Furthermore, being continuous and easily automated reduces the number of factory workers thus reducing labor costs. In this section, the focus is on the line modeling, specifically the throughput, web size, and number of simultaneous lines needed to meet demand. The actual design of the R2R machine tool (e.g., rollers) will not be covered since it varies case by case, for example, a paper making fourdrinier machine has different tool design requirements that R2R printed electronics. Web quality and handling is highly dependent on the web tension [345], which will also not be covered since the details are beyond the scope of the line scale modeling (see [296] for more information).

The throughput of the R2R line is primarily a function of the line availability (which is often equal to the tool availability) and the web speed. The total processing time of a roll process follows a similar calculation as conventional batch processing. Ignoring for a moment the line availability, the equation for batch processing time (commonly in unit of parts per hour) is given as:

$$T_b = \max_i \left(T_{su} + T_{no} + Q \cdot T_c + T_{in}\right) \tag{3.49}$$

Where T_b is the cycle time per batch, T_{su} is the setup time for station i, T_{no} is the non-operation time, including transfer time, for station i, T_c is the cycle time per batch for station i, Q is the batch size, and T_{in} is an optional inspection time. For R2R processing the batch size is set to one roll and the non-operation time most often is negligible (typically the time to remove the roll from the tool). The annual throughput is simply the product of the tool availability and roll processing time scaled to a year.

The calculation for process time becomes more complicated when accounting for less than 24-hour daily shifts by placing a constraint on the maximum number of rolls that can be processed per day. Furthermore, due to machine size and quality control limitations, roll processing is typically partitioned into several smaller size rolls as opposed to a single roll covering the entire day-shift.[10] To illustrate, the roll scheduling is schematically shown in Figure 3.19. In a day's worth of production, there are N equal length primary rolls, R^p that can be processed based on Equation 3.49 and the web speed. There is also an additional secondary roll of shorter length, R^s that can be processed from the remaining time to maximize the tool utilization. This takes advantage of the unique property of R2R

[10]Also depends on the nature of the product. For paper making a large single roll is possible, while ill-advised for high cost and risk printed electronics and solar cells.

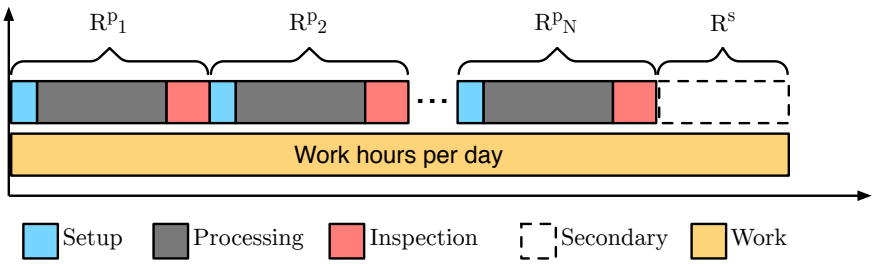

Figure 3.19: Diagram of daily roll-to-roll scheduling

processing in which the web length can easily be shortened, or created at any length, such as paper making and polymer films.

A methodology was devised to create an algorithm for determining the throughput, web dimensions (i.e., width and length), and the number of simultaneous lines for R2R processing. An overview of the methodology is laid out in a flow chart shown in Figure 3.20. The algorithm takes in an annual production volume input and through an iterative technique determines the maximum number of rolls based on the roll area (roll length$\times$width) and updates first the roll length followed by roll width and finally the number of lines after the maximum length and width have been reached. The increase in the number of lines is necessary in order to meet the daily production demand. An inspection step is also included and, depending on the configuration, will influence the throughput. For automated systems the inspection process is typically in-situ through various sensors and optical techniques. Manual inspection is typically performed post-processing and the added time is accounted for in the throughput.

As the number of lines increase the number of effective processing days decrease. The effective processing days is defined as the number of days required to produce a given annual volume based on the current number of production lines. For example, if the annual production volume is 200m^2 and the throughput per line is 100^2 per day, then for one line the effective processing days is two, and for two lines is one, four lines is half day, and so on. Therefore, the program terminates when the number of effective processing days is less than or equal to the actual number or working days in a year (typically 260 days excluding holidays).

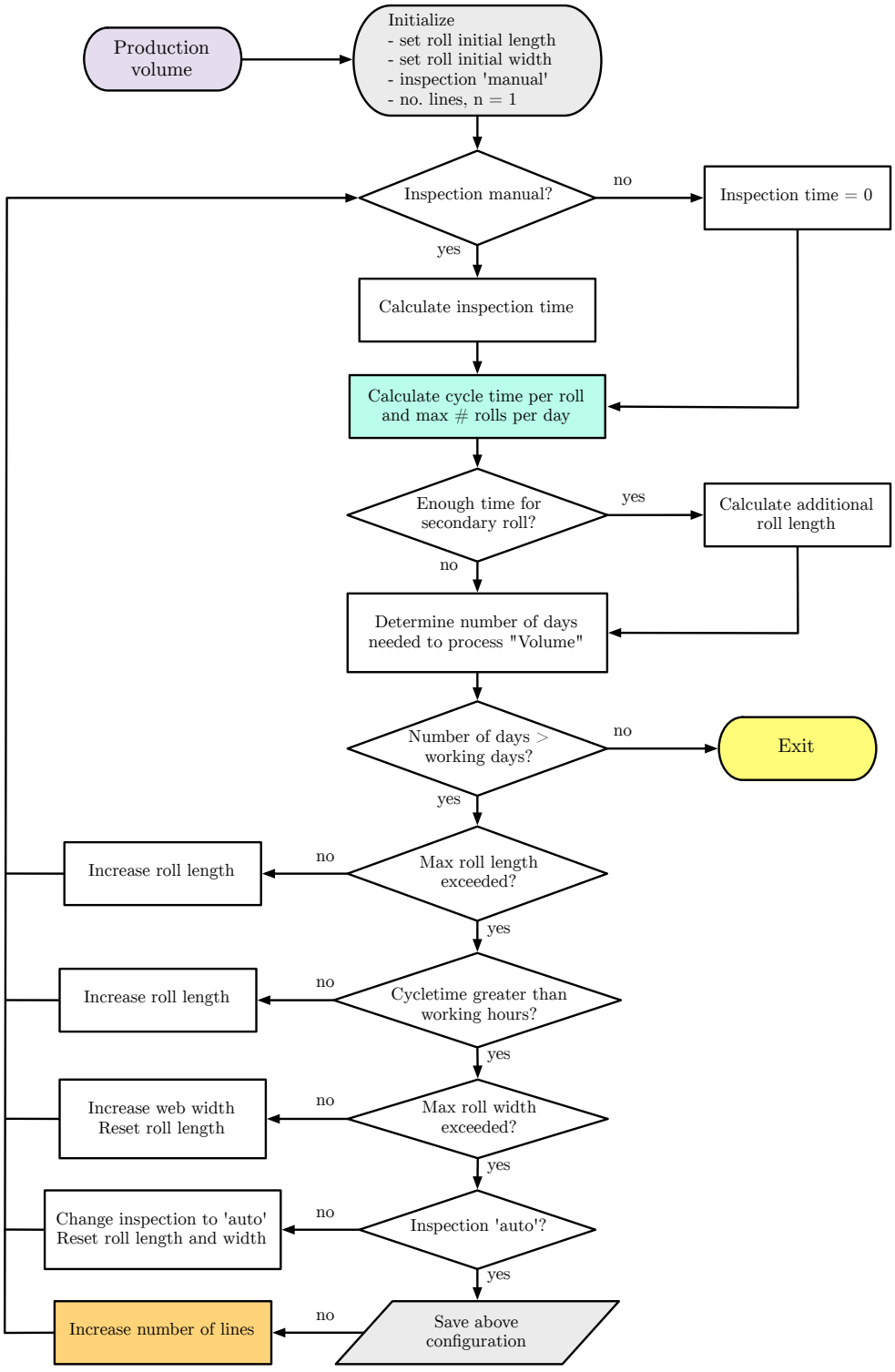

Figure 3.20: Algorithm for determining number of the lines and web dimensions

3.3 Facility HVAC Modeling

Impacts from facility scale in manufacturing are often overlooked as summarized in the green manufacturing section in Chapter 2. In many cases, exclusion of the facility scale impacts is a major oversight considering that considerable amounts of energy and resources are required to run and maintain a facility whether it is a commercial building or industrial facility. For instance, the building sector alone in the United States accounted for 7% and 41% of the global and U.S. primary energy consumption in 2010, respectively [74]. The 41% for the U.S. represents 44% more than the transportation sector for the same year. Of the energy consumed in the buildings sector, commercial buildings accounted for 46% where the top three end uses, space heating (27%), lighting (14%), and space cooling (10%), represented close to half of the total energy consumption. Besides energy, water use in the buildings sector in 2005 consumed nearly 10% of total water use in the U.S. Furthermore, the energy required to pump, treat, distribute, and clean the water accounted for nearly 1% of the U.S. net electricity generation.

On the industrial level, facility scale systems (e.g., HVAC, compressed air, process cooling water) accounted for roughly 40% of the onsite energy losses, with 8% of that for conditioning and lighting systems [250]. The majority of the facility energy loss (depending on industry) comes from steam system inefficiencies than can range from 50-85%. Stream is typically generated using electric or gas-fired boilers for pressurized systems that require steam, water and space heating, and controlling the humidity in a HVAC system. One study analyzed the life cycle energy consumption of a milling machine tool and found that the HVAC and lighting contributed to 40-65% of the total use phase energy, depending on the facility and production environment [69]. Another life cycle study revealed that the facility systems for a sheet manufacturing plant contributed to approximately 12% of the overall product carbon footprint, the second highest contributor [290]. In facilities that use compresses air such as in the automotive industry, large amounts of energy is consumed during the production of the compressed air. It was estimated that in 1997 about 3% to 9% of total energy consumed in U.S. manufacturing was for air compression [358].

Of the many facilities systems, the focus of the of the facility scale modeling will strictly be HVAC and lighting energy consumption. Other systems such as compressed air and water treatment will be case-by-case depending on the type of manufacturing processes involved. Modeling lighting energy consumption is a linear function of the facility floor space and production scheduling. HVAC energy modeling is much more complex. The purpose of the HVAC system is to heat, cool, and ventilate a confined area. It is responsible for controlling the indoor temperature, humidity, and air quality for maintaining both the machine tool working environment and addressing worker health and safety concerns. The thermodynamics involved is a intricate balance between outdoor environmental conditions, indoor heat generation and loss, and the ventilation rate connecting the two. High ventilation rates are typically needed in the summer whereas high enough rates are needed to supply fresh air in the winter to minimized heat loss [200]. In addition, the type of HVAC system plays a large role in the heating and cooling efficacy. For instance, heating and cooling could be

provided by a hydronic radiant system where heated and chilled water flow through the walls of the facility. Thermal energy could be supplied via solar thermal systems, geothermal heat (heating in the winter and cooling in the summer), and cogeneration applications utilizing the excess or generated heat from power generation systems [315]. Due to the complexities of such systems and their current limited use in industry, the HVAC modeling will only consist of conventional blower/duct systems with resistive heating and chilled water heat transfer cooling.

Energy Modeling Methods

There exists numerous methods and tools for modeling the HVAC and lighting energy consumption of a building/facility. In fact, over a hundred software programs have be developed in the past 50 years to address building energy and cost [56]. These programs range vastly in capabilities and complexity as well as price. Software programs such as *EnergyPlus* by the U.S. DOE have the ability to input an internal thermal load, building design, and actual weather data from different climate zones and simulate the energy consumption based on different temperature set points, ventilation (natural versus forced), and HVAC designs (e.g., efficiency). An overview of twenty major simulation software programs can be found in [56]. Although these software programs provide comprehensive algorithms and simulations, the intended use is for standalone applications. Therefore, it is not possible, nor is the intention, to integrate such softwares with the scales of manufacturing. Thermal loads from the process to line scale can be separately calculated and manually input to the software, however, that eliminates any convective heat transfer coupling between the ventilation and machine tool heat loss.

Another possible modeling method is to use empirical data or a meta-study on HVAC energy consumption. The U.S. Energy Information Administration (EIA) provides a publicly available building energy database called the Commercial Building Energy Consumption Survey (CBECS). This database provides a national level source of data on the facility energy consumption for various building types and sizes (square-footage), and gives a breakdown by fuel type and electricity and thermal consumption for heating, cooling, ventilation, and lighting [219]. The database is useful in obtaining high level energy data, however, is too aggregated and static for the level of precision and robustness required for integration with the SGM.

The most practical method for integration is to build a model in a similar manner as the unit process analysis. The type and depth of the modeling can vary widely. The following non-exhaustive list covers several commonly practiced modeling techniques for modeling HVAC energy consumption:

- Forward Modeling: the classical approach using sound thermodynamic engineering principles to create an analytical model based on physical systems such as the building geometry and characteristics, geographical location, equipment and HVAC, and building operation and schedule. The forward modeling uses methods such as the

heat balance method, weight-factor method, and thermal-network method (see [54]), which discretizes the building into a network of nodes to solve the heat transfer balance problem [13]. The model is very flexible (i.e., customizable) and the results can be very precise. The drawback is the potentially high computational cost required to solve the analytical equations. Furthermore, the model is highly sensitive where a small errors may drastically propagate causing large deviations in the results [200].

- Data-Driven Modeling: also referred to as Inverse modeling, data-driven modeling involves using empirical HVAC energy data to correlate the input (e.g., outdoor temperature) to the response of the HVAC system using statistical or regression modeling techniques [13]. The major advantage of the data-driven model is simplicity and accuracy (in terms of total energy consumption) under the specific conditions. The difficulty, however, is correlating data to heat demand and the accuracy of the model suffers when the system is dynamic such as unpredictable heat loads. There is also the obvious drawback of obtaining the data in the first place where more often than not the HVAC energy metering is coupled with the total building energy [200].

- Degree-days and Bin Methods: the degree-day method is a simplistic analytical method, which assumes that on a daily average (typical buildings have a time constant of about one day [13]), where the building heat load and HVAC efficiency are relatively static, the HVAC energy is proportional to the difference between the daily mean outdoor temperature and mean reference temperature (typically annually averaged). The difference is multiplied by an fuel efficiency factor that changes depending whether the daily mean temperature is lower (heating) or higher (cooling) than the reference. The bin method is a higher order version of the degree-days where multiple reference temperatures are incorporated and the difference is calculated on a per hour or per several hour basis [200]. The degree-days and bin method can yield remarkably accurate results on an annual basis for single-zone buildings. However, the initial assumption of constant heat load demand greatly limits the efficacy of the approach for an industrial facility.

- Hybrid Modeling: There are various variations for the hybrid modeling. Hybrid modeling combines all the above modeling techniques with a foundation using forwarding modeling. For example, a thermal-network can be used to precisely model the response of the HVAC system and an empirical approach to fine tune the results to match the data. Another example would be to discretize (i.e., bin method) the forward modeling into hourly time steps and at each time step determine if heat, cooling, or just ventilation is required.

HVAC Model

The remaining portion of this section will cover the methodology for computing the HVAC energy consumption and the necessary thermodynamic analytical equations for setting up

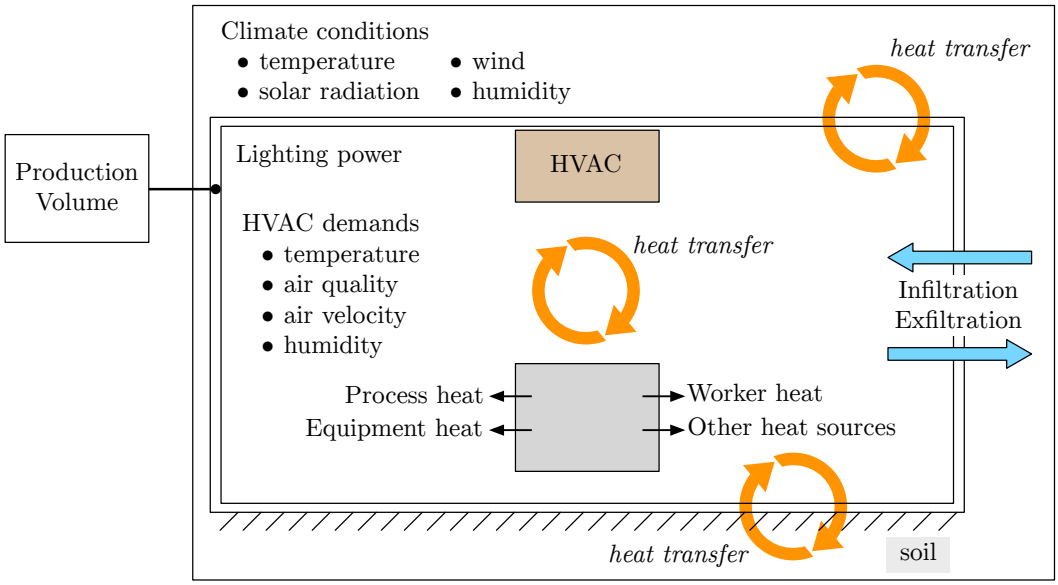

Figure 3.21: Schematic overview of the facility scale model

and solving the thermal-network problem. Figure 3.21 shows the interaction between the facility scale control volume and the outdoor environment. Within the control volume, the key considerations are internal air temperature (assumed to be uniform throughout the entire volume), exit air velocity from the HVAC ventilation, air quality in terms of freshness from outdoor air, and humidity. The thermal balance includes the interaction between the released internal heat from sources such as processes, machine tools, office equipment, worker body heat, and lighting heat, to the necessary thermal energy from HVAC system to offset the heat demand. Simultaneously, there is the interaction between the facility control volume and the outdoor environment and the Earth (i.e., soil). Key considerations for the outdoor environment are outdoor temperature, net solar irradiation, wind (for convective flow), and humidity. For buildings with windows, there is an addition coupling between the incident solar irradiation and resulting internal heat generation. The soil generally acts as a conductive heat sink in the summer and heat source in the winter.

The model becomes more complicated when both infiltration and exfiltration are taken into account. Infiltration is the rate of air leakage into the facility and exfiltration is the rate of air leakage exiting the building. Air leakage may be caused by numerous unintentional means such as cracks and seams, workers entering and exiting the building, and ventilation leaks, and the exact values can be are very difficult to quantify. The final model parameter is external to the thermal-network itself and is the input of production volume, which determines the size (i.e., square-footage) of the facility. More specifically, the production volume dictates the number of production lines, which sets the facility size, number of workers, and so forth.

In addition to the thermal-network model, the Bin method allows discretization and

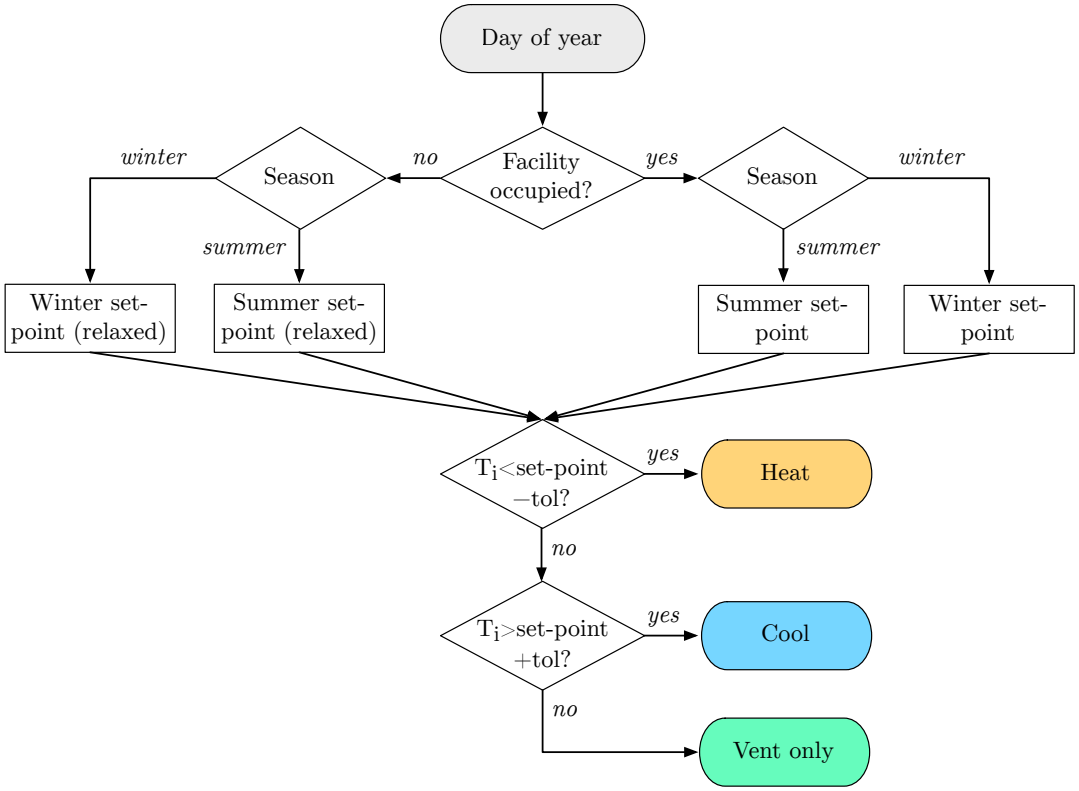

Figure 3.22: HVAC set-point temperature algorithm

temperature control relative to a reference temperature. The reference temperature is the set-point temperature controlled by the thermostat and changes depending on the season in the year and for geographic location (e.g., set-points in Washington will be different than Arizona due to different in mean temperatures). For model simplicity, it will be assumed that only two seasonal, winter and summer, type set-points are used. Figure 3.22 shows the flow chart algorithm for assigning the proper set-point temperature.

The algorithm inputs the current the day in the year and first determines whether or not the facility is in operation (i.e., workday) or shutdown such as the weekends, holidays, and off-working hours. During the working hours of a workday the set-point is either set to the summer set-point or winter set-point temperature. During non-operational hours the set-points are relaxed by, for example several degrees, to reduce the loading on the HVAC. As the thermal-network equations are solved at each bin, the program checks if the internal temperature, T_i, is less than, greater, or equal to the set-point temperature taking account a tolerance factor, *tol*. The tolerance factor is an important parameter that represents a thermal time delay or compensation factor for the HVAC system to avoid constant on-off fluctuations. For example, if the set-point temperature in the winter is 18°C and the tolerance is 1°C, the HVAC heating system will initiate in at 17°C and heat until 19°C. Note, that the air ventilation is constantly on at a steady flow rate during working hours and at a reduced

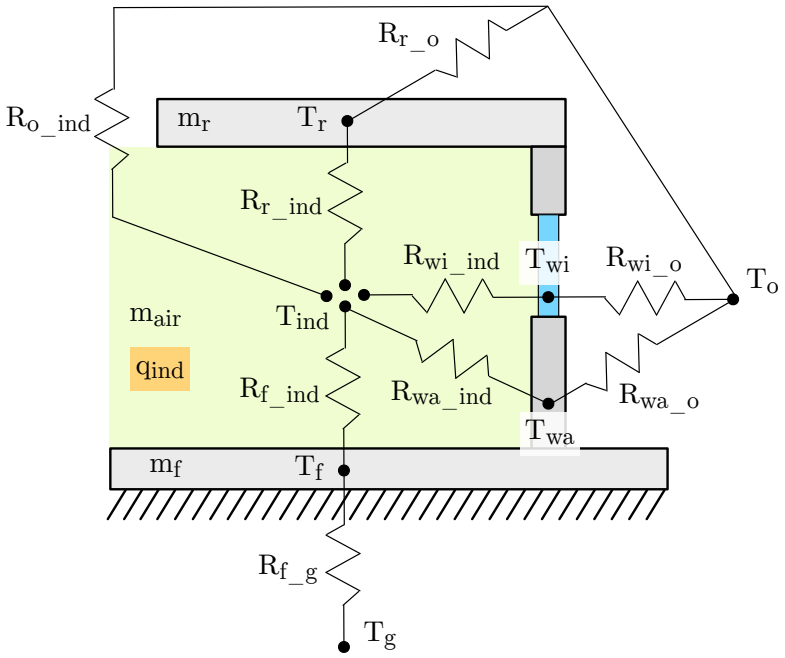

Figure 3.23: Thermal network of a building

flow rate during non-working hours.

Thermodynamic Network

A schematic of the thermal-network for a building is shown in Figure 3.23. A total of nine thermal resistances and five thermal capacitances (internal air, roof, floor, walls, windows) are accounted for. Each thermal resistance represents an effective heat transfer (conduction, convection, radiation) between two nodes. The thermal capacitance represents the thermal energy storage, which creates a dampening effect or time response in the form of thermal inertia. For every component with a thermal capacitance there is an unknown temperature node to be solved. Hourly outdoor temperature, T_o, for most major cities can be obtained online through weather databases. The soil temperature, T_g, can be modeled using a sinusoidal function with the average soil temperature. Explanation on the soil temperature model is explained in the last subsection of this chapter.

Before diving in to the analytical portion of the model several assumptions are to be made. First, for simplicity, only one-dimensional heat transfer is considered. Therefore, uniform temperature distributions are assumed at every node. Higher order modeling is not necessary to obtain sufficiently accurate results, especially considering the difficulty of obtaining high enough resolution of detailed for modeling the building in two or three dimensions, and the precision of data needed on the outdoor and soil temperatures and solar irradiation and wind gradients. However, aspects of a three-dimensional model will be incorporate. For instance,

the angle of incidence for solar irradiation is dependent on the time of day, geographical location, and orientation and angle of the building facets. It is also assumed that the effects of internal air pressurization is negligible. Buildings (typically commercial) are pressurized to control infiltration for humidity and air quality reasons [13]. Is is also assumed that internal heat transfer dominated by convection and conduction, thus neglecting heat transfer due to radiation.

Solving the thermal-network in Figure 3.23 involves breaking down the heat transfer equation at each node. The thermal balance is taken from the First Law of Thermodynamics and at each node:

$$q_{stored} = q_{in} - q_{out} + q_{gen} \tag{3.50}$$

Where

- q_{stored}: is the rate of energy (i.e., heat) stored in a controlled volume
- q_{in}: is the rate of energy entering a controlled volume (e.g., solar irradiation)
- q_{out}: is the rate of energy exiting a controlled volume (e.g., via exfiltration)
- q_{gen}: is the rate of energy generated within the controlled volume from such sources as lighting, workers, machine tools, etc.

The rate of the heat storage term in Equation 3.50 is function the thermal capacitance and the rate change in temperature, and is expressed as:

$$q_{stored} = mC_p \frac{dT}{dt} \tag{3.51}$$

Where m is the mass of the body storing energy, C_p is the specific heat capacity (which is a function of the temperature), dT/dt is the rate change in temperature. Alternatively, the temperature can be at a steady-state in which the mass of a control volume changes over time. The transfer of heat in and out of the control volume, q_{in} and q_{out}, is characterized by the thermal resistance between two bodies of mass and their corresponding temperatures. For thermal conduction the thermal resistance is expressed as:

$$R_{t,cond} \equiv \frac{T_{s,1} - T_{s,2}}{q} = \frac{L}{kA} \tag{3.52}$$

Where $T_{s,1}$ and $T_{s,2}$ are the surface temperatures for body 1 and 2, respectively, L is the spatial distance between the two surfaces, k is the thermal conductivity, A is the cross-section area orthogonal to the heat flow, and q is the heat rate. A similar expression can be written for convection:

$$R_{t,conv} \equiv \frac{T_s - T_\infty}{q} = \frac{1}{hA} \tag{3.53}$$

Where T_s and T_∞ are the exposed surface temperature and convective fluid temperature, respectively, h is the heat transfer coefficient, and q and A are the same as Equation 3.52. Combining Equations 3.50 to 3.53 the thermal-network from the i^{th} node to j^{th} surface can written in the general form:

$$\sum_{j=1}^{N} \frac{T_j - T_i}{R_{i\_j}} = m_i C_{p,i} \frac{dT_i}{dt} - q_i^{gen} \tag{3.54}$$

Applying the above equation to each of the five unknown temperature nodes results in the full analytical expressions:

$$@T_{ind} : \frac{T_o - T_{ind}}{R_{o\_ind}} + \frac{T_r - T_{ind}}{R_{r\_ind}} + \frac{T_f - T_{ind}}{R_{f\_ind}} + \sum_{i=1}^{N} \frac{T_{wa}^i - T_{ind}}{R_{wa\_ind}^i} + \sum_{j=1}^{M} \frac{T_{wi}^j - T_{ind}}{R_{wi\_ind}^j} = m_{air} c_{p,air} \frac{dT_{ind}}{dt} - q_{ind}^{gen} \tag{3.55}$$

$$@T_f : \frac{T_{ind} - T_f}{R_{ind\_f}} + \frac{T_g - T_f}{R_{g\_f}} = m_f c_{p,f} \frac{dT_f}{dt} - q_f^{gen} \tag{3.56}$$

$$@T_r : \frac{T_{ind} - T_r}{R_{ind\_r}} + \frac{T_o - T_r}{R_{o\_f}} = m_r c_{p,r} \frac{dT_r}{dt} - q_r^{gen} \tag{3.57}$$

$$@T_{wa}^i : \frac{T_{ind} - T_{wa}^i}{R_{ind\_wa}^i} + \frac{T_o - T_{wa}^i}{R_{o\_wa}^i} = m_{wa}^i c_{p,wa}^i \frac{dT_{wa}^i}{dt} - q_{wa}^{gen,i} \tag{3.58}$$

$$@T_{wi}^j : \frac{T_{ind} - T_{wi}^j}{R_{ind\_wi}^j} + \frac{T_o - T_{wi}^j}{R_{o\_wi}^j} = m_{wi}^j c_{p,wi}^j \frac{dT_{wi}^j}{dt} - q_{wi}^{gen,j} \tag{3.59}$$

Where T_{ind}, T_f, and T_r are the indoor, floor, roof temperature nodes, respectfully, T_{wa}^i and T_{wi}^i are the i^{th} wall and j^{th} window, respectively. If, for example, a building has 4 sides (i.e., walls) with a window per side, the number of unknown temperature nodes to be solved is $1 + 1 + 1 + 4 + 4 = 11$. Note, the thermal resistances are not directional meaning $R_{x\_y} = R_{y\_x}$.

In most buildings, the walls, roof, and flooring layers are constructed with multiple layers providing structural integrity, thermal insulation, and sound and fire proofing. The thermal resistance of such composite layering can be lumped into an effective thermal resistance or commonly referred to as the overall heat transfer coefficient:

$$U = \frac{1}{\sum R_t} \tag{3.60}$$

Where the total thermal resistance is expressed as:

$$\sum R_t \equiv \sum_i^N \frac{1}{h_i A} + \sum_j^M \frac{L_j}{k_j A} \tag{3.61}$$

Where N and M are the number of convective surfaces and conductive layers, respectively. Equation 3.61 assumes the layers are connected in series, ignoring any in-plane conduction (which would lead to a parallel type configuration).

Solving the thermal-network problem involves time discretization of Equations 3.55-3.59 with the thermal resistances substituted with Equations 3.60 and 3.61. Time discretization is required to numerically solve for the time differentiation in the dT/dt term. To a first order approximation the time discretization is the first expression in the Taylor Series expansion, and is such that $t^{n+1} = t^n + \Delta t$. Using this concept, there two common methods for representing the discretization:

$$T^{n+1} = T^n + f\left(t^n, T^n\right)\Delta t + \mathrm{O}\left(\Delta t\right)^2 \tag{3.62}$$

$$T^{n+1} = T^n + f\left(t^{n+1}, T^{n+1}\right)\Delta t + \mathrm{O}\left(\Delta t\right)^2 \tag{3.63}$$

The first method, Equation 3.62, is referred to as Forward Euler and is an explicit time discretization scheme. The updated temperature value, T^{n+1}, depends strictly on the time differential function at the previous time step. This explicit scheme is the simplest to implement with relatively low computational cost. The drawback, however, is that small time steps are required for numerical stability. This is not always practical especially in cases where data such as q_{gen} is not known *a priori* and in situations using non-deterministic data (potentially random fluctuations). An arbitrary small time can be used, however, that undermines the advantage of low computational cost. The second method, Equation 3.63, is referred to as Backward Euler and is an implicit time discretization scheme. The unique feature about the implicit scheme is that the updated temperature value, T^{n+1}, depends on the updated time differential function. This leads to a dramatic increase in the numerical stability since the function is always being evaluate at a "future" time step. The main drawback to the implicit scheme is difficulty in integration and potentially expensive computational cost due to simultaneously solving a system of linear equations. Furthermore, if the time step is too large, the accuracy greatly deteriorates and in some instances the numerical solver can fail to converge. Despite these limitations, the implicit scheme is preferred due to the stability of the solution and noting the fact that the computational power is not a constraint with today's advance processor speeds. Note that both the explicit and implicit schemes have higher order terms from the Taylor Series expansion and are assumed to be negligible.

Using the implicit scheme of discretization and using Equation 3.56 as an example with the overall heat transfer coefficient, the $(k+1^{th})$ time step iteration can be written as:

$$U_f\left(T_{ind}^{k+1} - T_f^{k+1}\right) + U_g\left(T_g^{k+1} - T_f^{k+1}\right) = m_f c_{p,f}\frac{T_f^{k+1} - T_f^k}{\Delta t} - q_f^{gen,k+1} \tag{3.64}$$

Rearranging Equation 3.64 and converting into a more convenient linear matrix equation form (i.e., $[A]T = b$) yields:

$$\left[\; U_f \quad -\left(U_f + U_g + \frac{m_f c_{p,f}}{\Delta t}\right) \; \right] \times \left\{ \begin{array}{c} T_{ind} \\ T_f \end{array} \right\}^{k+1} = \left\{ -\frac{m_f c_{p,f} T_f^k}{\Delta t} - q_f^{k+1} + U_g T_g^{k+1} \right\} \quad (3.65)$$

The linear matrix expression gives a clear picture of what is being solved. The left and right terms in the above discretization are known quantities. Recall that both T_o and T_g are known *a priori* at each hour for the entire year. Putting all the equations into matrix form and generalizing for N walls and M windows yields the following:

$$\underline{\underline{\mathbf{A}}} = \left[\begin{array}{cccccccc} A_{11} & U_{f,ind} & U_{r,ind} & U^1_{wa,ind} & \cdots & U^N_{wa,ind} & U^1_{wi,ind} & \cdots & U^M_{wi,ind} \\ U_{f,ind} & A_{22} & 0 & 0 & \cdots & 0 & 0 & \cdots & 0 \\ U_{r,ind} & 0 & A_{33} & 0 & \cdots & 0 & 0 & \cdots & 0 \\ U^1_{wa,ind} & 0 & 0 & A_{44} & \cdots & 0 & 0 & \cdots & 0 \\ \vdots & \vdots & \vdots & \vdots & \ddots & \vdots & \vdots & \ddots & \vdots \\ U^N_{wa,ind} & 0 & 0 & 0 & \cdots & A_{N+3,N+3} & 0 & \cdots & 0 \\ U^1_{wi,ind} & 0 & 0 & 0 & \cdots & 0 & A_{N+4,N+4} & \cdots & 0 \\ \vdots & \vdots & \vdots & \vdots & \ddots & \vdots & \vdots & \ddots & \vdots \\ U^M_{wi,ind} & 0 & 0 & 0 & \cdots & 0 & 0 & \cdots & A_{N+M+3,N+M+3} \end{array} \right] \quad (3.66)$$

$$\underline{\mathbf{T}} = \left\{ \begin{array}{c} T_{ind} \\ T_f \\ T_r \\ T^1_{wa} \\ \vdots \\ T^N_{wa} \\ T^1_{wi} \\ \vdots \\ T^M_{wi} \end{array} \right\}^{k+1} \quad (3.67)$$

$$\text{-}\underline{\mathbf{b}} = \left\{ \begin{array}{c} \frac{m_{air}^{k+1} c_{p,air}^{k+1}}{\Delta t} T_{ind}^{k} + q_{ind}^{k+1} + U_{o,ind} T_{o}^{k+1} \\ \frac{m_f c_{p,f}}{\Delta t} T_{f}^{k} + q_{g}^{k+1} + U_g T_{g}^{k+1} \\ \frac{m_r c_{p,r}}{\Delta t} T_{r}^{k} + q_{r}^{k+1} + U_{r,o} T_{r}^{k+1} \\ \frac{m_{wa}^{1} c_{p,wa}}{\Delta t} T_{wa}^{1,k} + q_{wa}^{1,k+1} + U_{wa,o} T_{wa}^{1,k+1} \\ \vdots \\ \frac{m_{wa}^{N} c_{p,wa}}{\Delta t} T_{wa}^{N,k} + q_{wa}^{N,k+1} + U_{wa,o} T_{wa}^{N,k+1} \\ \frac{m_{wi}^{1} c_{p,wi}}{\Delta t} T_{wi}^{1,k} + q_{wi}^{1,k+1} + U_{wi,o} T_{wi}^{1,k+1} \\ \vdots \\ \frac{m_{wi}^{M} c_{p,wi}}{\Delta t} T_{wi}^{M,k} + q_{wi}^{M,k+1} + U_{wi,o} T_{wi}^{M,k+1} \end{array} \right\} \tag{3.68}$$

Where:

$$A_{11} = -\left(\frac{m_{air} c_{p,air}}{\Delta t} + \sum U \right) \tag{3.69}$$

$$A_{22} = -\left(U_{f,ind} + U_g + \frac{m_f c_{p,f}}{\Delta T} \right) \tag{3.70}$$

$$A_{33} = -\left(U_{r,ind} + U_{r,o} + \frac{m_r c_{p,r}}{\Delta T} \right) \tag{3.71}$$

$$A_{44} = -\left(U_{wa,ind}^{1} + U_{wa,o}^{1} + \frac{m_{wa}^{1} c_{p,wa}^{1}}{\Delta T} \right) \tag{3.72}$$

$$A_{N+3,N+3} = -\left(U_{wa,ind}^{N} + U_{wa,o}^{N} + \frac{m_{wa}^{N} c_{p,wa}^{N}}{\Delta T} \right) \tag{3.73}$$

$$A_{N+4,N+4} = -\left(U_{wi,ind}^{1} + U_{wi,o}^{1} + \frac{m_{wi}^{1} c_{p,wi}^{1}}{\Delta T} \right) \tag{3.74}$$

$$A_{N+M+3,N+M+3} = -\left(U_{wi,ind}^{M} + U_{wi,o}^{M} + \frac{m_{wi}^{M} c_{p,wi}^{M}}{\Delta T} \right) \tag{3.75}$$

To obtain the values at the new time step of the unknown temperature, the linear matrix equation, $\{T\} = [A]^{-1}\{b\}$ is numerical solved using matrix inversion. Alternatively, iterative techniques such as the conjugate gradient method (CGM) may be implemented for higher numerical efficiency.

The next several subsection will cover some of the various heat sources (other than machine tools).

External Heat Sources

The primary external heat source considered in this model is solar radiation. Other forms of low wavelength radiation such as from other buildings are considered to be negligible. The incoming incident solar radiation absorbed by the building structure can be broken into three components: direct beam, diffuse, and reflect irradiation. Direct beam irradiation represents the directional component of the solar radiation emanating directly from the atmosphere whereas diffuse irradiation represents the non-directional re-radiation from the rest of the sky (e.g, clouds). The reflective component takes into account the reflected and re-radiated radiation from the ground and surroundings. The total net heat gain caused by solar radiation is the sum of the three components and can expressed:

$$Q_{rad} = E_b \cos\theta + E_d \left(Y \sin\Sigma + \cos\Sigma\right) + \left(E_b \sin\beta + E_d\right) \rho_g \frac{1 - \cos\Sigma}{2} \tag{3.76}$$

The fist, second, and third terms in Equation 3.76 denotes the direct beam, diffuse, and ground reflective solar irradiation, respectively. The parameters, E_b and E_d, denote the clear-sky solar beam and diffuse irradiance flux, respectively, as measured perpendicularly (beam) and horizontally (diffuse) from the surface of the Earth. The second term parameter, Y, is a correction factor to account for the non-isotropic nature of the diffusion radiation and is equal to the clear-sky diffuse irradiance ratio of a vertical surface to the horizontal. The parameter, ρ_g, in the reflective solar irradiation term represents the ground reflectance and is typically taken to be 0.2 [13]. Both E_b and E_d are geographical location specific and can be obtained via online weather databases.

The irradiance fluxes, E_b and E_d, represent the flux emanating directly from sky. To determine the actual net irradiation reaching the surface of the building the solar angles: θ, Σ, and β, need to be determined (see Figure 3.24). For the direct beam component the magnitude of the solar irradiance is determined by the angle of incidence, θ:

$$\cos\theta = \cos\beta \cos\gamma \sin\Sigma + \sin\beta \cos\Sigma \tag{3.77}$$

Where β is solar altitude angle, γ is the deviation angle from the normal direction of the vertical surface (i.e., building wall), and Σ is the tilt angle of the incident surface (equals 90^o for a vertical surface). Determination of the solar altitude angle involves calculating the sun's position relative to the incident surface, which is also a function of the solar time. In fact, all components are influence by the time of day and day in year (e.g., seasons). For more information on calculating the solar altitude see [13].

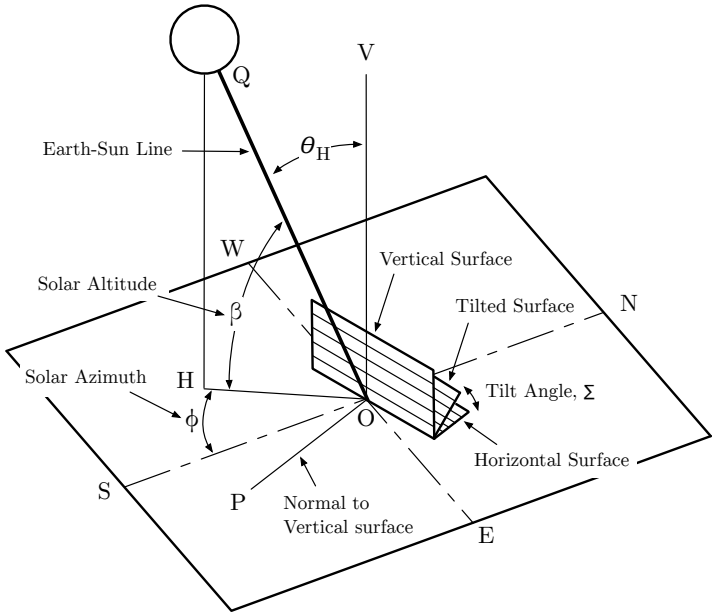

Figure 3.24: Solar angles. Redrawn from [13]

Internal Heat Sources

There are four main internal sources of heat: machine tools including sub-processes, office equipment (e.g., computers, copiers), workers, and lighting. Machine tool heat loss is very dynamic and is dependent on the process, production scheduling, tool utilization, and indoor environmental conditions such as temperature and ventilation flow. Time discretized values of the machine tool heat loss are calculated on the process, tool, and line scale models. Heat loss from office equipment will depend on the equipment type, utilization, and power state (i.e., off, standby, on, running). Data on the static steady state heat loss for office equipment can be found from several sources publicly available sources [13]. In general, the . Heat gain from lighting is typically not a significant contributor to the total internal heat gain and will vary depending on lighting technology. Calculation of the lighting heat is proportional to the light wattage and the fraction of exposed fixture from the surface of the ceiling (e.g., recessed or protruding) [13].

The fourth main source of internal heat gain is the heat dissipation from the human body. For a similar reasons as the lighting heat, the influence of human body heat is often not included. However, depending on the setting, there may be instances where the worker density is quite larger such as production lines involving high utilization of manually labor. Considering that the heat dissipation from a person can range from 50W to over 250W depending on the activity, it worthwhile to incorporate a model to account for the body heat loss. The following heat loss model and suggested values can be found in [13]; a summary is given below.

Body heat dissipation is a function of the temperature, humidity, type of clothing and

body coverage, and level of work activity, which is represented by the metabolic rate. Heat loss mechanisms includes convective and radiative losses, evaporative through body moisture, and respiratory losses. An expression for the body heat loss is given as:

$$Q_{loss} = A_D f_{cl} \left(q_{cr}^{''} + E_{sk}^{''} + C_{res}^{''} + E_{res}^{''} \right) \tag{3.78}$$

Where A_D is the Dubois surface area for a nude body, f_{cl} is the clothing to skin area ratio, $q_{cr}^{''}$ is the convective and radiative body heat loss flux, $E_{sk}^{''}$ is evaporative heat loss flux from body moisture, $C_{res}^{''}$ and $E_{res}^{''}$ are the sensible and latent respiratory heat loss flux, respectfully. From Equation 3.78, the total heat loss is proportional to the body surface area. The most useful measure was originally proposed by DuBois, which is a semi-empirical model for determine the nude body surface area (in units of DuBois surface area, m^2):

$$A_D = 0.202 m^{0.425} * h^{0.725} \tag{3.79}$$

Where m is mass of the body and h is the height. The clothing to skin area ratio parameter, f_{cl}, in Equation 3.78 has been empirical approximated using photographic method and can be modeled as:

$$f_{cl} = 1 + 0.3 * I_{cl} \tag{3.80}$$

Where I_{cl} is the clothing insulation efficiency (in units of clo) and is dependent on the thermal resistance of the clothing fabric.

The four heat flux terms are as follows. The combined convective and radiative heat loss flux is expressed as:

$$q_{cr}^{''} = \left(T_{sk} - \frac{h_r \bar{T}_r + h_c T_a}{h_r + h_c} \right) \left(R_{cl} + \frac{1}{f_{cl}(h_c + h_r)} \right)^{-1} \tag{3.81}$$

Where T_{sk} is the skin temperature associated with comfort, T_a is the ambient air temperature, $\bar{T}_r$ is the mean body to ambient temperature, h_r is the linear radiative heat transfer coefficient, h_c is the convective heat transfer coefficient, and R_{cl} is the thermal resistance of the clothing fabric. The convective heat transfer coefficient is also a function of the air velocity, hence a function of the ventilation rate from the HVAC. The evaporative heat loss from the skin is a function of the moisture content on the skin:

$$E_{sk}^{''} = \frac{w \left(p_{sk} - p_a \right)}{R_{e,cl} + \frac{1}{f_{cl} h_e}} \tag{3.82}$$

Where w is a dimensionless parameter that denotes the skin wettedness, p_{sk} is the water vapor pressure at the skin, p_a is the water vapor pressure in ambient air, $R_{e,cl}$ is the evaporative heat transfer resistance of the clothing layer (which is related to R_{cl}), and h_e is the evaporative heat transfer coefficient (which is related to h_c).

Lastly, the respiratory heat loss is often expressed as the two subcomponents - sensible and latent heat loss. Sensible heat loss represents the thermal energy of the expelled dry air

whereas latent heat loss is due to the released moisture. An express for both losses can be written as:

$$C''_{res} = 0.0014M(34 - T_a) \tag{3.83}$$

$$E''_{res} = 0.0173M(5.87 - p_a) \tag{3.84}$$

Where M is the metabolic rate and is influenced by the work activity (e.g., sitting at desk, walking, heavy lifting). A table listing various work activities to metabolic rates can be found in the Appendix.

Soil Temperature

The temperature at the Earth's surface, soil temperature, is said to vary annually with daily fluctuations influenced primarily by variations in the air temperature and solar radiation. The profile of the annual soil variation follows a sinusoidal function and can be expressed as [238]:

$$T_g(t) = T_a + A_o \sin\left(2\pi\frac{(t - t_o)}{365} - \frac{\pi}{2}\right) \tag{3.85}$$

Where $T_g(t)$ is the soil temperature at the day time, t, T_a is the average annual soil temperature, A_o is the amplitude of the annual temperature at the soil surface, and t_o is the time lag that denotes the occurrence of the minimum temperature in a year. The time lag is chosen such that sinusoidal soil temperature profile matches in phase with any arbitrary outdoor air temperature profile. A more complex version of Equation 3.85 gives the soil temperature at a depth, z from the surface by following a decaying exponential. For more information on soil temperature modeling see [238] and [13].

3.4 Uncertainty Modeling

The reliability of LCA and the iSLCD for that matter strongly depends on the quality of the data and the representativeness of the models. More often than not, LCA models are constructed deterministically with results that are presented as single values or point estimates [204]. However, the straightforwardness of this approach undermines the efficacy of LCA due to its inherent variability and uncertainty. Results may be misleading with decisions that may lead to costly and detrimental consequences [28]. The variability and uncertainty in LCA necessitates the inclusion of uncertainty analysis in all phases of the LCA framework. However, incorporating uncertainty analysis is not a trivial task primarily due to the fact that there lacks a consensus on the methodology [28]. This section covers an overview of the uncertainties in LCA and proposes a novel methodology to quantify, particularly data, the uncertainty in a systematic manner. For convenience, the term "uncertainty" from here on will represent both variability and uncertainty. However, it should be noted that uncertainty differs from variability, which is attributable to the inherent heterogeneity of values,

while uncertainty relates to the accuracy and precision of the measurements. Furthermore, unlike uncertainty, variability can not be further reduced with increasing accuracy and precision, although a more thorough understanding of the system can improve the knowledge on variability [28].

Sources of Uncertainty

Uncertainty in LCA arises from numerous sources and at every stage in the LCA framework. Generally speaking, uncertainty can be categorized into four main typologies [28][313]: 1) data quality, 2) scenario choices, 3) construction of the models, and 4) human induced, which is summarized in Table 3.5 with different types of uncertainty and examples of possible sources. Uncertainty in data quality arises from inaccuracy and inconsistency such as measurement errors and random variations, missing data, and unrepresentativeness such as data from similar processes. Scenario uncertainty relates to the normative choices in data manipulation and model definition and ranges from data averaging and trends based on imperfect fit to defining the functional unit and choice of global warming potential time horizon. Model uncertainty pertains to the simplification and approximation of real-world systems. This may range from the exclusion of certain processes or approximations of non-linear behavior with linear models to data aggregation and models based on forecast and extrapolations. The last main typology is simply human error and lack of knowledge, which is arguably the fundamental source of uncertainty in LCA. Termed as epistemological uncertainty, lack of knowledge relates to the infeasibility to fully understand the system behavior at all stages of the LCA framework, particularly when attempting to assess future systems due to the fact that the future is inherently uncertain. In relation to epistemological uncertainty, linguistic imprecision is the uncertainty of quantifying qualitative attributes of data and models, which can be highly subjective [204]. Other types of human induced uncertainty include mistakes, which can be difficult to identify, and the method of estimating uncertainty is in itself a source of uncertainty.

Analyzing Uncertainty

The tools and methods to address the uncertainty in LCA have been derived from existing statistical methods such as risk assessment in economics and health and safety. However, as previously stated, there lacks a consensus in the methodology and how the uncertainty should be treated. Despite this limitation the ISO 14040 standard states that such analysis, in some form or another, should still be performed to facilitate in resolving ambiguity and supporting the LCA results [28]. Several uncertainty analysis techniques for LCA have been proposed and implemented in literature. Some of the more common techniques are listed below with a more detail list found in [28].

- **Interval arithmetic**: data expressed as uniform intervals with upper and lower bounds (arithmetic operation on the extremities)

Table 3.5: Potential sources of variability and uncertainty in LCA (stages Classification and Characterization excluded for illustration purposes). Based on [204][28]

.

Component	Type	LCA Framework Stage		
		Goal and Scope	Inventory	Impact Category
Data	Data inaccuracy		Inaccurate emissions measurements	
	Data gaps		Lack of inventory data	
	Unrepresentative data		Lack of representative inventory data	
Scenario	Spatial variability		Regional differences in emission inventories	
	Temporal variability		Differences in yearly emissions inventories	
	Uncertainty due to choices	Choice of functional unit, system boundaries	Choice of allocation methods, technology level, marginal/ average data	Leaving out known impact categories
Model	Model uncertainty		Static instead of dynamic modeling, linear instead of non-linear modeling	
Human induced	Epistemological uncertainty	Ignorance about relevant aspects of studied system	Ignorance about modeled processes	Impact categories are not known
	Mistakes	Any	Any	Any
	Estimation of uncertainty		Estimation of uncertainty of inventory parameters	

- **Analytical uncertainty propagation**: treating the uncertainty as an error around an expected value, often requires complex mathematical models
- **Fuzzy data sets**: the idea that uncertainty arises from ambiguity and is treated as a possibility as opposed to probability where data and models are subjective or fuzzy. See [312][313] for more information.
- **Sensitivity analysis**: also referred to as scenario modeling and uncertainty importance analysis [28], highlights the influence of an independent parameter or scenario to the outcome of the model
- **Bayesian statistics**: assumes qualitative or subjective approximations can be treated using classical statical analysis with distributions based on expert judgement [28]
- **Probabilistic simulation**: assumes uncertainty can treated as a frequency or distribution of random or stochastic samples around an expected value and can be modeled

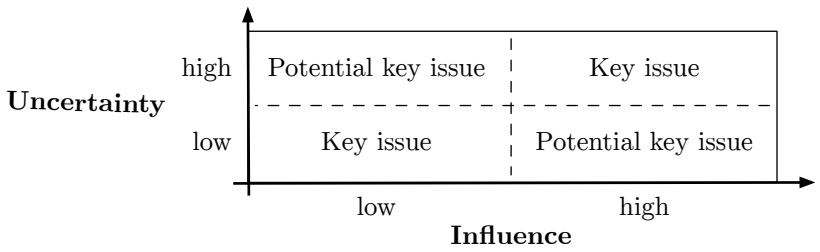

Figure 3.25: Screening matrix for identifying critical parameters. Adopted from [28]

using non-deterministic methods such Monte Carlo and Latin Hypercube simulation [312]

A survey on uncertainty analysis approaches for LCA [204] found that out of the six techniques listed above probabilistic simulation was the most popular (67%) followed by scenario modeling (29%) and fuzzy data sets (17%). The same survey also concluded that interval arithmetic, analytical uncertainty propagation, and fuzzy data sets may lead to less accurate approximations in LCA. Interval and fuzzy data sets, although effective in some instances, lack the ability to incorporation correlation information among input variables and are more likely to overestimate uncertainty. For large LCA models, representation in analytical form can be highly complex and often not practical [204]. Multiple sources highlight the importance of sensitivity analysis [28][204] and argue that it may potentially be the most valuable technique in assessing the credibility of LCA. The reasoning is LCA models can be highly complex and including all aspects of uncertainty may be difficult or even infeasible. By using sensitivity analysis the significant contributors (e.g., parameters) can be screened and prioritized in a systematic and effective manner, as illustrated in Figure 3.25. Sensitivity analysis does have several weaknesses that limits its implementation such as overlooking any potential coupling effects of the parameters and sensitivity variability, primarily in non-linear models [312][28].

Classical probability theory has been traditionally modeled to represent data uncertainty, and over time has led to probabilistic or stochastic simulations as models became increasingly complex [312]. Not all types of uncertainty can be modeled stochastically (at least not practically), although numerous studies [204] have treated data uncertainty (e.g., LCI) as a certain distribution with an expected value and some level of deviation or max-min interval. The shape and type of distribution depends on the data type (e.g., measurements) and the degree of uncertainty or variability. Figure 3.26 shows three types of distribution curves commonly used to represent probabilistic data uncertainty. A normal or bell shaped distribution (curve 1.) is considered to be the mostly widely used type of distribution due to the assumption that most data follows the central limit theorem [204]. When the tails or extreme values are known a triangle (curve 2.) or uniform (curve 3.) distribution can be modeled. Uniform distributions are useful particularly when only the bounds or range of the

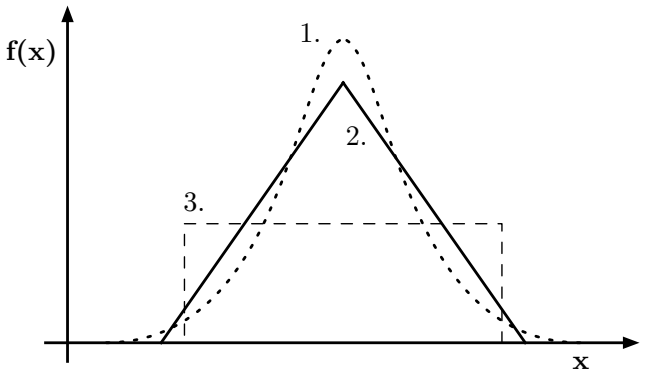

Figure 3.26: Examples of probability functions: 1) normal distribution, 2) triangle distribution, 3) uniform interval. Adopted from [28].

data are known, but offer a pessimistic view by overestimating the tails and underestimating the shoulders of the distribution [28].

The major drawback in applying probabilistic simulation is that there does not exist a well defined methodology to map the degree of data quality to the size of the distribution curve. There is uncertainty in quantifying data quality, which some consider to be associated more with ambiguity due to subjectiveness than statistical variability [312][313]. Instead, expert judgement is often exercised to enhance the quality of the data and give the best estimate of the distribution based on experiences from an expert [28]. Furthermore, data quality can be mapped using data quality indicators (DQIs) in which attributes of the data (e.g., inaccuracy, unrepresentativeness) are graded a numeric value (typically a sliding scale of 1-highest quality to 5-lowest quality) in a pedigree matrix [340][166]. By doing so, attributes of the data can be quantified and be further mapped onto an error or uncertainty range. For example, an indicator score of 2 might represent $\pm 5\%$ error or range in standard deviation while a 4 might be $\pm 20\%$. The obvious drawback is the additional uncertainty when mapping an indicator score to an error range since there is limited or no basis for choosing a particular range [204]. Therefore, there needs to be a systematic methodology to quantify data quality and uncertainty to take advantage of classical probability theory and stochastic simulations.

Proposed Methodology

For large and complex LCA models, stochastic methods have been largely used to propagate uncertainty pertaining to data quality. Of the various methods to characterize uncertainty (examples illustrated in Figure 3.26), Beta Density Functions (BDFs) have been shown to effectively model various degrees of uncertainty [173][41], particularly when knowledge of the actual probability distribution is limit or unknown. BDFs are a unique class of continuous probability density functions (PDFs) with a distribution that is dependent on two shape factors, α and β, and with endpoints that are bounded by an interval, typically (0,1) [173].

Like standard PDFs, BDFs provides an indication on the likelihood a particular value, x, will occur. The formulation of the standard Beta PDF at an interval $x \in (0, 1)$ is given in Equation 3.86 below:

$$\text{Beta}\,(\alpha, \beta) : f\,(x|\alpha, \beta) = \frac{x^{\alpha-1}\,(1-x)^{\beta-1}}{B\,(\alpha, \beta)} \tag{3.86}$$

where B is the Beta function:

$$B\,(\alpha, \beta) = \int_0^1 t^{\alpha-1}\,(1-t)^{\beta-1}\,dt$$

There are several advantages with BDFs compared to conventional PDFs such as the normal or triangle distributions. The main advantage is that the BDF's shape factors can be manipulated in a way to virtually represent any probability distribution [41]. This allows a single function to represent all distribution types for consistency and robustness. To illustrate, Figure 3.27 plots several BDFs with varying α and β centered around a mode. The mode, which denotes the peak in the distribution, can be centered at the middle ($\alpha = \beta$) forming a normal-type distribution or shifted ($\alpha \neq \beta$) to change the skewness of the distribution. For the purposes of modeling data uncertainty, α and β will always be greater than or equal to one to ensure a mode exists within the bounds and not at the edges. Setting $(\alpha = \beta) > 2$ will form a bell-shaped profile with the tightness of the bell increasing with increasing α and β. At $\alpha = \beta = 2$ and $\alpha = \beta = 1$ the distribution resembles a triangular (in the shape of a parabola) and uniform distribution, respectively. Combining profiles 2. and 3. can also form a trapezoidal distribution. Another advantage is the fact that the BDF distribution is bounded by to a predefined interval where the worst case lower bound is always zero. This is particularly useful when assigning uncertainty to parameters such as yield and efficiency where there is a clear minimum and maximum, and the mode can easily controlled by varying different values of α and β.

Determining the appropriate values of α and β can be very challenging. Kennedy et al. [173] and Canter et al. [41] both assigned a predefined symmetric (i.e., $\alpha = \beta$) distribution based on an expert judgement DQI sliding scale of 1 to 5 at increments of 0.5 thus yielding nine degrees-of-freedom. In addition, both studies modified Equation 3.86 to linearly transform $x \in (0, 1)$ to the interval $x \in (a, b)$, shown in Equation 3.87. The limits (a, b) represent the maximum error around the expected value with a sliding scale of $\pm 10\%$ to $\pm 50\%$ determined by expert judgement. With the limited availability of information regarding the data quality, the authors argued that equal probability of $\pm 5\%$ increments was valid [173].

$$f\,(x|\alpha, \beta, a, b) = \frac{1}{b-a}\frac{\left(\frac{x-a}{b-a}\right)^{\alpha-1}\left(1-\frac{b-x}{b-a}\right)^{\beta-1}}{B\,(\alpha, \beta)} \tag{3.87}$$

Expert judgement seems appropriate when determining the maximum error limits, (a, b), especially considering that some of the data may have hard (e.g., efficiency) or theoretical limits or in some instances provided on a technical specification sheet or manual. However,

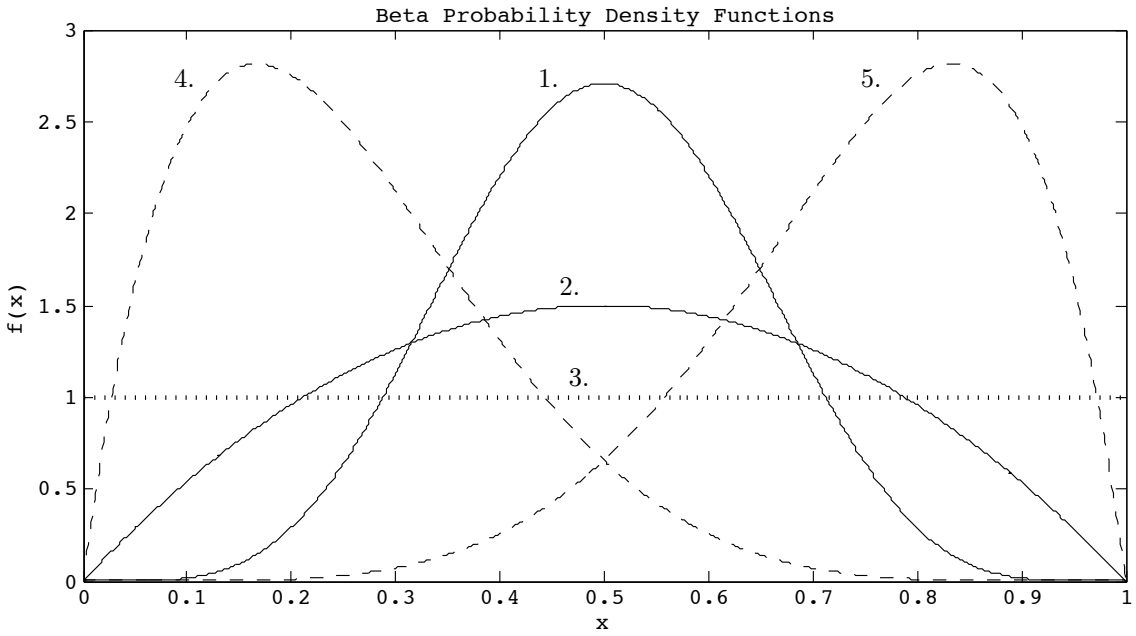

Figure 3.27: Various Beta probability density functions (α,β): 1:(6,6), 2:(2,2), 3:(1,1), 4:(2,6), and 5:(6,2)

there needs to be a systematic method of determining α and β. For example, in the aforementioned studies, the same α and β pair were used for DQI 1 through 3. The expert judgement used to determine such relationship may be valid for these specific cases, but there does not appear to be any systematic basis for their selection. A more effective method would be to utilize the intrinsic properties of BDFs, namely computing the moments, that describe the shape of the distribution. The first two moments are the expected value (Equation 3.88) and variance (Equation 3.89), respectively [164]. The third and forth moment defines the skewness and kurtosis, respectively, and will not be incorporated since the first two moments are sufficient in determining the shape of the distribution.

$$E(x) = \frac{\alpha}{\alpha + \beta} \quad : \quad \forall x \in [0, 1] \tag{3.88}$$

$$v(x) = \frac{\alpha\beta}{(\alpha + \beta)^2 (\alpha + \beta + 1)} \quad : \quad \forall x \in [0, 1] \tag{3.89}$$

In addition, the mode of the BDF denotes the value of x at the distribution's peak and equals the expected value when the distribution is centered (i.e., $\alpha = \beta$). By this definition, the mode is preferred over the expected value because it better represents the uncertainty distribution particularly for distributions that are uniform and have a non-zero skewness. Since it was previously defined that $(\alpha, \beta) \geq 1$, there exist only one mode or maxima. Therefore, the mode can be determined by differentiating Equations 3.86 or 3.87

with respect to x and equating to zero. Doing so with Equation 3.86 yields the following equation:

$$M(x) = \mu = \frac{\alpha - 1}{\alpha + \beta - 2} \quad : \quad \forall x \in [0, 1] \tag{3.90}$$

Combining Equations 3.89 and 3.90 yields two equations and two unknowns, α and β. By reducing one parameter, the other parameter can be rearranged and solved in the cubic form under the condition that both α and β must be greater than or equal to one. Solving in terms of α gives the following cubic form shown in Equation 3.91:

$$f(\alpha) = 0 = A\alpha^3 + B\alpha^2 + C\alpha + D \quad : \quad \alpha \geq 1 \tag{3.91}$$

Where

$$\begin{aligned} A &= v \\ B &= 7v\mu - 3v + \mu^3 - \mu^2 \\ C &= 16v\mu^2 - 14v\mu + 3v - 2\mu^3 + \mu^2 \\ D &= 12v\mu^3 - 16v\mu^2 + 7v\mu - v \end{aligned}$$

The output to Equation 3.91 reveals three solutions of which only one is feasible ($\alpha \geq 1$). Subsequent to obtaining α, β can be easily solved using Equation 3.90. The remaining missing piece of information is the value of the variance since the mode is given by the value of the input data. As others have done before, the variance can be determined using a set of independent DQIs along with an assigned sliding-scale "score" to semi-quantify the quality of the data. The set of DQIs that will be used in this dissertation is listed in a pedigree matrix shown in Table 3.6. This pedigree matrix, adopted from [166], expands on the original pedigree matrix proposed by Weidema and Wesnaes [340] where an addition indicator on the data supplier is included. The pedigree matrix is intended to aid in data quality assessment by covering indicators such as data reliability, representativeness, completeness, spatial and temporal influences, and so on.

The resulting data quality assessment will yield a set of six indicator scores ranging from 1 to 5. Traditionally, the set of indicators are subjectively associated to some α and β or aggregate coefficient of variance based on expert judgement [173][204][25]. However, a more systematic and consistent approach would be to compute an effective or overall pedigree score and map the score to some value of the variance. To do so requires an intelligent method of aggregating the indicator scores involving multi-criteria decision making (MCDM). The simplest, considering the degree of uncertainty at this level in the methodology, is to cardinal rank the six indicators (1-highest, 6-lowest) in terms of importance and assign a corresponding weight. What is deemed least to most important remains highly subjective, however, generally speaking, the data should reflect as closely as possible to the LCA model. For LCI data that would translate to the processes and materials under study and likewise for

Table 3.6: Pedigree Matrix Based on [166]

	Indicator score				
Item	1	2	3	4	5
Acquisition method	Measured data	Calculated data based on measurements	Calculated data partly based on assumptions	Qualified estimate	Nonqualified estimate
Independence of data supplier	Verified data, information from public or other independent source	Verified information from enterprise with interest in the study	Independent source, but based on nonverified information from industry	Nonverified information from industry	Nonverified information from the enterprise interested in the study
Represent-ativeness	Representative data from sufficient sample of sites over an adequate period to even out normal fluctuations	Representative data from smaller number of sites but for adequate periods	Representative data from adequate number of sites, but from shorter periods	Data from adequate number of sites, but shorter periods	Representativeness unknown or incomplete data from smaller number of sites and/or from shorter periods
Temporal correlation†	Less than t years of difference to year of study	Less than $5t$ years of difference	Less than $10t$ years of difference	Less than $20t$ years of difference	Age unknown or more than $20t$ years of difference
Geographical correlation	Data from area under study	Average data from larger area in which the area under study is included	Data from area with similar production conditions	Data from area with slightly similar production conditions	Data from unknown area or area with very different production conditions
Further technological correlation	Data from enterprises, processes and materials under study	Data from processes and materials under study, but from different enterprises	Data from processes and materials under study, but from different technology	Data on related processes or materials, but same technology	Data on related processes or materials, but different technology

† t is subjective and dependent on the technology

Table 3.7: Rank order and weights for data quality indicators

Indicator	Rank	Weight
Further technological correlation (F)	1	0.286
Independence of data supplier (I)	2	0.238
Acquisition method (A)	3	0.190
Representativeness (R)	4	0.143
Geographical correlation (G)	5	0.095
Temporal correlation (T)	6	0.048

the greenhouse gases that contribute to the global warming potential in defining the impact categories. From then the ranking should move on to the data itself. Is the data verified? How was the data measured or populated? Is the data an aberration or a representative sample? Where and when was the data captured? Once the rank order is determine the weights are calculated in Equation 3.92 using a normalized weighting scheme where rank 1 to 6 is weighted 6 to 1, respectively.

$$w_i = \frac{W_i}{\sum_{i=1}^{6} W_i} \tag{3.92}$$

The summation term in Equation 3.92 normalizes the weights to the interval $(0, 1)$. This allows the effective pedigree score to remain bounded between the original sliding-scale of 1 to 5. The advantage of weighting each DQI allows a higher degree-of-freedom and thus higher resolution in calculation of the variance. The total number of possible scores for six indicators is 5^6 or 15625 possible combinations (recall that Kennedy et al. and Canter el at. had nine degrees-of-freedom). Table 3.7 list the rank order of the indicators along with their corresponding weights. The effective pedigree score can be calculated using Equation 3.93 from scoring each of the six DQIs using the pedigree matrix and assigning the appropriate weights.

$$EPS = w_1F + w_2I + w_3A + w_4R + w_5G + w_6T \tag{3.93}$$

The final stage in this process is to determine the relationship between the effective pedigree score and the variance. To begin, it is recognized that the EPS is bounded by the indicator scores of 1 to 5. Therefore, the variance should be bounded by a v_{min} and v_{max} such at a EPS of 1 maps to v_{min} and a EPS of 5 maps to v_{max}. The upper bound variance is in fact already known. Identifying the worst possible BDF profile to be the uniform distribution (equal probability), reveals the shape factors $(\alpha, \beta) = 1$, and hence the variance is obtained as $v_{max} = 1/12$ by using Equation 3.89. Using the same approach for the lower variance limit will not work due to the shape factors being positively unbounded. From literature, Kennedy et al. assigned a $\pm 10\%$ error range for the highest quality data whereas Saur et al. assigned a $\pm 2.5\%$ standard deviation range to data with very small error [204]. There is

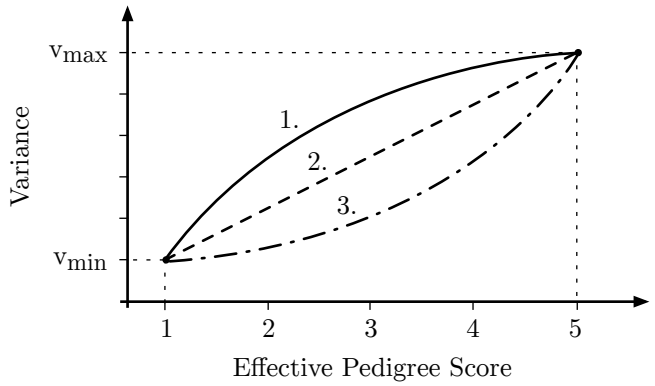

Figure 3.28: Mapping profiles from EPS to the Variance

no optimal method of selecting the error range, however, a data error range of ±5% seems to be reasonable for representing the highest quality data. Furthermore, it will be assumed that the ±5% has a confidence interval of 95% (i.e., 95% confident than the error associated with the highest quality data is bounded by ±5%). By assigning a confidence interval, the variance moment in classical probability theory can be utilized as:

$$V = \sigma^2 = \left(\frac{x - \mu}{z}\right)^2 \tag{3.94}$$

Where σ is the standard deviation, x is the raw score, μ is the mean, and z is the standard score (i.e., number of standard deviations). Note that the standard score for the 95% confidence interval is, $z = 1.96$, and the raw score is take as the error value from the mean. Using the standard interval scale of $x \in (0, 1)$ and the mean of the interval as the optimum mode (i.e., normal distribution profile), the lower bound variance is calculated as: $v_{min} = \left({}^{0.05 \cdot 0.5}/_{1.96}\right)^2 = 1.627 \times 10^{-4}$.

The next step in building the variance function is to determine the shape of the mapping profile. Figure 3.28 shows three types of relationship profiles: 1 - pessimistic, 2 - neutral, and 3 - optimistic. The pessimistic profile places higher emphasis at the lower scores (higher quality data) and is strictly greater or equal to the neutral profile. The optimistic profile is the opposite where higher emphasis is placed at the higher scores (lower quality data) and is strictly lesser than or equal to the neutral profile. Higher order profiles such as a s-curve could be consider, however, would be unnecessarily complex.

Most studies utilize the neutral profile, which is simply a linear sliding-scale model for interpolation. The neutral profile model implies that the uncertainty at an indicator score of 2 and 5 is twice and five times larger than an indicator score of 1, respectively. However, judging by the pedigree matrix in Table 3.6, it can argued that significance between a score of 1 and 2 is not the same as between 4 and 5. Likewise, although the indicator score is capped at 5, a score of 5 could potentially represent higher orders of uncertainty that are not capture in the pedigree matrix. Therefore, the more accurate model would be the non-linear

profile that is concave-up and penalizes at higher indicator scores, which is best represented by the optimistic profile. Of the various non-linear models that can represent the optimistic profile, an exponential fit, shown below in Equation 3.95, will be employed.

$$f(n) = V(n) = Ae^{bn} \tag{3.95}$$

Where V is the variance, n, is the effective pedigree score, and the coefficients, A and b, are determined using linear regression with the endpoints at $(1, v_{min})$ and $(5, v_{max})$. Linearizing Equation 3.95 using natural logarithms and placing in matrix form yields the following matrix of linear equations:

$$\begin{bmatrix} 1 & 5 \\ 1 & 1 \end{bmatrix} \begin{pmatrix} \ln A \\ b \end{pmatrix} = \begin{pmatrix} \ln(v_{max}) \\ \ln(v_{min}) \end{pmatrix}$$

Where A and b is solved by performing a matrix inversion resulting. Doing so results in $A = 3.42 \times 10^{-5}$ and $b = 1.56$.

The combination of Equations 3.87 - 3.95 describe the methodology for using Beta distribution profiles in modeling data uncertainty. Using Equation 3.95 as the input to Equation 3.89, the shape factors can be obtained (only drawback is solving the 3$^{\text{rd}}$ polynomial, which requires some computational cost). This methodology is summarized in a flow chart shown in Figure 3.29. The outcome of the methodology provides three different types of distributions that have been previously mentioned. Single value point estimate data will consist of normal or skewed-normal type shape distribution bounded by the endpoints $[a, b]$. For range type data without an expected value two possible distributions can be generated. If the interval values have equal probability of occurrence then the distribution will be uniform. Otherwise, the distribution will take on a trapezoidal profile where the lower and upper bound distributions are defined by the interval values (note that the resulting distribution can be asymmetrical).

Any method of uncertainty analysis will be plagued with uncertainty and as the last entry in Table 3.5 states, the method and estimation of uncertainty itself is a source of uncertainty. Each stage in the proposed methodology (data quality assessment, data variance, BDF) contains some degree of uncertainty. There is uncertainty in defining the endpoints (a, b), scoring and weighting the DQIs, assigning the variance, and generating the BDFs. However, what the proposed methodology does provide is a comprehensive, robust, and more importantly, a systematic and consistent means to incorporate data uncertainty in LCA.

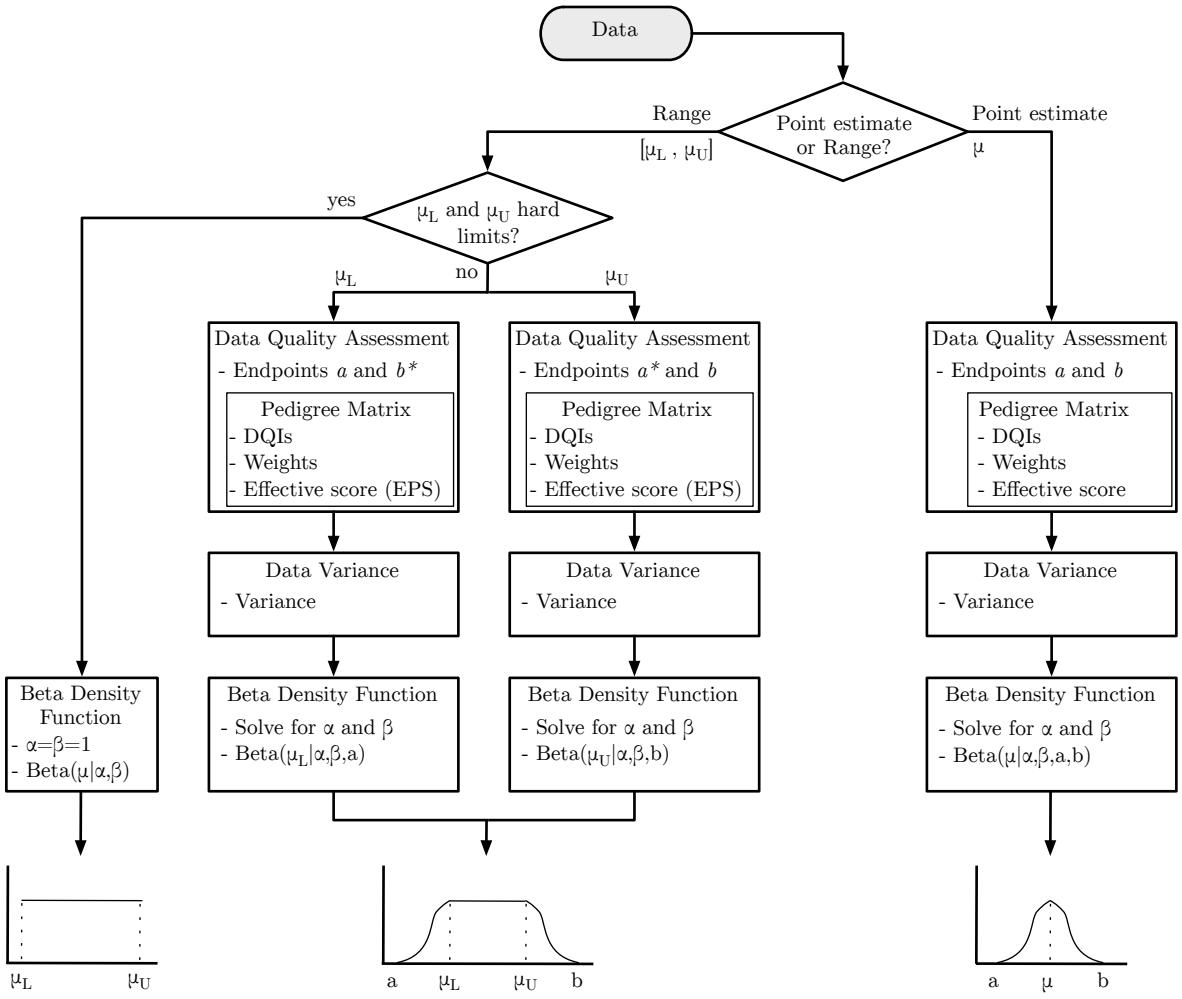

Figure 3.29: Methodology for generating data uncertainty profiles

Part II

Case Study: PEM Fuel Cells

Chapter 4

Introduction to Fuel Cells

It was introduced in Chapter 1 the concept of technology wedges where implementing energy efficient or carbon-free technologies on a global scale can aid in reducing and stabilizing anthropogenic carbon emissions. One viable area of stabilization is in the transportation sector where the electrification of light-duty vehicles (LDV) (e.g., passenger car) has the potential to reduce an entire wedge. There are two major technological pathways for electrifying LDVs - battery electric vehicles (BEVs) and fuel cell vehicles (FCVs), both of which have zero carbon emissions during operation. BEVs have the advantage of operating as a pure energy storage and delivery system thereby eliminating the need for fuel conversation and enabling direct energy recovery. In addition, batteries such as lithium-ion are capable of high discharge rates thus providing on-demand power, which is advantageous for frequent start-and-stop operation. However, the major criticisms of BEVs are practicality issues such as range limitation and long charging times. FCVs on the other hand function in a similar manner as conventional gasoline powered vehicles in the sense that fuel (e.g., hydrogen) is pumped into a storage tank at comparable pumping times, and converted to electricity when needed. Coupled with the fact that fuel cells have a much higher effective energy density (kWh per liter), FCVs can provide more than twice the useful energy (i.e., range) than a lithium-ion BEV. Furthermore, a study that compared FCVs to BEVs concluded that FCVs were more advantageous 9 out of 11 metrics (e.g., vehicle weight, cost, energy) for ranges greater than 200 miles [319]. That is not the say that FCVs are preferred over BEVs or that one technology will cannibalize the other, but rather FCVs are to complement and coexist with BEVs for different areas in the market such as larger vehicles and longer distance transportation [242].

The biggest limitations on the commercialization of FCVs have been high costs and lack of a hydrogen infrastructure. It is the classic chicken and the egg problem where automotive manufacturers are reluctant to invest in the high manufacturing capital and fuel providers are reluctant to build an infrastructure for a non-existing market. However, the impetus for commercialization is growing. Since inception, by the end of 2009 approximately 75,000 fuel cells were shipped worldwide with an additional 15,000 units shipped in 2010, a 40% increase over 2008 [103]. In the U.S. transportation sector as of August 2011, there are over 200 fuel

cell LDV, over 20 fuel cell buses, and approximately 60 fueling station nationwide [103]. On the infrastructure front, California is taking charge by adding an additional 19 new fueling stations (under development) to the existing 10 and planning to open and fund 100 publicly available fueling stations by 2024 [23]. Furthermore, several notable auto manufacturers such as Daimler-Benz, Honda, Toyota, GM, Nissan, and Hyundai, have announced rollout plans for mass commercialization of FCVs between late 2014 to 2017 [23][237][282].

One auto manufacturer, Daimler-Benz, has greatly invested enormous time and resources to perfect the polymer electrolyte membrane (PEM) fuel cell technology and the manufacturability thereof. In the early 1990's, Daimler-Benz began initiating fuel cell developments along with the collaborative efforts of PEM fuel cell pioneer, Ballard Power Systems, and later in 1998 with Ford Motors [240]. In 2005, Daimler and Ford created NuCellSys GmbH, a joint venture that specifically focused on the systems side of the fuel cell such as the balance-of-plant (BOP). In 2007, Daimler and Ford took over the fuel cell stack business from Ballard and created the joint venture, Automotive Fuel Cell Cooperation (AFCC). In 2009, Daimler completely took over the fuel cell systems development from Ford, thus converting NuCellSys to a 100% subsidiary of the Daimler-Benz group. Most recently, in early 2013, Nissan-Renault formed an agreement with Daimler and Ford in aim to increase fuel cell development and speed up the delivery to market [237].

Developments of Daimler's FCV have seen dramatic improvements over the last couple decades. Table 4.1 shows a list, ordered by year, of Daimler's passenger hydrogen FCVs (Daimler also manufacturers fuel cell buses). Since the introduction of the first concept car, the Necar1, power densities have increase by over an order of magnitude, with efficiencies steadily increasing. The first production FCV, the A-Class F-Cell, occurred a decade after the Necar1, and was focused primarily on technology development. Next the couple generations, the B-Class F-Cell, was aimed to prove the viability of the technology to consumers. As a demonstration, in January 2011 three Gen2/3 FCVs (depicted in Figure 4.1) were driven across 14 countries in 125 days for a "world tour" [100]. Future generations for the F-cell include Gen4, which is currently beginning ramped-up for production with a targeted annual production volume of 1000-3800 units, and Gen5 in 2015 with a targeted annual production volume of 10000-50000 units [352]. The development of a new generation FCV is made possible through dramatic cost reductions from technological developments and taking advantage of economies-of-scale. Particular focus has been on the fuel cell stack (unit consisting of hundreds of individual cells) where it makes up of over 50% of the fuel cell system production cost. It is forecasted that the transition from Gen2/3 to Gen4 will reduce overall product costs by approximately 70% at the anticipated volume, and a further 60% reduction in the transition to Gen5 [132].

The advancement in cost reduction will greatly facilitate in the adoption of FCV and shift towards lowering the carbon emissions stabilization curve. However, what has been neglected or overlooked are the the environmental impacts resulting from the remaining life cycles phases such as manufacturing and end-of-life. The reduction of a wedge relies on the assumption that the impacts due to the technological transition from existing conventional ICEs to electrification systems are solely at the tailpipe emissions. This assumption may

Table 4.1: Timeline Development of Daimler Hydrogen FCV [349][284][352]

Year	Model	Production (cumulative)	Power (kW)	Power Density (kW/L)	Efficiency (%)	Range (km)
1994	Necar1	concept	50	0.15	n.a.	130
1999	Necar2	concept	50	1.15	n.a.	>250
1999	Necar4	concept	70	1.15	37%	450
2000	Necar4a	concept	70	1.31	n.a.	>180
2001	Sprinter	concept	70	1.31	n.a.	190-250
2004[1]	F-Cell (Gen1)	60	70	1.3-2	54%	170
2009[1]	F-Cell (Gen2/3)	300	75	>2	58%	380
2013[1]	F-Cell (Gen4)	11,000	75	>3	62%	n.a
2015[1]	F-Cell (Gen5)	500,000	75/90	>3.5	62%	n.a.

[1] Begin production

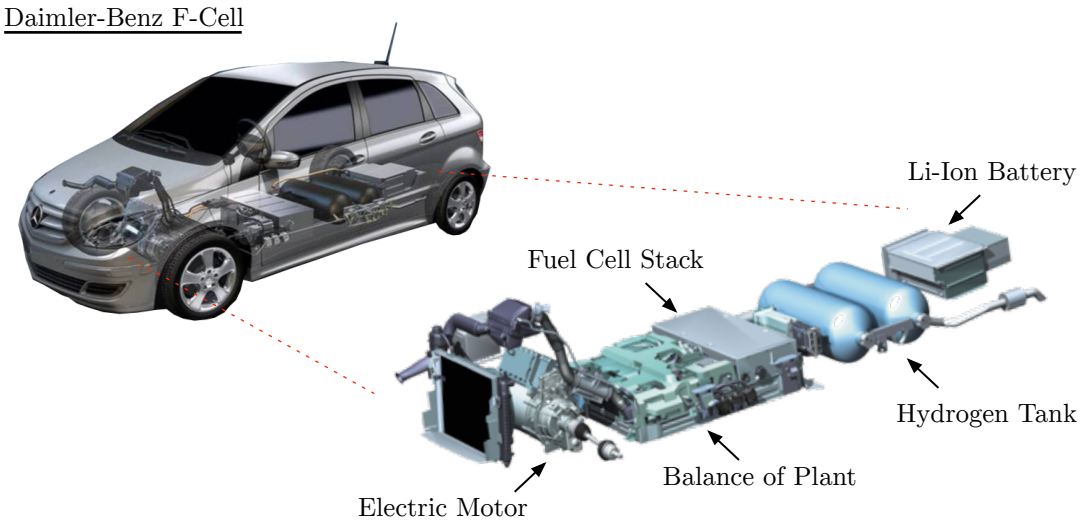

Figure 4.1: Daimler B-Class F-Cell and fuel cell system (Images courtesy of Daimler [352])

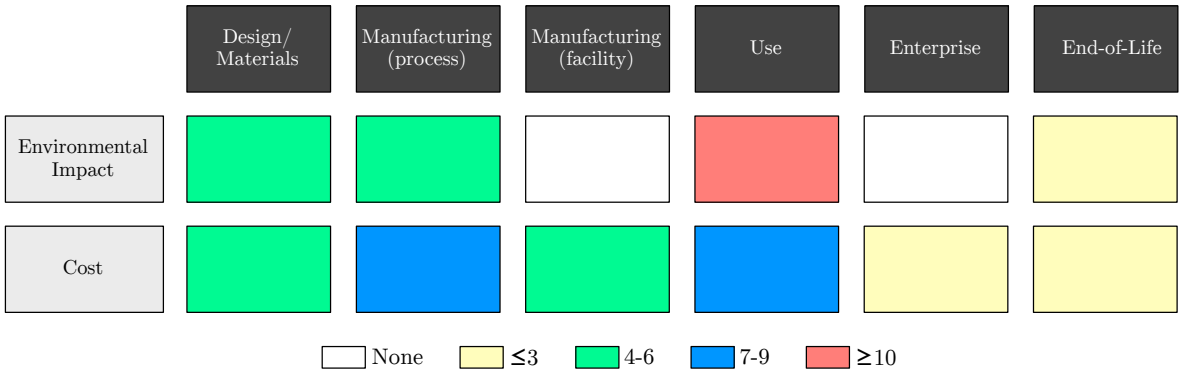

Figure 4.2: PEM fuel cell life cycle phases literature survey

prove to be invalid considering the vast differences in the design and materials for a fuel cell system compared to the conventional drivetrain system (the majority of the body-in-white (BIW) for both vehicle types are comparable). Therefore, the real analysis in determining if fuel cells are indeed the preferred technology wedge pathway is to compare the impacts of the materials, manufacturing, enterprise, and end-of-life (use phase is known) of the fuel cell system to that of the ICE equivalent (engine, transmission, and drivetrain). Furthermore, because fuel cells are still considered at its infant stage, there is a large potential to leverage design to achieve an optimal balance between lowest environmental impact and cost.

An extensive survey was carried out on existing literature regarding efforts in fuel cell environmental impacts and cost for automotive applications (i.e., PEM fuel cells). A summary of the results is illustrated in a color matrix shown in Figure 4.2. A total 43 studies were collected with 25 being related to PEM fuel cells. Of the 25, nearly half had at least some focus, if not all, on strictly the use phase of the fuel cell in terms of levelized cost (e.g., hydrogen fuel and infrastructure) and environmental impact offsets compared to other alternative and conventional energy technologies [93][6][341]. The remaining phases garnered less attention, particularly at the manufacturing facility scale, enterprise scale, and end-of-life phase. Cost assessments were generally well perceived and thorough in both manufacturing and use of the fuel cell. Some of the most comprehensive studies in fuel cell stack costing used a DFMA approach at various production volumes to determine the material and manufacturing costs [161][42][160]. A more recent studied (currently in progress) funded by the U.S. DOE Hydrogen and Fuel Cell Program is assessing the total cost-of-ownership of stationary PEM fuel cells from stack production cost to fuel consumption and the cost benefit of offsetting current stationary energy options (e.g., natural gas, diesel backup power generation) [339].

On the environmental side, most of the studies found focused on the material impacts and claimed to include the production of the fuel cell, however, the scope for the manufacturing was ambiguous [249][146][308]. More comprehensive studies were found that focused on a particular component of the fuel cell stack. Cooper [50] conducted an energy analysis of the production for several bipolar plate designs using the embodied energy of the material

and corresponding specific energy consumption (kWh per kg) obtained from the Cambridge Engineering Selector (CES) software by Granta Design. The most comprehensive environmental impact assessment study on PEM fuel cells was that of Schabert [281]. Although Schabert's analysis was static with linear input-output relationships, a near complete LCA from materials, manufacturing (combination of theoretical analysis and screening approach), and end-of-life (recovered material embodied energy) impacts was performed. Furthermore, results for multiple impact categories such as global warming potential, acidification, and eutrophication were reported.

None of the studies found included all life cycle phases regarding the production of the fuel cell. In addition, of the studies that analyzed the materials and manufacturing were limited to an inventory analysis and static non-integrated manufacturing. Therefore, the objective of this case study is to implement the iSLCD framework and methodology in attempt to reveal the true environmental impacts and costs and determine if fuel cells are indeed a sustainable option.

4.1 Fuel Cell Background

The origins and roots of fuel cells dates back to over 200 years, during the development period of physical chemistry and electrochemistry [278]. Th foundations of physical chemistry pertaining to fuel cells began with the discovery of hydrogen in the 18^{th} century by the English physicist, Henry Cavendish. The discovery eventually led to a new theory of combustion where the French chemist, Antoine-Laurent Lavoisier, in 1775 investigated the interaction between hydrogen and oxygen. Nearly half a century later came the discovery of the catalytic reaction where in 1823, the German chemist, Johann Wolfgang Döbereinger discovered the instantaneous combustion of hydrogen upon contact with powdered platinum [278]. The discovery was further supplemented by the Swedish scientist, Jöns Jacob Berzelius, where he introduced the term 'catalysis'.

During the same period of the development in physical chemistry was the development of electrochemistry in the late 18^{th} century. Contributions in electrochemistry originated with Italian physicists Aloysio Galvani and Allesandro Volta in the 1790's where an electric potential was detected with various materials (particularly metals) when contacted with the muscle tissue of frog legs. This phenomena was later refined in the same decade by the German chemist, Johann Wilhelm Ritter, where his experiments with various metals eventually led to the formulation of the electromotive series. The research in electrochemistry continued for several decades and in 1834 the English scientist, Michael Faraday, established two laws known as Faraday's Laws that relates the electrochemical reaction to the electrical current and charge [278]. Faraday, at the same time, introduced the nomenclature for an electrochemical cell: electrode, electrolyte, anode, anion, cathode, and cation.

The advancement of physical chemistry and electrochemistry eventually led to the discovery of the fuel cell in 1839 by English scientist, Sir William Rober Grove [278]. Although, Grove was not necessarily the first to discover the 'fuel cell effect', he was the first to recognize

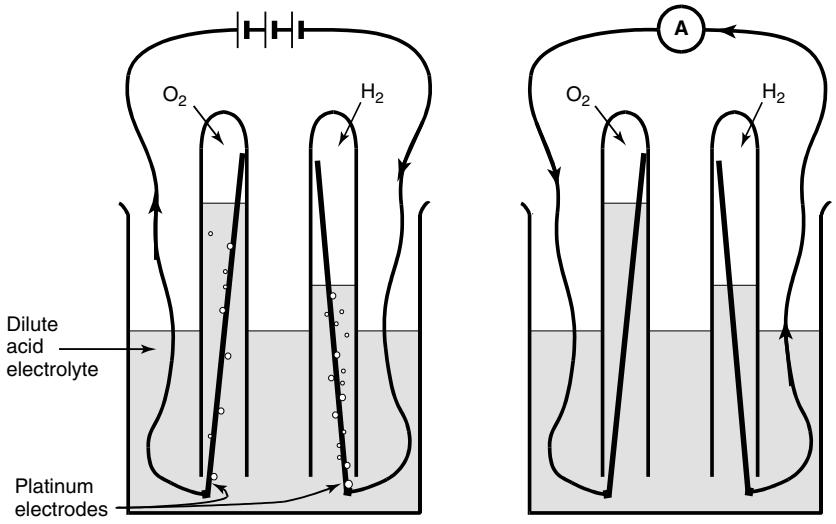

Figure 4.3: Grove's fuel cell [187]

the term and attribute it to the chemical reaction of hydrogen with oxygen. Interestingly however, Grove did not use the term 'fuel cell' in his publication, which he called "gaseous voltaic battery". The term 'fuel cell' was first published by the English chemist, Sir Humphry Davy, in his 1802 publication titled "Carbonaceous Fuel Cell with Aqueous Electrolyte at low-temperature". Furthermore, it was not until 1889 when chemists, Ludwig Mond and Charles Langer, re-coined the term again to describe their fuel, which for the first time had all the components of the modern day low temperature fuel cell.

For the next half century after Grove's discovery of the fuel cell, various researchers and scientist worked on improving the power density of the fuel cell with electrodes and electrolytes. In 1902, James H. Reid filed a patent for a fuel cell that for the first time used an aqueous alkaline electrolyte - the same electrolyte type used for the alkaline fuel cell (AFC) in the Apollo space missions. In 1938, the English engineer, Francis Thomas Bacon, invented an alkaline electrolyte fuel cell that not only had remarkable performance, but was also reversible [278]. Upon further improvement of his fuel cell, Bacon managed to achieve current densities over $1A/cm^2$ and fuel cell systems that could deliver in the kilowatt regime. In the 1950's, fuel cell R&D took a boom in the U.S. with contributions from over 50 companies. General Electric (GE) developed and introduced the proton exchange membrane fuel cell (PEMFC) in 1957 by Willard T. Grubb, which he originally named an ion exchange membrane (IEM), but was later changed to solid polymer electrolyte (SPE) by GE. The PEMFC technology made its way in the Gemini 5 spacecraft in 1965, which was used to power the onboard electronics. In 1961, the American company Pratt & Whitney obtained the license for the Bacon AFC, which they redeveloped and was used in for the Apollo mission in 1966 [278].

The 1960's saw plenty of advancements on different fuel cell technologies despite the lack commercial interest. High temperature fuel cells (approx. 500-1000^{o}C) were being developed,

namely the Molten Carbon Fuel Cell (MCFC) and Solid Oxide Fuel Cell (SOFC), which were able to obtain relatively high carbon-fuel to electricity efficiency [356]. The Direct Methanol Fuel Cell (DMFC) became of interest in the late 1950's and early 1960's due to methanol being an attractive fuel for direct conversion to electricity. The successful research from AFC led to the development of the Phosphoric Acid Fuel Cell (PAFC), which was envisioned to be the ideal co-generation system due to its operating temperature of 200°C [278].

The boom in fuel cell research and development slowed down in the 1970's where the primary applications were for space and military use or for smaller distributed power generation using high temperature fuel cells. It wasn't until the mid-1980's when the Canadian company, Ballard Power Systems, managed to achieve current densities of over several amps per cm^2 and came up with a reformer system that directly converted methanol or hydrocarbon fuels to hydrogen [278]. The efforts by Ballard paved the way for non-space and military applications and gained interest by automotive manufacturers. In fact, General Motors (GM) was one of the first to demonstrate a fuel cell vehicle 1966. However, GM's global fuel cell initiatives would not take off for another 30 years, when in 1997 GM demonstrated to the Department of Energy (DOE) a 50kW methanol reformer fuel cell system and the Gen3 stack was born [270]. During the same period, research was underway at Daimler-Benz to come out with compressed hydrogen fuel cell car. In 1994 Daimler introduce the NECAR1, a concept van more than a passenger vehicle, which included a 50kW stack yielding a maximum speed and range of 90km/h and 130km, respectively [284]. Several years later to 1999, Japanese auto manufacturer, Honda, introduced the FCX-V1 and FCX-V2 experimental prototype fuel cell vehicles, which demonstrated zero emissions, zero carbon emissions, direct hydrogen charging of a metal hydride fuel tank [208]. Nearly a decade later, Honda introduced the FCX Clarity in 2008, which was the first commercially available fuel cell vehicle for lease.

4.2 Fuel Cell Technologies

The term "fuel cell" is commonly associated with the PEM fuel cell technology due to its familiarity in the large automotive market. However, there are nearly a dozen of various other fuel cell technologies that have been developed, in use today, and are being developed for niche and upcoming markets. A background of the some the more popular and well known fuel cell technologies are detailed in this section with a more comprehensive list and description found in [332]. Table 4.2 lists several of the major fuel cell technology types in order of their operation temperature along with corresponding characteristics. The variety of fuel cell technologies is quite vast with power options ranging from milliwatts to beyond ten's of megawatts. The output maximum power is somewhat correlated to the operating temperature where lower power fuel cells are typically less than 100°C and can range to over 1000°C for high power applications. A common denominator between the technologies types is the use of a hydrogen rich fuel (e.g., methanol, hydrogen gas, natural gas) and the oxidation of hydrogen at the anode as shown in the half-reactions listed in Table 4.3.

Table 4.2: Overview of the major fuel cell technologies

Fuel Cell	Application	Power [kW]	Temp [°C]	Fuel	Electrolyte
Direct Methanol (DMFC)	Portable	0.001 - 0.1	20-90	Methanol	Acidic Polymer
Low Temp PEM (LTPEM)	Distributed, Portable, Transportation	0.001 - 1000	30-100	Hydrogen	Acidic Polymer
Alkaline (AFC)	Portable, Backup	1 - 10	50-200	Hydrogen	*aq.* KOH
High Temp PEM (HTPEM)	Backup	0.1 - 10	120-180	Hydrogen	PBT
Phosphoric Acid (PAFC)	Distributed, Transportation	10 - 100	220	Hydrogen	Phosphoric acid
Molten Carbonate (MCFC)	Distributed	100 - 10000	650	Hydrogen or natural gas	Molten Li2CO3
Solid Oxide (SOFC)	Electric Utility, Distributed, APUs	1 - 10000	500-1000	Hydrogen or natural gas	Yttria cubic zirconia

Table 4.3: Anode and Cathode half reactions

Fuel Cell	Anode Reaction	Cathode Reaction
Alkaline (AFC)	$H_2 + 2\,(OH)^- \longrightarrow 2\,H_2O + 2\,e^-$	$\frac{1}{2}\,O_2 + H_2O + 2\,e^- \longrightarrow 2\,(OH)^-$
Low Temp PEM (LTPEM)	$H_2 \longrightarrow 2\,H^+ + 2\,e^-$	$\frac{1}{2}\,O_2 + 2\,H^+ + 2\,e^- \longrightarrow H_2O$
Direct Methanol (DMFC)	$CH_3OH + H_2O \longrightarrow CO_2 + 6\,H^+ + 6\,e^-$	$\frac{3}{2}\,O_2 + 6\,H^+ + 6\,e^- \longrightarrow 3\,H_2O$
High Temp PEM (HTPEM)	$H_2 \longrightarrow 2\,H^+ + 2\,e^-$	$\frac{1}{2}\,O_2 + 2\,H^+ + 2\,e^- \longrightarrow H_2O$
Phosphoric Acid (PAFC)	$H_2 \longrightarrow 2\,H^+ + 2\,e^-$	$\frac{1}{2}\,O_2 + 2\,H^+ + 2\,e^- \longrightarrow H_2O$
Molten Carbonate (MCFC)	$H_2 + CO_3^{2-} \longrightarrow H_2O + CO_2 + 2\,e^-$ $CO + CO_3^{2-} \longrightarrow 2\,CO_2 + 2\,e^-$	$\frac{1}{2}\,O_2 + CO_2 + 2\,e^- \longrightarrow CO_3^{2-}$
Solid Oxide (SOFC)	$H_2 + O^{2-} \longrightarrow H_2O + 2\,e^-$ $CO + O^{2-} \longrightarrow CO_2 + 2\,e^-$ $CH_4 + 4\,O^{2-} \longrightarrow 2\,H_2O + CO_2 + 8\,e^-$	$\frac{1}{2}\,O_2 + 2\,e^- \longrightarrow O^{2-}$

Alkaline Fuel Cell (AFC)

Alkaline Fuel Cells (AFC) can be consider the most mature fuel cell technology having been invented in 1902 by Reid and then further improved by Bacon in the 1940's and 1950's. The key defining attribute of an AFC is the electrolyte, which, as the name suggest, is an alkaline solution primarily consisting of either sodium hydroxide (NaOH) or potassium hydroxide (KOH). The basic solution provides less activation voltage loss than with an acid electrolyte in a typical PEM fuel cell. Additionally, the advantage of using either NaOH or KOH is low cost, highly soluble, and not excessively corrosive [187]. The low cost electrolyte coupled with the fact that the cathode electrode can be fabricated from non-precious metal or exotic materials makes AFCs a very attractive cost effective technology.

The primary application for AFC have so far been for space and military use, despite the fact that AFCs have been in existence for over a century and can be manufactured at relatively low costs. This is due to the fact that the hydroxide ions (OH^-) in the alkaline electrolyte reacts with carbon dioxide to form carbonate, which negatively affects the number of mobile ions in the electrolyte. As a result, the reaction rate at the anode decrease, mass transport losses increase due to increase in electrolyte viscosity, and the formation of carbonate will precipitate out thus blocking the active pores and causing damage to the electrodes [187]. Using pure hydrogen and oxygen eliminates these issues, however, the practicality is also reduced and hence the use in extraterrestrial applications.

Direct Methanol Fuel Cell (DMFC)

The direct conversion of liquid methanol to electricity was first investigated by E. Müller in 1922 [278]. At the time, the conventional fuel for fuel cells, namely hydrocarbons and methanol, had to be convert to hydrogen using a reformer for proper operation. Potentially large costs savings in the fuel could be achieved if it could be directly oxidized electrochemically. Methanol was the preferred choice in fuel for several reasons: 1) being a liquid it easily transported and stored, 2) cheap and abundant, and 3) potentially renewable from wood alcohol [131]. The DMFC can be fabricated using standard existing techniques with an acidic electrolyte such as sulfuric acid or a solid polymer electrolyte.

However, the reaction kinetics of methanol using the standard platinum based catalyst is relatively slow. This results in a lower power density, particularly compared to its hydrogen fueled counterpart. The reaction kinetics can be improved through higher catalyst utilizations and high operating temperatures. However, operating at high temperatures (approximately 200°C) leads to addition issues including methanol crossover, which decrease the fuel utilization, and membrane degradation by both thermal mechanism and the methanol itself [131]. Adding additional complexity is the fact that there is an exhaust stream at both the anode and cathode, which differs from standard hydrogen/oxygen fuel cell. From the reaction kinetics for the DMFC (shown in Table 4.3), carbon dioxide and water is produced at the anode and cathode, respectively. The production of both fluids acts as a barrier for the reactants thus resulting in mass transport losses. Furthermore, the production of carbon

dioxide is a disadvantage from an environmental stance, where 1kg of methanol produces approximately 1.4kg of carbon dioxide.[1]

Despite these issues, there are potential application of DMFC for portable electronics. Methanol fuel cartridges can be used for low power applications thus eliminating the need for higher temperatures and have the advantage over rechargeable batteries in the sense that the recharging time is dramatically reduced.

Phosphoric Acid Fuel Cell (PAFC)

Development of the Phosphoric Acid Fuel Cell (PAFC) began in the 1960's to address the carbon dioxide poisoning problem for AFCs. Phosphoric acid provided the advantage of being able to reject carbon dioxide and was a lower cost solution compared to acid polymer membranes (e.g., Nafion) [174]. The operating temperature of the PAFC had to be increased due to the phosphoric acid freeze point of about 42°C. Furthermore, when the PAFC was first introduced at the lower temperature regime of 80°C, the performance of the cell was rather poor. With the improvements in materials and design, the operating temperature was increased to roughly 200°C, which yielded higher reaction kinetics and thus higher power densities. Furthermore, the higher temperature yielded the additional benefit of being greater carbon monoxide and sulfur tolerant [187].

The tolerance to carbon dioxide lead to the popularity of PAFCs first from the military in the 1970's, but more so for stationary applications starting the in 1980's. PAFC systems have been installed for commercial and residential use to provide back-up or continuous power using existing natural gas piping infrastructure with system life expectancy of over 40,000 hours [174]. System sizes can range from several kilowatts and up to tens of megawatts (by connecting smaller systems in series and parallel) with the typical size of 200kW. High system efficiencies can be achieved (>90%) by recirculating the high thermal energy coolant water (150-180°C) for combined-heat and power (CHP) [187]. PAFCs have also entertained the transportation sector where in the 1990's the U.S. DOE funded a project to install 100kW PAFCs into buses.

Molten Carbonate Fuel Cell (MCFC)

The Molten Carbonate Fuel Cell (MCFC) is classified in the category of high temperature fuel cells having operating temperatures up to 650°C (see Table 4.2). Having being first discovered in the early 20^{th} century and the bulk of the R&D in the 1960's, MCFCs are currently in operation all over the world providing small to mid size power generation in the range of 100kW and up to 30MW and yielding overall efficiencies of 65% to 75% [27][356]. The high temperature was required to melt (hence molten) and increase the conductivity of the electrolyte mixture consisting of alkali metal carbonates in a ceramic matrix of $LiAlO_2$. A unique characteristic of the MCFC is that carbon dioxide is required to be supplied at the

[1]The molecular weight of methanol and carbon dioxide is 32g/mol and 44g/mol, respectively

cathode along with oxygen to create the carbonate ions required for ionic conductivity. In a modern day MCFC system, the carbon dioxide byproduct at the anode (see Table 4.3) is directly recirculated to the cathode [187].

The high operating temperature give the MCFC several key advantages over the lower temperature PEMFCs, AFCs, and PAFCs. First, the reaction kinetics are greatly increased thereby eliminating the need for noble catalyst and thus reducing costs. For a standard MCFC system, nickel is used at the anode and nickel oxide at the cathode [187]. Second, internal reforming is possible due to the high temperature thus direct carbon fuel such as natural gas or coal gas can be used without the need of a reformer. The drawback of having a systems with a phase changing electrolyte is the generation of stresses during thermal cycling. These systems are assembled and completely packaged in the solid state hence stresses are induced during the melting of the electrolyte. MCFC stacks typically take 14 hours or more to condition and the slow heat up is to prevent cracking of the electrolyte tile, which may lead to fuel crossover [187]. Thus, MCFC systems are best for continuous power applications where thermal cycling (i.e., duty cycle) is minimized.

Solid Oxide Fuel Cell (SOFC)

Many parallels can be drawn between the Solid Oxide Fuel Cell (SOFC) and MCFC. Both had major developments around the same time (1960's), operate at high temperatures (500-1000°C), eliminate the need for noble catalyst, internal reforming for direct fuel, and achieve similar system efficiencies. The key difference appears in the material choice for the electrolyte. SOFCs uses a solid rather liquid electrolyte, typically an oxide ion-conducting ceramic such as yttria-stabilized zirconia (YSZ) [330]. Using a solid electrolyte simplifies the system, eliminating the need to for liquid management of the electrolyte. In addition, solid electrolyte increases the stability of the fuel cell with low reactivity and slow diffusivity [356]. Another key difference is in the design of the stack itself. Unlike any other fuel cell, SOFC are typically constructed in a tubular fashion. This provides the advantage of eliminating high-temperature gas-tight seals [187].

At the other end of the spectrum, using a solid electrolyte poses several disadvantages. First, the high temperature required to achieve the proper ion-conductivity of the YSZ raises the Gibbs free energy of water formation to be less negative. As a result, the open circuit voltage (OCV) is decreased and thus potentially yielding lower efficiencies than a MCFC system. Second, the contact resistance between the solid-solid electrode and electrolyte contact is greater than solid-liquid in a MCFC and thereby yielding a lower power density. Last, the high cost of YSZ and the brittle nature of the zirconia ceramic creates challenges in manufacturing, transportation, and installation [356]. Despite these challenges, SOFC have been popular in recent years, particularly by Bloom Energy with over 30 customers across the U.S. including large corporations such as Google and eBay.

PEM Fuel Cell (PEMFC)

Polymer Electrolyte Membrane, also referred to as Proton Exchange Membrane or Solid Polymer Electrolyte, fuel cells are the most extensively studied and widely implemented fuel cell technology due to the balance and range of output power, operating temperature, and efficiency. PEM fuel cells can be classified into two categories: low temperature (LTPEM) and high temperature (LTPEM). The majority of the PEM research has been on LTPEM due to commercial applicability in the automotive space. HTPEM have the advantage of operating at temperatures above the boiling point of water thereby simplifying or eliminating the humidification and water management systems in the balance-of-plant [14]. Furthermore, the higher operating temperature allows a higher tolerance to impurities in the fuel stream (e.g., CO) and reduced catalyst loadings by improving the reaction kinetics and higher proton conductivity of the membrane. However, the higher operating temperature is also the limitation for use in automotive applications where additional heaters are required to warmup the fuel cell resulting in long start-up times.

Out of the lower temperature technology fuel cells, DMFC, LTPEM, and AFC, LTPEM offer the highest power density and efficiency necessary for the automotive space. For the development of the LTPEM technology, the U.S. DOE has set specification targets, shown in Table 4.4, that are hypothesized to be required for mass commercial success. The power density of the LTPEM is far superior compared to the specific power of AFCs (400W/kg compared to <50W/kg). The power density of the DMFC stack (350-500W/kg [131]) is comparable to LTPEM, however, the mass of methanol required for the same range is several orders higher than the mass of hydrogen gas thereby becoming mass the volume limited. Therefore, the concentration of fuel cell technology in this case study is strictly on LTPEM, or simply referred to as PEM.

4.3 The PEMFC

A fuel cell is an electrochemical reactor that directly converts chemical energy into electricity. The conversion takes place via reduction-oxidation (redox) reactions where electron transfer occurs between an anode and cathode, spatially separated by an electrolyte membrane. Figure 4.4a shows a diagram of the redox mechanism of a hydrogen PEM fuel cell. Fuel in the form of gaseous hydrogen enters the anode where oxidation of hydrogen occurs at the anode electrode. The corresponding half reaction of hydrogen is given by:

$$\mathrm{H_2} \longrightarrow 2\,\mathrm{H^+} + 2\,\mathrm{e^-}$$

Two electrons are stripped from the diatomic hydrogen molecule (one for each atom) with the assistance of a catalyst that, by definition, lowers the activation energy threshold for reaction. The resulting hydrogen protons are conducted through the acidic electrolyte membrane while the electrons travel through the electrode to an external circuit that is electrically connected to the cathode. Air or diatomic oxygen is fed to the cathode electrode

Table 4.4: DOE Technical Targets for Automotive Applications (80kW net)[a] [103]

Characteristic	2011 Status	20117	2020
Energy efficiency @ 25% of rated power [%]	59	60	60
Stack efficiency @ 25% of rated power [%]	65	65	65
Power density [W/L]	400	650	850
Stack power density [W/L]	2,200	2,250	2,500
Specific power [W/kg]	400	650	650
Stack specific power [W/kg]	1,200	2,000	2,000
System Cost[b] [$/kW$_e$]	49	30	30
Stack cost[b] [$/kW$_e$]	22	15	15
Cold start-up time to 50% of rated power [s]			
@ -20°C ambient temperature	20	30	30
@ +20°C ambient temperature	<10	5	5
Start up and shut down [MJ]			
@ -20°C ambient temperature	7.5	5	5
@ +20°C ambient temperature	n.a.	1	1
Durability in automotive drive cycle [hours]	2,500	5,000	5,000
Assisted start from low temperatures [°C]	n.a.	-40	-40
Unassisted start from low temperatures [°C]	-20	-30	-30

[a] Excludes hydrogen storage, power electronics, and electric drive.
[b] Based on high-volume production of 500,000 systems per year.

where the reduction reaction simultaneously recombines the transferred hydrogen protons and electrons with the atomic oxygen. The point in which the simultaneously recombination or dissociation occurs at the catalyst site is call the triple point, shown in Figure 4.4b (refer to the Catalyst Layer section below for further details on the triple point). The half reaction of the reduction process is given by:

$$\tfrac{1}{2}\,O_2 + 2\,H^+ + 2\,e^- \longrightarrow H_2O$$

Where the product of the reactants, hydrogen and oxygen, is water. The amount of work a fuel cell can harness from the chemical energy of the reactants is characterized by the difference in free energy or the Gibbs free energy of formation,[2] G_f [331]. The Gibbs free energy can be defined as 'the energy available to do external work, neglecting any work done by changes in pressure and/or volume [187]. Analogous to mechanical potential energy, the change or difference in the potential between the products (H_2O) and reactants (H_2, O_2)

[2]Formation denotes the zero energy point at standard temperature (25°C) and pressure (0.1MPa)

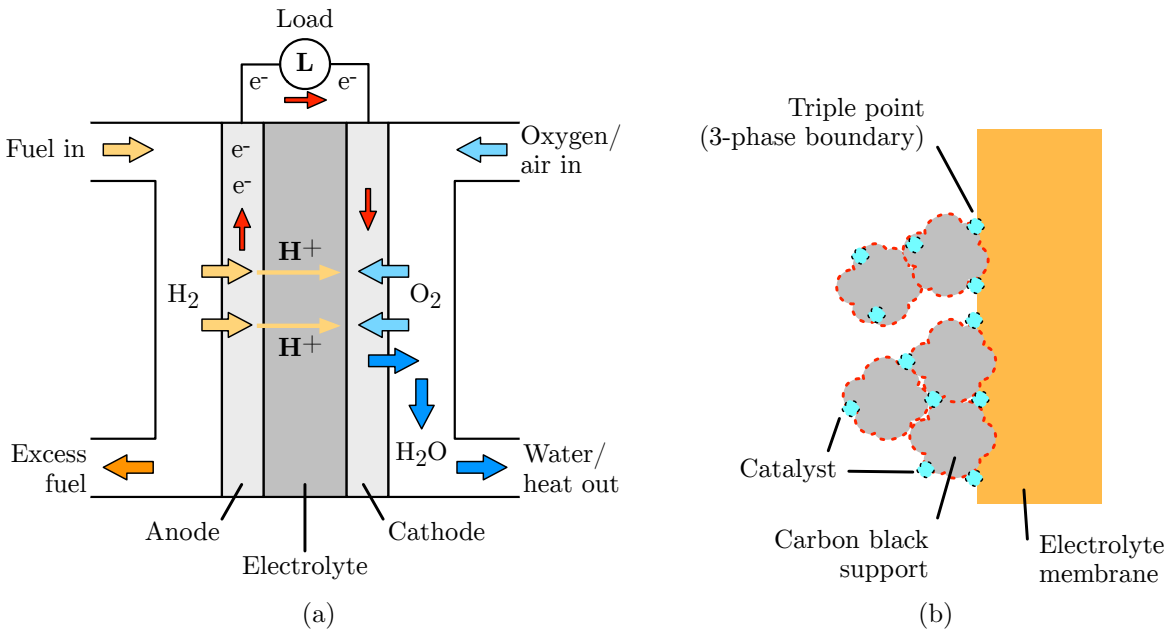

Figure 4.4: a) how pemfc works, b) triple point

denotes the energy released for useful work. In 'per mole' form, the change in molar Gibbs free energy of formation is expressed as:

$$\Delta\bar{g}_f = \bar{g}_f \text{ of products} - \bar{g}_f \text{ of reactants}$$

Which for a hydrogen fuel cell yields:

$$\Delta\bar{g}_f = (\bar{g}_f)_{\mathrm{H_2O}} - (\bar{g}_f)_{\mathrm{H_2}} - \tfrac{1}{2}\,(\bar{g}_f)_{\mathrm{O_2}} \tag{4.1}$$

In a reversible process (i.e., no losses in the fuel cell), the Gibbs free energy in Equation 4.1 is completely converted into electrical energy, denoted as the open-circuit voltage (OCV). Electrical energy or electrical work is defined as the product of voltage and total charge, therefore, the Gibbs free energy in Equation 4.1 can be equated as[3]:

$$\Delta\bar{g}_f = -zFE \tag{4.2}$$

Where $\Delta\bar{g}_f$ is the released molar free energy (joules), z is the number of electrons (per mole of product), F is Faraday's constant[4], and E is the electromotive force (EMF) or voltage. Equation 4.2 can be rearranged to yield the EMF or reversible open-circuit voltage (OCV) of a fuel cell:

[3]The expression for electric work is negative due to the convention that the fuel cell is doing work.

[4]$F = N \cdot e$, where N is Avogadro's number (6.022×10^{23}) and e is the electron charge (1.602×10^{-19}C) [187]

$$E = \frac{-\Delta \bar{g}_f}{zF} \tag{4.3}$$

The reversible OCV or more precisely $\Delta \bar{g}_f$ of a reaction is not static and in fact changes with temperature and phase (i.e., liquid or gas), and in a more complex manner, pressure and gas concentration[187]. For the formation of water during the fuel cell operation:

$$\mathrm{H_2} + \tfrac{1}{2}\,\mathrm{O_2} \longrightarrow \mathrm{H_2O}$$

The Gibbs free energy of formation for the above reaction at 25°C (liquid) is -237.2kJmol^{-1}, while at 100°C (gas) is -226.1kJmol^{-1}. Noting the fact that two electrons are transferred per mole of H_2O (i.e., $z = 2$), the reversible OCV at 25°C and 100°C is 1.23V and 1.17V, respectively. It will be covered later that although operating at a lower temperature will yield a high voltage, the ionic conductivity decreases and the amount of catalyst increases.

It was stated earlier that 100% of the Gibbs free energy is directly converted to electrical energy. However, the Gibbs free energy only states the amount of available energy rather than the total released energy from the reaction (i.e., exergy). In thermodynamics, the total release energy (per mole) is represented by the Enthalpy of formation, h_f, which is equal to the sum of the Gibbs free energy and entropy. The entropy terms implies that the reaction enthalpy is dependent on the state of the product, namely water in the vapor or liquid phase. The enthalpy for water vapor (i.e., steam) product is:

$$\Delta \bar{h}_f = -241.83\text{kJmol}^{-1}$$

and for liquid water product:

$$\Delta \bar{h}_f = -285.84\text{kJmol}^{-1}$$

where the difference between the enthalpy value of the two phases is the molar enthalpy of vaporization of water [187]. The lower value is referred to as the 'lower heating value' (LHV), while the higher value is referred to as the 'higher heating value' (HHV). For determining the efficiency of the fuel cell the proper heating value must be stated since the LHV will give a higher efficiency figure. The max efficiency, or thermodynamic efficiency, ε_{max}, can therefore be expressed as the ratio of the Gibbs free energy and enthalpy of formation [187]:

$$\varepsilon_{max} = \frac{\Delta \bar{g}_f}{\Delta \bar{h}_f} \times 100\% \tag{4.4}$$

Thus the maximum thermodynamic efficiency at standard temperature and pressure using the HHV is -237.2kJ/-285.84kJ = 83% at the maximum voltage of 1.23V. Note, that the thermodynamic efficiency can be greater than 100% if heat from the surroundings is transferred to the fuel cell as useful work such that the change in entropy is greater than zero [331]. To determine the maximum possible voltage at 100% system efficiency for the fuel cell, the Gibbs free energy in Equation 4.3 is replaced with with enthalpy of formation yielding:

$$\begin{aligned} E &= \frac{-\Delta \bar{h}_f}{2F} \\ &= 1.48\text{V with HHV} \\ &= 1.25\text{V with LHV} \end{aligned}$$

Lastly, the actual cell efficiency can be expressed (using the HHV) as:

$$\varepsilon_{cell} = \frac{V_c}{1.48} \times 100\% \tag{4.5}$$

where V_c is the actual OCV of the cell. Note, a quick sanity check shows that at maximum thermodynamic cell voltage yields an actual cell efficiency of 1.23V/1.48V = 0.83 or 83% as previously determined.

In reality, the reversible OCV of 1.23V is near impossible to achieve, not to mention the theoretical thermodynamic limit of 1.48V (using HHV). This is due the internal irreversible losses that reduces the theoretical OCV. There are three major categories that contribute to the irreversible losses - activation polarization, ohmic polarization, and concentration polarization, which are further described below:

- *Activation Polarization* - is the voltage loss due to the necessary voltage overpotential to drive the electrochemical reaction on the electrode surface. Analogous to overcoming the activation energy in a chemical reaction, the activation polarization is the dominate voltage loss at low current density and at lower temperatures, and is also a measure of the catalyst effectiveness [353]. The voltage overpotential is characterized by the exchange current density, i_o, in the Tafel equation, where larger the i_o the faster the reaction. Several factors can increase the value of i_o, particularly at the cathode electrode of a hydrogen fuel cell where i_o for oxygen reduction is much lower than the i_o for hydrogen oxidation: raising cell temperature, more effective catalysts, higher electrode surface area, increase reactant (especially at the cathode) concentration, and increasing the system pressure [187].

- *Ohmic Polarization* - also known as resistive loss, ohmic polarization is the voltage loss due to the total internal resistance of the cell including the electrode, membrane, and supporting components such as the interconnects. The term stems from Ohm's Law ($V = I \cdot R$), which states that the voltage drop is linearly proportional to the current or current density. Using materials with higher conductivity and better design such as a thin cell can dramatically reduce the ohmic losses [187].

- *Concentration Polarization* - at high enough current densities, the reactant species at the electrodes enters a starvation regime where the supply of reactants can not keep pace with the rate of electrochemical reaction. Often considered as mass transport loss or concentration loss, concentration polarization creates a sharp decline in the output

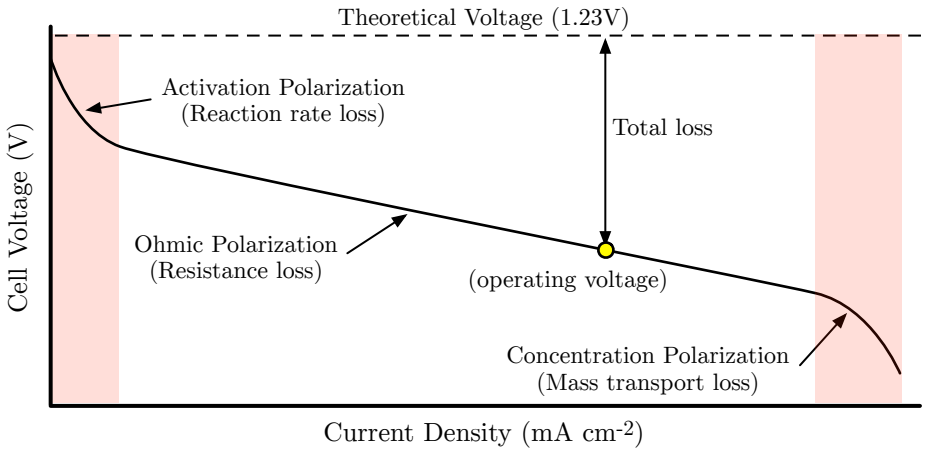

Figure 4.5: Generalized voltage vs. current density polarization curve.

voltage. Blockage to the electrode can also induce mass transport loss such as in the case of feeding air rather than pure oxygen where the excess nitrogen can effectively block the accessibility to the electrode [187].

Other irreversible losses include fuel crossover where the reactants (particularly hydrogen) diffuse through the membrane, and to a lesser extent, electron conduction through the membrane [187]. The three major irreversible losses are highlighted in Figure 4.5 on a generalized fuel cell polarization curve. The active polarization causes the OCV to immediately shift to a lower voltage followed by a sharp decrease in voltage. As the current density increases into the ohmic region the drop in voltage slows and becomes more linear. At the very high current density regime the cell becomes starved of reactants causing concentration polarization and the voltage to sharply decreases.

PEMFC Components

This section provides an overview of the major component in a PEM fuel cell. Figure 4.6 shows the structure of the fuel in terms of each sandwiched layer. The fuel cell is symmetric in the sense that the center layer is the membrane sandwiched by an anode and cathode catalyst layer (or catalyst electrode), which is sandwiched by an anode and cathode gas diffusion layer (GDL) and enclosed with an anode and cathode interconnect or bipolar plate (BIP). The 3-layer anode catalyst - membrane - cathode catalyst is referred to as the catalyst coated membrane (CCM) where the catalyst layers are deposited onto the membrane. Alternatively, the catalyst layers can be deposited on the GDL thus creating a gas diffusion electrode (GDE) structure. In most high powered applications such as for automotive, the CCM structure is preferred over the GDE due to a more achievable consistent and uniform catalyst layer [14]. The fuel cell stack is created by stacking (a series connection) multiple cells, connecting the anode of the BIP to the cathode of the adjacent cell.

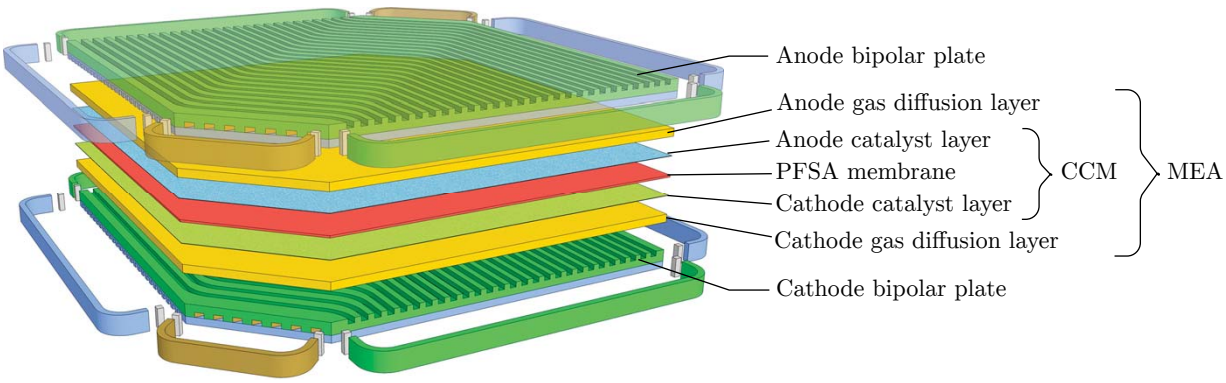

Figure 4.6: Expansion of the PEM fuel cell structure. Adopted from [344]

Membrane

The membrane, which is the structure that contains the electrolyte, can be considered the heart of the fuel cell and is often the one of the most expensive components. The primary purpose is act as a separator by allowing the conduction protons from the anode electrode while being electrically resistive to electrons. Therefore, primary candidates of membranes are solid polymers films, which can be categorized as being: 1) perfluorinate, 2) partially fluorinated, 3) non-fluorinated, 4), non-fluorinated composite, and 5) others [215]. Perfluorinate membranes are considered to be the industry standard polymer, which is a polymer based on polyethylene where the hydrogen atoms are substituted with fluorine thus creating polytetrafluoroethylene (PTFE). PTFE is advantageous because it is durable and resistant to chemical attack and highly hydrophobic to drive out excess water to prevent flooding of the membrane [187].

The most well known and widely used perfluorinated membrane for fuel cells is perfluorinated sulphonic acid (PFSA) under the name Nafion®. Nafion®, is an ionomer originally developed by DuPont in the early 1960's as a membrane separator for the production of chlorine and caustic soda and eventually used by GE in 1966 for the PEM fuel cell in the Gemini 5 spacecraft [17]. The sulphonic acid, HSO_3, is attached to the PTFE backbone as a sulphonated side chain, which is ionically bonded in the ionic form, SO_3^-. Formed by reacting tetrafluoroethylene (TFE) with sulfur trioxide, (SO_3), the SO_3^- ion allows the perfluorinated membrane to be ionically conductive [17]. Figure 4.7 shows the a diagram of the chemical structure of Nafion® (left) and the schematic depiction of the Nafion® nanostructure (right).

A unique property of sulphonic acid is that it is highly hydrophilic, which allows proper membrane hydration for the H^+ ions to move. The hydrophilic property delicately counteracts the hydrophobicity of the PTFE where there is a high enough water content for ion conduction without swelling and over flooding. Maintaing proper ionic conductivity is crucial especially at high current density operation, which tends to dehydrate the membrane, and also at very high temperatures (greater than the boiling point of water) where chemical instability and dehydration can occur [17].

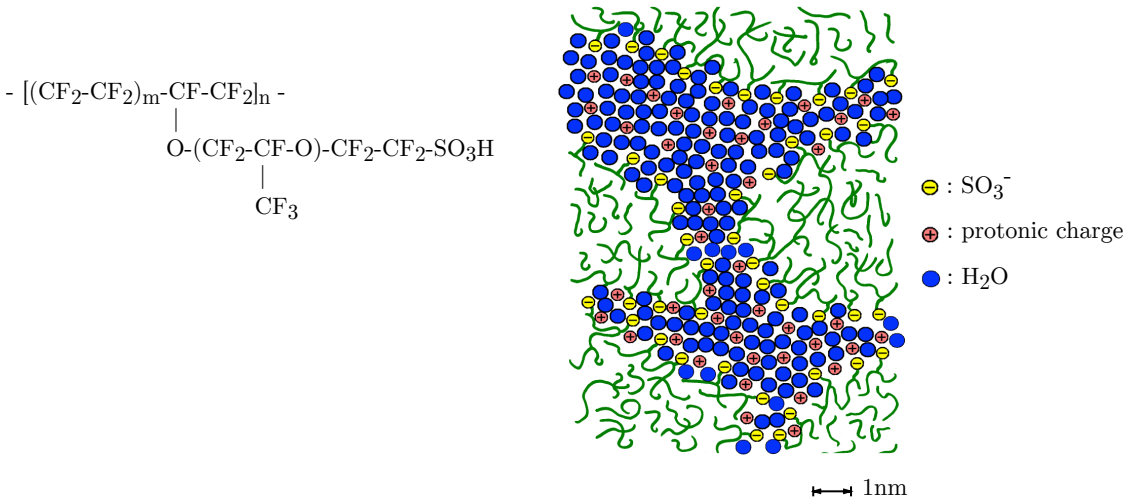

Figure 4.7: Molecular formula of Nafion® (left) and structure (right). Adopted from [167]

Nafion® membranes are typically sold as a thin-film rolls ranging from 20cm to 100cm widths and lengths of up to 100m or more (upon special request) [83]. Typical membrane thicknesses range from 25μm and up to 250μm [17].

Catalyst Layer

The redox reactions of hydrogen and oxygen occur at the surface of the catalyst layer, which is an electrode coated with a catalyst typically 5-15μm in thickness. The efficacy the oxidation and reduction is primarily dependent on the catalyst material and the exposed surface area to the reactants. The most proven and widely used catalyst for both the anode and cathode is platinum, however, non-platinum catalyst such as gold and palladium have been considered [187][215]. The choice of the electrode requires its structure to be porous to achieve a high surface area to volume ratio and allow the protons to permeate to the membrane. Furthermore, the electrode must be electrically conductive, chemically resilient, and have structural toughness to avoid cracking. For these reasons powered carbon black is used as the support catalyst. Figure 4.8 shows a scanning electron microscopy (SEM) image of an agglomerated carbon-support catalyst and an enhanced schematic of platinum on a carbon particle. The size of the platinum particle is typically an order magitude smaller than the carbon support particle. Adherence to the carbon black is facilitated by an ionomer coat (i.e., Nafion®), which also improves contact between the catalyst layer and membrane.

The efficacy of the catalyst layer is not only determined by the surface area of the exposed platinum, but also the contact point of platinum to the membrane called the 'three-phase contact' or triple point [187]. The triple point essentially describes the three-phase boundary where a platinum particle is simultaneously in contact with the carbon-support and membrane while being exposed to the reactant gas. In addition, the performance is highly

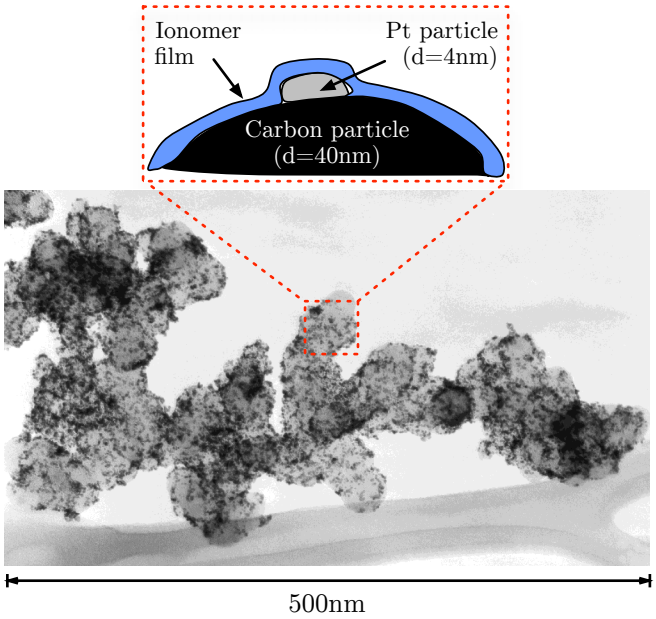

Figure 4.8: Catalyst on carbon support particle. Adopted from [167]

sensitive to the concentration of carbon-monoxide (CO). Even at relatively low concentrations (<100PPM) the performance of the catalyst layer greatly suffers. This is due to the strong chemisorption force of CO onto the catalyst where the platinum particle becomes saturated with CO [215]. Remediations to reduce or eliminate CO poisoning include an air or oxygen purge where CO has higher affinity to oxygen and forms and discards CO_2 as a product. A more permanent remedy is to use binary (or ternary) catalysts that pairs platinum with a CO inhibitor such as ruthenium [215]. For a more exhaustive list of catalysts refer to [66].

More recently, newer processing techniques have been developed in the mid 1990's that aims for reducing the required loading of platinum while increasing the effective surface area. Research in this area has lead to a relatively novel application of nano-technology thin-film depositions. Using nano deposition techniques such as sputtering and ion-beam deposition catalyst electrodes can be deposited at thicknesses at least an order magnitude thinner than the conventional carbon black support electrode [64]. The introduction of this technology has lead to significant cost reduction implications. During the initial development of PEMFCs platinum loadings were as high as 28mg-cm^{-2} and have now gone down to as low as 0.2mg-cm^{-2} using the conventional carbon-support structures. To reduce loadings even further, a catalyst electrode structure called the nano-structure thin-film (NSTF) was developed by 3M Electronics using nano deposition techniques [64]. The NSTF structure could achieve loadings as low as 0.05mg-cm^{-2} and lower are possible with 5x gain in specific activity, reduced mass transport loss at high current density, and does not require an expensive ionomer [63]. Figure

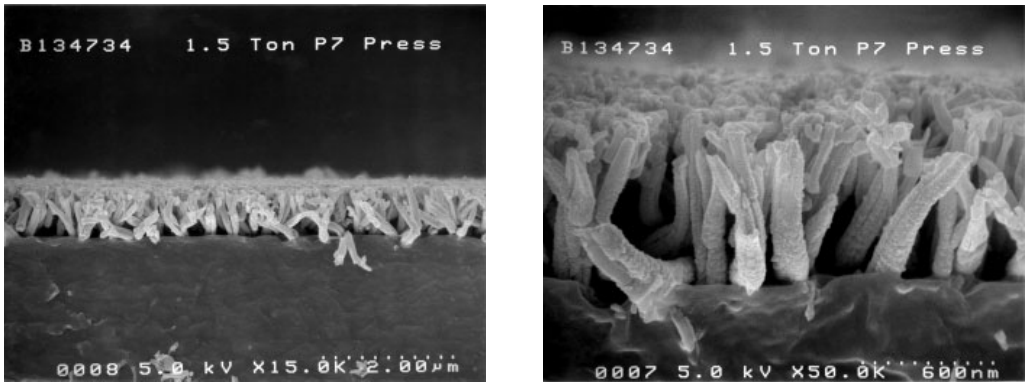

Figure 4.9: SEM 15,000x (left) and 50,000x (right) of the NSTF. Taken from [64].

4.9 shows a SEM image of the whisker structure NSTF catalyst layer at 15000x (left) and 50000x (right) magnification embedded on the membrane. The key feature to the NSTF is the supporting structure material, in which the organic pigment, Perylene Red (PR), has been found to be the most successful due to the growth and controllability of the whiskers created by screw dislocations at high temperatures. The NSTF catalyst electrode has been tested for automotive applications with sufficient durability of 2000 lifetime hours at >80°C operating temperatures and 5000 lifetime hours for ≤80°C under cyclic conditions [62].

Gas Diffusion Layer (GDL)

In theory, a functional fuel cells only requires the electrolyte membrane and anode/cathode catalyst layer electrodes. However, performance and and system integration is greatly improved by introducing the gas diffusion layer (GDL). The function of the GDL are as follows [207]:

- *Reactant permeability* - properly distribute the reactant gas both in-plane and thru-plane from the bipolar plate to the catalyst layer.
- *Product permeability* - provide a medium for the removal of product water from the catalyst layer to the bipolar plate.
- *Electrical conductivity* - an electrical bridge between the catalyst layer electrode to the bipolar plate.
- *Heat conductivity* - increase the effective thermal conductivity for proper heat removal generated by the redox reactions.
- *Mechanical strength* - mechanical support structure for possible pressure differential between the anode and cathode; protect the catalyst layer and membrane from damage (from the channels of the bipolar plate) during compression of the cell.

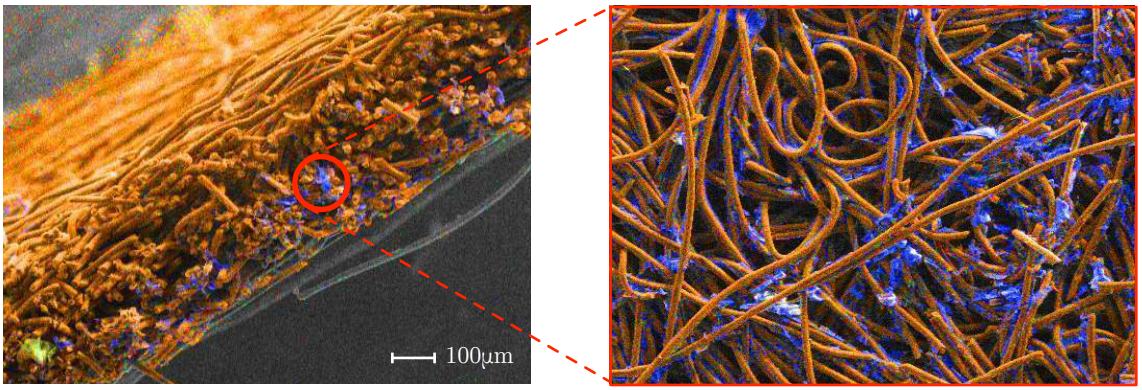

Figure 4.10: SEM of the gas diffusion layer. Taken from [167].

Typical variations of gas diffusion media have been considered including: carbon-fiber paper, coated or filled carbon cloths, and carbon-fill non-woven webs. However, carbon-fiber based diffusion media have shown to be the most promising and proven technology [207]. The advantage of carbon-fiber paper (or cloth) is high porosity ($\geq$70%, pore size 10-30μm) and good electrical properties through either graphitization and/or carbon/graphite powder fillers such as carbon black. The high porosity is particularly crucial for proper water management where the hydrophobic property of carbon-fiber assists in the removal of water generated at the cathode catalyst layer. The hydrophobicity is further increased by soaking the carbon-fiber media in PTFE dispersions resulting in 5-30wt% PTFE loadings [207]. Typical resulting thicknesses for carbon fiber paper GDL range from 100-500μm. Figure 4.10 shows a cross-sectional image of a carbon-fiber paper GDL with the fibers coated with PTFE.

Most state-of-the-art GDLs in practice have an additional layer, referred to as the microporous layer (MPL), of PTFE and carbon power (graphite powder or carbon black) composite and is coated onto the surface of the carbon-fiber media that becomes in contact with the catalyst layer. With a thickness of less than 50μm and pore size of 100-500nm, the MPL further enhances the extraction and transportation of water away from the catalyst layer while also decreasing the contact resistance between the carbon-fibers and electrode. The MPL can exist as a separate thin-film layer, however, it is typically directly coated onto the carbon-fiber media [207]. The term 'GDL' herein will be referred to as the bulk carbon-fiber media with MPL.

Membrane Electrode Assembly (MEA)

The assembly of the membrane, catalyst layers, and anode/cathode GDL is commonly referred to as the membrane electrode assembly (MEA). However, among the PEM fuel cell community there are varying definitions of what is included as the MEA, and a list of which is given in Table 4.5. The nomenclature used herein for MEA is the 7-layer structure with

Table 4.5: Sandwiched MEA nomenclature. [344]

Term	Definition
3-layer structure	Also referred to as the CCM: anode catalyst layer + membrane + cathode catalyst layer
5-layer structure	CCM with the addition of the anode and cathode GDL without MPL
7-layer structure	A 5-layer structure with the inclusion of the MPL on the GDL or GDE with MPL

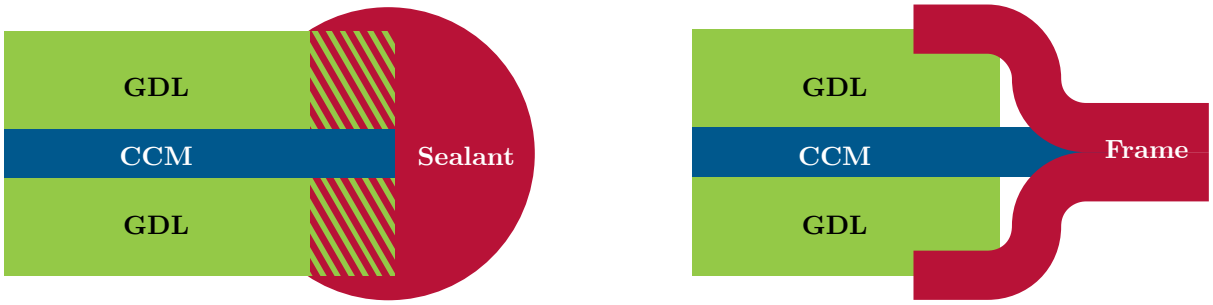

Figure 4.11: MESA (left) and MEFA (right) structures [14].

the catalyst layer coated onto the membrane (i.e., CCM) as opposed to the GDL.

A key attribute of a good MEA is the technology used to bond and seal the layers, or more precisely the bond between the CCM and GDL. Traditional methods included fusing the layers via hot pressing. However, hot pressing raises the issue of potentially drying out the membrane [187]. Newer methods and what is conventionally used for PEM fuels cells today is to use a frame-gasket technology that seals the edge of the MEA. Such technologies may include an elastomer type material that penetrates and fuses with the GDL or a border frame laminate using thin-film polymers as shown in Figure 4.11. Despite the added material cost and processing complexity, the framed technology avoids drying the membrane and potential damage during hot pressing. Furthermore, it has been tested that without an edge support structure, the added edge stress during cell compression causes catalyst damage leading premature failure of MEA [344][355]. The edge-seal design will be referred to the membrane electrode sealed assembly (MESA) and the bordered frame design referred to as membrane electrode framed assembly (MEFA).

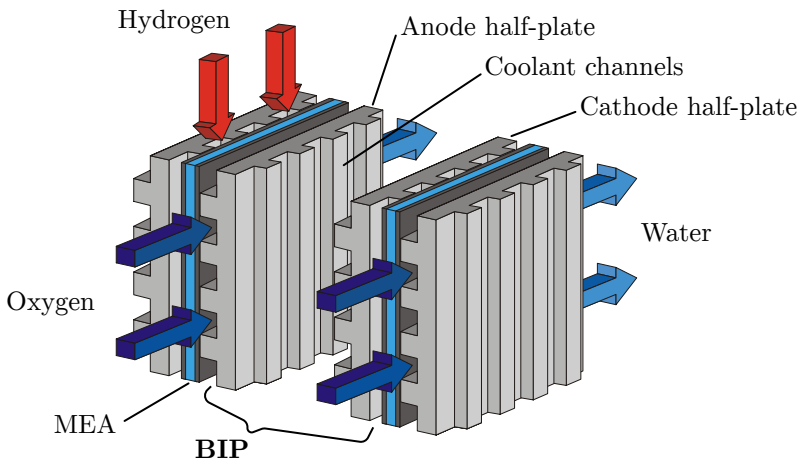

Figure 4.12: BIP formed by two half-plates from adjacent cells. Modified from [167].

Bipolar Plate (BIP)

Bipolar plates (BIP) play a crucial role in not only improving the performance of the fuel cell with flow fields, but also allowing proper functioning and assembly of the fuel cell stack. Typical operating cell voltages (depending on the polarization curve) are in the range of 0.6-0.7V, which is not practical for the majority of intended applications (e.g., automotive). To overcome the voltage limitation, BIPs are used in a similar manner as current collectors in batteries to connect multiple electrochemical cells creating a voltage increase that is directly proportional to the number of cells [45]. Modern day PEM fuel cells contains an anode and cathode half-plate for each cell that is bonded to the half-plate of the adjacent cell. Figure 4.12 shows a diagram of two adjacent cells connected by their anode and cathode half-plate. As seen in the figure, the advantage of the BIP design is reduction in material and space with interior channels between the half-plates thus allowing internal cooling.

A summary of several important characteristics and functions of the BIP are listed below:

- *Electrically conductive* - sufficient electrical conductivity is required to minimize ohmic losses and is recommended to be at least >10 Scm^{-1} [187].

- *Distribution of gases* - uniform distribution of the gases using flow fields is critical for fully utilizing the MEA and avoiding local hotspots, thus increasing the performance and lifetime of the MEA. Hence, proper design and pattern of the flow field channels is imperative [45].

- *Heat conductivity* - properly cooling is necessary to avoid over heating of the cell, BIPs with high thermal conductivity (>20 $Wm^{-1}K^{-1}$) are more effective of transferring the heat to the coolant channels [187]

- *Corrosion resistant* - the gases, materials (specially the membrane), and conditions (e.g., heat, humidity) create an acidic and corrosive environment in the cell, the BIP must be able to resist corrosion with an adequate lifetime [45]
- *Impermeability* - the BIP must be relatively impermeable to avoid leaking and reactant cross-over, which also has safety implications [45]
- *Mechanical strength* - to prevent distortion and bending of the MEA, the BIP needs to be sufficiently stiff with flexural strength >25 MPa, additionally needs to be strong enough to not flex or break during stack compression [45]

Furthermore, in addition to meeting the above requirements, it is advantageous for the BIP to be thin and lightweight for cost, mass, and volume reasons (the BIPs typically occupy 80% of PEM fuel cell stack volume [187]). Typical BIP thicknesses range from 1-5mm and is several times thicker than the MEA.

Common materials for BIPs fall into three categories: pure graphite, carbon-polymer composite, and metallic, with a list of advantages and disadvantages listed in Table 4.6. Some of the original PEM fuel cells used pure graphite for the BIPs. The advantage of graphite is good electrical conductivity, easy to machine, relatively low density, and reasonability stiff [187]. However, the drawback with graphite is the relatively high porosity, which generally resulted in the BIPs being several millimeters thick and thus offsetting the low resistivity and low density. Furthermore, the machining of the channels was highly time intensive and coupled with the fact that graphite is brittle and easily breaks during manufacturing resulted in prohibitively high manufacturing costs. More recent efforts have shifted towards carbon-polymer composites and metallic sheet metals. Carbon-polymer composites, consisting of polymer binder and carbon-based filler, have so far been the most popular due to lower manufacturing costs and adequate performance despite the disadvantages listed in the table. There have been numerous proposed materials for carbon-polymers BIPs [215] that fall into two categories - thermoplastics and thermosets. Thermoplastic binders include polypropylene and PVDF while epoxy and phenolic resin are the leading candidates for thermosets. The carbon fillers are used to increase the electrical conductivity of the composite, which includes carbon black and various shaped graphite powders [216]. Metallic BIPs have not gained the same attention as carbon-polymer composites despite being electrically, thermally, and mechanically superior. The primary reason is the corrosion of the metal under the harsh operating conditions. Various coatings can be deposited onto the metal surface such as gold, chrome, electrically conductive oxides, and nitrides, however, it comes at the price of high material (e.g., gold) and manufacturing costs (typically need a PVD or CVD system) [216]. At low volumes the cost becomes prohibitive, however, studies have shown that costs dramatically decrease at high volumes [160].

The most prominent feature of the BIP is design of the flow field channels that uniformly delivers the reactant gases to the MEA as well as effectively transport the water product out of the cell. In theory, there are limitless possibilities in the design of the channels, each with associated advantages and disadvantages [45]. Figure 4.13 shows four popular channel

Table 4.6: BIP materials pros and cons. Based from [187][45][216].

Material	Advantages	Disadvantages
Pure graphite	- Good electrical conductivity - Easy to machine - Low density - Reasonably stiff	- High porosity - Very long machine times - Thicker plate required - Very brittle
Carbon-polymer	- Low density - Molded-in flow fields - Known fabrication techniques - Corrosion resistant	- Poor electrical conductivity - Need high filler content - Relatively brittle - Temperature limitations
Metals	- High electrical conductivity - High strength - Thin - Known fabrication techniques	- Susceptible to corrosion - Contamination of MEA - Expensive alloys and coatings - High contact resistance

patterns, with parallel being the simplest and most widely used design. The parallel flow channel has the advantage of greater manufacturability, which is essential for high volume manufacturing where, for an example, a typical automotive fuel cell stack may contain several hundred BIPs. The serpentine, parallel-serpentine, and grid design will yield a higher channel area for gas flow at the cost of higher pressure drop, which may lead to mass-transport losses at high current densities. A major disadvantage of the parallel design is buildup of water or impurities (e.g., nitrogen in air) in the channels creating a blockage. However, the blockage can be mitigated by designing the channels such that the pressure drop along each channel is greater than the surface tension that holds a water droplet in place [45]. Further design considerations take into account the trade-off between land area (area in contact with the GDL) and channel area, where larger channel area leads to more reaction while larger land area reduces contact resistance and ohmic losses [45]. Other BIP flow designs with detail descriptions can be found in [198] and [205].

Another key attribute of the BIP are the manifolds that bridge the main fuel and coolant ports to all the cells. Each BIP is typically designed with three manifold inlets and outlets on opposing sides - hydrogen gas fuel manifold, air manifold, and coolant manifold [30]. More efficient designs such as described in the European Patent EP1009051 [106] have integrated manifold, fuel and coolant channels, where the backside of the plate are half channel coolant flow fields (typically parallel low) and form a complete channel when two half-plates are bonded together.

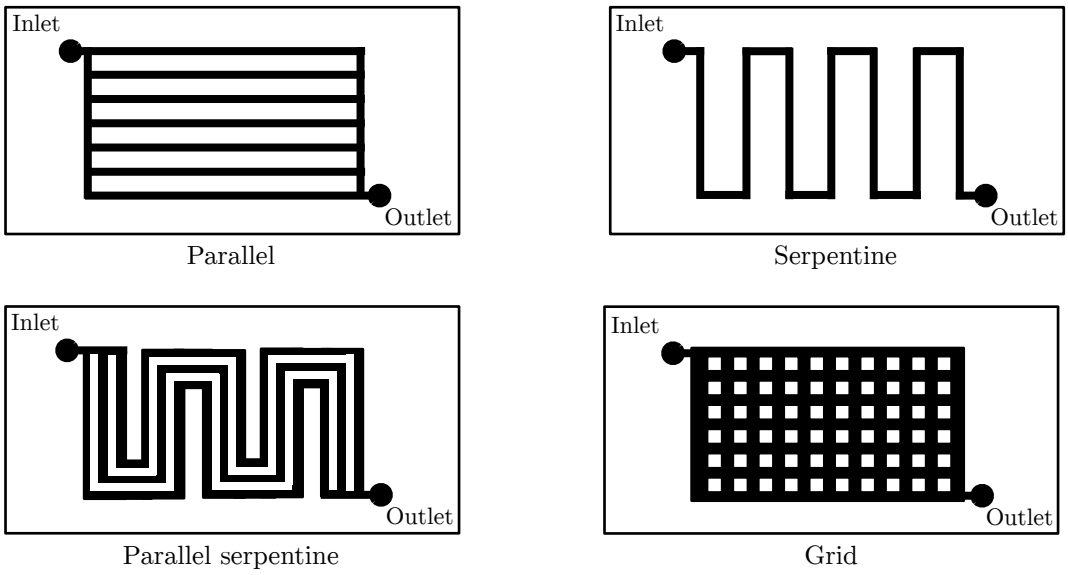

Figure 4.13: Various BIP flow field designs. Adopted from [187].

Chapter 5

PEM Fuel Cell Manufacturing

The historically slow pace of fuel cell commercialization has not been due to technological and scientific limitations, but rather barriers in manufacturing that made fuel cells cost prohibitive. Over the last couple decades technologies for fuel cell manufacturing have dramatically shifted from manual piece-by-piece batch production to more automated and roll-to-roll processing that takes advantage of economies-of-scale. In the U.S., the Department of Energy created the Hydrogen and Fuel Cells Program aimed at developing new fuel cell technologies across the entire value-chain and new materials and manufacturing processes that enable cost competitiveness with energy existing technologies. In addition, the DOE has set various cost and design targets (shown in Table 5.1) for the automotive fuel cell industry that are recommended to be met in order for mass commercialization.

The DOE targets do not represent actual fuel cell costs, but rather the potential if

Table 5.1: List of DOE targets for the fuel cell components [103].

Characteristic	Units	2011 Status	2017 Target	2020 Target
Fuel cell stack				
Cost	$\$/kW_{gross}$	132[a][160]	30	30
Membrane				
Cost	\$/kW	n.a.	20	20
Specific proton resistance[b]	Ohm cm^2	0.023	0.02	0.02
Electrocatalysts				
Platinum total content	g/kW	0.19	0.125	0.125
Platinum total loading	$mgPt/cm^2$	0.15	0.125	0.125
Membrane Electrode Assembly				
Cost (w/o frame, gasket)	\$/kW	13	9	7
Cost (w/ frame, gasket)	\$/kW	16	9	7
Bipolar Plates				
Cost	\$/kW	5-10	3	3

[a] Direct manufacturing only, $80kW_{net}$ at 1,000units/yr

[b] At maximum operating temperature and 40kPa pressure

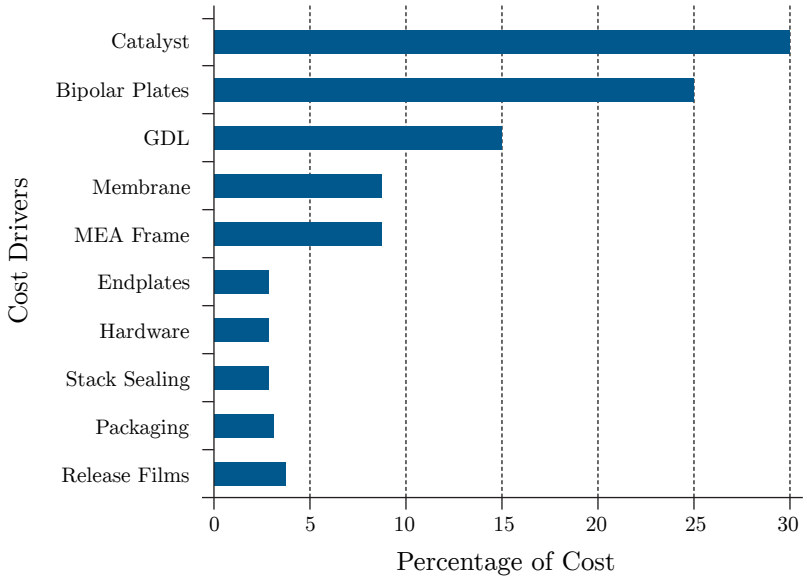

Figure 5.1: Drivers that influence fuel cell stack cost [14].

the right technologies are implemented and at the right volumes. Actual fuel cell stack manufacturing cost are on the order of $500-$1000/kW for automotive applications at current production volumes [351]. The key contributors to the high costs have been identified in a recent report by the Department of Defense: Manhattan Project in Fuel Cell Manufacturing [14]. The report lists several key drivers that influence the cost of the fuel cell stack shown in Figure 5.1, where the catalyst, bipolar plates, and GDL account for 70% of the total stack cost. Identifying the key cost drivers provides a direction where the efforts in improving manufacturing should be focused on. Although the raw materials have a large influence in determining the cost, the majority of the cost is attributed to the manufacturing phase. For example, the production cost break down for the GDL is approximately 33% materials, 17% mixing labor, 33% heat treatment and coating labor, and 17% quality labor [224], which translates to roughly two-thirds direct manufacturing costs. Furthermore, a portion of the the 33% material cost is due to scrap, which is greatly dictated by the manufacturing processes.

The scope and organization for the fuel cell stack manufacturing in this chapter is highlighted in Figure 5.2. The primary focus is in the cell row (emphasize in gray) where the highest costs incur due to the necessary hundreds of cells that contain the expensive materials and components. The manufacturing of remaining components will not be covered, however, are included in the model as purchased (i.e., commodity) parts. In terms of manufacturing processes, it is not possible to cover the entire spectrum of processes that have been proposed, implemented, and hypothesized. Instead, the focus will be on the processes that are considered current state-of-the-art and processes that are said to be used in current production settings. Therefore, much of the prototyping manufacturing process will not be

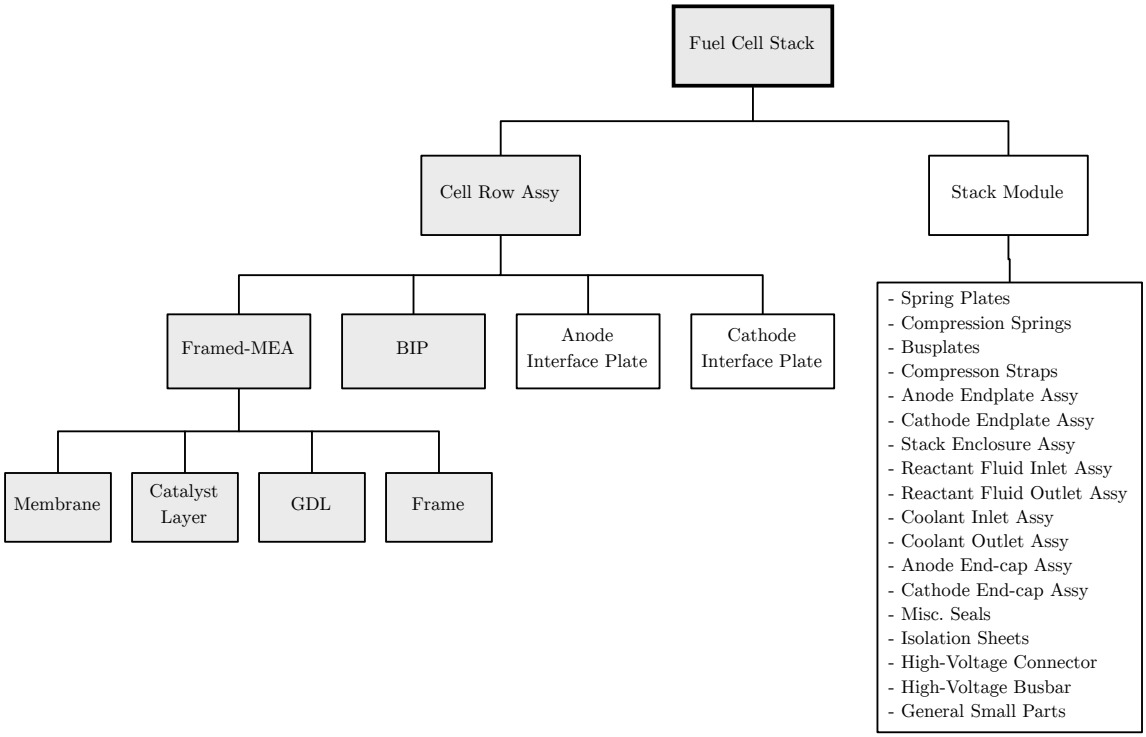

Figure 5.2: Fuel cell components covered for manufacturing

considered even at low volumes. For example, the MEA can be prepared by hand by manually cutting and hot pressing the layers together [347], which is acceptable at the prototyping volumes, but becomes rapidly unpractical and cost prohibitive post prototyping. It should be mentioned that due to proprietary reasons, the specifics of Daimler's manufacturing processes will not be pointed out. However, the range of technological processes covered do overlap with Daimler's current manufacturing practices.

5.1 Membrane

In the previous chapter it was stated that the most effective and widely used membrane technology for PEM fuel cells were perfluorinated ionomer membranes, specifically perfluorosulfonic acid (PFSA) based membranes. Among the PFSA based membranes, DuPont's Nafion® is the industry standard and will be the primary focus for membrane manufacturing. Nafion® membranes can be further categorized into two types: non-reinforced and reinforced. Non-reinforced membranes are based entirely on the Nafion® PFSA polymer while reinforced membranes include a porous polymer matrix, typically PTFE based, that is impregnated with Nafion® ionomer in solution form. A comparison of various commercially available Nafion® membranes is shown in Table 5.2.

Table 5.2: Commercially available Nafion® membranes [181].

Membrane	Thickness	EW	Ionic Conductivity	Conductance
Nafion® 112	60	1100	0.10	17
Nafion® 117	200	1100	0.14, 0.10	5-7
Gore-Select®	5	1100	0.028	56
Gore-Select®	12	900	0.096	80
Gore-Select®	20	1100	0.052, 0.053	26

Manufacturing of non-reinforced membranes are further divided into two processes: extrusion and dispersion cast. Polymer extrusion of non-reinforced Nafion® membranes represent the oldest processing technology and have been replaced for high performance applications. The extruded membrane manufacturing process was originally developed as "thick" films, typically greater than 125 micron, for maintaining mechanical stability [14]. The extrusion process involves melt processing Nafion® resin (DuPont R-1100 or R-1000) in sulfonyl fluoride form into thin sheets followed by hydrolysis and an acid exchange step. Dispersion cast is considered the newer generation of non-reinforced Nafion® membranes, taking advantage of high volume roll-to-roll production (high production rates compared to extruded films). Thinner films, thin as 5μm, can be formed by casting a solution of dispersed Nafion® in PFSA form (i.e., DuPont D520/521) onto a backing layer. Commercial products provided by DuPont in the Nafion® family are N-11X for extrusion cast and N-21X for dispersion cast, where X denotes the thickness in mils.

Nafion® membranes with a porous polymer reinforced matrix represent a relatively newer membrane technology type. Improvement to the mechanical properties and performance of convention cast membrane can be made by including a PTFE polymer matrix. Specifically, expanded-PTFE (ePTFE) is preferred due to relatively high mechanical strength and higher porosity than conventional PTFE. Processing involves impregnating the ePTFE matrix with Nafion® ionomer solution. The manufacturing processes for dispersion cast and ePTFE reinforced Nafion® membranes are be considered.

Dispersion Cast Nafion®

A manufacturing process flow for dispersion cast Nafion® membrane has been proposed in a subcontract study by Tiax LLC. Their process flow is primarily based on two key patents - DuPont's U.S. Patent No. 6,552,093 and Ion Power's U.S. Patent No. 6,641,862 for dispersion cast films [42]. An overview of the process flow is shown in Figure 5.3.

A liquid dispersion solution consisting of PFSA Nafion®, water, and isopropanol is coated onto a thin-film polymer backing layer of either PTFE or silicone-treated PET. The backing layer's low surface tension is necessary to peel off the membrane and often times a surfactant is added to the dispersion solution to further reduce the surface tension and promote even

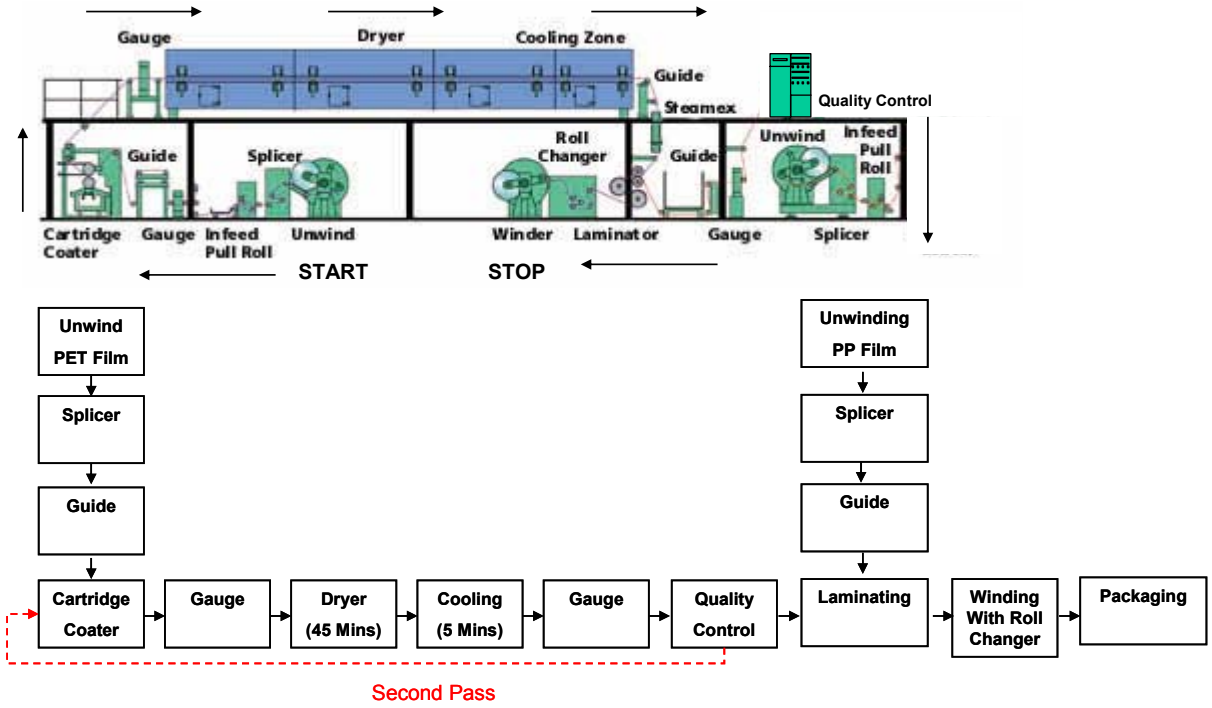

Figure 5.3: Roll-to-roll cast PSFA membrane manufacturing [42]

distribution of the film [42]. The process is perform on a continuous web at speeds ranging from 1ft/min to 20ft/min depending on production volumes and equipment size. Coating of the dispersion solution onto the backing layer is typically performed using a knife coater (e.g., using a doctored blade) or slot-die coater to a wet thickness of 2.5mil to 8mil. The coated film is dry and cured by passing through 3-staged heating ovens. The first stage evaporates the water and isopropanol at a temperature less than 100°C to prevent coalescence followed by a second and third stage heating at above coalescence temperature for curing and cooling. The multi-stage heating is believed to increase the quality of the film by fusing the PFSA polymer particles and thus forming a film with similar properties to an extruded film [42]. The coating and heating steps may be performed multiple times (typically at least twice) to achieve the desired thickness. The final stage post quality control is lamination with a polypropylene (PP) coversheet for packaging into rolls. The entire manufacturing process is requires a cleanroom environment of class 10,000 (ISO 4) to prevent particulate contamination [42].

Reinforced Nafion®

The introduction of cast Nafion® membranes have significantly improved cell performance by enabling thinner dimensions for reduced ohmic losses and improved hydration. However, the existing cast technology is limited to the extent in which such membranes can be thinned due to reactant cross-over, durability, and manufacturability [181]. These issues could be

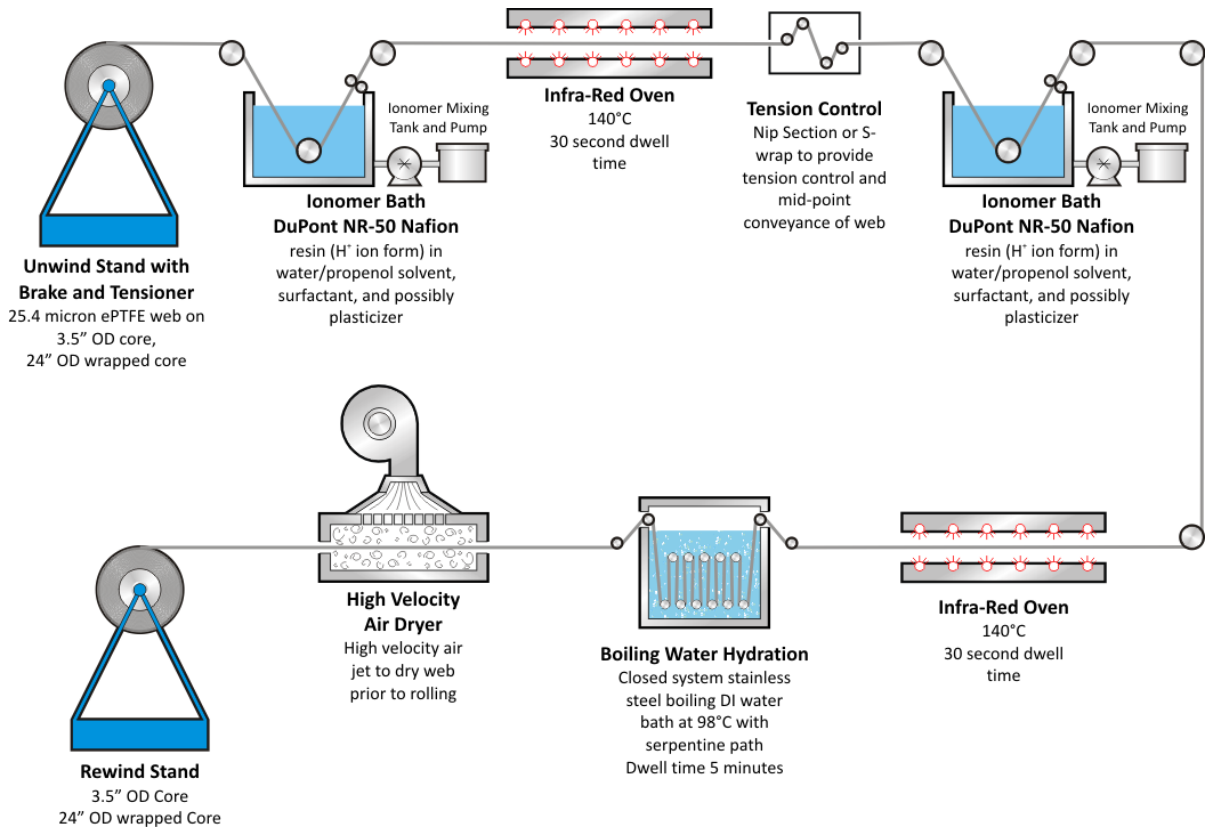

Figure 5.4: Roll-to-roll reinforced PSFA membrane manufacturing [160]

partially alleviated by providing a reinforced substate matrix such as woven PTFE, however, at the cost of increased thickness. The most promising solution is the use of expanded-PTFE (ePTFE), a highly porous (>90%) variation of PTFE by traverse and longitudinal expansion. Such membrane is described in the U.S. Patent No. 5,547,551 by W.L. Gore & Associates (also commercially known by Gore as Gore-Select®) [16]. The ePTFE substrate provides substantially superior mechanical properties over cast films thereby enabling thinner membranes and faster roll-to-roll processing. A proposed process flow for ePTFE reinforced Nafion® membranes has been developed by Directed Technologies, Inc. [160] and is shown in Figure 5.4.

The membrane production involves a two stage Nafion® impregnation process in which the ePTFE web is immersed into a Nafion® ionomer solution to fill the interior volume of the ePTFE. The Nafion® solution typically consists of 95vol.% PFSA resin solution (which itself is comprised of 5% PFSA resin, 45% water, and 50% low molecular weight alcohols) and 5% nonionic surfactant [16]. Post oven drying stages, the Nafion® filled membrane undergoes a hydration process in which the membrane is swelled with distilled water. Due to the added mechanical strength of the ePTFE substrate, processing speeds can vary from 5m/s and up to 35m/s, a significant improvement over dispersion casting [160]. Similar to the cast

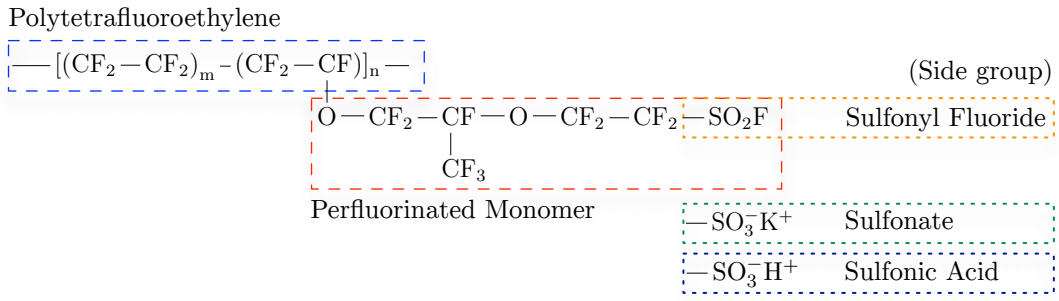

Figure 5.5: Chemical structure and the various forms of Nafion®.

film process, a coversheet and/or backing layer can be incorporate to protect the membrane during package and a class 10,000 cleanroom is required.

DuPont Nafion®

The production of Nafion® is relatively complex involving the synthesis of the perfluorinated vinyl ether monomer with the copolymerization of tetrafluoroethylene and final sulfonation steps to obtain the appropriate PFSA form [116]. The chemical formula for Nafion® was previous introduced in Chapter 4 and will be described in further detail to determine the production process. The chemical structure of the Nafion® ionomer is broken down into three distinct regions as shown in Figure 5.5. The first region is the polymerization of tetrafluoroethylene (TFE) to form a polytetrafluoroethylene (PTFE)-like backbone with repeatings units of m=6-7 and n=100-1000. The PTFE provides resistance to chemicals and corrosion while stabilizing the polymer to temperatures up to 160°C [29]. Branching off from one of the TFE molecules is the second region, a perfluorinated vinyl ether side chain containing a, third region, sulfonyl halide functional group to form the perfluorinated vinyl ether monomer [116]. The type of sulfonyl halide function group, $R{-}SO_2{-}X$, determines the variation of the Nafion® ionomer. In its original form, the halogen atom and the Nafion® ionomer is sulfonyl fluoride, a thermoplastic that can be extruded into thin-film sheets [211]. To obtain the PFSA form for hydrogen conduction, the fluorine atom is first replaced with a sodium ion, Na^+, yielding the sulfonate form, then through hydrolysis with an acid to obtain PFSA.

A detailed process on the production of PFSA Nafion® is described. The process begins with the synthesis of gaseous hexafluoropropylene (HFP), C_3F_6, from TFE, C_2F_4. A patent from DuPont, U.S. 3,873,630, describes a process involving the pyrolysis of TFE at temperatures from 700°C to 900°C and pressures of 0.75 to 2.0 atm (absolute) [343]. The conversion consumes three moles of TFE to produce two moles of HFP:

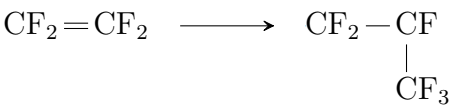

The pyrolysis is facilitated by mixing small amounts of CO_2 and continuous feeding hydrogen chloride, HCl, at low flow rates to prevent spontaneous polymerization of TFE. The patent claims TFE utilization or conversion ranges from 20% to 80% with HFP yields ranging from 80% to 90wt.%.[1] Unreacted TFE and CO_2 can be reclaimed or recycled via distillation after using a water-scrubber to remove the HCl [343].

The synthesis of HFP is used to produce hexafluoro propylene epoxide (HFPO), a key monomer for fluorocarbon and perfluorinated polymers. HFPO can be synthesized by the epoxidation of HFP using hydrogen peroxide at temperatures below 0°C or with oxygen at 100-200°C [116]:

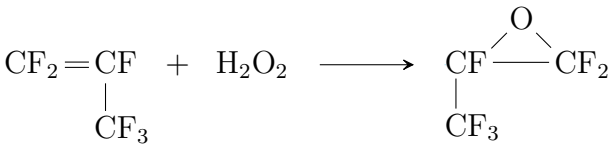

According to the patents, U.S. 3,358,003 and U.S. 3,536,733 by Dupont, there are numerous variations and methods for synthesizing HFPO, all of which are based on the reaction of HFP. The exact production details of HFPO are, not surprisingly, proprietary and depending on the type of oxidizing agent, epoxidation can be classified as a nucleophilic, electrophilic or radical reaction [220]. The most straightforward process appears to be nucleophilic synthesis from Example IV of U.S. 3,358,003 where hydrogen peroxide is used as the epoxidation agent. The described example (at laboratory scale) used a reaction vessel containing 750ml of methanol, 84 grams of potassium hydroxide (KOH) dissolved in 150 ml of water, and 525 ml of 30% concentration hydrogen peroxide (H_2O_2). After the reaction vessel was cooled down and maintained at -40°C, 80 ml of liquid HFP was added and mixed for 1.5 hours. The resulting reaction yielded 65% HFPO and 35% of unreacted HFP [95]. Although the patent does not specify, it is assumed that a large portion of the unreacted HFP can be recycled for continuous production.

Another key component to the synthesis of the perfluorinated vinyl ether monomer is the addition of the sulfonyl fluoride using a perfluorinated acid fluoride. The synthesis begins with the reaction of TFE and sulfur trioxide, SO_3, forming TFE sultone. The reaction is highly exothermic and improper control of the reaction conditions may lead to explosions and the release of carbonyl fluoride, which is highly toxic [116].

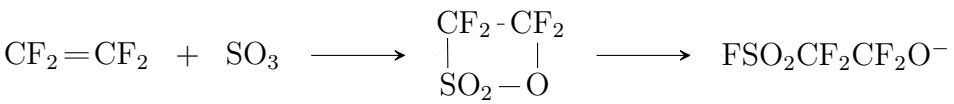

The synthesis of the sulfonyl fluoride side group involves rearranging the chemical structure of TFE sultone using fluoride ions, F^-, such as from cesium fluoride, CsF. The fluoride

[1] Some of the TFE is converted to carbon tetrafluoride and carbon [343].

ion acts as a catalyst by attaching to the sulfur dioxide molecule thus creating a perfluorinated alkoxide anion.

The perfluorinated acid fluoride TFE sultone is converted to the perfluorinated ionomer by the addition of HFPO. During synthesis, one mole of the perfluorinated alkoxide anion attaches itself to one mole of the central carbon atom of the HFPO molecule creating a mono adduct. The reaction is relatively favorable until the point where the affinity to HFPO is the same as to the fluoride ion [116]. A second mole of HFPO reacts with the mono adduct by the same catalytic mechanism using the fluoride ions forming a di-adduct. The addition of an addition mole causes phase separation and creates two layers of high and low molecular weight fluorocarbons.

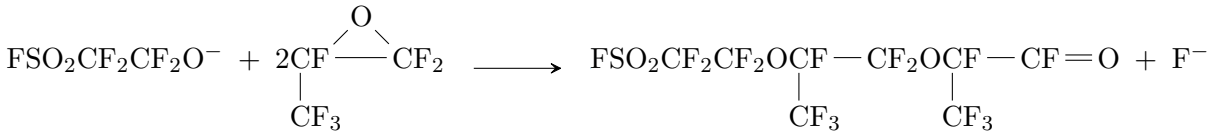

It is preferable to stop the reaction after relatively low conversions of mono adduct to di-adduct to avoid HFPO from further catalyzing. Exaction of the di-adduct can by performed via distillation of the lower layer caused by the phase separation, which contains less catalyst and mono adduct. The remaining mixture (i.e., upper layer) can be recycled for the next batch [116]. A suitable process for the di-adduct synthesis is explained in the DuPont patent, U.S. 3,301,893. The patents states 2.9g of dry cesium fluoride was placed into a clean, dry flask and placed under a vacuum in an ice bath. Injected into the flask was 40ml of dry dimethyl ether of diethylene glycol and 50g of TFE sultone. The flask was then opened and 115g of HFPO was added followed by pressurizing the flask to 4 psi(g). The complete synthesis occurred within 30 minutes and the lower layer residue of 158g was removed and distilled. The residue contained 40g of the di-adduct polymer along with higher molecular weight polymers [260].

At this stage, synthesis perfluorinated vinyl ether monomer is nearly complete. The di-adduct monomer is reacted with a weak acid containing an oxygen abundant sodium or potassium salt. Any salt of a weak acid is suitable with sodium carbonate, Na_2CO_3, being a common choice [117]. The synthesis can be performed by passing the vapors of di-adduct through a heated, packed bed of pellets of sodium carbonate at 300°C [116].

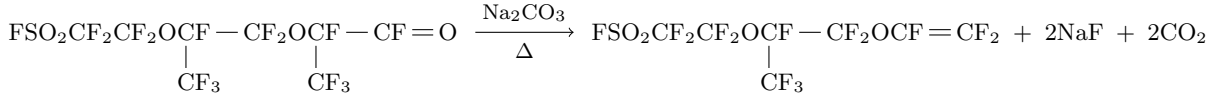

Copolymerization of the perfluorinated monomer with TFE produces the Nafion® ionomer with the sulfonyl fluoride side group. The copolymerization is held in an autoclave, pressurized with TFE and continuously agitated with an initiator such as ammonium persulfate and a perfluorinated surfactant. The level of TFE pressure determines the equivalent weight (EW) of the final percusor polymer where higher pressure increases the EW [116]. Depending

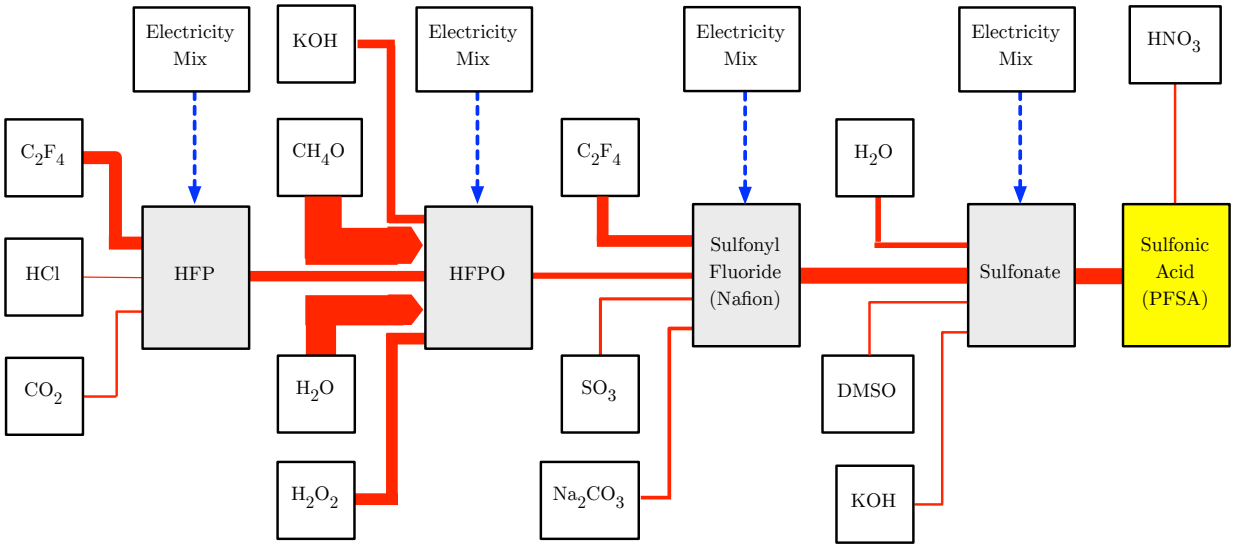

Figure 5.6: Material process flow for Nafion® and PFSA Nafion®.

on the process conditions the final Nafion® polymer has properties of m=6-7 and n=100-1000 [133].

The Nafion® precursor in the sulfonyl fluoride form does not have the cation-exchange capabilities for a useful ionomer. The conversion to sulfonate, a cation sulfonic functional group, involves the hydrolyzing the precursor in a hot solution bath of sodium (NaOH) or potassium hydroxide (KOH) [117]. A typical bath composition may consist of 15 wt.% KOH and 50 wt.% deionized water with optionally 35 wt.% dimethyl sulfoxide (DMSO) for increasing the rate of hydrolysis. The reaction is carried out at 80°C for 30 to 60 minutes or longer depending on the membrane thickness [73].

The final stage involves converting the sulfonate variation of Nafion® into an acid exchange or PFSA. As the name suggest, the sulfonate is soaked in an acid bath of either sulfuric acid (N_2SO_4), nitric acid (HNO_3) or hydrochloric acid (HCl) [44]. This process is typically performed immediately following the initial cationation of Na^+ or K^+. One U.S. patent, U.S. 2003/0204323, uses 2M H_2SO_4 to soak the Nafion® for 24 hours [225], while an European patent, EP1964874, uses a solution consisting of 15% to immerse HNO_3 under 80°C for 1 hour and is repeated at least three times to ensure proper conversion [44]. The advantage of processing with nitric acid is that standard stainless steel equipment can be used [116]. An overview of the entire process and relative mass flows (thickness of flow arrows) is shown in Figure 5.6.

5.2 Catalyst Coated Membrane

The manufacturing of the CCM is typically performed as a two-stage transfer coat process. The first stage is preparing the catalyst electrode onto a removable backing layer film using a wet or dry (e.g., NSTF) type process and the second stage is the transfer of the catalyst electrode to the membrane using a hot press or lamination technique. Depending on the design requirements of the fuel cell stack the catalyst electrode preparation may be two separate processes for different anode and cathode catalyst loadings. An alternative structure the CCM is the GDE where the catalyst electrode is directly coated onto the gas diffusion layer. Doing so eliminates the transfer stage thus simplifying the manufacturing. However, due to cell performance limitations at high power, the GDE structure has been disregarded for automotive applications [351].

Besides the conventional transfer coat process, there are processes being developed for direct coating onto the membrane or an in-situ layering process of the CCM. Direct methods are typically dry process involving thin-film deposition methods such as PVD, sputtering, and ion-beam assisted deposition [61]. The technology has been considered for nearly a decade and is still currently being researched for deposition quality and membrane stability and lifetime. A relatively nascent and upcoming process is the in-situ layering, which is a wet process that builds each layer vertically using a roll-to-roll process. The process begins with a the wet or dry coating of the catalyst layer onto a backing layer and dried. On the same roll post drying, liquid Nafion® is coated onto the catalyst layer and dried. Lastly, the second catalyst electrode layer is deposit on the Nafion® and dried to form the complete CCM structure. This process has been demonstrated by Gore & Associates, Inc [37] and in the DuPont patent U.S. 7,316,794 [241]. Although the layering process appears to be a viable technology that may potentially lower CCM cost, it will not be considered due to being in the infant stage.

The quality of the transfer coat process is dictated by the coating technology. For wet processes slot-die coating has been shown to be viable for high production processing, yielding uniform coats and high material utilization. Other wet processes that are suitable technologies, but will not be considered, are knife or doctor, roll, and spray coating. For dry processing, only the NSTF structure will be considered using a physical vapor deposition technique.

Slot-die Coating

The key components of the slot-die coating method are 1) the catalyst ink solution, and 2) the slot-die coater. Proper processing of the catalyst ink solution is crucial for controlling the quality of catalyst bound to the carbon particle support for high catalyst utilization. One potential process for dispersing platinum onto carbon power is the chloroplatinic acid (CPA) precipitation method [159]. Preparation of the CPA involves dissolving platinum sponge into a 4:1 mix of hydrochloric acid (HCl) and nitric acid (HNO_3) forming a mixture called "aqua regia." The aqua regia is then precipitated onto carbon powder (e.g., Vulcan XC-72)

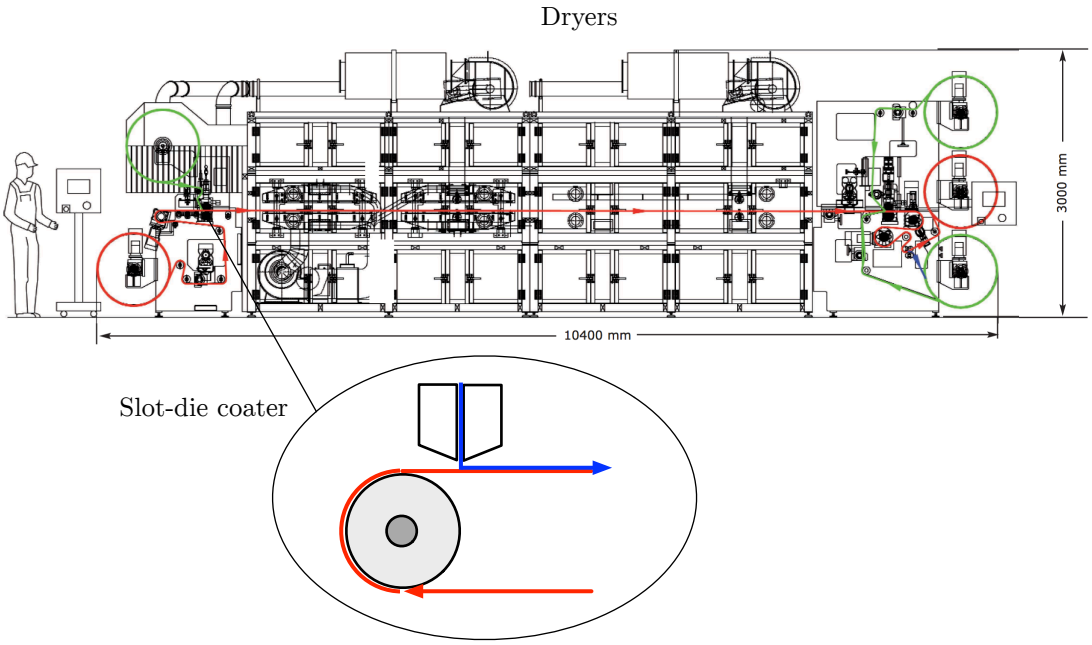

Figure 5.7: Roll-to-roll CCM slot-die coater (Coatema Linecoater [180]).

thereby creating the carbon-supported platinum catalyst with a mass ratio of 60% carbon and 40% platinum. The final step is mixing of the catalyst-carbon powder with an ionomer solution (typically 5wt.% PFSA Nafion) and a solvent mixture of methanol and de-ionized water using blade mixing, or rotary bill milling, or more commonly, ultrasonic mixing [159]. Considering that the catalyst is the most expensive material in the MEA careful preparation is taken when mixing the catalyst ink to minimize scrap.

The catalyst ink is coated onto a sacrificial substrate film using a slot-die technique. Common substrate films include Kapton and perfluoroalkoxy (PFA), both manufactured by DuPont [258]. At low production volumes the catalyst ink is manually mixed and added to the machine and is converted to automated mixed and pumping at high volumes [14]. Design and process control of the slot-die apparatus is critical for maintaining an uniform film. The coating is highly dependent on the viscosity of the solution, coating pressure, and line speed of the web. Figure 5.7 shows a schematic of the roll-to-roll Coatema Linecoater series slot-die coater.

The coating process has be described in the U.S. Patent No. U.S. 2009/0169950 by DuPont where the continuous substrate film passes through the slot-die coater (opening thickness of 178 microns) followed by a series of drying ovens at temperatures between 27°C and 71°C [258]. Alternatively, the coating can be patterned in a patch such that only the required size of the cell is coated to minimize ink loss. Typical processing parameters include line speeds of 0.2 - 8m/min and line widths up to 1m [159]. To enable higher production throughput, inline inspection is incorporated, which typically includes X-ray fluorescence

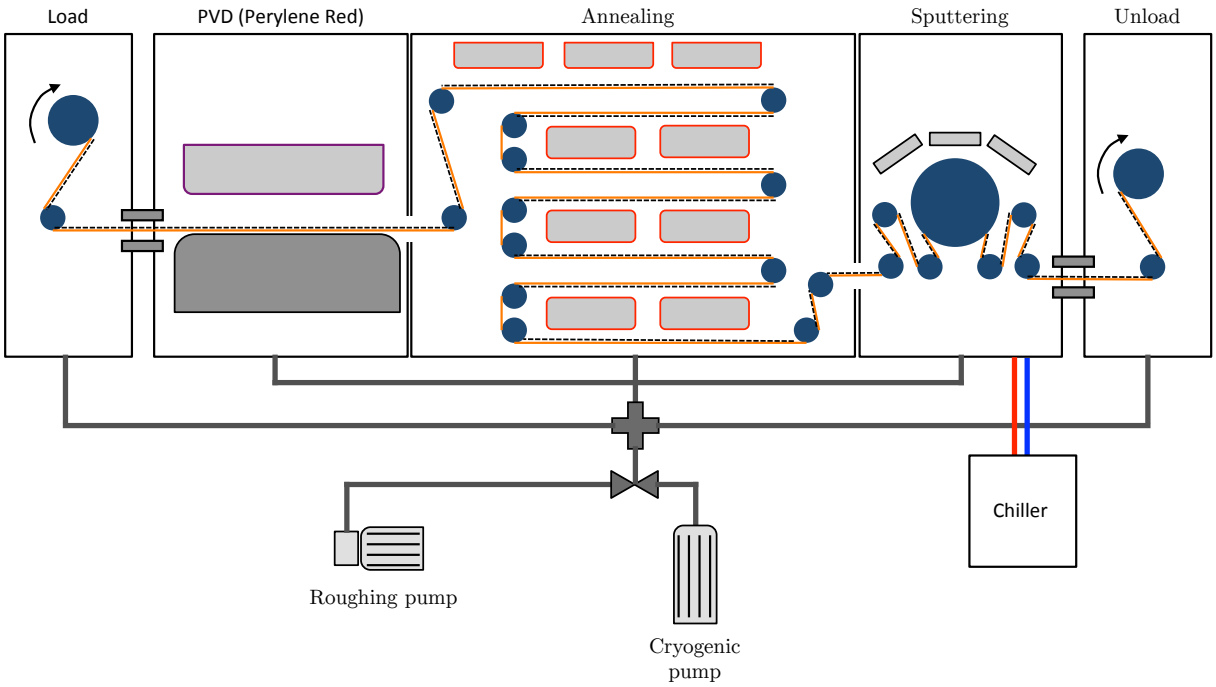

Figure 5.8: Roll-to-roll NSTF processing. Based on [160].

(XRF) and/or beta backscatter gauges [14]. The resulting catalyst electrode has a typical dry thickness (catalyst loading dependent) of 7.6 microns for the cathode and 2.5 microns for the anode [258]

NSTF

The inherent difference between the NSTF catalyst and conventional carbon-catalyst are the material of the support structure in which the catalyst adheres to and the method of the catalyst deposition. The most effective NSTF support structure is a crystalline organic pigment material referred to as perylene red (PR) and carries the shape in the form of whiskers that grow perpendicular to the film surface [64]. The whiskers have aspect ratios (length/width) on the order of 20 to 50 with an average cross-sectional diameter of 75nm and areal densities of 3 to 5 billion cm^{-2} [62]. The primary processing method for forming the initial PR film is using vacuum deposition, a dry process that can include physical vapor deposition (PVD) such as evaporation, sublimation and sputtering, and chemical vapor deposition (CVD). Immediately proceeding the deposition is a thermal annealing step that converts and orientates the film into the whiskers via a screw dislocation growth mechanism [64]. Post formation of the whiskers, deposition of the nano-particle catalyst can be performed using a conventional sputtering technique. Figure 5.8 illustrates a possible roll-to-roll configuration for depositing and growing the PR whiskers followed by sputtering of the platinum catalyst.

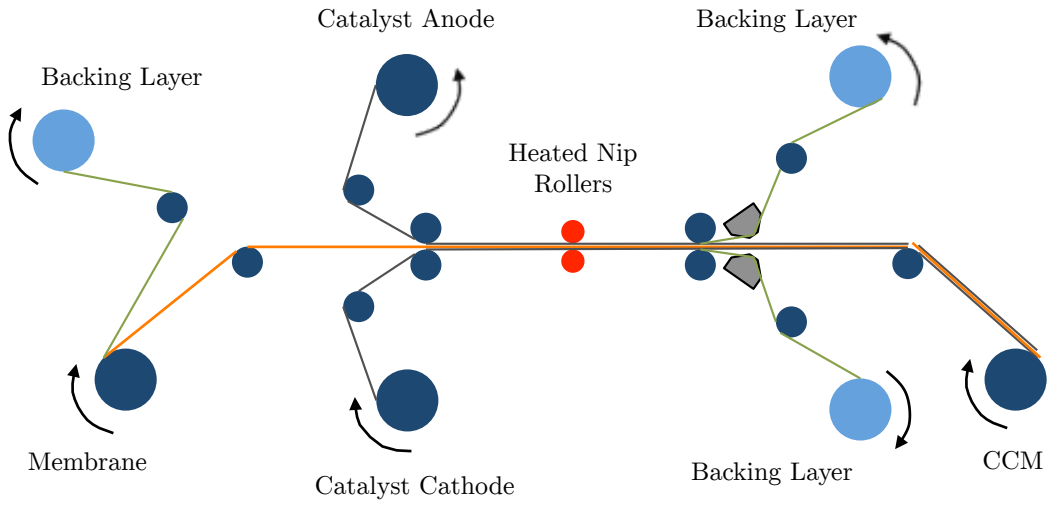

Figure 5.9: Roll-to-roll CCM anode and cathode decal lamination

Details of the NSTF process are as follows. A temporary deposition substrate (typically Kapton® polyamide web by DuPont [160]) is line fed from the load to unlock dock. The entire system is pumped down to pressures $<2\times10^{-6}$ Torr, which is necessary for deposition of the PR, thermal annealing, and sputtering of the catalyst. Perylene red in the form PR149 is first PVD deposited onto the Katon web via sublimation with depositions rates varying from 20 to >40nm/min and at temperatures >400°C [65]. The deposited PR149 undergoes thermal annealing for roughly 10 minutes or depending on the film thickness and at temperatures between 200-300°C to form the nanostructured whiskers [64][160]. The final stage is the deposition of the platinum nano-catalyst using magnetron sputtering at deposition rates of roughly 2.5nm/s or depending on the desired platinum loading. Since setup and pump down of the entire system can be time consuming it is recommended that large roll lengths up to 1500 meters are used [160]. For higher productivity an *in situ* optical inspection system may be implemented. The entire roll process is in a cleanroom environment.

CCM Lamination

The final procedure of the CCM is the application of the anode and cathode catalyst layer on to the membrane. For roll-to-roll processing the most effective method is a decal transfer process using hot lamination. Various configurations includes inline lamination with the slot-die coater, however, because the anode and cathode typically possess different catalyst loadings it is often more practical for the lamination to be a separate step. A method for the decal transfer process has been described in the U.S. Patent No. U.S. 2009/0169950 by DuPont [258], which is illustrated in Figure 5.9.

The three thin film rolls - membrane, anode and cathode catalyst layer, are guided through a series of rollers in which the exposed catalyst layers mate the topside and bottom

of the membrane. The protective backing layer of the membrane is peeled and round onto a spool while the membrane is sandwiched between the catalyst layers. The substrate backing film on the catalyst layers protect the CCM as it passes through a pair of heated rubber coated nip rollers. The patent U.S. 2009/0169950 suggested a lamination temperature of 140°C and pressure between 620-690kPa [258]. The lamination will cause a very small fraction of the catalyst layer to be embedded into the membrane. The resulting CCM assembly can be round up for package or, more commonly, the catalyst layer substrates are peeled away using peel-bars for easier processing of the MEA. Processing lines speed can vary widely with a speed of 0.4m/min claimed by the aforementioned patent and up to 5.84m/min [160]. Inspection of the CCM is crucial for quality control and can be automated via inline optical inspection or manually post processing. The entire process is performed in a cleanroom environment.

5.3 Gas Diffusion Layer

Modern day media for the gas diffusion layer (GDL) employs a carbon fiber paper based substrate treated with PTFE as previously introduced in Chapter 4. The manufacture of the GDL can be divided into four stages: carbon fiber formation, carbon fiber paper making, bulk PTFE treatment, and the optional coating of the microporous layer (MPL). The stages leading up the bulk PTFE treatment form what is called the macroporous layer and is sometimes used synonymously with the GDL. Depending on the degree of vertical integration, the macroporous layer can be purchased through a supplier and MPL coated in house or purchased.

Historically, due to low volumes, the macroporous layer was manufactured using discrete, sheet-by-sheet processing where rolls of carbon fiber paper would be trimmed into sheets and coated individually. This method proved to be highly labor intensive and have low yields and ultimately not cost effective for high volume production [298]. Conversely, modern GDL manufacturing is entirely roll-to-roll based processing with state-of-the-art systems processing at line speeds of 10-20m/min [293][207] and employing continuous mixing, multilayer coating, and automated visual inspection, which reduces handling and setup time and is more consistent in quality [224]. The capital expense for such roll-to-roll processing can be quite high, reaching over an estimate $11 million USD (in 2010) for a 2 meter wide system that excludes the manufacturing of the carbon fiber [293]. Production scale carbon fiber systems can reach an investment of $15-$45 million USD [4], which become uneconomical for in house production.

Macroporous Layer

Various works [207][293][14] have previous outlined the manufacturing process for the macroporous layer and will be summarized in this section. Figure 5.10 outlines the flow chart from polymer processing of the carbon fibers to the final bulk treatment of the macroporous layer.

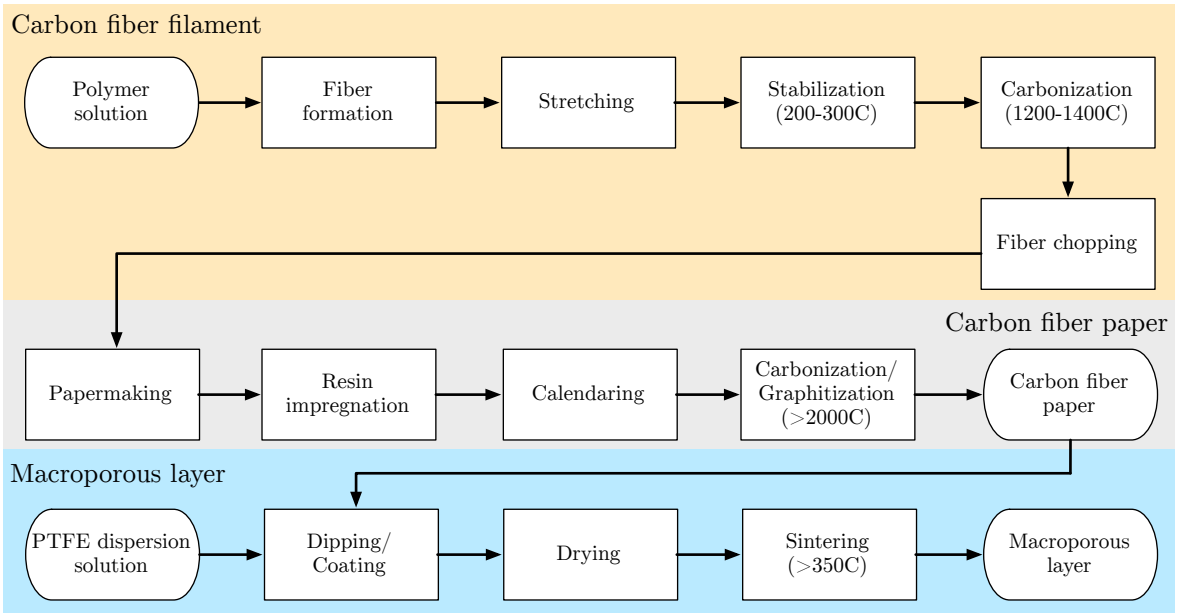

Figure 5.10: Process flow from carbon fiber to macroporous layer production

Each of the three stages can be manufactured as a separate commodity or continuously as one product.

The process begins with formation of the carbon fibers with the most popular choice being a copolymer comprising of greater than 90% polyacrylonitrile (PAN) [207]. A solution consisting of PAN, water, and dimethyl sulfoxide (DMSO) is filtered and forced through a spinneret (hundreds orifices with diameters on the order of tens of microns) where the continuous nascent fibers are collected and washed [297]. Post drying, the fibers are stretched via differential roller speeds and then stabilized in air to transform fibers from a thermoplastic to a thermoset thereby preventing degradation of the fibers in the subsequent thermal processing. The last procedure is a carbonization step where the carbon fibers are heated to 1200-1300°C in a nitrogen rich environment. The carbonization causes the fibers to lose approximately 50% of its initial weight and yielding a fiber with >95% carbon content [207].

The second stage is the formation of the carbon paper substrate using a similar wet-laid papermaking process as the fourdrinier machine for conventional papermaking. Carbon fibers are chopped into lengths of 3-12mm and dispersed and continuously mixed in a solution consisting of water and binders such as polyvinyl alcohol. The solution is poured onto a rotating porous drum or on a conveyor wire screen with a vacuum dryer to remove the water. The resulting web is dried through a series of rollers leaving a binder content of roughly 5-15wt.% [207]. The final steps involve impregnation with a carbonizable resin, typically phenolic resin due to high carbon yield and low cost, to provide stiffness and formability. Post heating that evaporates the solvent, the resin impregnated carbon fiber composite is feed through a heated calendaring process to achieve the desired thickness and density

(alternatively, compression molding can be used for batch processing). The final form of the carbon fiber is achieved after an additional carbonization and graphitization step by first ramping to below 1000°C to decompose the phenolic resin and then over 2000°C to convert the fibers from amorphous carbon to crystalline lamellar graphite. The composite loses about 30-40% of its initial weight and thickness an yielding over 99% carbon content. The graphitization gives the final carbon paper an increase in electrical and thermal conductivity [207].

The final stage for the macroporous layer is the bulk treatment of PTFE for enhanced water management. Depending on the design of the fuel cell the PTFE loadings for the anode and cathode may be different. However, for simplicity and robustness, the two GDL types are typically the same. PTFE dispersions is applied onto the carbon fiber paper using in a variety of ways, most commonly by a dipping into a bath, but can also be brushed or sprayed on. Post drying, the PTFE coated carbon fiber paper goes through a sintering process where the concentration of PTFE is highly dependent on the heating rate. A rapid treatment tends to have a high PTFE concentration on the surface while a slow diffuse heating will yield a more uniform distribution through the carbon fiber paper. The resulting PTFE loadings typically fall between 5-30% [207].

Microporous Layer

The macroporous layer provides enough conductivity and water management to be used in fully functional fuel cell. However, the addition of the MPL drastically increases the performance by reducing the contact resistance between the catalyst layer and macroporous layer as well as further enhancements in the water management [247]. A mixture of carbon or graphite powder and PTFE dispersion, typically 50/50wt.% [293], is coated onto the surface of the macroporous layer that contacts the catalyst layer. The coating can be applied with various methods including doctor blading, screen printing, spraying, and rod coating [207]. The carbon powder increases the conductivity while the enhanced water management is due the the MPL having pore sizes is on the order of the carbon agglomerates, between 100-500nm versus 10-30μm in the bulk substrate. Post MPL application, the solvent in the dispersion solution must be evaporated slowly to prevent cracking. An optional calendaring step can be incorporated to further fuse the MPL to the macroporous layer. The final sintering step leaves the MPL to be typically less than 50μm thick [207].

The entire MPL application process can be preformed roll-to-roll with an approximate capital expense of $1.3 million USD (of 2010) yielding in output line speed of up to 10.2 m/min [160]. Figure 5.11 shows the process flow applying the MPL to the final GDL.

5.4 Membrane Electrode Assembly

The assembly of the MEA layers (GDL, catalyst layer, and membrane) has historically garnered less attention than the layers themselves. This is due to the relatively low contribution

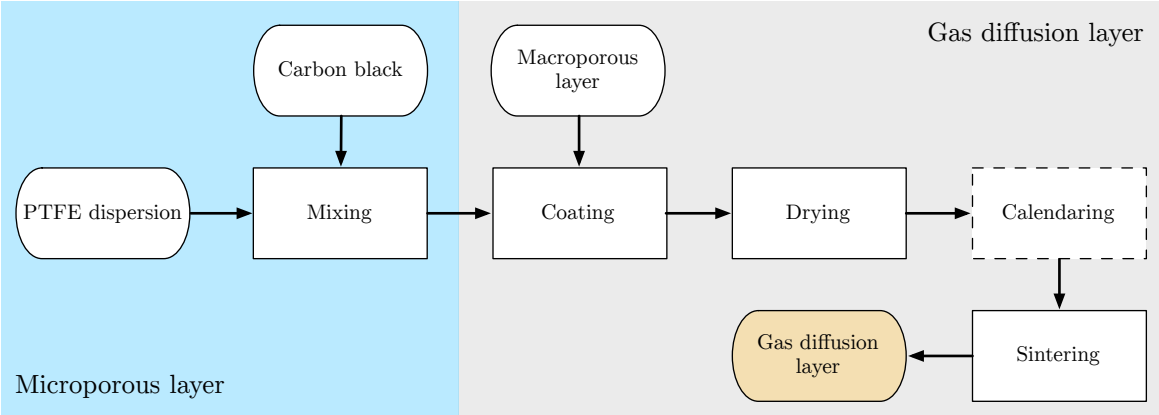

Figure 5.11: MPL manufacturing and coating onto the GDL

to the overall manufacturing costs (roughly 5% at low volumes [160]) of the PEM fuel cell stack. Nevertheless, the materials and manufacturing are key considerations in terms of MEA reliability and lifetime. For instance, the degradation and dissolution of silicone in the edge-seal technology or membrane electrode sealed assemlby (MESA) may diffuse and poison the catalyst or delamination may occur from excess compression [355]. The focus, as mentioned in Chapter 4, will be strictly on the MESA and MEFA technologies as they are the most representative of the industry for automotive applications.

There are two stages in assembling the MEA structure. The first stage involves combining the anode and cathode GDL with the CCM to form the 5-layer sandwiched MEA and the second stage pertains to the sealing. The conventional method for joining the MEA layers is through a batch process where individual sheets on the order of the cell size are joined together using a hot pressing technique or with adhesives. Hot pressing is the most straightforward method and has been cited by numerous sources and from various U.S. and European patents [309][177][179]. The basic concept is to fuse the surface of the membrane to the catalyst/GDL layers by softening the membrane. This method works particularly well with the GDE structure where the catalyst layers is coated onto the GDL as opposed to the membrane.

For proper fusing of the layers it has been recommended to control three key hot pressing parameters: temperature, pressure, and press time [178][20]. At too low temperatures, the Nafion® (glass transition temperature of approximately 150°C) will not flow and if the temperature is too high the membrane runs the risk of drying out. Alternative methods for prevents membrane dehydration is to use a “stream press” technique in which the membrane is soaked and sealed in water such that he hot pressing is in the presence of pressurized steam. Recommended ranges are temperatures between 120-160°C, pressure of 5-15MPa, and process time of 1-5 minutes [178]. Another source performed a design-of-experiments to determine the optimal values of temperature, pressure, and press time. The study found, that at least for the described setup, the optimal temperature (100-150°C), pressure (2.5-

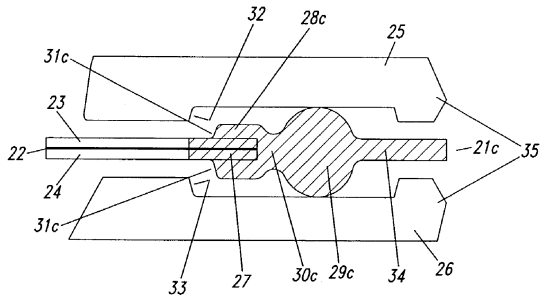

Figure 5.12: Revised edge-sealing design (MESA) [11]

8.8MPa), and press time (1-5mins) was 130°C, 5MPa, and 2mins, respectively [20]. The hot pressing technique can also be performed roll-to-roll as described in [160] where sections of 1.5 meters are hot pressed at a time and cut into individual sheet in the subsequent step.

The alternative bonding technique for joining the MEA layers is to use an adhesive at the outer perimeter of the MEA. The adhesive may be a liquid that is screen printed and oven or UV-cured, or a thin-film double-sided pressure or thermal cured adhesive cut into a picture frame shape [243]. Both adhesive types prove to be adequate, however, the thin-film adhesive creates more scrap since the center cutout is discarded [351] and the screen printing tends to have higher capital cost. The advantage of using an adhesive over hot pressing is to avoid the risk of drying out the membrane. Furthermore, it is more difficult to hot press the GDL to CCM since it would require the fusion between the PTFE of the GDL and ionomer of the catalyst layer or penetration of the carbon fibers through the catalyst layer and into the membrane. However, the drawbacks to the adhesive technology are a higher material cost, loss of active area where covered by the adhesive, add thickness to to the MEA, and potentially expense equipment such as UV-curing. Other nascent bonding technologies include ultrasonic bond where high frequency mechanical energy is used to fuse the membrane and GDE with less energy and lower cycle times [21].

MESA

The introduction of the edge-seal gasket design provided the benefit of a tight sealing while eliminating the issue of having on the order of thousands of o-rings. The original design was simply a beaded edge with partial impregnation into the fibrous GDL. This design proved to be unreliable due cyclic swelling of the membrane thereby causing breakdown and delaminate from the MEA [14]. An improved design by Ballard Power Systems is described in the U.S. patent, U.S. 7,070,876 [11]. To prevent excess stress during compression and swelling, the beaded compression area is extended away from the MEA while a thiner layer of sealant is impregnated in the MEA as illustrated in Figure 5.12.

The proper choice of sealing material is crucial for high throughput, low cost, and minimal contamination impact. In Ballard's patent, it was proposed that capable sealing materials are the elastomer type such as silicones, EPDM, and fluoroelastomers with Shore A hardness

Table 5.3: MEA-gasket materials [160]

Parameter	Generic Silicon	Loctite Silicon	Viton GBL-600S	Viton GF-S	Loctite LIM Hydrocarbon
Density [g/cc]	1.4	**1.05**	1.84	1.92	**1.05**
Cost [$/kg]	14.33	56.70	**36.87**	**36.87**	43.37
Cost [$/L]	20.06	59.54	67.84	70.79	**45.54**
Cure Time [s]	150	540	420	180	**60**
Cure Temp [°C]	**127**	130	177	187	130
Durability [hr]	5,000	5,000	15,000	15,000	10,000
Inj. Pressure	**low**	**low**	mid-high	mid-high	**low**

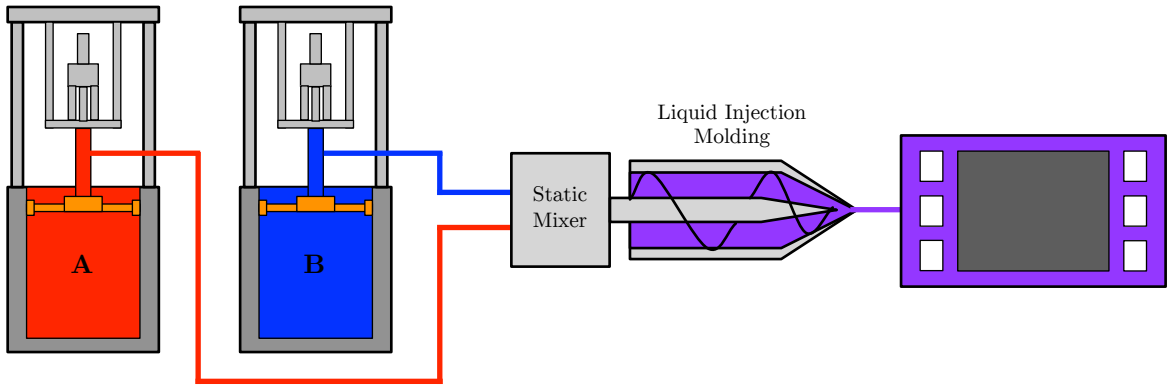

Figure 5.13: 2-component liquid injection molding process for MESA

of about 40 and tension modulus of about 0.2 MPa at 40% strain [11]. Table 5.3 shows a comparison in a report published by [160] that looks at several different elastomers types. The report concludes that the Loctite LIM hydrocarbon (polyacrylate based) is the preferred material (over the silicone and fluoroelastomer materials).

There are limited process tools that can mold the seal structure with sufficient impregnation in the MEA. The most common is to use a liquid injection molding (LIM) machine tool. Figure 5.13 shows the schematic diagram of the LIM seal process with a two component sealing material. The two-component elastomeric material is force feed into the LIM machine and through a static mixer. A more thorough mixing is provide by the screw drive and an injection shot is forced into the mold with the MEA. Depending on the sealing material, the sealed may be cured in the tool or taken out for post curing either thermally or through UV-radiation. Notable drawbacks to this process including handling the MESA during stack assembly and volume production limitations due to batch processing.

MEFA

The boarded or picture-frame MEA or membrane electrode framed assembly (MEFA) is a relatively newer sealing technique aimed to address the cost, degradation (shown to last >20,000 hours) and manufacturability limitations of the MESA structure [14]. The frame is formed by bonding two opposing polymeric thin-film layers that encompasses the edge of the MEA. Alternatively, the frame may first encompass the CCM while the GDL layers are attached by an adhesive. The latter method is typically preferred to avoid the potentially large thickness variation between the edge of the frame and the edge of the MEA.

The choice of frame material is more robust than elastomers, capable of handling higher stresses and temperatures and is more stable in the corrosive environment. A recent paper by [355] lists out the potential candidates to be: polyethylene naphthalate (PEN), polyethylene terephthalate (PET), polytetrafluoroethylene (PTFE), polyvinylidene fluoride (PVDF), ethylenevinylalcohol (EVOH), biaxially oriented polypropylene (BOPP), polyether sulphone (PES), fluorinated ethylene propylene (PEP), polyimide (PI), and so on. More specifically, U.S. Patent US7,267,902 details a polyethylene (PE) frame [36], U.S. Patent, U.S. 2005/026326 incorporates the Dyneon THV fluoroplastic provided by 3M [354], and U.S. Patents U.S. 2011/0123910 uses PEN films with a urethane-based hot-melt type adhesive layer (both 25μm thick) [243].

Assembly of the MEFA typically involved laminating or pressing the two frame films. Processes include pressing (with or without thermal assistance), laser and ultrasonic bonding [351]. At low volumes the stacking of the MEFA and lamination is performed manually and becomes highly labor cost at high volumes. However, the advantage of the MEFA over MESA is the potential for roll-to-roll processing. Various patents have surfaces over the last few years depicting a roll-to-roll MEFA setup such the one shown in Figure 5.14 from the U.S. Patent 8,288,059 by 3M [256]. Rolls of polymeric frame with protective backing layer are fed through a roll punch to expose the active area followed by pealing of the backing layer. A pre-patterned roll of CCM and two sides of the frame film are joined together and laminated to form the framed CCM, which can be rolled or continued onto the application of the GDL. If successfully implemented, the cost of CCM, GDL, and frame assembling would drastically reduce due to much higher throughputs and less labor involved.

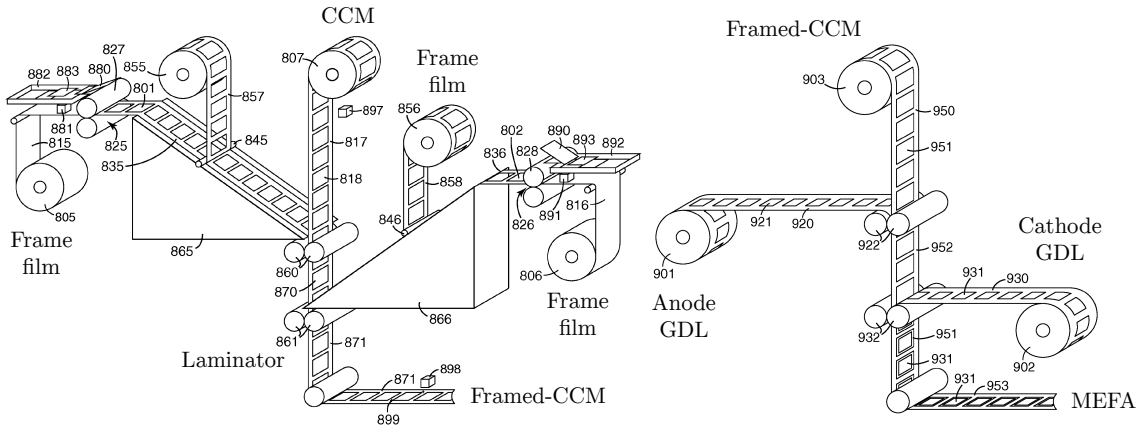

Figure 5.14: Continuous roll-to-roll MEFA process by 3M U.S. Patent 8,288,059 [256].

5.5 Bipolar Plate

The design and manufacture of the bipolar plates (BIP) have garnished a lot of attention due to the high contribution to the overall stack cost and weight. The reason being is simply due to the somewhat stringent requirements for BIP performance. Table 5.4 shows a list of the key characteristics and respective minimum requirements recommended by the Hydrogen and Fuel Cell Program from the U.S. DOE. Out of the characteristics listed, electrical conductivity, mechanical strength, and corrosion resistance have been identified as the three key characteristic that drive the material selection. Addition requirements have been proposed such as rapid manufacturing and low thermal expansion [57].

Numerous studies have focused on BIP material selection and trade-offs between the different materials. As mentioned in Chapter 4, material choices can be classified into two groups[2]: carbon-based and metallic-based plates. The advantage of carbon-based plates is primarily chemical stability in the presence of fuel, oxidant, water and acidic conditions. However, depending the design and materials, carbon-based plates typically suffer from poor electrical conductivity and mechanical strength [57]. The carbon-based plates can be further divided into four types: pure graphite, carbon-carbon, and polymer composites. Conversely to carbon plates, metallic-based plates have very high electrical conductivity and mechanical strength, but suffer from poor corrosion resistance. Metals that meet the corrosion requirements such as titanium are often cost prohibitive. To overcome the corrosion limitation, a corrosive resistant and conductive coating is deposited or grown on to the surface of the plate.

The choice of material selection dictates the manufacturing processes with the formation of the channels being the most challenging and complex [57]. Table 5.5 give a high level summary of the the various manufacturing processes for each of the material types. Historically,

[2]A third, less common, group exists consisting of both carbon and metal materials and for more information see [215]

Table 5.4: BIP requirements from [103].

Characteristic	Units	2011 Status	2017 Targets	2020 Targets
Cost	$/kW	5-10	3	3
Plate H_2 permeation	Std $cm^3/(sec\text{-}cm^2\text{-}Pa)$	N/A	$<1.3\times10^{-14}$	$<1.3\times10^{-14}$
Corrosion, anode	$\mu A/cm^2$	<1	<1	<1
Corrosion, anode	$\mu A/cm^2$	<1	<1	<1
Electrical conductivity	S/cm	<100	<100	<100
Areal specific resistance	Ohm-cm^2	0.03	0.02	0.01
Flexural strength	MPa	>34 (carbon plate)	>25	>25
Tensile strength[57]	MPa	>41	>41	>41
Forming elongation	%	20-40	40	40
Thermal stability[57]	°C	120	120	120
Thermal conductivity[57]	W/(m-K)	>10	>10	>10

channels were formed by conventional machining, particularly with pure graphite plates. Channels were machined on both sides of a plate or produced on one side of two half-plates and joined together [50]. However, conventional machining was extremely time consuming, often taking several hours to produce one graphite BIP [57]. Furthermore, due to the brittle nature of graphite, machining required thicker plates (exceeding several millimeters), which increased the plate resistance and mass of the plate. Improving in the material selection have effectively eliminated the need for machining and instead use a molding (for carbon-based) or forming (metallic-based) approach. For these reasons nature graphite plates are not considered a viable option for automotive fuel cells.

Moldable graphite plates switches from single bulk graphite to to a graphite particulates impregnated with a resin such as phenolic resin (carbon-carbon) to act as a binder and ensure low levels or porosity [14]. The advantage of the carbon-carbon plates over natural graphite are that thinner plates can be produced using a emboss compression molding technique (see U.S. patent 6,663,807 [175]) thereby decreasing the plate resistance. At the same time the resin matrix gives the plate higher toughness and is less susceptible to fracture. However, the drawback is the reduced conductivity with the introduction of the resin. To compensate, the plates are heated to high temperatures (>2000°C) for several hours to carbonization and graphitize the resin. Large batch sizes are required to overcome the long heat treatment times. Alternatively, the long high temperature heat step can be front ended to the graphite

Table 5.5: Classification of BIP manufacturing process.

Carbon				**Metal**	
Pure Graphite	Expanded Graphite	Thermoset	Thermoplastic	SS,Al,Ti,Ni	Coating
·Machining	·Compression molding	·Compression molding ·Transfer molding	·Compression molding ·Injection molding Laser sintering [45]	·Stamping[160] [293][195][251][46] ·Hydro-forming [253] ·Die-forging [335] [288] [190]	·Cr-nitrides [33][336][360]

particles. Doing so increases the surface area to volume ratio of the graphite particles and creates expanded-graphite, as describe in the U.S. patent 3,404,061 [287]. The decreased density allows a greater concentration of graphite (50wt.% graphite particles to >90%wt. expanded-graphite) thereby eliminating the high temperature step post impregnation. This technologically is commercially available as Grafoil® by GrafTech International and for more information regarding the manufacturing of BIP using Grafoil® see [42][3].

Carbon Plates

Carbon plates herein will specifically be referred to as polymer composite plates. Polymer composite plates are comprised of several various materials each with a particular responsibility. The polymer portions refers to the polymeric binder, either a thermoset or thermoplastic. The additives to form the composite include carbon-powers such as graphite and carbon black to enhance conductivity and carbon fibers to provide mechanical strength. A list of various proposed and developed polymer composite for bipolar plates is shown in Table 5.6.

Thermoset-based BIPs are typically compression molded and have the advantage of high moldability, capable of withstanding higher operating temperatures and harsher chemical environments and higher filler loadings than compared to thermoplastic-based [275]. Conversely, thermoplastic-based BIPs offer the advantage of manufacturing robustness that include both compression molding and injection molding processes. Furthermore, thermoplastic-based BIPs are recyclable thus potential for material cost savings. Both material types are considered suitable for high performance and mass production.

The process flow for manufacturing both BIP types is shown in Figure 5.15. The selection of the proper molding technology is crucial for both the performance of the BIP and cost (in terms of production throughput). A study by Mitani and Mitsuda [221] reveled that compression molded thermoset BIPs with graphite filler had consensually more than twice the conductivity than injection molded thermoset BIPs. The same study also looked at various thermoplastics with graphite filler and found a similar relationship, although not to the same degree. There were some cases in which in the injection molded BIP had

Table 5.6: Summary Carbon-based BIP materials.

Resin	Type of Resin	Filler	Fiber	Ref.
Phenolic Resin	Thermoset	Graphite powder	n/a	[96][277]
Phenolic Resin	Thermoset	Graphite powder	Cellulose	[326]
Phenolic Resin	Thermoset	Graphite powder	Carbon fiber	[276]
Phenolic Resin	Thermoset	Graphite powder	Graphite lump	[314]
Poly(vinylidene fluoride)	Thermoplastic	Graphite powder	n/a	[189][323]
Vinyl ester	Thermoplastic	Graphite powder	n/a	[348][145]
Polyethylene	Thermoplastic	e-Graphite flake	n/a	[291]
Polyethylene	Thermoplastic	e-Graphite flake	Carbon fiber	[291]
Polypropylene	Thermoplastic	Graphite powder	n/a	[189]
PET	Thermoplastic	Graphite powder	Carbon fiber	[145]
PET/PVDF	Thermoplastic	Graphite powder	n/a	[144]
PPS	Thermoplastic	Graphite powder	Carbon black	[236]
PPS	Thermoplastic	Graphite powder	Carbon fiber	[145][276]

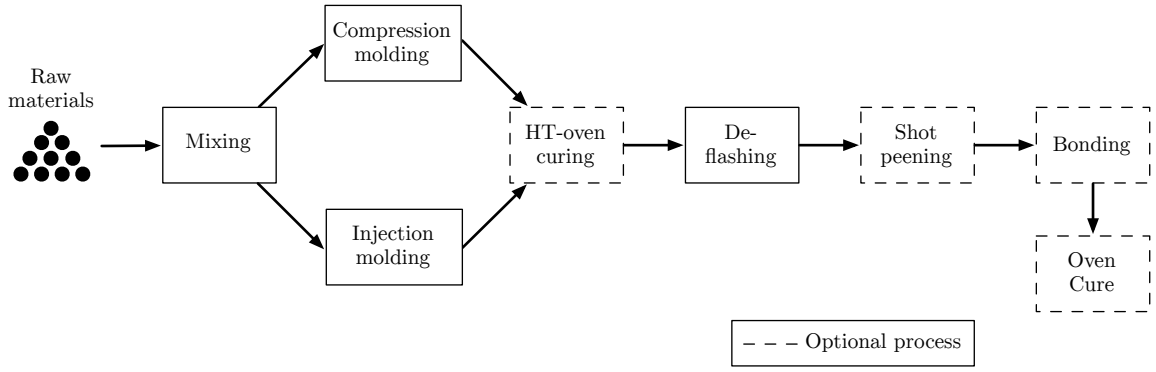

Figure 5.15: Process flow for carbon BIP manufacturing.

higher conductivity and it related to the material having higher flowability. Along the same lines, a study by Derieth et al. [67] looked at the influence of graphite morphology on the moldability and conductivity of injection molded BIPs. The findings showed that smaller and flake-shaped particulates required higher injection pressures and had lower compounding rates (throughput) than compared to larger flakes and spherical particulates. However, the smaller flake-shaped particulates had the highest bulk conductivities followed by spherical-shaped.

Generally speaking, thermoset BIPs follow the compression molding pathway whereas thermoplastic BIPs follow the injection molding pathway due to higher capable throughput. Both material types follow the same process flow post molding, in which depending the design of the plate will dictate the necessary steps. Compression molded thermosets require a post cure either in-situ in the compression molding machine or a post cure. Depending on

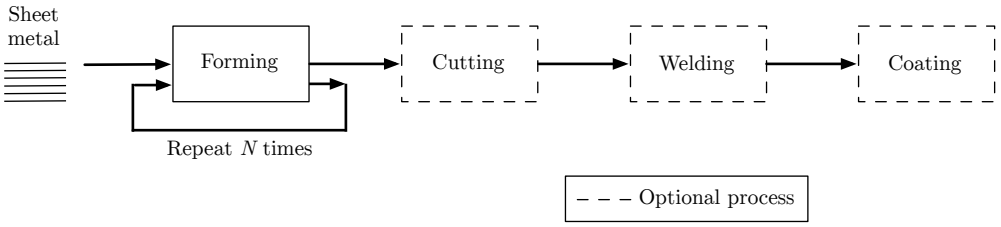

Figure 5.16: Process flow for carbon BIP manufacturing.

the thermset the curing times can range on the order of minutes (e.g., vinly ester resins) to hours (e.g., epoxies) [57]. Injection molded thermoplastics do not have a post heat treatment step, however, do require cooling prior to part ejection. The ejection time is dependent on the material and design on of the plate and are typically under a minute.

Metal Plates

The manufacturing of metallic BIP is typically a three phase process: 1) forming the single side plate or half-plate, 2) welding two half-plates to form a BIP, and 3) coating the BIP for corrosive resistance. Figure 5.16 shows the described process flow for metal BIP manufacturing. Rolls or pre-cut sheet metal is formed into half-plates using the various processes listed in Table 5.7. The forming is typically performed in three-stages where the flow field channels are first formed than the manifold openings are punched out, and finally a blanking or cutting step to separate the half-plate from the bulk sheet metal. Depending on the design of the BIP and the requirements for cell operation, the welding and coating steps are optional, but in most cases are required. Welding of the plates is typically performed using a high precision laser welder that rapidly welds several locations at the trench of the channel. Once completed, the BIPs go through a coating procedure, which depending on the desired coating material will dictate the coating process. Table 5.8 lists several common coating technologies and corresponding processes and materials.

The most widely use material for metal BIPs is stainless steel. Other metal options include aluminum, titanium, and nickel. Both titanium and nickel offer excellent corrosion resistance and mechanical strength, however, are cost prohibitive. Aluminum is relatively inexpensive, however, the drawback is challenges in forming the channels with thin-film aluminum (100μm) and issues with the variation in thermal expansion between the aluminum and thin-film coatings where delamination can occur during fuel cell operation [57]. For stainless steels there are different grades that influence the performance and manufacturing of the BIP. In general, stainless steels with higher corrosive resistant material content (e.g, chromium, nickel, molybdenum) have a lower corrosion rate (349TM > 904L > 317L > 316L > 304). Furthermore, the corrosive rate is lowered with higher surface quality (i.e., lower surface roughness) due to a higher quality oxide film layer of Cr_2O_3 rather than Fe_2O_3 [191].

The grade of stainless steel also influences type of coat material. One of the most common

Table 5.7: Various metal BIP forming techniques.

Technique	**Advantage**	**Disadvantage**	**Reference**
Stamping	Simple and relatively low cost (capital), high press forces available, high production rates possible with multiple dies (e.g., progressive die stamping)	Lower surface quality, prone to thinning a fracture, dimensional accuracy issues with spring-back	[293][160][195][46]
Flex Forming	Uses an elastic pad and only one rigid die thereby increase precision robustness, surface quality, and reduced die cost	Pad lifetime is an issue with replacements on the order of a hundred cycles	[252][203]
Hydroforming	Has increased precision robustness, higher drawing ratio, less spring-back, higher surface quality	Difficult to integrate for continuous production; longer cycletimes compared to progressive die stamping	[253]
Impact forging	Takes advantage of adiabatic softening thus minimizes strain hardening and fracture; capable of very high production rates	Unproven technology for BIP; questions regarding the shape and draw ratio capabilities of the channels	[335]

Table 5.8: Various coatings materials and processes [160][336][360].

Technology	**Description**	**Process**	**Common materials**
Nitriding	Surface conversion of the metal composition, typically in a nitrogen rich environment at high temperatures (>550°C)	Thermal furnace, plasma arc lamp	CrN
PVD	Uses high ionic energy to bombard the target(s) creating a charge molecular vapor cloud, which adheres to the surface of the BIP	Sputtering, ion-beam deposition, evaporation	TiN, CrN, Cr_2N, ZrN, gold, titanium
Electroplating	Uses an electrical field to deposit metallic ions in an aqueous bath onto the surface of the BIP	Electric current	Gold, conductive polymer, nickel, chromium

coating techniques is nitriding where the chromium at the exposed surface of the stainless steel is chemically converted to a chromium-nitrided (CrN) film by a diffusion mechanism [33]. The corrosion quality of the CrN is dependent on the stainless steel grade. For instance, one study found that CrN was better than a TiN or TiAlN coating and that properties of CrN coated SS304 were superior to those of SS316 [360]. For a detailed review of metal BIP coatings see [10].

5.6 Stack Assembly

The stacking and assembly of the fuel cell components is a much overlooked step that potentially has significant cost and production rate implications. The assembly of a fuel cell stack involves loading the elements of the stack ends (e.g., spring plate, end plates, current collector) and the repeated process of stacking the BIP followed by a MEA until the desired number of cells have been stacked, often reaching over a couple hundred cells. Traditionally, the stacking is perform in a single workstation and manually by hand using a jig with vertical tie-rods that hold and compresses the stack and acts as a facilitator for stacking alignment. The time it takes to complete a stack may take several hours and is prone to human error and risk of injury (repetitive lifting movement) [188]. Alignment error becomes an issue despite have a jig in place, which can lead to performance degradation and damage to the cell components upon compression. If the BIPs are aligned such that the channels from one BIP cell are offset to the adjacent BIP cell non-uniform stress distributions will be created in the MEA causing membrane failure [202].

At very low volumes, manually assembly is more economical and the operator is allowed more time to rest. However, at high volume production, manually assembly is not a viable option. Semi-automated processes and designs have been proposed and assessed in terms of cost [188][160][294]. An example diagram of a semi-automated stack robot is shown in Figure 6.19. Typically two side-by-side robot-arms in a work cell are used for stacking, one for the BIPs and the other for the MEAs [188]. The completed stacks are manually carted or conveyed on a continuous line to a workstation for placement of the end stack elements, which is typically performed manually, but can be easily automated. The time savings from manual to semi-automated assembly is drastic with one study yielding an 80% reduction in time for a 5-cell stack [188].

The remain step is the compression and holding of the stack components. Traditionally, tie-rods were used where the number of tie-rods were typically between 5-10, which were manually tightened by hand using a torque wrench. Moving towards semi-automated processes, the tie-rods have been replaced with steel bands or straps as described in the U.S. Patent 5,993,987 [350]. A completed stack is placed into a compression machine where it is simultaneously compressed at leak tested. Upon passing the leak test, several steel straps are manually or automatically wound around the stack and are spot welded in place.

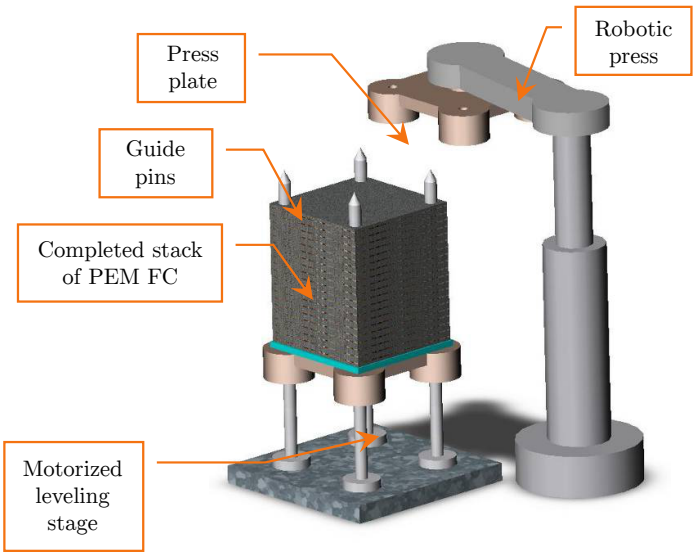

Figure 5.17: Conceptualized automated cell stacking using a single robot [294].

Chapter 6

Fuel Cell SGM Modeling

The life-time environmental and economical implications of PEM fuel cell technology for automotive applications is heavily influenced by the design and manufacture of the fuel cell system. In particular, fuel cell enterprises have primarily focused on improving the fuel cell stack where the use of exotic materials and complex and energy intensive manufacturing processes has led to prohibitively high costs. Furthermore, it has been generally regarded that fuel cells are less environmentally burdensome due to the zero emissions during operation, without the consideration of the impacts generated during manufacturing. Therefore, the goal of the assessment is determine the holistic environmental and economical impacts of a fuel cell stack throughout its entire life cycle that are within the bounds of an enterprise.

To achieve this, the assessment requires the comprehensive and precise modeling of the entire fuel cell stack value chain captured by the product life cycle zodiac. Hence, the iSLCD framework is employed where the green manufacturing scales (i.e., SGM) at each life cycle phase are integrated as described in Chapter 3. The environmental impact and cost are determined by tracing the energy and material resource flows throughout each unit process in the SGM and along the PLCZ phases. The integration also enables a more comprehensive analysis of the design sensitivities where the interdependencies from the unit processes level to the various life cycle phases are captured.

The fuel cell stack value chain varies from one enterprise to another in terms of the design and components used, manufacturing flows, and process recipes. Therefore, the representative reference fuel cell stack for the analysis is based on the Mercedes-Benz A/B-Class F-Cell that is currently in the initial phases of ramp-up production. Exact design details and manufacturing process flows are highly propriety, however, sufficient levels of designs and process flow details are obtained through a collaborative effort with Daimler-Benz. The various designs, materials, and manufacturing technologies modeled reflect the current general practices as well as anticipated designs for improved (in terms of performance and forecasted costs) future generation fuel cell stacks. Furthermore, it is of interest, especially from an economic perspective, to conduct the analysis at varying levels of vertical integration. The degree of vertical integration (DVI) dictates the decision to "make" a component in-house versus "buy" as a purchased component from a supplier. In addition, the DVI has environ-

mental implications in terms transportation emissions and emissions due to the local power generation mix. A key factor in determining the DVI is the influence of demand that directly sets the required annual production volume. The decision to make versus buy will change as costs generally decrease with increasing volume by taking advantage of higher utilizations with economies-of-scale.

The remaining sections of this chapter detail the construction of the model along an overview of the aspects of the fuel cell stack design and manufacturing that are included in the modeling.

6.1 Model Overview

The scope of the product life cycle for the fuel cell stack assessment is shown in Figure 6.1. The majority of the PLCZ phases are considered in the modeling, as depicted with a solid line, beginning from raw material extraction to new product distribution and the appropriate end-of-life phase depending on the specified scenario. As previously mentioned, the use phase will not be considered due to being out of the bounds of the enterprise in terms of both the operation of the fuel cell stack and the require hydrogen fuel. The effects of the raw material generation from the Earth and material waste in landfills and incineration are ignored, although, future assessments will want to include the environmental and economical consequences of potentially toxic materials in the landfill phase. Lastly, the direct re-use of the fuel cell stack is considered the trivial case where the associated impacts, such as re-installing the stack into a new vehicle, is negligible.

At the module level of the iSLCD framework, the approach for the LCI methodology in the LCA module is shown in Figure 6.2. The majority of the inventory analysis for each of the life cycle phase is Process-based, which enables the resolution required for precise integration. For inventory that is represented as capital, such as the embodied energy of the machine tools or the construction of a facility where the elementary flows are non existent, an Economic I/O-based approach is used. It is assumed that the level of uncertainty associated with the economic I/O LCI is acceptable and will improve with with increasing allocation (i.e., production volume). For the process-based LCI, the elementary flows of interests are primarily raw materials, consumables, and energy in terms of both electricity and natural gas. The trace of other resource flows such as water are not included due to lack of information for each process. However, for processes where the water consumption is known the embodied energy is included in the analysis. The selected impact category and characterization factor representing the environment impacts is global warming potential (GWP) in units of kilograms of carbon dioxide equivalence ($kgCO_2e$). The consideration of only GWP is due to the wide availability of data for both process- and economic I/O-based in various LCI databases such as the GaBi Software. Furthermore, GWP is arguably the most representative metric for assessing the released anthropogenic carbon emissions which the stabilization wedges are based on. At the LCCA module level, a DFMA approach is implemented as described in Chapter 2 with an addition element of direct transportation

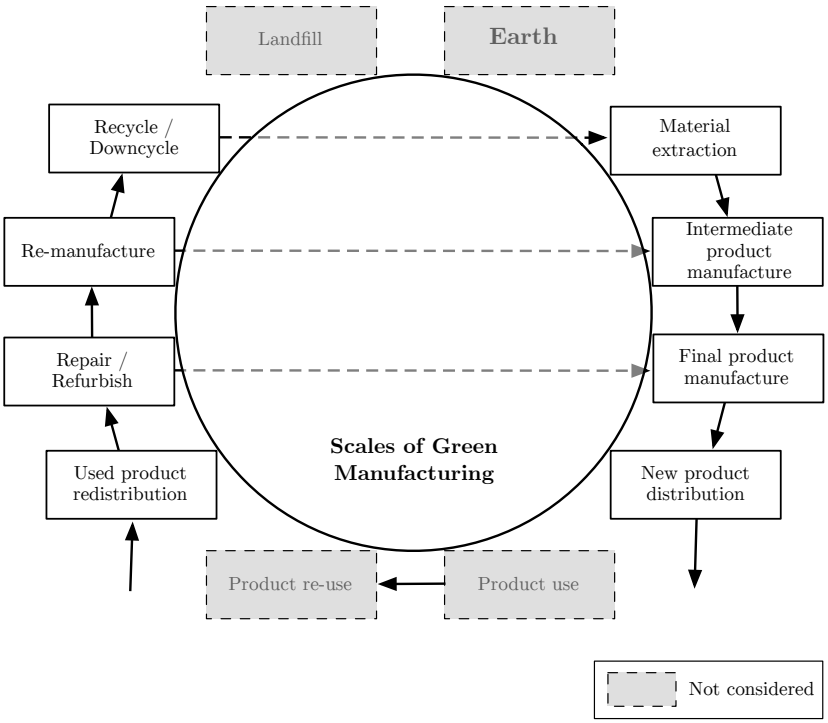

Figure 6.1: Modeling scope of the product life cycle zodiac.

Table 6.1: Modeled production volume scenarios.

Daimler F-Cell	Gen2/3		Gen4		Gen5	
Annual Volume (units)	100	500	1000	5000	10000	50000

costs. All monetary flows are converted to the U.S. dollar and scaled to the 2013 year using the Consumer Price Index inflation calculator [184].

Each iteration of the model includes the influence of the annual production volume and the DVI. Table 6.1 lists the annual fuel cell stack volumes of interest beginning with the assumed current production rate of 100 units per year and up to 50000 units. By automotive manufacturing standards an annual production of 50000 units is considered low volume production for a single enterprise. Most cost assessment on fuel cell stack manufacturing such as [160] and [293] assume production volumes of up to 500,000 per year. However, equating fuel cell stack manufacturing to current automotive volumes creates large uncertainties. Due to the rapidly evolving nature of fuel cell technology many of the materials and designs as well as the manufacturing processes may become obsolete in a relatively short period of time. Therefore, it is assumed that with the introduction of the F-cell Gen5 model the within next decade, a maximum of 50000 units per year is reasonable under the current manufacturing technologies modeled.

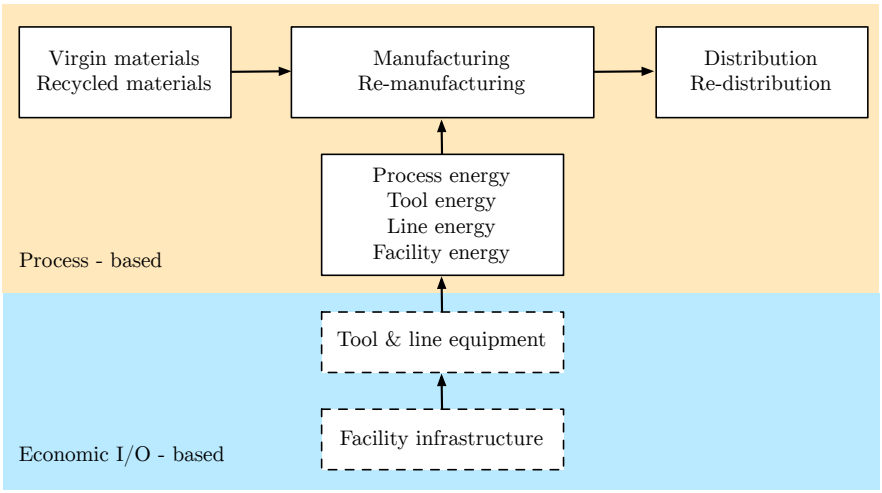

Figure 6.2: Model scope of the LCA module.

Table 6.2: Degree of Vertical Integration scenarios.

	DVI				
Component	0	1	2	3	4
Membrane	n/a	n/a	buy	buy	buy
GDL	n/a	buy	buy	buy	make
BIP	buy	buy	buy	make	make
CCM	n/a	buy	make	make	make
MEA (with frame)	buy	make	make	make	make
Stack Assy	make	make	make	make	make

In addition, the model includes the strategic decision of the DVI at the enterprise level for each production volume. Table 6.2 shows the breakdown of the make versus buy decision at each DVI. At a DVI of "0" the scenario assumes near horizontal integration where the bipolar plates and the full MEA (i.e., CCM+GDL+frame components) are completely out-sourced and are purchased from a global supplier and assembled in-house at Daimler's facility. The opposite scenario is the near complete vertical integration of every component, excluding the membrane itself, is manufactured in-house where only the raw materials are purchased from the various suppliers. The exclusion to manufacture the membrane in-house is due to the fact that Nafion® based membranes are considered a relatively mature commodity with consumptions and applications spanning multiple industries and products. Although the membrane is included as a purchased component, the manufacturing analysis is still conducted to determine the embodied energy and the purchase cost (using DFMA) of the membrane.

The entire model for determining the GWP and cost of a fuel cell stack at a given production volume and DVI is shown in Figure 6.3. The model takes in the inputs of the

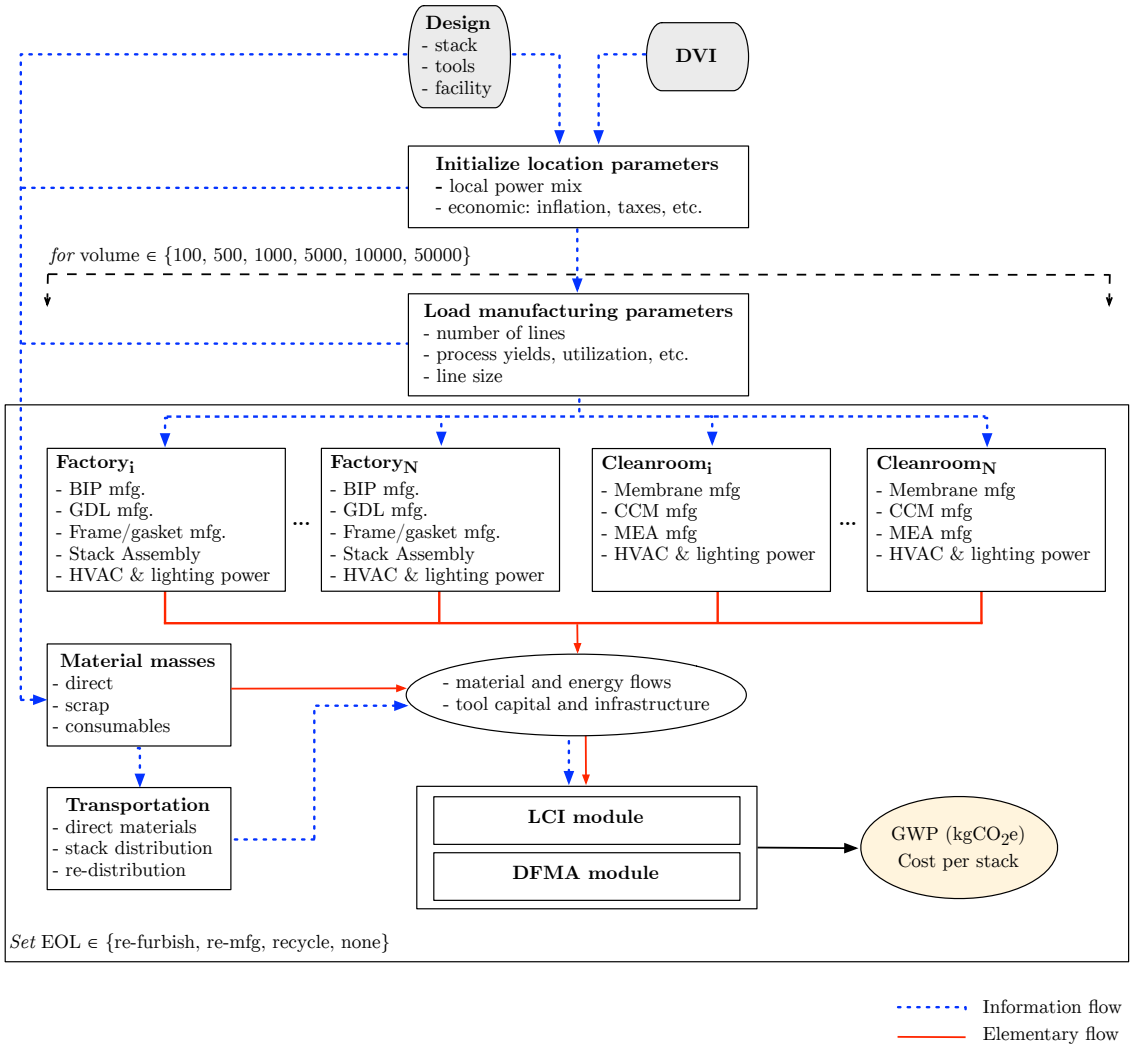

Figure 6.3: Methodology for fuel cell stack GWP and cost modeling based on the SGM.

DVI along with the fuel cell stack design such as materials and dimensions, certain tool designs such as the mold runner design of an injection molding machine, and the factory design and layout such as the location, orientation, construction materials, and size of the factory. Information at the design level (dotted blue lines) is percolated throughout the model. The model starts by initializing the relevant location parameters for Daimler and the supplier enterprises. At this initial stage of the model the location parameter of interest is the number of available annual working days per location, which assumes that each country has a different number of holidays in a year.

The information parameters are loaded into the manufacturing parameter module where the layout of the production line is established. In this module, the number of lines is determine given the production volume, number of working days, and the cycle time, setup

time, and inspection time of the process. Some manufacturing flows have multiple process options. For example, at low volume production the bipolar plates are produced in single die sets and are manually inspected whereas at high volumes the die sets double and the inspection is automated using a visual robotic system. The manufacturing module automatically determines the appropriate option using a recursive iteration that targets the fewest number of lines (it is assumed that the number of lines is directly proportional to the cost and energy consumption).

The design and manufacturing parameter information is taken as inputs to the process, machine tool, and facility scales of each fuel cell stack component. The number of facilities (factories and cleanrooms) is dependent on the DVI. For each facility, the energy consumption of all processes and machines tools within the facility are calculated in parallel with the HVAC energy model described in Chapter 3. At each hour time step, the model calculates the appropriate convective heat loss from the machine tools given the indoor temperature and ventilation flow. The heat loss from the machine tool also influences the energy consumption at the unit process level. It is assumed that the machine tools are temperature stabilized, hence, the thermal mass of the machines is ignored. The cleanroom model is a simplified version of the HVAC energy model where the cleanroom is assumed to be situated inside a factory as opposed to a standalone building (this is reflective of the current fuel cell manufacturing industry). The cleanroom model drastically simplifies due to lack solar radiation and the assumption that the boundaries (i.e., walls) are isothermal to the factory. Additional information is transferred from the design level to the material module where the direct masses of the fuel cell stack and the scrap waste resulting from the design and manufacturing the yield loss, are tabulated. The masses are also necessary for determining the transportation emissions and cost under the set locations.

The GWP and cost results are assessed at the LCI and DFMA modules using LCI data from commercially available databases and cost data found from publicly available sources and price quotes (see Appendix A6 for table of values and references). The energy and material flows, as shown as the solid red lines are segregated into material embodied energy, machine tool and facility infrastructure embodied energies, process energy and facility energy emissions per location, and direct transportation emissions. Additional steps are required (not shown) for the various end-of-life-phases. Choosing an end-of-life option will trigger the following:

- **Refurbish:** The fuel cell stack shipped back to Daimler's manufacturing facility and N cells are replaced while keeping intact the stack hardware. The refurbish stack is re-assembled then shipped back to the customer. It is assume that the stack and cells are only refurbished once and that the end-of-life impacts of the replaced cell(s) is not include at this stage.

- **Re-manufacture:** It is assumed that the stack cells are no longer functional at the expected performance. The stack is shipped back to Daimler's manufacturing facility and the materials are reprocessed directly into the manufacturing process stream. Due

to the material composition and packaging of certain components, not all parts can be re-manufactured and are thereby considered as discarded waste. A new stack is manufactured with the existing stack hardware and is shipped back to the distributor.

- **Recycle:** It is assumed that the stack is in a condition where the majority of the components can not be refurbished or re-manufactured (e.g., contaminated). The stack is sent to a local recycling center where the recyclable materials are reverted back into the raw material supply stream. Non-recyclable materials are considered as discarded waste.

Further assumptions to modeling are listed below.

- Uncertainty in the model was capturing using the the proposed Beta function uncertainty model detailed at the end of Chapter 3. In total, over 400 parameters were associated with some level of uncertainty with a typical maximum and minimum value of $\pm 50\%$ and for the select few low uncertainty data (e.g., directly from Daimler) an error of $\pm 10\%$ was associated, and for the select few high uncertainty data an error to $+100\%$ and beyond was assigned.
- A Monte Carlo simulation technique is conducted for assessing the data uncertainty using a random number generator with the Beta functions. The minimum number of iterations required to achieve to desired error is 100 (refer to section A3 in the Appendix).
- The LCIA methodology for GWP is chosen to be the CML2001 (November 2010 update) at a time frame of 100 years.
- It is assumed that the transportation cost is a linear function of mass and distance and a static factor of cost per mass per distance is obtained from the U.S. Department of Transportation [322].

6.2 Fuel Cell Stack Design

The functional unit of the assessment is an 80kW (gross power) hydrogen PEM fuel cell stack. The 80kW output power well represents the light-duty vehicle market and that the Mercedes B-Class F-cell has an 80kW stack coupled with a 20kW lithium-on battery for a total of 100kW or roughly 134HP. The proposed design of the fuel cell stack is shown in Figure 6.4 along with the dimensions and a list of materials for each component tabulated in Table 6.3. Note that the design specifications and materials listed have been modified and simplified and therefore does not completely reflect Daimler's F-cell technology, but rather an archetype of a state-of-an-art fuel cell stack.

As seen in the figure, the bulk of the fuel cell stack is the cell row where hundreds of repeated cells connected in series. The number of repeated cells is adjusted depending on

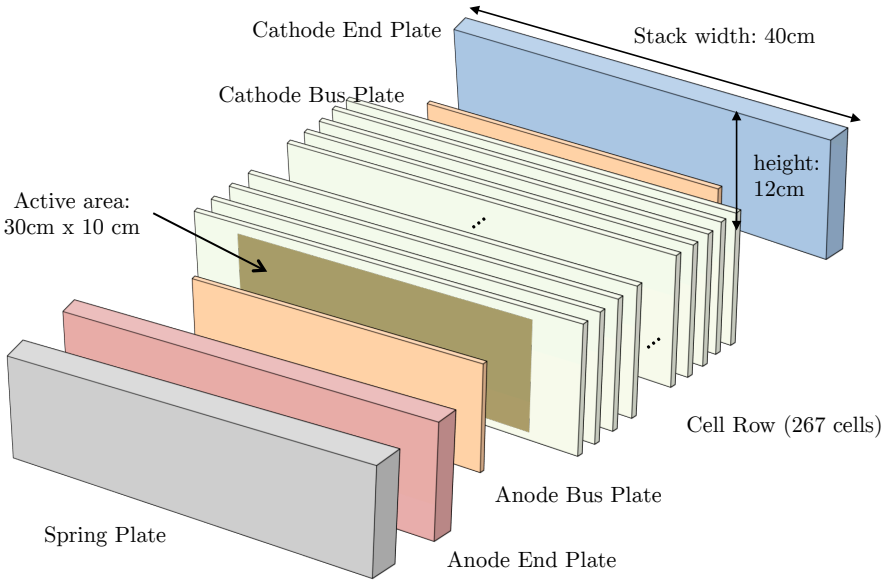

Figure 6.4: Included fuel cell stack components.

the desired stack output power. It is assumed that for a state-of-the-art automotive fuel cell stack the power density of the active area (the MEA area exposed to the reactants) is $1W/cm^2$, which, according to Daimler, is a valid assumption [351]. Therefore, to achieve the desired 80kW output power a total active area of $8m^2$ is required. The designed MEA active area is 30cm long by 10cm wide thus translating to a cell row depth of 266.67 or 267 individual cells. The physical dimensions of the stack are larger at 40cm in length and 12cm in wide due to the required sealing around the MEA and the manifolds running along the outer areas of the cell (not shown).

The material selection for each component in Table 6.3 has been selected to represent the current practiced designs along with proposed or anticipated designs for future generation stacks (within the time frame of the maximum production volume). Every component labeled with an option 'a' denotes the material used for the current generation, which will be referred to as the Reference stack. Therefore, the reference stack design for the F-cell consists of an unreinforced Nafion[2] membrane, slot-die coated platinum ink CCM, MESA encapsulation of the MEA and sealing, and carbon-based BIP. The assumed future technology reference design determined by various sources in literature and communications with Daimler, is denoted with the option 'b'. The materials and corresponding specifications have been selected such that the two technology variations are functionally equivalent where it is reasonably assumed that both designs will yield the same output power. The future generation design will be referred to as the Future stack. Furthermore, it is assumed that the performance of each component is mutually exclusive thereby yielding functional equivalence between any combination of 'a' and 'b'. An additional option dimension is added for the BIP where each option is separated into two manufacturing flows. For example, equivalent carbon BIP can

Table 6.3: Fuel cell stack component options and descriptions.

Component	Option	Type	Material	Length	Width	Thickness
Membrane	1a.	Unreinforced	Cast Nafion®	30cm	10cm	50μm
	1b.	Reinforced	Nafion® ePTFE	30cm	10cm	25μm
CCM	2a.	Slot-die	Platinum Carbon black	30cm	10cm	0.5mg/cm^2
	2b.	NSTF	Platinum PR-149	30cm	10cm	0.2mg/cm^2 100nm
GDL	3	Substrate	Carbon fiber PTFE	30cm	10cm	180μm
		MPL	PTFE Carbon black	30cm	10cm	30μm
MEA	4a.	MESA	Silicone	Figure 6.5	Figure 6.5	Figure 6.6
	4b.	MEFA	PEN	Figure 6.5	Figure 6.5	200μm
BIP	5a$_1$.	Carbon (compm)	Epoxy resin Graphite	Figure 6.7	Figure 6.7	1.5mm
	5a$_2$.	Carbon (injm)	Polypropylene Graphite Carbon black	Figure 6.7	Figure 6.7	1.5mm
	5b$_1$.	Metal (thermal)	SS304 Nitrogen	Figure 6.7	Figure 6.7	100μm (stock) 2μm (coating)
	5b$_2$.	Metal (PVD)	SS304 CrN	Figure 6.7	Figure 6.7	100μm (stock) 2μm (coating)
Bus plate	6	Anode Cathode	Copper	30cm	10cm	1mm
End plate	7	Anode Cathode	PA6-6 with GF	40cm	12cm	15mm
Spring plate	8	n/a	SS304	40cm	12cm	10mm
End cap	7	Anode Cathode	Aluminum	41cm	13cm	50mm 30mm
Straps (3x)	9	Strips	Generic steel	12cm+2*D	20mm	1mm

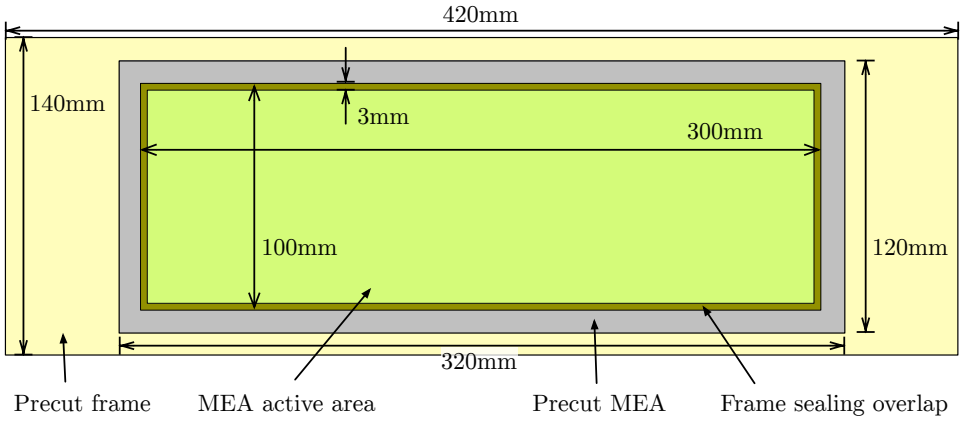

Figure 6.5: Manufacturing cutout of the MEA and Frame. The outer dimensions represent the precut Frame size where the excess material is considered as scrap. Actual footprint dimensions of the Frame is the same as the BIP.

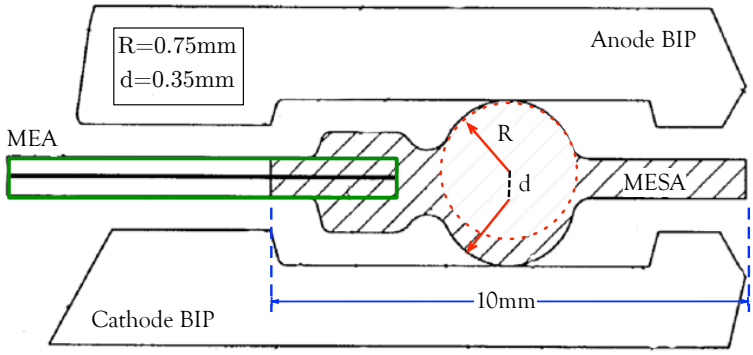

Figure 6.6: MESA sealing architecture and estimated dimensions. Image from [11].

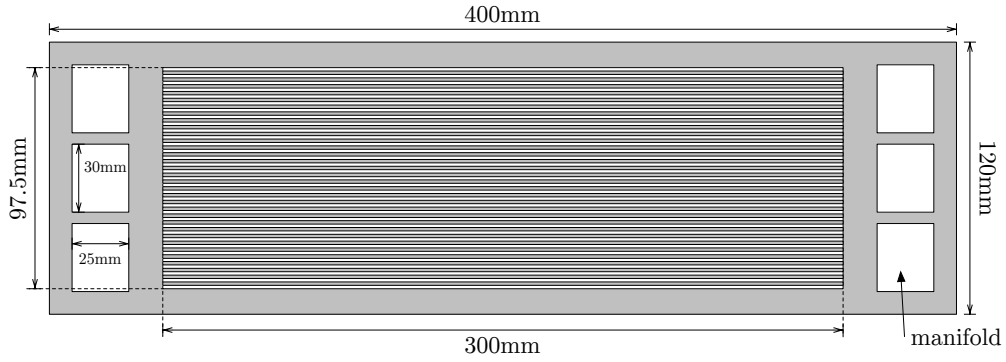

Figure 6.7: Design and dimensions of the bipolar plate for both carbon and metal.

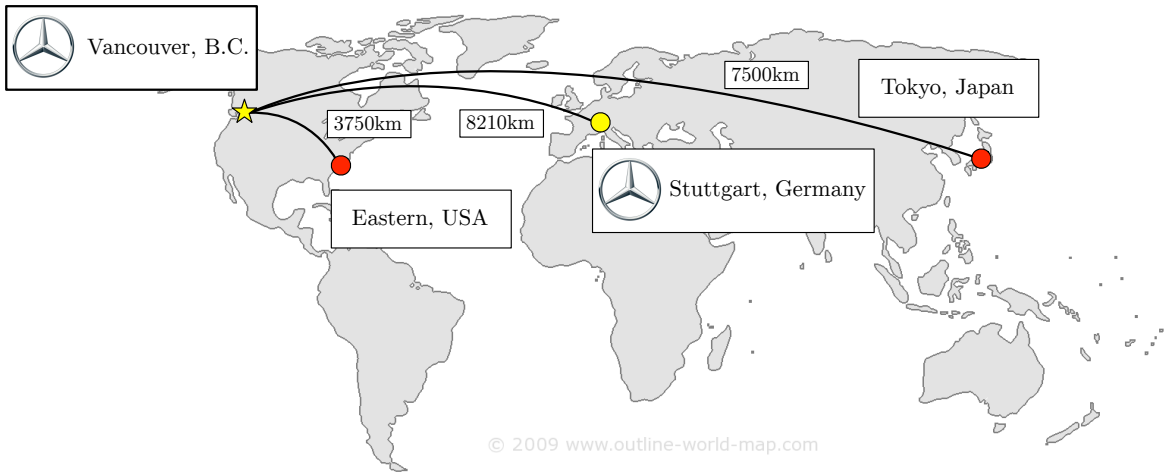

Figure 6.8: Global enterprises using in the modeling.

be manufactured either using the compression molding (*compm*) pathway with a thermo set polymer or injection molded (injm) using a thermoplastic polymer with an additional filler. For the Reference design, the compression molded BIP is consider the base case while the injection molded BIP is an alternative option. The actual forming of the metal BIP is identical for option 5b. Where it differs the the process in coating the protective layer onto the surface of the metal. The PVD option is considered as the base case for the Future stack whereas the thermal nitriding is the alternative option.

6.3 Enterprise Scale

At the enterprise scale the model sets the location parameters that defines where the fuel cell is manufactured and where the materials and components are supplied from. Figure 6.8 shows a map of the geographical locations considered in the model. Daimler's headquarters is located in Germany in the city of Stuttgart (yellow dot) and is where the majority of the fuel cell R&D takes place. However, Daimler's main production facility is located in Vancouver (yellow star) in the province of British Columbia, Canada. The decision to locate the manufacturing facility in Vancouver was primarily due to the hub of fuel cell manufacturing expertise and capabilities with Vancouver being the headquarters of Ballard Power Systems and AFCC. Despite being manufactured in Vancouver, the desired use of the fuel cell stacks is in Germany. Therefore, the model initializes the manufacturing location parameters based on Vancouver and includes the transportation of the fuel cell stack from Vancouver to Germany (Stuttgart).

Suppliers for fuel cell materials and components range globally with the major enterprises located in the U.S., U.K., Germany, and Japan. For the membrane, it is assumed to be entirely supplied from the U.S. where DuPont is headquartered. More specifically, Nafion®

Table 6.4: Supplier minimum annual production capacities.

Component	Capacity	Cost mark-up
Membrane	150,000	100-200%
CCM	100,000	30-100%
GDL	200,000	20-70%
MEA	100,000	30-100%
Frame	100,000	30-100%
BIP	500,000	30-100%
Stack hardware	n.a.	200-400%

membranes are manufactured in DuPont's Fayetteville, North Carolina plant [82], which is categorized as the Eastern half of the U.S. The CCM and MEA are manufactured in various countries spanning the U.S. and Europe and will be assumed to be supplied by 3M's fuel cell division primarily located on the Eastern half of the U.S. (e.g., Minnesota, Connecticut). The GDL is assumed to be manufactured in Germany from large carbon fiber manufacturers such as SGL Carbon. Lastly, the BIPs are assumed to be supplied from Japan (e.g., Nisshinbo) and companies stemming from the Eastern U.S. (e.g., Dana Corporation) for the carbon and metal BIP, respectively. For simplicity, it is also assumed that the raw materials used for in-house production are supplied by the corresponding enterprise that manufacturers the component (e.g., carbon BIP raw materials will come from Japan). For each enterprise location the appropriate location parameters data is retrieved such as economic activity (e.g., inflation, mortgage rate), weather data, and power grid mix. The full list of relevant parameters and value can be found in the Appendix. It is also assumed that for each component purchased from a supplier utilizes the suppliers existing production capacities as opposed to the required demand at low volumes. For instance, DuPont Nafion® membrane production has a annual capacity of approximately 150,000m^2[245]. Therefore, for the cutoff minimum annual membrane demand is set to 150,000m^2 only increases when the demand is greater. Table 6.4 list the minimum production capacities for purchase components assumed in the model as well as the assumed cost mark-ups (base on communications with Daimler).

The data for the location parameters are considered to be static with the lone exception being the cost of electricity for the Vancouver manufacturing facility. The electric tariff or cost of electricity (dollars per kWh) is a complex function determined by the appropriate rate schedule for the enterprise. Depending on the rate schedule, the electric tariff is a function of the electricity consumption, monthly power demand, supplied voltage connection, zone location, type of service, and historical baseline level (HBL), if applicable. The algorithm to determine the electricity rate is given by the local utility, BC Hydro[130], for Vancouver. It is assumed that the rate schedule for fuel cell manufacturing falls under the large service category, which represents users that require at least 150kW of supplied power and consume over 550,000 kWh annually. Figure 6.9 plots the electricity rates ($/kWh) for three scenarios: below 150kW, near 150kW, and much larger than 150kW, around a monthly HBL of 50,000 kWh. According to the cost algorithm, at low monthly electricity consumptions the rate

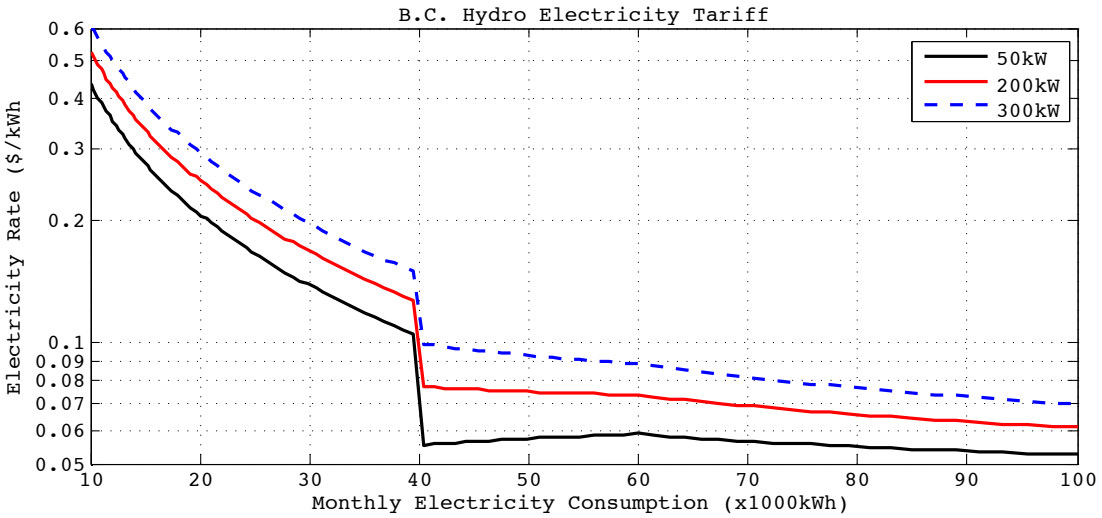

Figure 6.9: Tariff rate schedule for B.C. Hydro, Vancouver.

decrease asymptotically until at an offset near the HBL. At the offset point the rate drops and the electric rate is determined using a different algorithm where below the HBL the difference in electricity consumption is credited back while consumption above the HBL is penalized. The penalty of power demand is linear, however, according to the cost algorithm, power demands over the specified 150kW is heavily taxed.

6.4 Facility Scale

The reference factory included in the model is based on Daimler's manufacturing facility in Vancouver and is referred to as the Mercedes-Benz Fuel Cell (MBFC) manufacturing facility. Figure 6.10 shows a top-down Google Map image of MBFC along with the identification of the factory floor space and the office space. The building housing the MBFC facility is occupied by several other companies including Ballard Power Systems. However, it is assumed that MBFC represents the entire building and that the dimensions are approximate based on the Google Map scale and communications with Daimler.

The size or footprint of the facility is dependent on the production volume and the DVI. The office space is considered to have a static floor space of 20 meters in length and 30 meters in width for all production volumes and DVIs. The factory floor space as assumed to have a static width of 60 meters and increases in length as necessary with a minimum length of 30 meters. To determine the length of the facility, the required area is first determined using the following equation:

$$A_{factory} = f_s \cdot (A_{tools} + A_{storage} + A_{inventory} + A_{cleanroom}) \tag{6.1}$$

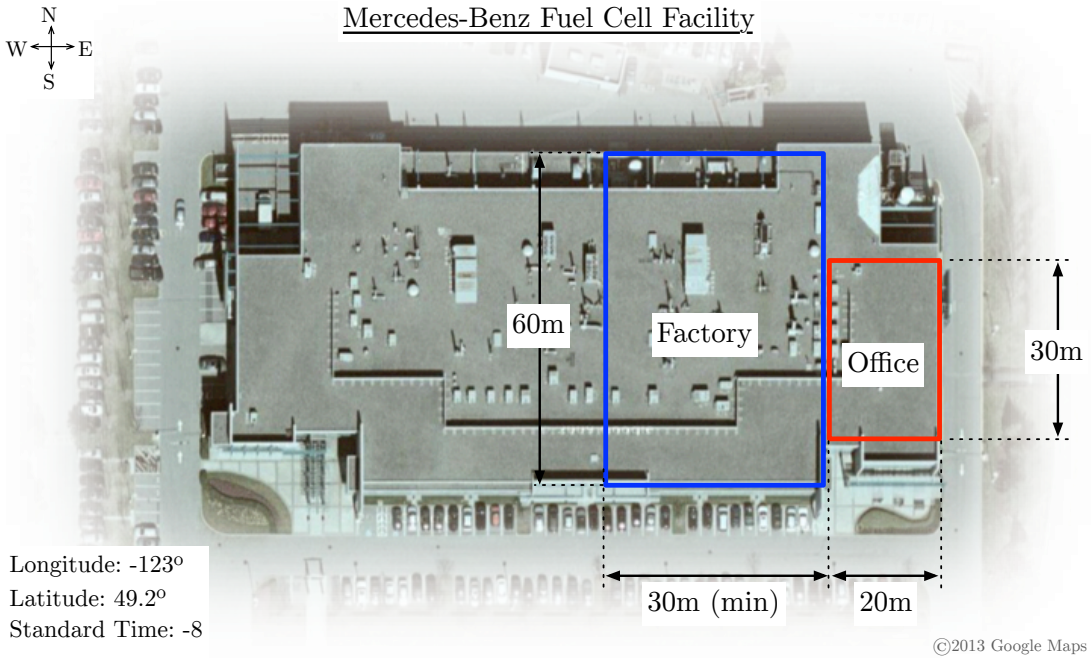

Figure 6.10: Bird's-eye view of MBFC in Vancouver.

Where A_{tools} is the total occupied area of the machines for in-house production, $A_{storage}$ represents the area housing the replacement and miscellaneous parts and is assumed to be 20% of A_{tools}, $A_{inventory}$ is the holding area for completed fuel cell stacks and is approximated as $2A_{stack}\sqrt{volume}$ where A_{stack} is the dimensional footprint of the stack and $volume$ is the annual production volume, $A_{cleanroom}$ is the cleanroom footprint and is only include if the MEA is manufactured in-house, and f_s is a safety factor term set to 1.5. Therefore, the required factory length can be calculated as $A_{factory}/60$ and rounded up to the nearest 10 meters.

The facility model is constructed using the materials and dimensions listed in Table 6.5. Obtaining actual material compositions and dimensions for MBFC was not feasible, however, the materials listed sufficiently represents a generic factory and office building. As seen in the table the majority of the building materials for both the factory and office are similar, although the office has slightly more stringent requirements due to comfort and acoustic reasons. The temperature set point inside the office is to 22±2°C during working hours and 22±4°C during non-working hours compared to a warmer 23±3°C and 23±6°C for the factory. Furthermore, the air change per hour (ACH) is fours times higher in the office area to maintain clean fresh air while it is assumed that the machine tools on the factory floor have local fume exhausts directly connected to the outdoor environment.

The mathematical modeling of the facility HVAC energy consumption was covered in Chapter 3. The require temperature inputs to the thermodynamic model are the hourly outdoor environment and soil surface temperatures for Vancouver. Hourly datasets for the

Table 6.5: Build materials and attributes for the facility model.

	Factory				
Element	Material	Thickness (cm)	Density (kg/m^3)	k (W/m-K)	C_p (J/kg-K
Roof					
	Light-weight concrete slab	10	1280	0.53	840
	Built-up roofing (BUR)	0.95	1120	0.16	1460
	Insulation	7.5	43	0.03	1210
Floor					
	Heavy-weight Concrete slab	30	2240	1.95	900
Walls					
	Concrete block	20	512	0.29	880
Windows					
	Glass (single pane)	0.3	2500	1.0	750
	Facility height (m)	ACH	Set temp. (°C)	Set temp. tol. (°C)	LPD (W/m^2)
	10.5 (exterior), 10 (interior)	1	23	3/6	13

	Office				
Element	Material	Thickness (cm)	Density (kg/m^3)	k (W/m-K)	C_p (J/kg-K
Roof					
	Light-weight concrete slab	15	1280	0.53	840
	Built-up roofing (BUR)	0.95	1120	0.16	1460
	Insulation	7.5	43	0.03	1210
	Plywood	1.6	544	0.12	1210
	Air gap	163	1.2		
	Acoustic tile	1.91	368	0.06	590
Floor					
	Carpet	1.0	288	0.06	1390
	Insulation	7.5	43	0.03	1210
	Heavy-weight Concrete slab	30	2240	1.95	900
Walls					
	Gypsum board	1.6	800	0.16	1090
	Concrete block	20	512	0.29	880
Windows					
	Glass (double pane)	0.635	2500	1.0	750
	Facility height (m)	ACH	Set Temp. (°C)	Set Temp. Tol. (°C)	LPD (W/m^2)
	5 (exterior), 3.1 (interior)	4	22	2/4	17

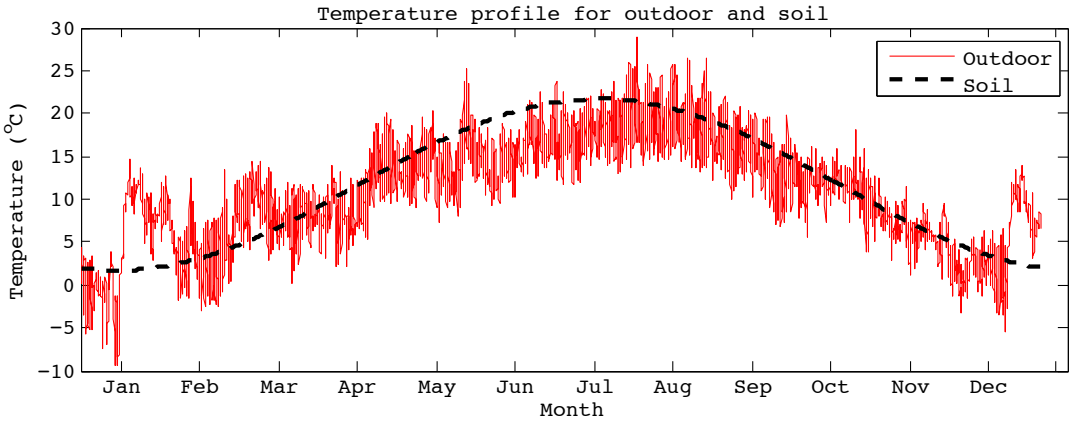

Figure 6.11: Vancouver outdoor temperature profiles.

outdoor temperature were obtained online from the Climate division of the Department of Environment Canada (`http://climate.weather.gc.ca`). The corresponding hourly soil surface temperatures is determined using the soil temperature equation found at the end of the HVAC energy modeling section in Chapter 3. Figure 6.11 plots the hourly outdoor temperature and modeled soil surface temperature for Vancouver. As expected, the two temperature profiles are well correlated with similar phase and amplitude.

The solar radiation data for the model was extracted from the Canadian Weather Energy and Engineering Datasets (CWEEDS) obtained online (`http://climate.weather.gc.ca`). The datasets provides hourly solar radiation in the component form of direct normal irradiance and diffusion horizontal irradiance measured from the surface of the Earth. The components of the irradiance was converted to the appropriate radiation heat flux for each side of the building using the solar angles described in Chapter 3. Figure 6.12 plots the CWEEDS data for both direct (red dashed) and diffuse (blue solid) irradiance. The data represented in the figure shows sparse events for the direct irradiance while the diffuse is more uniform over time. A plausible explanation for the spareness is due to the interference from passing clouds, rain, and snow. The diffuse irradiance component represents the scattered solar beams from the sky and surrounds and therefore are less susceptible to passing weather conditions.

From the temperature and solar radiation profiles the HVAC energy model determines the necessary HVAC load for offsetting the internal (e.g., machine tools, office equipment, personnel) and external heat gain and losses. A key functionality of a HVAC system is to balance the thermal loading with rate of fresh air (infiltration) and unwanted exfiltration. During the winter season when the outdoor temperature is much lower than the set point temperature, it is advantageous to minimize the infiltration to reduce the required heating load. On the other hand, during the summer months it is advantageous to maximize the infiltration rate when cooling is required. The HVAC model takes this dynamic into account by varying the infiltration rate depending on the temperature differences and the set point

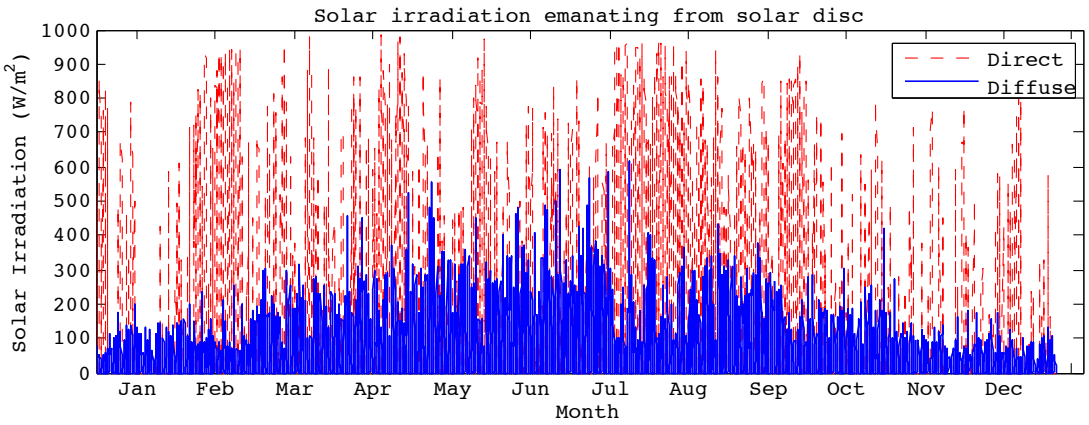

Figure 6.12: Vancouver solar irradiation profiles.

temperature tolerance. For health and safety reasons, the ASHRAE recommends at least 10L/s/person of fresh air into a commercial facility [13], which provides a constraint on the lower bound infiltration rate. The upper bound infiltration rate is restricted by the maximum set flow rate of the ventilation, which is proportional to the ACH.

The model assumes isothermal boundaries between the office space and the factor space. Therefore, the HVAC energy consumption of the office area is independent of the production of the fuel cell stack and can be treated as a separate model. Preliminary results were obtained by running the office HVAC energy model at hourly time steps. Figure 6.13 shows the annual power demand profile (6.13a) separated into heating load, cooling load, ventilation and lighting, and the total energy consumption of the facility, and zoomed version of the same profile to a period of one week (6.13). As expected, the profile shows high heating loads during the winter months and high cooling loads during the summer. The ventilation and lighting profile appears to exhibit a binomial distribution at 1.5kW and 6.5kW. However, closer examination of the profile reveals that the power turns to maximum during the working hours of the weekdays and set to a lower state during the off hours. The binary switching of power profiling was modeled by choice as a reasonable assumption that the facility system is intelligent enough to conserve electricity. Furthermore, the zoomed profile reveals that during certain days the HVAC heating turns on during the morning and switches to cooling mode during the day time. The behavior of the sudden switching can be due to various reason such as the large temperature swings in the outdoor temperature profiles and due the fact that internal thermal mass such as the office equipment was not taking into consideration. A quick sanity check of the HVAC energy consumption for the office space shown in Table 6.6 shows that the model is well within the expected range of energy intensities for office type builds (data provided by the U.S. EIA Commercial Buildings Energy Consumption Survey [89]).

Further assumption for the facility model are listed below.

- No work is conducted on holidays and weekend and non-working hours. The start of

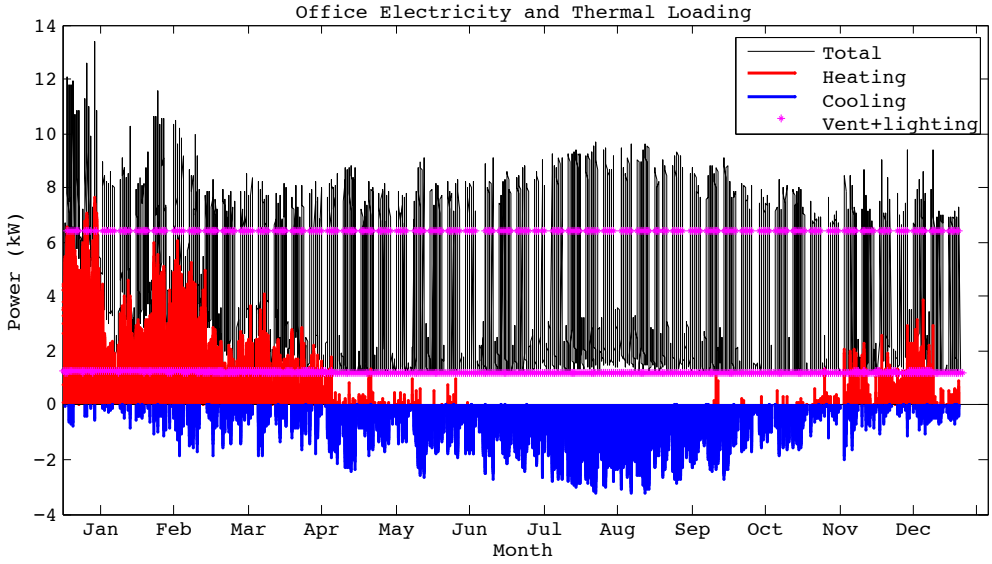

(a)

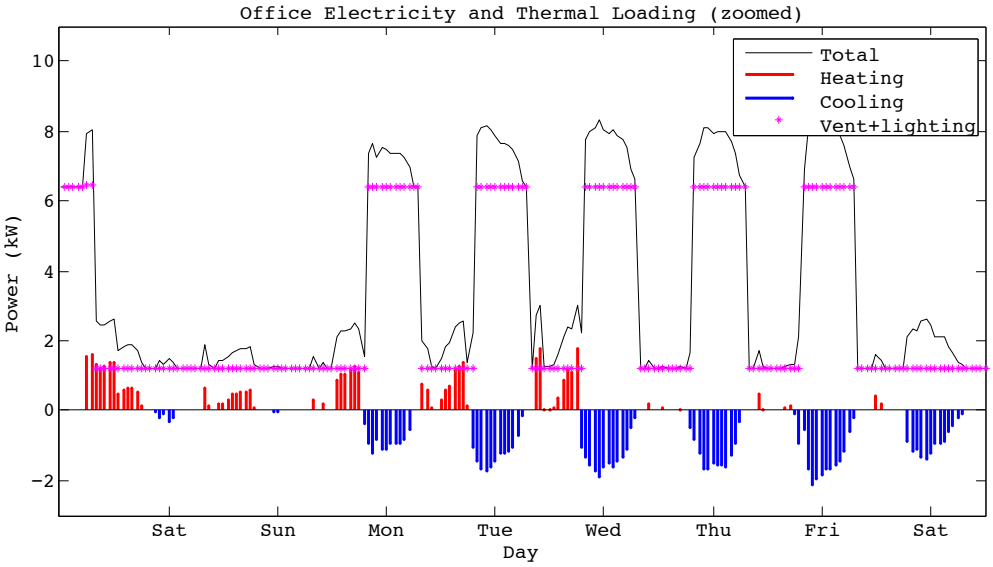

(b)

Figure 6.13: Facility power profiles for the office space.

Table 6.6: Office HVAC energy results (kWh/square foot).

Heating	Cooling	Ventilation	Lighting	Total	CBECS2003[89]
0.7	1.0	1.1	5.9	9.3	6.9-11.5

work depends on the daily number shift, which depends on the production volume. During non-working hours the facility lighting is reduced by a factor of 4 and the ventilation flow is reduced by a factor of 2 (only in the office space)

- It is assumed that the number of employees in the office is 50 (50% male/female) and that the factory employees are determined separately. The number of employees or workers in the factory is dependent on the number of lines and the equipment type.
- The cleanroom ambient temperature is set to a constant 22°C with no tolerance. The air flow is determined by the cleanroom class, which is set to class-10000 (ISO7). It is assumed that the cleanroom exterior is isothermal and the heat internal heat generation is directly offset by the cleanroom HVAC system.
- The solar radiation data was obtained for the year 2005 from the CWEEDS database. The 2005 year is the most recent available dataset. To match the solar profiles, outdoor temperature data was also obtained for the 2005 year.
- The magnitude and direction of wind blowing across the facility building is including in the thermal modeling. Hourly data for the wind was found on the CWEEDS database.
- The convection term for all thermal processes is assumed to be uni-directional in the $-z$-direction flow (i.e., downward) unless the free convection heat transfer coefficient is larger than the forced convection.

6.5 Production Line Scale

At the production line level the primary attribute of interest is the number of simultaneous lines required to process a given annual volume. The methodology for determining the number of lines was outlined in Chapter 3 where the same methodology can be applied to batch processing. The key parameters that are needed to be determined are the the process cycle times, line setup time, line process yield, and line availability. The process cycle times are presented in the next section at the process and tool level. For determining the remaining three parameters a learning curve type relationship [324] is implemented given the assumption that the overall line yield, availability, and setup time improves with increasing production volume and the improvement is dictated by some power function.

The formulation of the learning curves is as follows. The simplest learning curve equation is represented in the form:

$$y = \frac{A}{B^n} \tag{6.2}$$

where y is represents the yield, setup time, or availability, n is the volume (e.g., annual number of plates, volume of GDL), A and B are known shape parameters of the equation to

Table 6.7: Line parameters for the learning curve function.

Component	Volume	Yield (%)	Availability (%)	Setup Time (mins)
Membrane(m^2)	13950[160]	80[14]	80[42]	n/a
	6975000[160]	95[42]/99[14]†		
CCM(m^2)	10000	70	70	60
	1000000	99.9[14]	95	5/10††
GDL(m^2)	1000	80[14]	70	60
	1000000	99.5	95	5
MEA(m^2)	1000	80	70	60
	1000000	99.5[14]	95	10
BIP (ea.)	100000	60[14]	70	60
	10000000	99.5	95	5
Stack Assy (ea.)	500	100	80	30
	50000	100	95	5

† Non-reinforced/Reinforced
†† Slot-die/NSTF

be solved for. Linear regression techniques can be used to solve the above equation by first linearizing using the natural log to yield:

$$ln(y) = ln(A) - n * ln(B) \tag{6.3}$$

or

$$ln(y) = ln(A) - log_{10}(n) * ln(B) \tag{6.4}$$

where the base 10 logarithm is more convenient to use due to the multiples order of magnitudes for the volumes. Solving Equation 6.4 requires two data points that represent the extremas (best and worst values). For the data points $(N_1, 1Y_1)$ and $(N_2, Y2)$ the function for the learning curve can be solved as:

$$A = exp\left\{ln(Y_1) + \frac{log_{10}(N_1)}{log_{10}(N_2) - log_{10}(N_1)} * (ln(Y_1) - ln(Y_2))\right\} \tag{6.5}$$

and

$$B = exp\left\{\frac{ln(Y_1) - ln(Y_2)}{log_{10}(N_2) - log_{10}(N_1)}\right\} \tag{6.6}$$

Applying the learning curve equation for all volumes, it is assumed that volumes less than N_1 and greater than N_2 will be equal to Y_1 and Y_2, respectively. As an illustrative example or the curves, Figure 6.14 plots the line yield, availability, and setup times for the GDL and a list of the parameter values for all components incorporated in the model is shown in Table 6.7. Note that values lists are regarded as educated assumption with certain data points referenced.

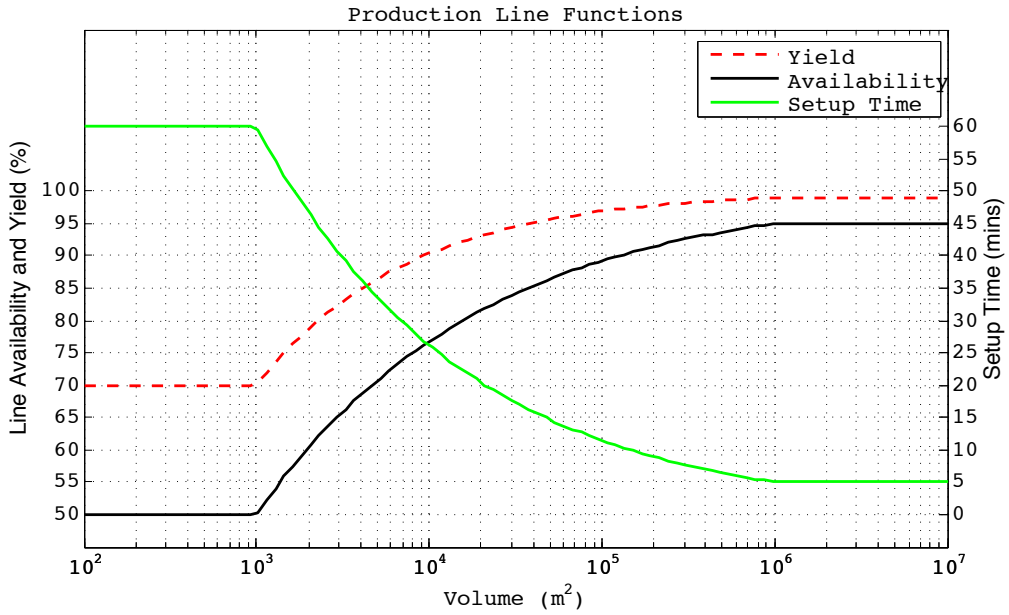

Figure 6.14: Example of the yield, availability, and setup time by volume for the GDL.

6.6 Process and Machine Tool Scale

The majority of the processes and process flows for fuel cell manufacturing was covered in Chapter 5 with more detailed unit process models (i.e., compression molding, injection molding, stamping) covered in detail in Chapter 3. This section provides and overview of the manufacturing parameters incorporated in the process and machine tool scale modeling. The values listed in the tables represent the expected values where actual values are determined in-situ during the production line modeling (e.g., line yields that translate to material masses) and the unit process model where the energy consumption is determined in hourly intervals from the facility model. A more detailed breakdown as well as the remaining inventory data such as material costs and the LCI impact factors can be found in the Appendix A6.

Membrane

An overview of the roll-to-roll non-reinforced cast and reinforced soak membrane process was covered in Chapter 5. The same manufacturing flows are incorporated in the model due to the assumption that the membrane is a purchased component for all production volumes and DVI. The details of the parameter inputs and the calculated direct masses can be found in Table 6.8. The lines speed and tool costs were estimated by interpolating the data obtained from [160] as a function of manufactured volume. The results of the interpolation for both membrane type are shown in Figure 6.15. Furthermore, the tool power for the reinforced membrane was obtained by the same reference and interpolated with respect to the line speed.

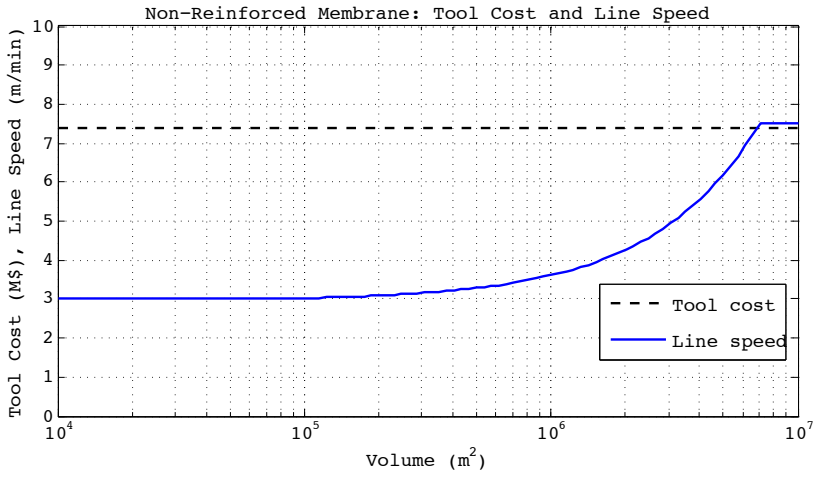

(a)

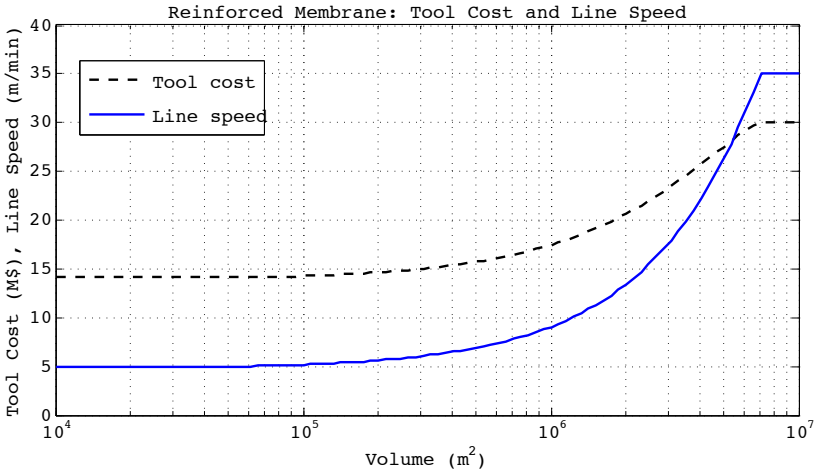

(b)

Figure 6.15: Membrane tool cost and line speed as a function of production volume.

Table 6.8: Membrane manufacturing parameters and calculated direct materials for a complete stack.

Parameter	Units	Non-Reinforced	Reinforced
Web width	m	0.61[83]	1
Line speed	m/min	See Figure 6.15a	See Figure 6.15b
Tool size	m^2	30[42]	20[160]
Line power	kW	140[42]	4.17×{Line speed}+204.2[160]
Tool cost	2013USD	7,400,000	See Figure 6.15a
Material masses			
Nafion®	g/stack	792.6	376.5
ePTFE	g/stack	0	20.11
Consumables masses			
Isopar-K	g/stack	0	5.69

Table 6.9: CCM manufacturing parameters and calculated direct materials for a complete stack.

Parameter	Units	Slot-die	NSTF
Web width	m	0.5[159]	0.4[160]
Line speed	m/min	4[180]	5.84[160]
Tool size	m^2	9.6[180]	6.2
Line power			
Process	kW	40.3	141
Baseline	kW	19.7	350
Tool costs	2013USD	995,000[159]	1,260,000[160]
Material masses	g/stack		
Platinum		40.05	12.02
Carbon black		60.08	0
Nafion®		24.03	0
Perylene Red		0	2.24
Consumables masses			
DPG	g/stack	456.6	0
Methanol	g/stack	43.38	0
DI Water	g/stack	43.38	0
Argon	g/stack	0	1.5×10^{-4}
Kapton®	g/stack	1282	1282

CCM

The manufacturing parameters and calculated direct material masses for the slot-die coated and NSTF CCM are shown in Table 6.9. The table shows that the NSTF process is more energy intensive, however, has a lower catalyst (platinum) mass and does not require to use of multiple chemical consumables. The Kapton® is a protective polyimide film manufactured by DuPont that serves as a backing substrate layer for the coating. The model assumes that the Kapton® is discard and not recycled after CCM lamination.

Table 6.10: GDL manufacturing parameters and calculated direct materials for a complete stack.

Parameter	Units	GDL A	GDL B	GDL C
Web width	m	0.4	0.8	1.2
Line speed	m/min	1.5/10[160]† + 3(m)/n.a.(a)		
Tool size	m^2	21.4(m)	42.8(m)	n.a.(a)
	m^2	19.4(a)	38.8(a)	58.2(a)
Line power				
Process	kW	28.5(m)/59.5(a)	n.a(m)/71.1(a)	n.a(m)/100(a)
Baseline	kW	38.4(m)/93.5(a)	n.a(m)/94.4(a)	n.a(m)/ 117.6(a)
Tool costs	2013USD	633,000(m)	979,000(m)	1,382,000(m)
	2013USD	670,000(a)	1,036,000(a)	1,462,000(a)
Material masses				
Carbon fiber	g/stack		400.5	
PTFE	g/stack		304.4	
Carbon black	g/stack		256.3	
Graphite	g/stack		132.2	
PF resin	g/stack		528.7	
Consumables masses				
PVA	g/stack		80.1	
Methanol	g/stack		2115	
Water	g/stack		19380	
Nitrogen	g/stack		23460	
Triton X-100	g/stack		28.04	

†1.5m/min for in-house mfg. and 10m/min for supplier

GDL

The GDL process flow is a two step manufacturing process that is dependent on the DVI. At a DVI of less than 4, the entire GDL (macro porous layer substrate and mirco porous layer, (MPL)) is purchased and is assumed to be manufactured at the highest capacity (i.e., largest width). At DVI4 the application of the MPL is preformed in-house while the carbon fiber paper substrate is purchased. The size of the MPL manufacturing line is dependent on the production volume. Table 6.10 shows three options for in-house GDL manufacturing (note option C is selected is the GDL is out-sourced). The production line model automatically selects the line size such that the minimum number of simultaneous GDL lines are required. Furthermore, each option is split into two process flows with manual inspection (m) and automated in-line inspection (a). The obvious advantage of the automated inspection is the reduced cycle time as indicated by the line speed. However, the tool cost and energy consumption increases when the automated inspection is added.

MEA

The MEA process refers the joining of the CCM and GDL layers prior the full framed assembly. Two options for joining are considered: film adhesive and liquid adhesive. The

Table 6.11: MEA joining manufacturing parameters and calculated direct materials for a complete stack.

Parameter	Units	Film Adhesive	Liquid Adhesive
No. cavities		2	2
Cycle time	sec/MEA	90	70
Tool size	m^2	16	18
Line power			
Process	kW	3.7	4.0
Baseline	kW	30.8	29.2
Tool cost	2013USD	587,000	847,000
Material masses			
Film adhesive	g/stack	42.92	0
Liquid Adhesive	g/stack	0	66.91

film adhesive is assumed to a double sided adhesive that is picture frame cut to cover the edges of the MEA and hot pressed to join. The exact material of the film adhesive was not obtainable due to propriety reason, however, it is assumed to be HDPE based (film) coated with a polyurethane based adhesive. The liquid adhesive requires the application of a screen printer to coat the edges of the MEA and in most cases UV cured prior to hot pressing. The advantage of the liquid adhesive is the potential for less material scrap due to high utilization, however, at the expense of higher capital costs and energy consumption. Likewise, the material for the liquid adhesive is highly propriety. Searching for a suitable UV curable adhesives online resulted in the Henkel Loctite 5251 [138] and 3526 [137]. Due to the uncertainty of the material and available of the data (cost and LCI), was assumed that liquid adhesive consisted of the same polyurethane adhesive material. Post joining the precut MEA is placed into a CNC plotter where the excess edges of the MEA are trimmed and discarded. The manufacturing and material parameters can be found in Table 6.11.

Frame

The manufacturing flow for the framing and sealing of the MEA is a batch process where individual MEAs are processed one at a time. In Chapter 5, it was suggested that a roll-to-type type process is possible as presented by the 3M patent, however, the technology is considered to be to be extremely nascent and out of the scope of the time frame and production volume of interest. The manufacturing parameters are listed in Table 6.12 with two sets of alternative process flow for each denoted by the number of cavities. For the MESA architecture, the liquid injection molding (LIM) process is used with silicone as the sealing material. The MEFA framing takes advantage of thin-film roll process, therefore a hybrid roll-to-roll and batch processing is assumed as shown in Figure 6.16. Roll thin-film sheets of the frame material, assumed to be polyethylene naphthalate (PEN), is picture frame punch to expose the active area and manifolds. A robotic arm sandwiches two framed sheets with a MEA and is transferred to the hot precess for lamination. At low levels of production for

Table 6.12: Frame and seal manufacturing parameters (split by cavity size) and calculated direct materials for a complete stack.

Parameter	Units	MESA	MEFA
No. cavities		1/2	1/2
Cycle time	sec/MEA	90.7/64.2	95/50
Tool size	m^2	7.6/7.8	7.4/7.6
Line power			
Process	kW	0.9/1.1	1/1.3
Baseline	kW	14.1	9.3
Tool cost	2013USD	255,000/318,000	402,000/468,000
Material masses			
Silicone	g/stack	2788	0
PEN	g/stack	0	1152

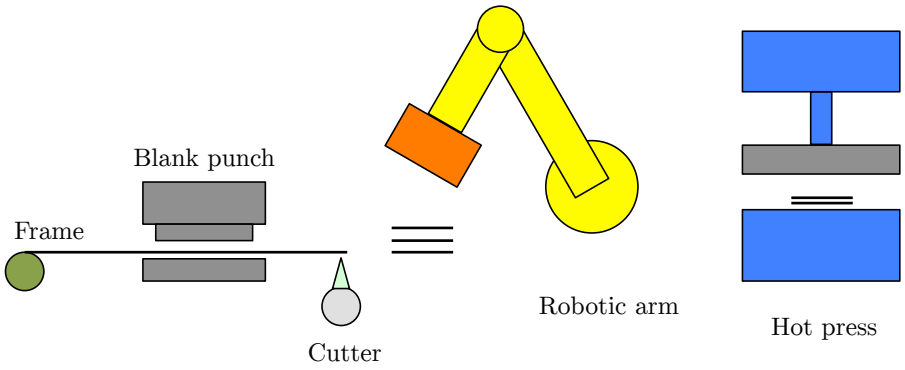

Figure 6.16: Visualized manufacturing flow for the MEFA architecture.

both technology options it is assume that only one cavity (LIM for MESA and hot press for MEFA) is utilized and the transition to duel cavity is determined by the line model.

Bipolar Plates

The manufacturing of the BIP is split into a total of four pathways depending on the material type. For carbon and metal plates the primary differentiating process is the molding step and coating process, respectively. Carbon plates with a thermoset set material (epoxy resin with graphite filler) are compression molded after the mixing and extrusion of the plate. It is assumed that the material is extruded and cut at the same dimensions of a half-plate and hence the molding process is to from only the channels and manifolds. The thermoplastic BIP utilizes polypropylene with graphite and carbon black fiber and is injection molded. The process assumes that the material is pelletized and feed into the injection molding unit where the plate is automated molded and ejected. The remaining process steps are equivalent with the exception of an additional oven cure for the compression molded plates (required to cure the resin). For each molding operation two sets of batch sizes are considered in

Table 6.13: Carbon BIP manufacturing parameters (split by batch size) and calculated direct materials for a complete stack.

Parameter	Units	Compression Molding	Injection Molding
Batch size	BIP	180/360	90/180
Press size	U.S. tons	420/840	240†/670
Cycle time	sec/BIP	60.1/36.5	60.2/30.1
Tool size	m^2	25.5/50.1	24.6/50.9
Line power			
Process	kW	2.0/11.9	8.8/196
Baseline	kW	26.5/54.3	47.2/99.6
Tool cost	2013USD	1,239,000/2,222,000	623,000/1,279,000
Material masses			
Epoxy resin	kg/stack	9.3	0
Graphite	kg/stack	37.3	26.7
Polypropylene	kg/stack	0	12.0
Carbon black	kg/stack	0	1.41
Adhesive	kg/stack	0.20	0.20
Silicone	kg/stack	0.18	0.18

†For a single half-plate molding

a similar manner as the framing process where the line model determines the appropriate batch size for a given volume. Furthermore, it is assumed that the larger batch size the inspection procedure switches from manual to automated visual inspect. The batch size for the injection mold process is halved due to the limitations in pressing capacity. As shown in the manufacturing parameters table, Table 6.13, transitioning from a single (one half-plate) cavity to a dual cavity injection molding requires nearly three times the press force.

The process flows for the metal BIP are nearly identical for both coating procedures with the manufacturing parameters listed in Table 6.14. Figure 6.17 layouts a representative manufacturing flow for high volume PVD coated metal BIP. The plate stamping process to the last clean step are identical for both metal BIP types with the differentiating process being the PVD or thermal nitriding coating process. The PVD option assume a sputtering type technique is used to deposit the film material, CrN, using chromium sputtering targets in an nitrogen rich environment. The thermal nitriding option does not require additional chromium material and utilizes the chromium in the stainless steel to form the protective layer via diffusion of nitrogen. Similarly to the carbon plates, the manufacturing flows are split by batch size, however, it is assumed that the number of cavities for the stamping process is constant.

In terms of the stamping operation, it is assumed that roll of sheet stainless steel metal is directly feed and automatically progressed. The process also assumes that progressive die stamping is used where multiple die sets can be utilized for higher production throughputs. Figure 6.18 shows the layout of the die sets that forms the channels and punches out the manifolds (and blank cuts the plate from the stock sheet metal). For each stamp cycle a complete BIP is produced due to the duel stamping of the anode and cathode half-plate and

Table 6.14: Metal BIP manufacturing parameters (split by batch size) and calculated direct materials for a complete stack.

Parameter	Units	PVD Coated	Thermal Nitrided
Batch size	BIP	50/100	50/100
Press size	U.S. tons	400	400
Cycle time	sec/BIP	12.4/7.1	14.4/7.2
Tool size	m^2	35/47	31.3/39.8
Line power			
Process	kW	12/47.5	10.5/31
Baseline	kW	26.6/38.6	24.9/48.1
Tool cost	2013USD	2,813,000/3,880,000	2,580,000/3,530,000
Material masses			
Stainless Steel	kg/stack	18.4	18.4
Chromium	kg/stack	0.2	0
Silicone	kg/stack	0.18	0.18
Nitrogen	kg/stack	0.052	0.49
Consumable masses			
Argon	kg/stack	0	0.098

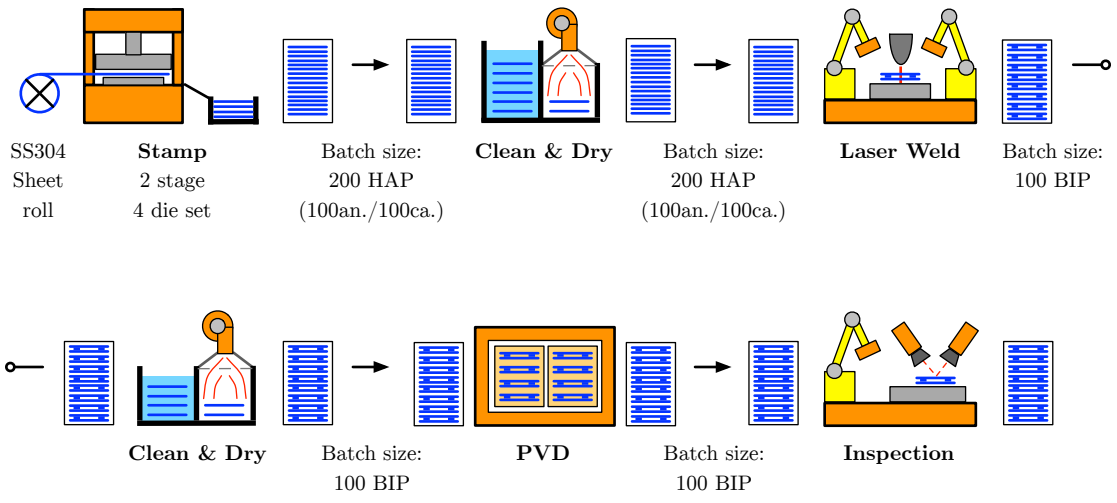

Figure 6.17: Visualized metal BIP manufacturing flow (at high volumes).

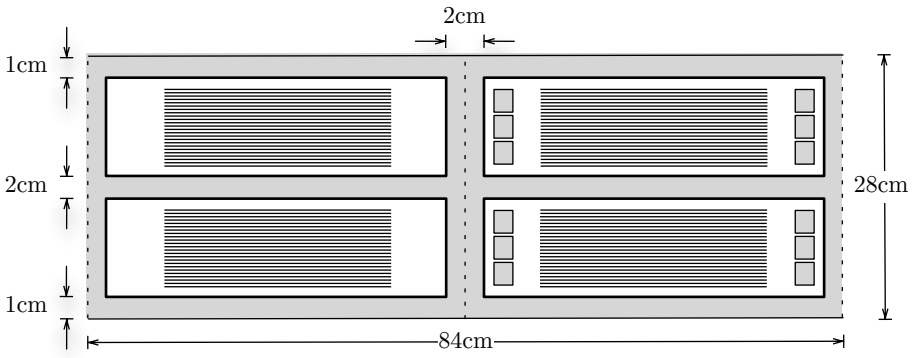

Figure 6.18: Die layout for duel cavity anode and cathode stamping.

the multiple die sets. The scrap metal from the manifolds and the blanked sheet metal can by recycled, which is option for the end-of-life module.

Stack Assembly

The assembly of the fuel stack is modeled as two separate flows. At low volumes manual stacking of the plates is considered whereas a robotic stacking system in implemented at high volumes. Figure 6.19 shows the process for a manual stack operation (6.19a) and semi-automated stacking (6.19b). The semi-automated flow still requires manually stacking the cathode (or anode) end of the stack hardware before loading into the stacker. Likewise, after stacking is complete the remaining stack hardware is manually assembled. Both flows utilizes an automated compression tool that compressions and measures the appropriate stack compression pressure. For process flow (a), the steel strap bands are manually place and welded whereas the strapping and welding is automated in process flow (b). The manufacturing data for the stack assembly is shown in Table 6.15.

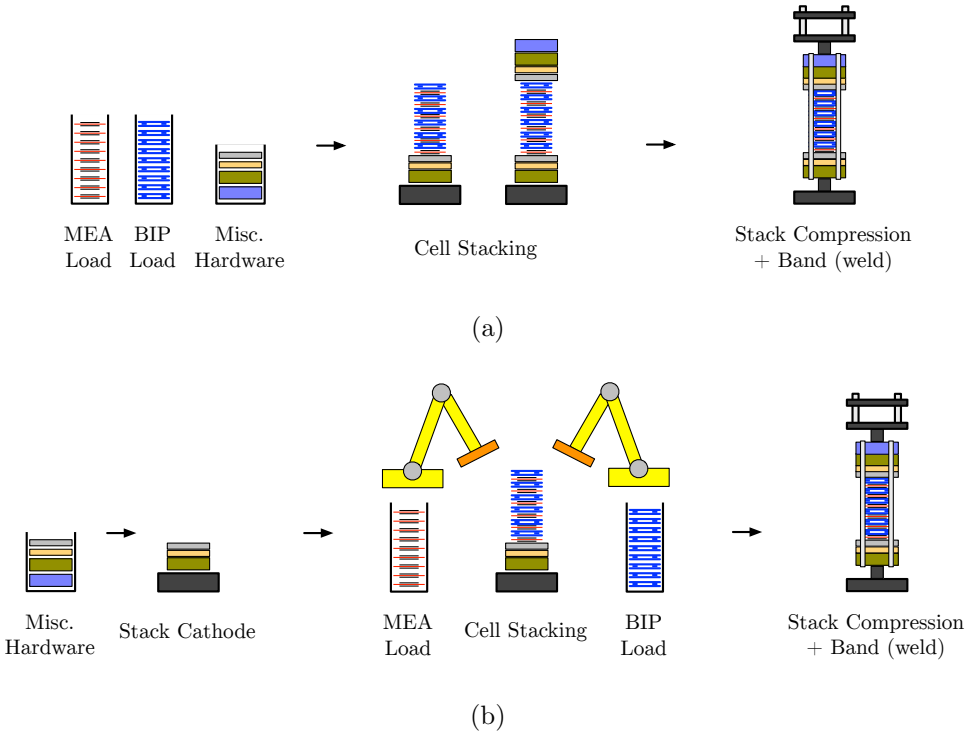

Figure 6.19: Visualized stack assembly for low (a) and high (b) volumes.

Table 6.15: Stack assembly manufacturing parameters and calculated direct materials for a complete stack.

Parameter	Units	Manual	Semi-Auto
Cycle time	min/stack	60.9	24.8
Tool size	m^2	10	19.5
Line power			
Process	kW	0.7	5.6
Baseline	kW	6.5	11
Tool cost	2013USD	110,000	550,000
Material masses			
Copper	kg/stack	0.54	
PA6,6 GF filled	kg/stack	2.15	
Stainless steel	kg/stack	3.44	
Steel	kg/stack	0.96	
Aluminum	kg/stack	6.0	

Chapter 7

Model Results

A model using the iSLCD framework with integrated SGM was created for the environmental and economical assessment of PEM fuel cell stacks. The design variables considered in the modeling include two each for the membrane, CCM (i.e., catalyst layers), MEA manufacture, frame, and four designs (two each carbon and metal plates) for the BIP, yielding a total of 64 design combinations. Each set of design combinations had a corresponding production volume (PV) and DVI. With six levels of PVs (100, 500, 1000, 5000, 10000, 50000) and five DVI scenarios (0, 1, 2, 3, 4) the total number of design iterations amounted to $64\times6\times5=1920$. A detailed coverage of all 1920 combinations will not be covered for practicality reasons. Instead, the design options are grouped into two two technology types: *Reference* and *Future*. Reference is the base case and denotes the design that assumes to closely represents the current status of Daimler's F-cell stack. The Reference design includes a unreinforced cast-type membrane, slot-die coated CCM, film adhesive MEA, MESA architecture, and compression molded carbon BIP (recall there is only one design option for the GDL and stack hardware). The Future technology, as the name suggests, denotes the assumed design for future generation stacks based on communications with Daimler and various sources in literature. The options for the Future design include a reinforced soak-type membrane, NSTF catalyst layers, liquid adhesive MEA, MEFA architecture, and stamped metal BIP with PVD coating. Note that the future stack design is not necessarily superior to the reference design, and in fact are assumed to have to equal performance, but merely indicates the direction of the fuel cell industry for automotive applications. In addition to the two technology options, two of PV- 100 and 10000, and two of DVI- 1 and 3 stages will be emphasized and considered throughout all results. The PV100 represents the current status of fuel cell manufacturing today whereas a PV of 10000 represents the potential volume of the next one or two generation stacks. Likewise, a DVI of 1 has been chosen to most closely reflect the enterprise level of Daimler's F-Cell and a DVI of 3 for the forecasted level at high volume production. The remaining design options, namely the injection molded and thermal coated BIPs, and the various permutation options will be reflected in the sensitivity analysis.

The presentation of the results are as follows. Section 7.1 covers the the overview of

GWP and cost results from the Monte Carlo simulation and compares the results to already publish data from literature. Section 7.2 details the breakdown of the GWP and cost results in terms of per component and per element of manufacturing (e.g., materials, machine tools, infrastructure). Section 7.3 investigates and details the comparison between the four BIP technology options. Section 7.4 analyzes the behavior of the SGM through sensitivity analyses and scenario trade-offs and uses an example of the BIPs to substantiate the necessity of the SGM integration. Lastly, Section 7.5 analyzes the impact of including the end-of-life phases to the overall GWP of the fuel cell.

7.1 Results Overview

Monte Carlo simulations were computed for the Reference and Future designs at several stages of PVs and DVIs. Two sets of simulations were run at 500 iterations for visual purposes of histogram whereas the remaining iterations were conducted at 100 iterations. An overview of the results is presented in Table 7.1. Figure 7.1 and Figure 7.2 shows the initial GWP and cost histogram results for the Reference case at the base scenario of DVI1 and at a PV100 and PV10000, respectfully. The simulations with 500 iterations generated more well defined probability distribution profiles resembling normal and triangular shaped distributions. As shown in the figure, the GWP of a single Reference design fuel cell stack at current levels of production and DVI scenario is approximately 4480±344kgCO_2e with a cost of \$1700±256/kW normalized on a per kilowatt basis. The same design scaled at PV10000 reduces the the GWP to approximately 3860±236kgCO_2e with the dramatic reduction in costs to \$318±22/kW.

The simulation shows very reasonable bounds of the 95% confidence interval with relative errors for the GWP and cost equaling 8% and 15%, respectfully. Note that although the presented results show 4 significant figures (sig fig) of precision, the appropriate number of sig figs should only be two. The reason being is that due to the inherent uncertainty in the data and model the precision of the standard deviation should only be taken at one sig fig and considering that for all results the standard deviation is roughly an order magnitude smaller than the mean. For instance, the reported result of 4480±344kgCO_2e should be properly reported as 4500±400kgCO_2e (actual standard deviation of 176 rounded to 200). The shape of the profiles have a consistent near symmetrical triangular distribution. A possible explanation is that the majority of the beta functions for the data uncertainty were normal shaped and equal interval distributions. As a result, the interval distributions raises the tail ends and thus creating a triangular type shape. The precision of the distributions at 100 iterations can be confirmed by plotting the convergence rate as a function of the number of iterations. Figure 7.3 shows the convergence rate for the cost component of the Reference case (DVI1, PV10000). As shown in the figure, after approximately 100 iterations the relative uncertainty is bounded by the ±5% standard error interval.

Expanding further beyond the Reference case, it is interesting to compare the effects of production volume and DVI. Figure 7.4 and Figure 7.5 charts the GWP and cost results at the

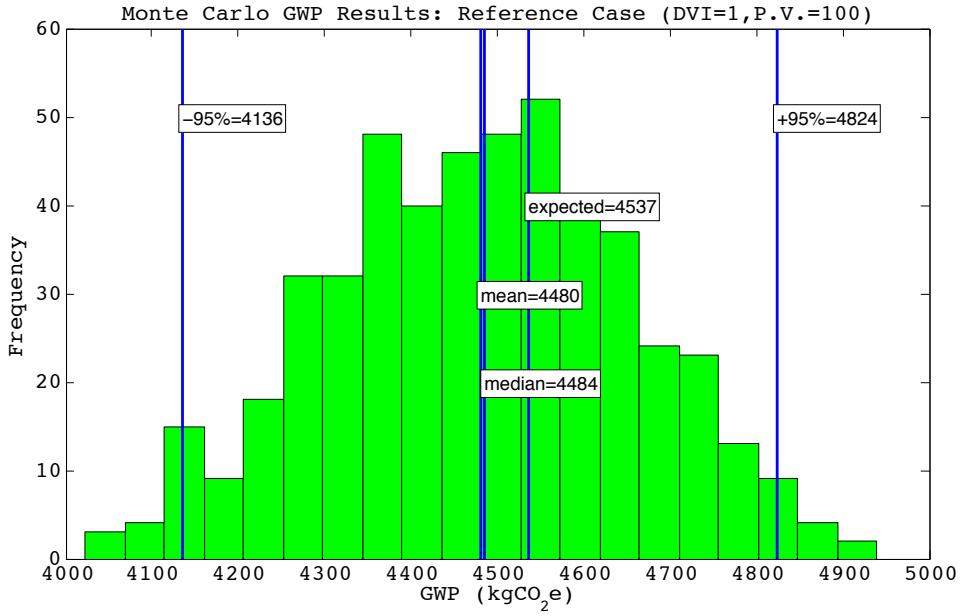

(a)

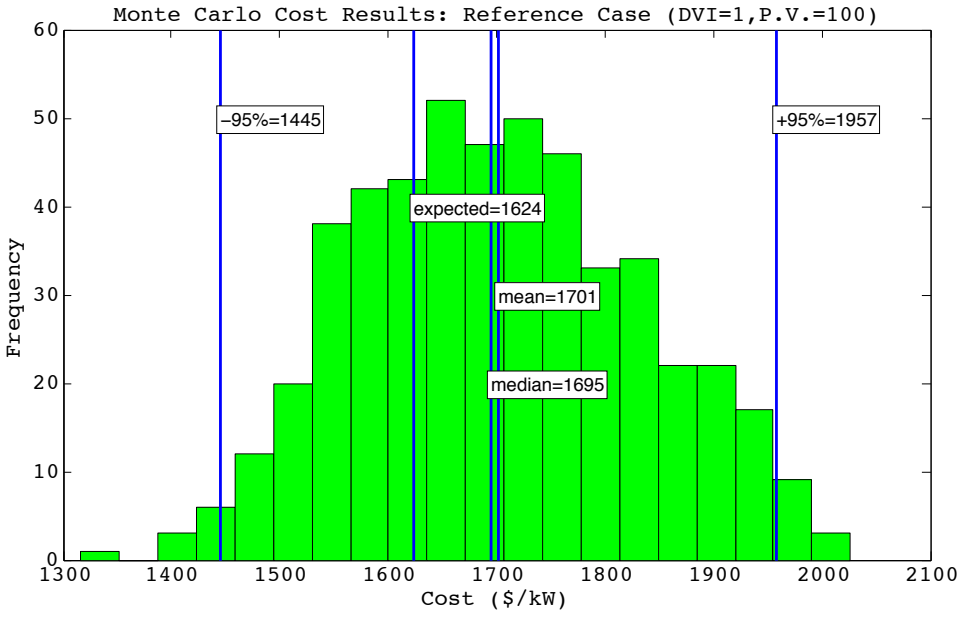

(b)

Figure 7.1: Histogram of results after 500 iterations for Reference case at DVI1 and PV100 for a) GWP, and b) Cost.

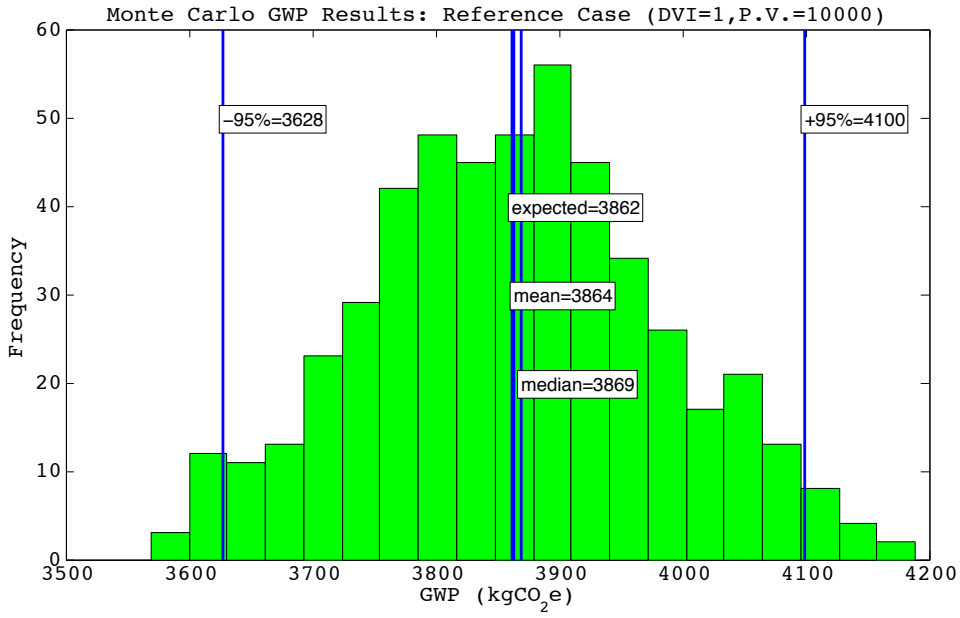

(a)

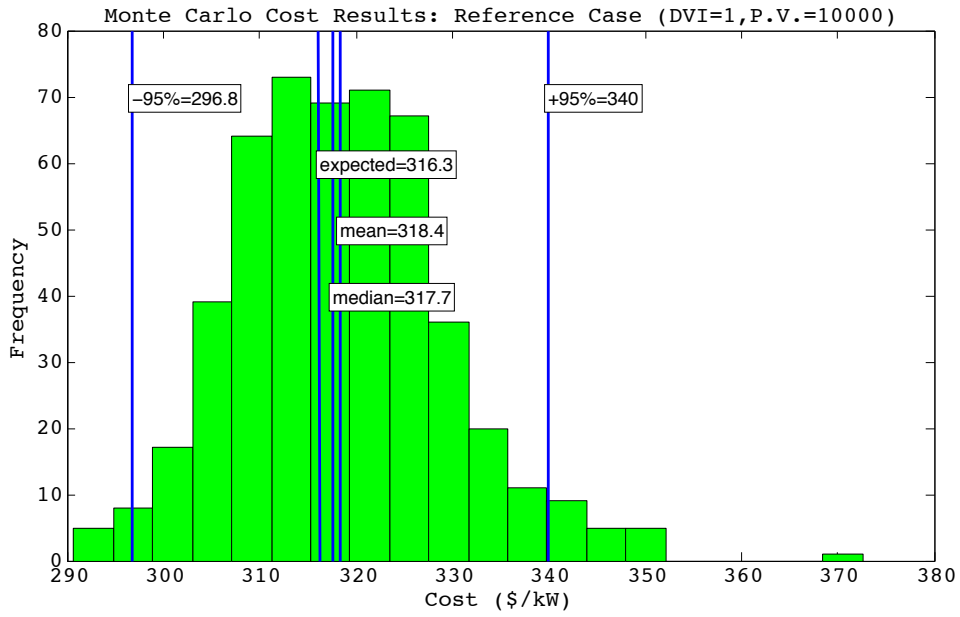

(b)

Figure 7.2: Histogram of results after 500 iterations for Reference case at DVI1 and PV10000 for a) GWP, and b) Cost.

Table 7.1: Summary of Monte Carlo results for GWP and cost.

Option	DVI	PV	Metric	Expected Value	Mean	Median	95% CI	Adjusted Error†	% Change from base case††
Reference	1	100	GWP	4537	4480	4485	344.3	±8.9%	0
Reference	1	10000	GWP	3863	3864	3869	235.8	±12%	-14.9%
Reference	3	100	GWP	5695	5656	5661	490.0	±11%	**25.5%**
Reference	3	10000	GWP	3506	3524	3520	196.0	±5.7%	-22.7%
Future	1	100	GWP	3082	3037	3038	231.5	±6.7%	-32.1%
Future	1	10000	GWP	2178	2199	2197	144.3	±9.1%	-51%
Future	3	100	GWP	4676	4687	4726	623.6	±13%	3.1%
Future	3	10000	GWP	2005	2002	2005	133	±10%	**-55.8**%
Reference	1	100	Cost	1624	1701	1695	256.2	±12%	0
Reference	1	10000	Cost	316.3	318.4	317.7	21.60	±6.3%	-80.5%
Reference	3	100	Cost	2562	2737	2742	427.7	±15%	57.7%
Reference	3	10000	Cost	255.9	261.6	261.0	23.11	±7.7%	**-84.2%**
Future	1	100	Cost	2370	2478	2472	293.412	±8.0%	45.9%
Future	1	10000	Cost	308.1	310.2	310.2	23.57	±6.5%	-80%
Future	3	100	Cost	3570	3797	3743	656.5	±16%	**120%**
Future	3	10000	Cost	277.0	280.1	280.6	22.03	±7.1%	-82.9%

†Taking account the significant figures

††From the expected value

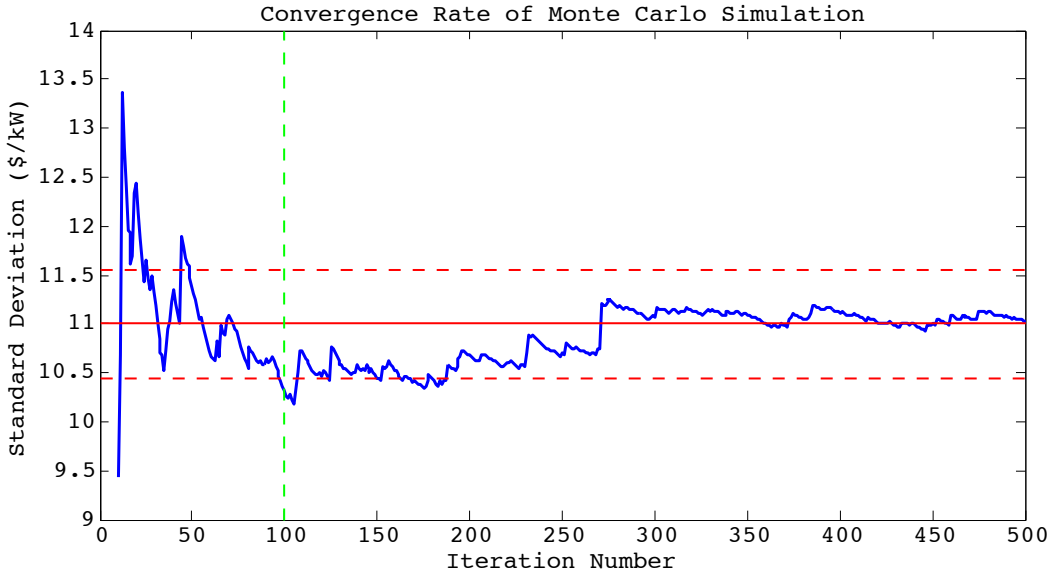

Figure 7.3: Convergence rate of Monte Carlo simulation.

Reference and Future design as a function of the production volume and DVI, respectively. The solid and dotted bars represents the Reference and Future designs, whereas the blue and red bars represent the respective scenarios. There are several notable interpretations that be concluded from the results. Both GWP and costs scale inversely proportional with the production volume, taking advantage of economies-of-scale from the increased level of overall utilization (e.g., materials, equipment, capital). The cost results are more sensitive to the volume where roughly two orders of increased production decreases costs by an order of a magnitude. The variation in production volume (Figure 7.4) shows that it is more advantageous (both GWP and cost) to be at a lower level of DVI (i.e., more horizontally integrated) for low volume production and gradually increase the level of integration with increasing volume with a break even point between 1000-5000 units per year. Another interesting result is from the comparison between the Reference and Future designs. Results show that the Future design has consistently lower GWP (approximately half) than the Reference design for all volumes. In addition the Future design is significantly more volume sensitive with higher costs (roughly 50% increase at same DVI) at low levels of production and decreasing to lower costs at high production. Volume sensitivity also appears in the error bars where generally the error is larger at lower volume (due to volume normalization).

The comparison of the results with varying DVI (Figure 7.5) resonates similar findings as the by volume case. Generally, at constant production volumes, the GWP and cost increases as the DVI increases. The rate of increase varies by design and production volume. The GWP results show a monotonic increase with DVI at low production volumes until stabilizing at near vertical integration. However, as the volume increases the stabilization point occurs at a lower level of DVI as highlighted by the Reference PV10000 case where the maximum GWP occurs at DVI1. The reason for the shift and stabilization is due to the trade-off between the increased volume and marginal increase in impact due to capital/manufacturing. Furthermore, higher DVI translates to more in-house manufacturing (at the MBFC facility) where the local power generation emissions per kWh is significantly lower. In terms of cost, transitioning from DVI0 (completely out-sourced components) to DVI1 (in-house MEA-Frame assembly) at low production volumes has the most significant increase, nearly doubling at each DVI before stabilizing at DVI3.

The results provide a unique multi-dimension view the GWP and cost behaviors under the various scenarios that has not yet been investigated and published in literature. The results show the dramatic increase in the GWP costs when compared to the various publicly available sources. In terms of cost, the U.S. DOE estimate of a hydrogen fuel cell start is currently at \$49/kW (2011 status) [76] for high volume production and the DFMA cost analysis by Directed Technologies (now Strategic Analysis) estimates an 80kW$^{\text{net}}$ hydrogen fuel cell stack at \$145/kW (2010 status) for the production of 1000units/year. The model results for the PV1000 case yields a stack of \$500/kW to \$670/kW depending on the design and DVI. Daimler's own internal assessment shows that for similar production volumes the costs can vary widely from \$250-550/kW [351], well above the the U.S. DOE estimates. In terms of the GWP, assessments found in literature have extremely high uncertainties with very little listings on the assumptions of the analysis. Figure 7.6 shows the model results for

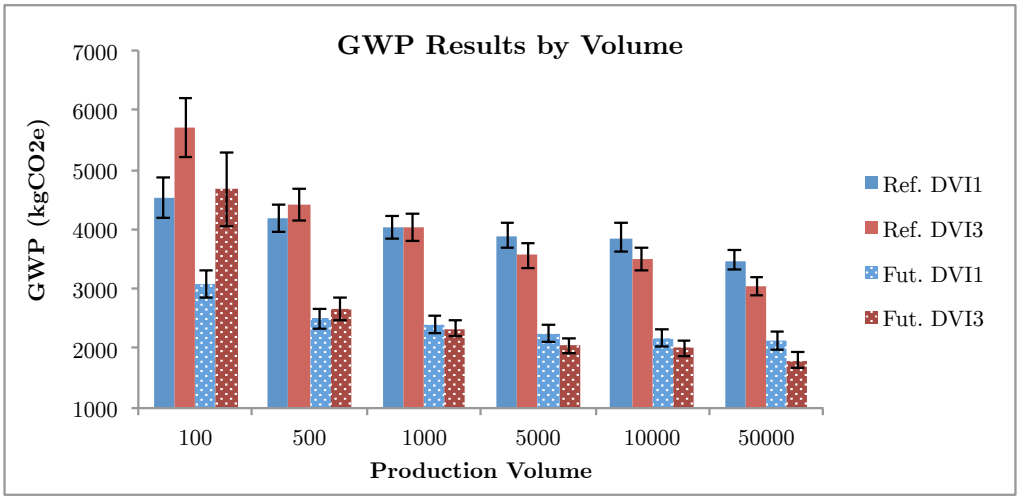

(a)

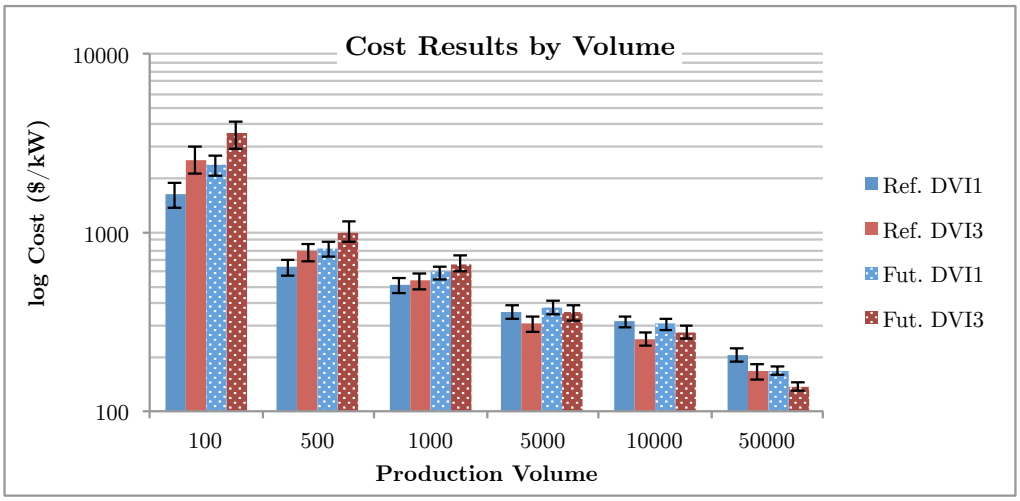

(b)

Figure 7.4: Final results by production volume for a) GWP, and b) cost.

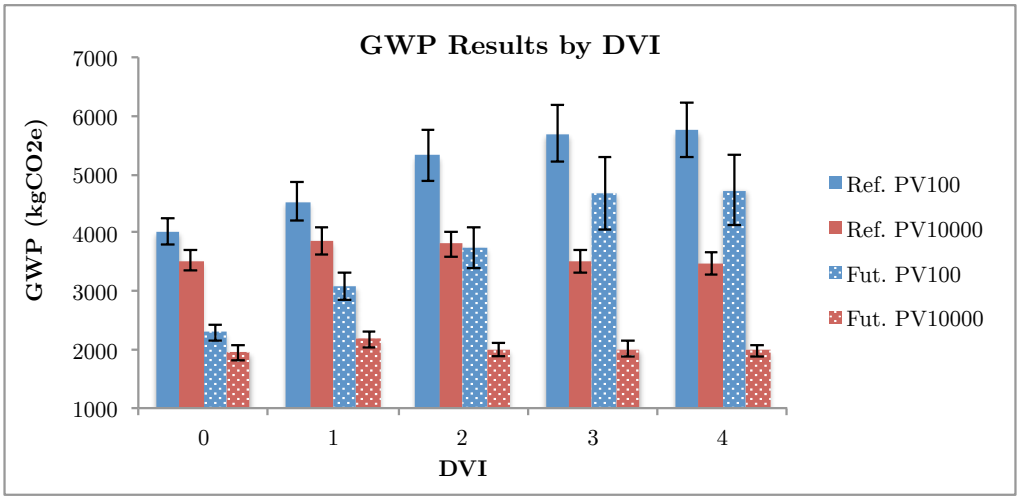

(a)

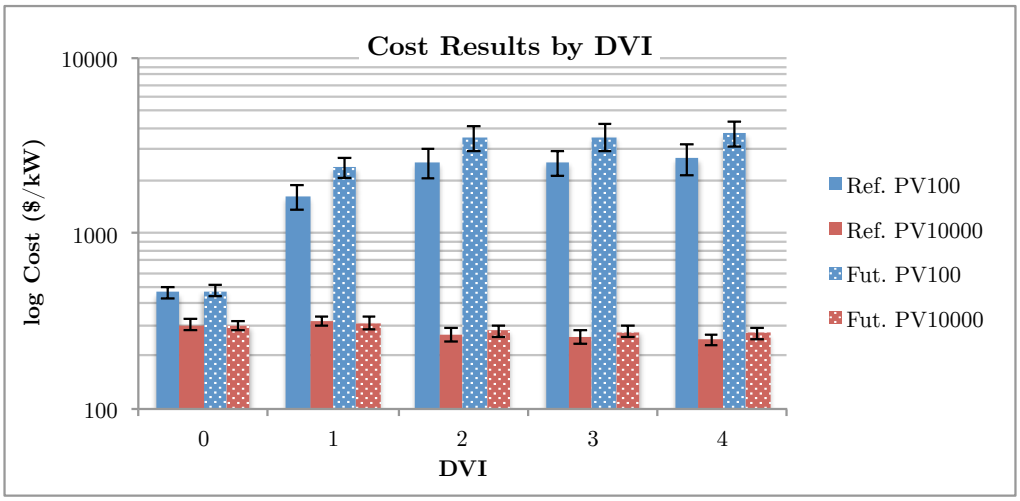

(b)

Figure 7.5: Final results by DVI for a) GWP, and b) cost.

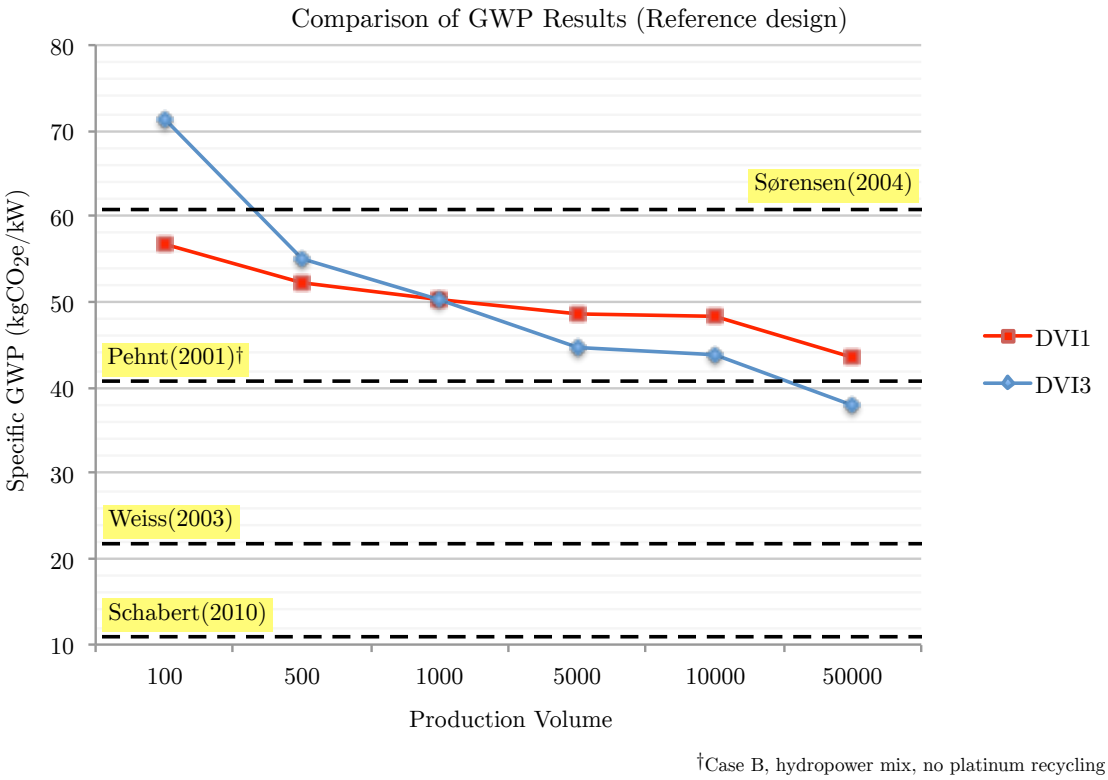

Figure 7.6: Specific GWP ($kgCO_2e/kW$) comparison with literature. Data from [249][308][281][341].

the GWP (normalized to per kW) of the Reference design at DVI1 and DVI3 compared to several reported values in literature. The selection of the Reference design over the Future design was due to the incorporation of the carbon plates and the representative technologies during the time of publishing. The comparison shows that most assessments underestimate the GWP with virtually no robustness in the analysis. The lone exception is the findings from Sørensen[308] where the early stages for Daimler's A-Class fuel cell (production 60-80 units/year) was investigated. Taking account the production volume of 60-80units/year, the model the results at DVI1 and PV100 for Daimler's B-Class fuel cell matches quite well.

7.2 Breakdowns

The breakdown section provides a deeper understanding of the factors contributing to the GWP and cost in terms of the fuel cell stack components as well as to the elements of manufacturing. The breakdown results presented reflect the low (PV100) and high (PV10000) volume cases as well as the base DVI1 and the anticipated DVI3 scenarios.

Figure 7.7 shows the GWP and cost breakdowns by component for the Reference and

Future designs at the base case of DVI1 and PV100 (a-b) and PV10000 (c-d). For both designs the breakdown in component contributions is fairly similar for both GWP and cost, particularly at the lower volume. However, there is a large discrepancy between the component contributions within each design. The largest discrepancy stems from the impact of the membrane where the GWP amounts to less than 5% of the total GWP yet accounts for roughly 50% of the costs for both membrane types, and is particularly exaggerated with the Future design (reinforced membrane). Conversely, at low volumes, the catalyst layers (CCM excluding the membrane) and the processing for assembling the CCM represents approximately 25% of the total GWP while only contributing to roughly 5% (averaged) of the total costs despite the use of expensive platinum for the catalyst. At the high volumes the CCM discrepancy is diminished with contribution percentages nearly equal for both designs. Likewise, the BIPs of both the compression molded carbon composite and PVD coated stainless steel reflect a much larger impact to the total GWP than compared to costs and is fairly consistent for both volumes. The results for the MEA (assembly only) and frame surprisingly shows a relatively large contribution to the overall costs and GWP at low volumes despite contributing to very little mass (only the adhesive and frame) and processing complexity. The primary reason is due to the fact that at DVI1 both the MEA and frame components process are manufacturing in-house, thus contributing to a significant portion of the capital and overhead. As the volume increases the MEA and frame contributions significantly decrease, as expected, with the MEA processing having negligible influence to the stack GWP (0.3% down from 7.9% for the Reference design). The remaining components are less sensitive to the volume as purchased components with the catalyst layer having the least sensitivity with contributions for both the GWP and cost increasing (suggesting that the remaining components decrease in contribution or increase at a much slower rate). An interesting observation is that the entire frame-MEA component (membrane+CCM+GDL+frame) contributes between 65-75% and >90% of the total GWP and cost, respectfully, for both designs and volumes.

A similar analysis can be performed at DVI3 where the components are manufactured in-house (excluding the membrane and GDL). As shown in Figure 7.8, the large majority of the breakdowns are similar to the DVI1 case. The two major differences between DVI1 and DVI3 are the cost contributions of the CCM and the GWP impact of the BIP at low volumes. For the CCM, the contribution increases by an approximate factor of 5 and 10 for the Reference and Future design, respectfully. The large increase is primarily due to the increased capital cost where 85% and 90% of the total CCM cost is attributed to the capital equipment for the slot-die coating (Reference) and NSTF (future), respectfully. From a similar reasoning, the increase in GWP from the BIP is attributed to the embodied energy of the purchased machine tools. The impact from the tool is roughly 14 times higher compared to the equivalent tool of the purchased BIP due to the assumption that a supplier has a much higher tool utilizations from the higher production volumes.

The breakdowns by components give an overview of the key component sensitivities from the stack design perspective. An alternative view is to look deeper into the manufacturing scales in terms of which manufacturing elements, such as materials and energy, have the

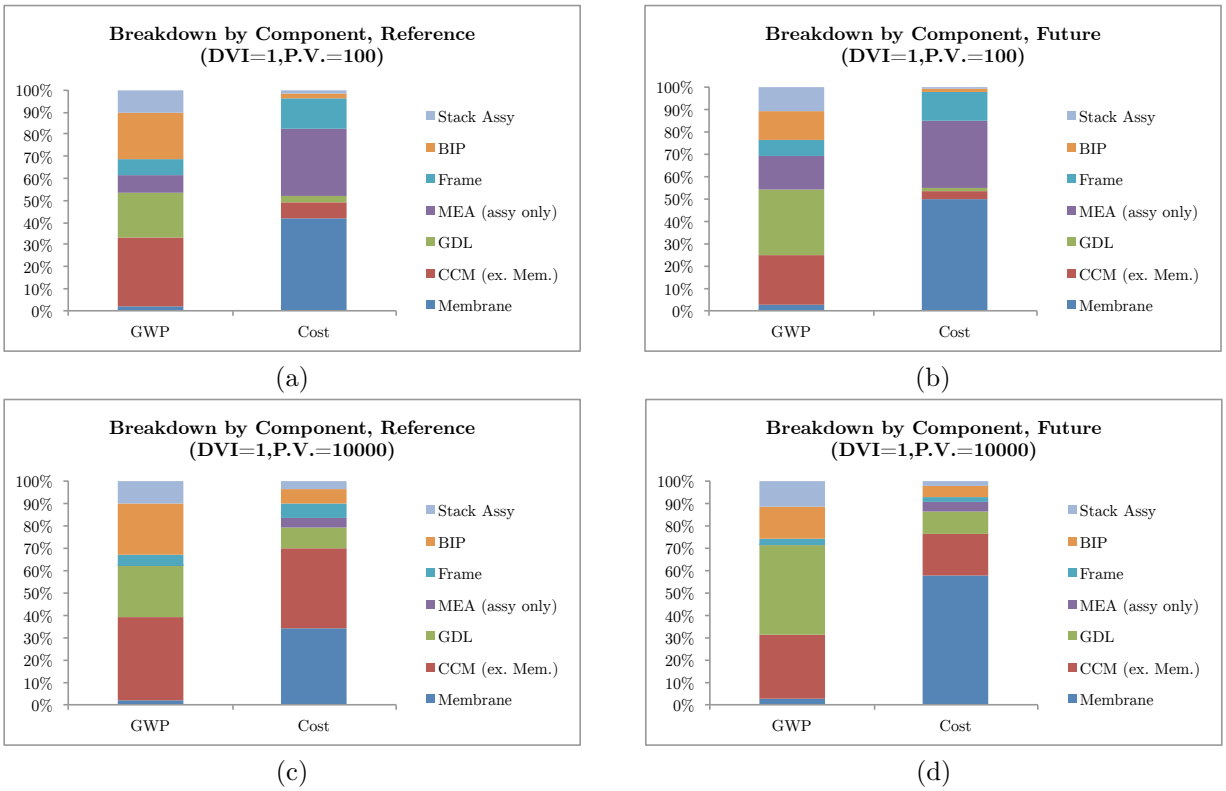

Figure 7.7: Breakdown of GWP and cost by component at DVI1 for a) Reference (PV100), b) Future (PV100), c) Reference (PV10000), and d) Future (PV10000).

highest contributions. Figure 7.9 shows four figures of the breakdowns by manufacturing elements at DVI1, split by GWP and cost by Reference and Future design. The GWP and cost required to be separated due to different manufacturing categories, for example, the effects of labor is not captured in the GWP calculation. For the GWP breakdowns, the contributions from each manufacturing element is consistent between both stack design technologies. In every case, the GWP of the materials, direct from the stack and scrap from manufacturing yield loss, contributes to over 50% of the total GWP, where at least 20% is attributed to the material scrap (note the results does not reflect an end-of-life scenario at this point, which is covered in Section 7.5). The results also show relatively significant contributions from transportation phase with an approximate average of 10% of the total GWP. The most significant contributor to the transportation emissions occurs during the stack transportation from Vancouver to Germany where a stack mass of 65kg and 35kg is shipped over 8000km for the Reference and Future designs. The remaining contributions stems from the embodied energy of the machine tool, which has a higher impact for the Future design components, and the process energy, which slightly decreases with higher tool utilization. The impacts from the infrastructure (i.e., building) is minimal and is overshadowed by the infrastructure energy consumption (i.e., HVAC and lighting).

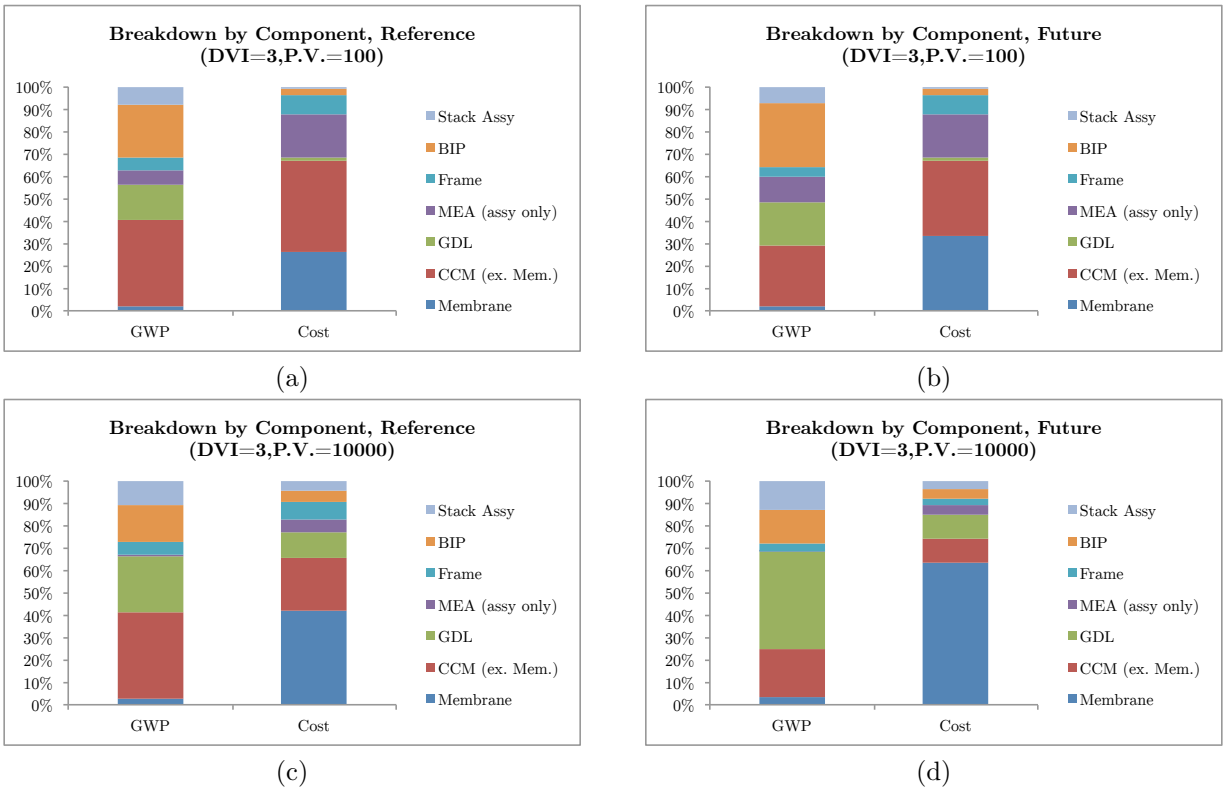

Figure 7.8: Breakdown of GWP and cost by component at DVI3 for a) Reference (PV100), b) Future (PV100), c) Reference (PV10000), and d) Future (PV10000).

The cost breakdowns by manufacturing element reflect another picture. At low volumes the majority of the costs comes from the capital equipment and operational costs. Operational costs are categorized as costs associated with process and tool energy consumption and maintenance costs. The maintenance cost is a fix percentage of the amortized capital costs (common practice) and thereby scaling with volume. Furthermore, as the volume increases causing higher energy consumptions, the cost per kWh decreases thus in effect creating a larger volume discount that decreases faster than the capital cost. The cost results shows a discrepancy when compared to the GWP contributions. The tool GWP (i.e., capital) scales with volume whereas the cost scales marginally or not at all for the Future design case. This phenomenon can be explained by volume discount pricing for electricity and materials. From the BC Hydro electricity rate schedule, the cost per kWh decreases as electricity consumption increases. Furthermore, several of the purchased components, specifically the Nafion® membrane and GDL, have volume discount pricing that does not translate to the GWP (e.g., profit). Therefore, the drastically decreasing operational costs coupled with decreasing material cost results in constant relative contribution of the capital costs. For instance, the decrease in the material GWP and cost from PV100 to PV10000 for the Future design is approximately 0.5% and 13%, respectfully, with decreasing tool energy GWP and

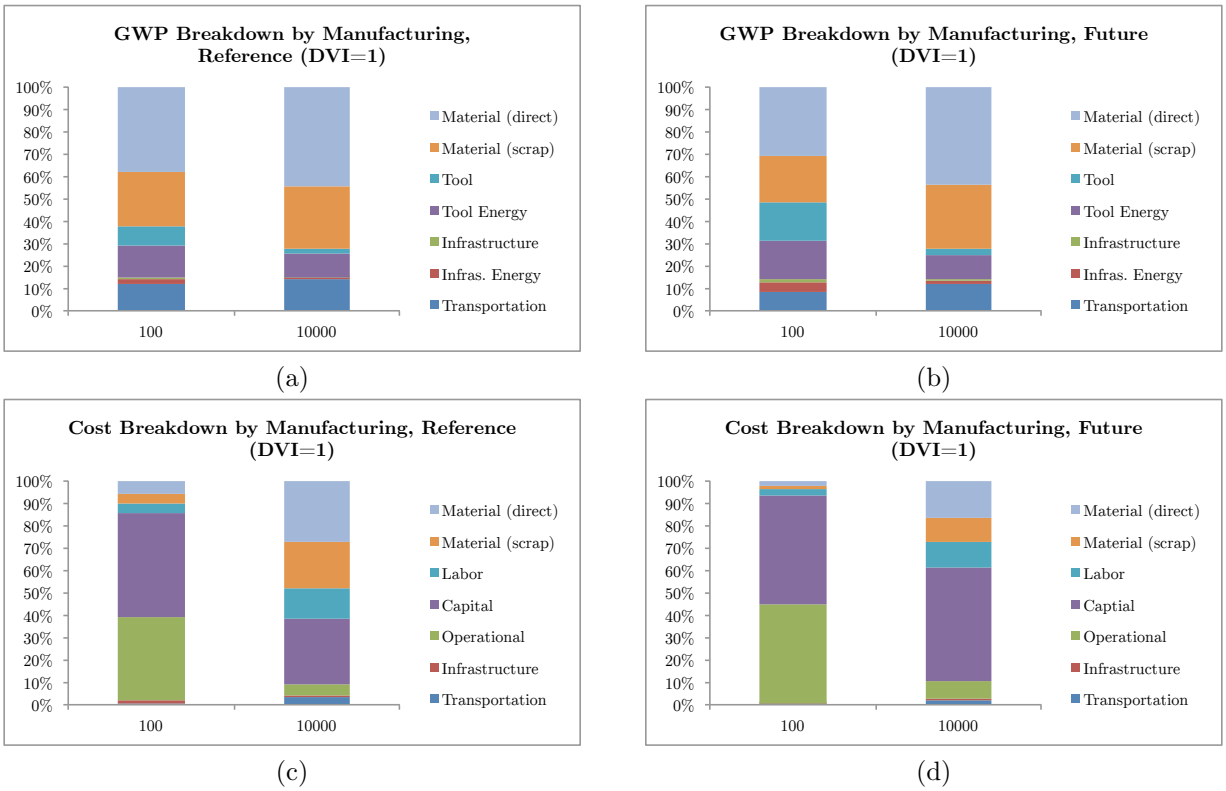

Figure 7.9: Breakdown by manufacturing element at DVI1 for PV100 and PV10000 for a) Reference (GWP), b) Future (GWP), c) Reference (cost), and d) Future (cost).

operation costs of 89% and 98%, respectfully. The results for the DVI3 reflects nearly the same relationships as with DVI1 and can be found in the Appendix A7.

A key realization from the breakdowns of the GWP for all design technologies, DVIs, and production volumes, is the significant contribution of the manufacturing elements that are not traditional captured when conducting a LCI assessment. For instance, the exclusion of material scrap immediately reduces the accuracy of the results by as much as 30% (for PV10000, DVI3). The exclusion of transportation and infrastructure, especially HVAC energy consumption, further reduces the outcome by an average of 15%. Lastly, as will be exemplified in Section 7.4, oversimplification of the process and tool energy consumption may contribute to an additional 10% reduction. Thus overall, improper exclusion of the manufacturing elements may potentially lead to large errors and misleading interpretations of the GWP.

7.3 Bipolar Plate

The bipolar plates presents numerous design and manufacturing options not seen with the remaining fuel cell components. The membrane and GDL are generally supplier constrained, although leverage may shift to the fuel cell manufacturer at the high automotive volumes. The CCM and MEA are generally limited to roll-to-roll processing where the number of design options are few (e.g., limitations on catalyst materials and deposition techniques). The BIPs, however, have numerous degrees of freedom in terms of material selection, processes for each material selection, and the unique design of the plate flow fields. Two unique BIPs are analyzed, carbon and metal BIP, each with two semi-different process flows. For the carbon BIP, the molding of the plates is processed using compression molding (*Compm*) and injection molding (*Injm*), while the metal BIP are split into two different coating process, PVD coating (*PVD*) and thermal nitride annealing (*Thermal*). Figure 7.10 shows the GWP and cost comparisons of all four BIP types at DVI1 for PV100 and PV10000. The results show that the GWP for both metal BIPs are significantly lower than their carbon counterparts at both production volumes. The largest contributor of the GWP is the process and tool energy consumption, particularly for the carbon plates where large activity of thermal processing is required. The advantage of the metal BIP is quite clear. The metal plates can be made thinner and lighter than carbon plates thus reducing both the material and transportation GWP. In both cases the reduction is approximately 70% and for both production volumes. A comparison between the two carbon BIP shows that using the thermoplastic material is preferable over the graphite-resin thermoset (both plates have the same volume). However, the injection molding manufacturing flow results in greater material scrap due to the discarded sprue and runner. Furthermore, although the injection molding process has the lowest machine tool embodied energy, the GWP during the consumption phase is the greatest, despite the additional oven curing step required for the compression molded plates. The GWP difference between the PVD coat and thermal nitrided plates is, not surprisingly, small due to the the coating process being the only difference. However, the overall tool embodied energy and processing energy for the line is approximately 10% and 15% lower, respectfully. Note that influence of production volume at DVI1 is minimal due to BIP being a purchased component.

From the cost perspective, the difference between the plates are greatly reduced with thermal nitrided metal BIP having the lowest cost at both volumes. The breakdown of costs shows two different areas of large contributions. The carbon plates have a high labor cost, primarily due to the longer over all process cycle times. The metal BIPs are penalized with high material scrap costs, which is attribute to both the higher cost of stainless steel compared to the carbon materials and the relatively poor utilization of the sheet metal during stamping. An interesting observation is that the operational cost for the carbon plates is marginally higher that then metal plates whereas the GWP is approximately 5 and 10 times higher for PV100 and PV10000, respectively. Another interesting observation is the negligible infrastructure cost for the metal plates. This can be explained by two factors. First, the overall line cycle time for metal plates is significant lower than the carbon plates as shown in

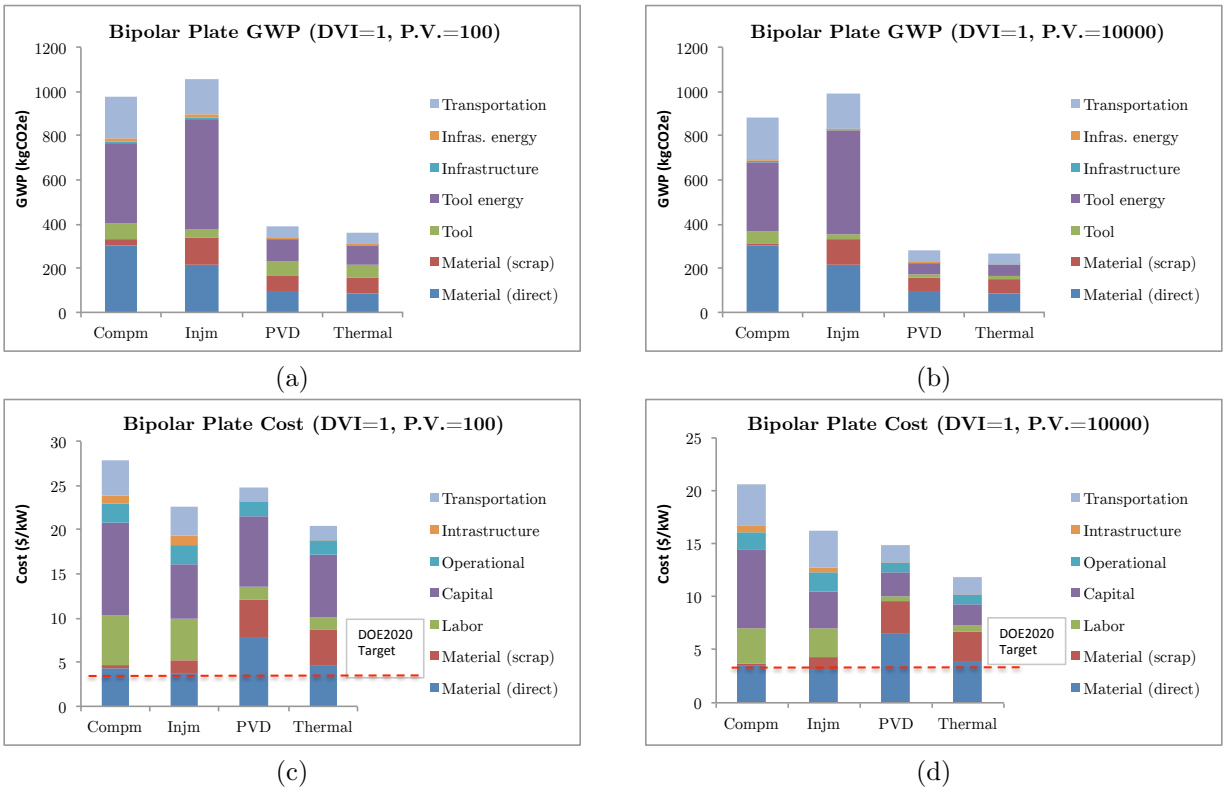

Figure 7.10: Breakdown of the BIP GWP and cost at DVI1 for a) GWP at PV100, b) GWP at PV10000, c) Cost at PV100, and d) Cost at PV10000.

Figure 7.11 where daily BIP is throughput is plotted as a function of the production volume. As clearly seen in the profiles, the metal BIP have a significantly higher process capacity, particularly between the 300,000 to 400,000 mark where the process flow shifts to the larger batch size. Thus for the same production volume the number of simultaneous lines is reduced. The fewer number of lines results in a lower factory floor space cost where the model assumes infrastructure costs scales linear with floor space. Second, the manufacturing of out-sourced metal BIP takes place in the Eastern U.S. location whereas the carbon plates are assumed to be manufactured in Japan where the cost per square-meter of space is approximately twice that of the U.S. (referred to Appendix A6 for the actual values).

For the DVI1 scenario it is obvious that the metal BIP provides and advantage in both the GWP and costs. However, as production volumes increase lower overall stack costs are obtainable at DVI3 as concluded from Section 7.1. The BIP results for DVI3 are shown in Figure 7.12. The affects of vertical integration have significant negative effects on the metal BIP at low volumes. Not surprisingly, the tool embodied energy and capital dominates at low volumes to the point where the metal BIP are significantly more costly with no to little added reduction in GWP. The results show that there is a widespread increase in GWP for all elements except for tool energy consumption. The transportation emissions increase due

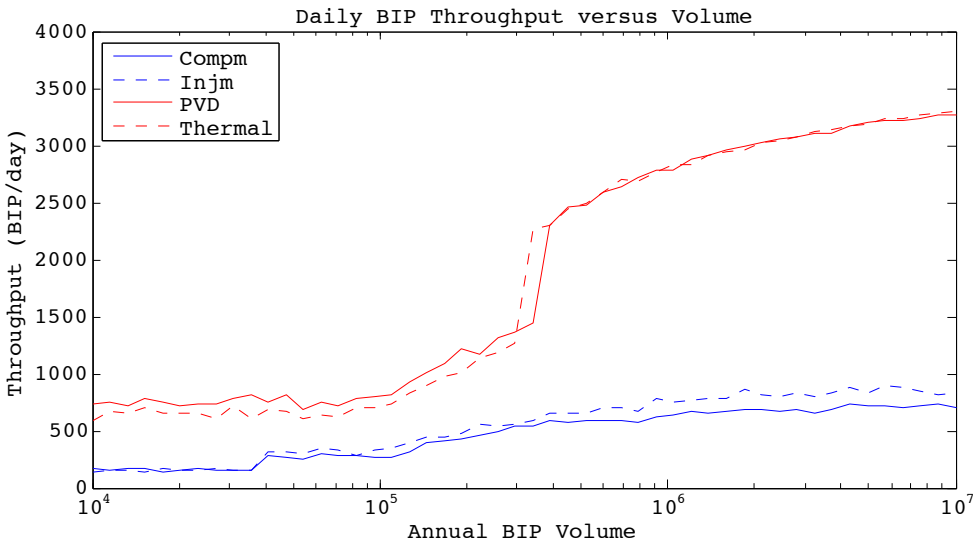

Figure 7.11: Daily carbon (blue) and metal (red) BIP line throughput as a function of production volume.

to both the import of the total raw materials to the MBFC facility and the export of the completed plates (in the stack) to Germany. The material scrap is significantly increased due to lower material utilizations while the infrastructure energy GWP increased due to the inclusion of the overhead facility energy from the office space. The benefit of the in-house manufacturing is apparent with the energy consumption where the impact of tool energy and simultaneously operational costs are decreased due to lower carbon emission and cost per kWh in Vancouver. An interesting observation with the compression molded plates at high volume is the significant reduction in material scrap, which is due to the high material utilization of the process.

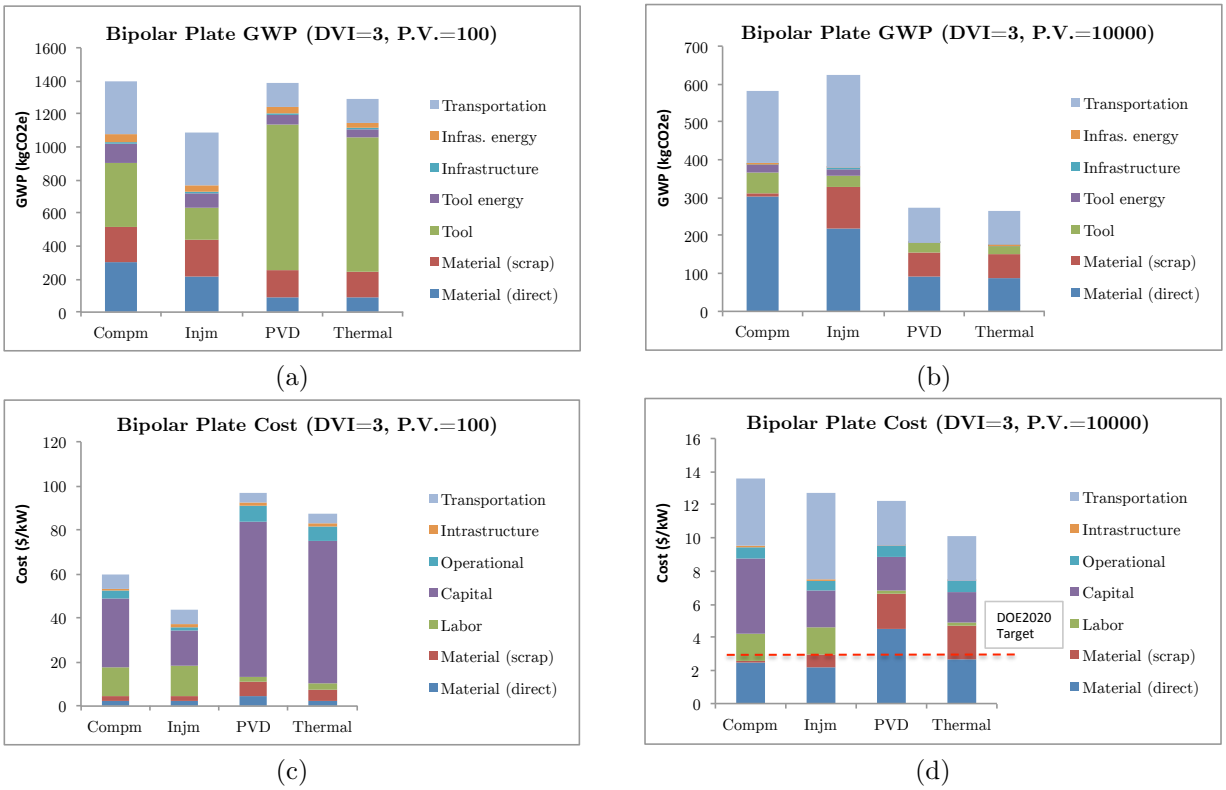

Figure 7.12: Breakdown of the BIP GWP and cost at DVI3 for a) GWP at PV100, b) GWP at PV10000, c) Cost at PV100, and d) Cost at PV10000.

7.4 Sensitivities

The sensitivity and scenario analysis provides a more comprehensive assessment on the behavior of the model and allows the designer to make intelligent decisions for improving the design and reducing the impact of the existing design. A complete sensitivity analysis for all parameters is beyond the presentable capacity this dissertation. Instead, several select parameters and scenarios were chosen to demonstrate the uniqueness of the iSLCD model and provide insight on reducing the GWP and cost of the fuel cell stack. The analysis is presented in manner such that each scale of the SGM is analyzed starting with the influence of the stack design.

Stack Design

A key metric that was excluded from the modeling was the influence of stack performance (assumed to be equal for all designs). However, in reality certain components such as the CCM play a large role in determining the overall performance of the fuel cell stack. Therefore, it is of interest to analyze the model sensitivity to the power density of the cell. The power

density was varied between ±10% around the default value of 10kW/m^2. As a result, the lower bound sensitivity (9kW/m^2) yielded an additional 30 cells while the upper bound (11kW/m^2) yield 24 cells fewer. Figure 7.13 shows the GWP and cost sensitivity results for both design types at low (PV100) and high (PV10000) volumes separated by DVI1 and DVI3. The results show that increasing the performance (power density) of the stack has decreases the GWP and cost. However, the degree of reduction varies between each scenario. For both DVI1 and DVI3 the top three largest sensitivities are (in order): GWP of Reference at PV10000, GWP of Future at PV10000, and GWP Reference at PV100, with the GWP of Reference at PV10000 having a sensitivity factor of greater than one (for the -10% case). On a whole the Reference design is more sensitive to the power density than the Future design, which agrees with the earlier findings of higher manufacturing impact and embodied energy for the Reference design. The sensitivity to manufacturing is further emphasized by the transition from low to high volume where higher manufacturing volumes have a greater sensitivity. However, shifting from purchased components (DVI1) to in-house manufacturing (DVI1) shows a drop in sensitivity. This result suggests that there is greater sensitivity to the components that are purchased, which may be partially explained by the lower GWP per kWh when shifting to in-house manufacturing. The cost sensitivities reflect the same relationship with a much larger change from low to high volume. Intuitively this makes sense because at low volumes the overhead costs outweigh the manufacturing costs and at high volumes the contribution of the added-valued costs such as materials play a much larger role.

Enterprise

At the enterprise scale the question of interest is the change in the location of the enterprise. The analysis considers the scenario in which Daimler's fuel cell production is relocated to the headquarters in Stuttgart, Germany. By doing so the economic cost factors change, the GWP impact of electricity dramatically increases, and the transportation of the fuel cell stack from manufacturing is virtually eliminated. Figure 7.14 shows the GWP and cost sensitivities due to the relocation of manufacturing from Vancouver to Germany at DVI1 and DVI3. As the results show in nearly every case the relocation yields a larger GWP and cost. On average the GWP for the low production volumes doubles and nearly triples for the Reference and Future designs, respectively. This due to the higher manufacturing energy (process and infrastructure energy) per manufactured stack at the low volumes due to lower utilizations. However, at high volumes the sensitivity to relocation becomes a non-factor and even shows preferable results at DVI1. The decrease in sensitivity is attributed to the higher tool and energy utilization and the added benefit of reduced transportation, which does not exhibit the effects of volume discounting. Note, a limitation to these finding is that the input weather data for the HVAC model is the same as Vancouver. This is due to the fact that hourly temperature, solar, and wind data was not readily obtainable. However, the solar angles were modified to account for the change in geographical location.

Another area of interest is the impact of the electricity cost from the incorporation of the dynamic electric tariff rate schedule. Throughout the model it has been assumed that

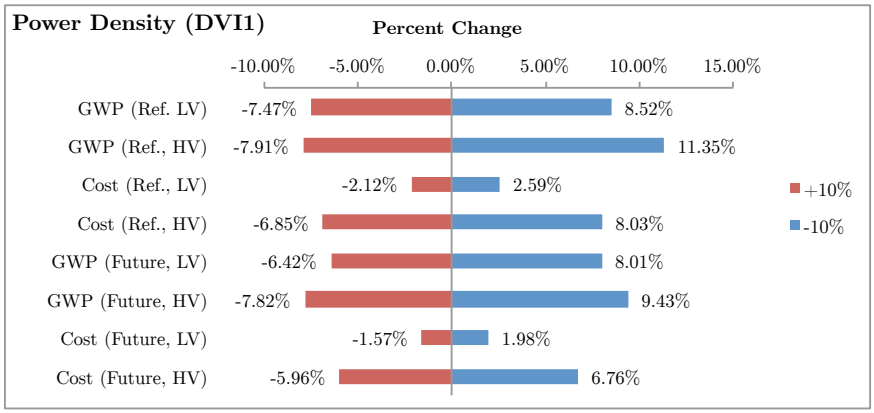

(a)

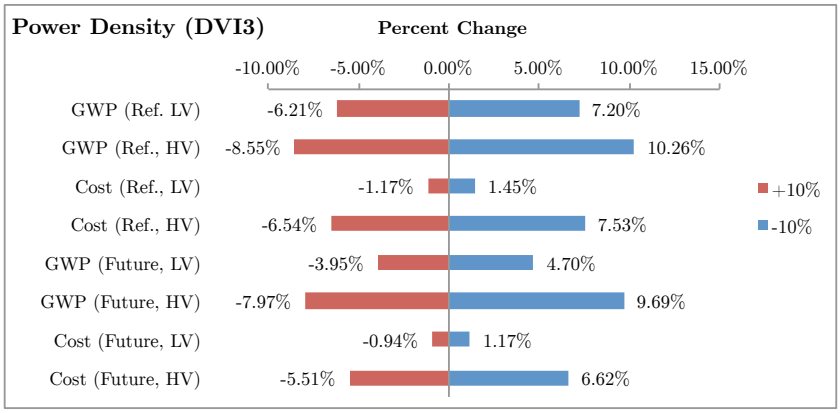

(b)

Figure 7.13: Sensitivity analysis on the stack power density for a) DVI1, and b) DVI3

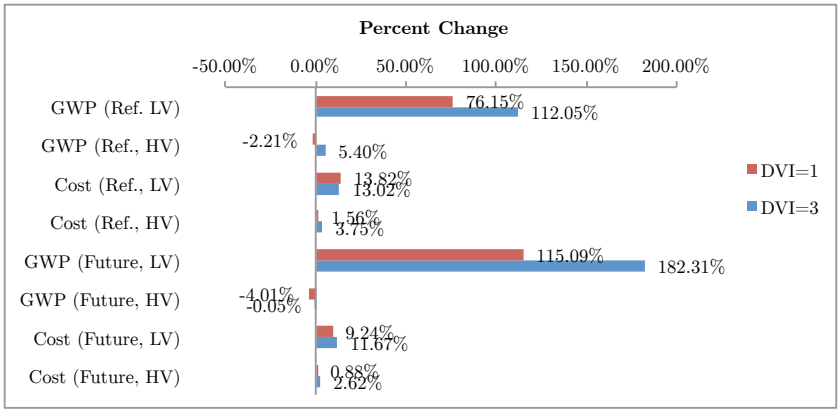

Figure 7.14: Sensitivity analysis on relocating manufacturing to Germany.

Table 7.2: Overall stack cost sensitivity to the HBL.

Reference Case	Volume	Base Energy (kWh/mo.)	PV100 ($/stack)	PV10000 ($/stack)	% Change
DVI1					
	PV100	43821	129830	138600	6.8%
	PV10000	97523	24396	24398	<0.1%
DVI3					
	PV100	78576	207340	218510	5.4%
	PV10000	179120	19982	19985	<0.1%

the electricity costs is based on an older rate schedule and thereby does not factor in the historical baseline level (HBL). The influence of the HBL was tested by assigning the monthly energy demand of PV100 to PV10000 and vice versa for DVI1 and DVI3. Table 7.2 shows the stack cost results of assign a HBL. The results show that setting the HBL to a lower value (e.g., 43821kWh/mo versus 97523kWh/mo) than the actual energy consumption has a relatively significant impact in the total stack costs (6.8% and 5.4% for DVI1 and DVI3, respectively) just from a change in the HBL. However, the converse is not the same and the results show negligible cost decreases. Note that in reality the HBL is reevaluated after every month and therefore the results presented in the table represents an extreme scenario where the energy consumption is assumed to be consistently increasing.

Facility

The facility HVAC model provides numerous degree-of-freedom in terms of the set temperatures, temperature tolerances, heat sources, and the building design. Of the aforementioned parameters, the set point temperature is the easiest and most accessible to control that directly influences the HVAC operation. For the sensitivity analysis the set point temperature was varied ±10% from the default temperature of 23°C, which provides a reasonable range in temperatures. The sensitivity results are shown in Figure 7.15 for both design cases and at low (PV100) and high (PV10000) volumes for DVI1 and DVI3. Several interesting observations arise from the results. For higher levels of in-house manufacturing whether due to the increase in production volume or the transition from DVI1 to DVI3, changing the set point temperature has the inverse effects on the HVAC energy (e.g., increasing the set point decreases the HVAC energy consumption). This suggests that on average, the cooling demand to offset the internal heat generation is greater than the heating demanding. Thus increasing the temperature set point allows a greater buffer of internal heat thereby reducing the cooling load. Reducing the set point temperature when the internal heat generation is already high further increases the cooling load require to offset the extra heat. Therefore, in all cases of high volume production the sensitivity to the lower temperature bound is greater.

The two low volume DVI1 cases exhibit a radically different behavior where the Reference case is non-linear (i.e., exhibits a minimum extrema). The results show that by increasing or

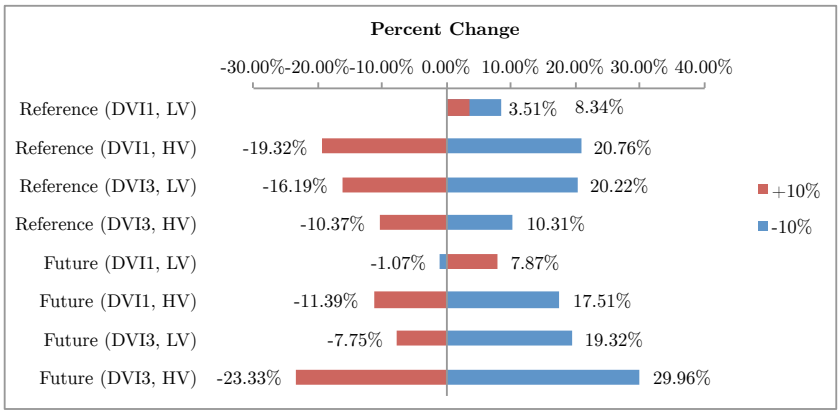

Figure 7.15: Sensitivity analysis on the HVAC energy due to change in the set point temperature.

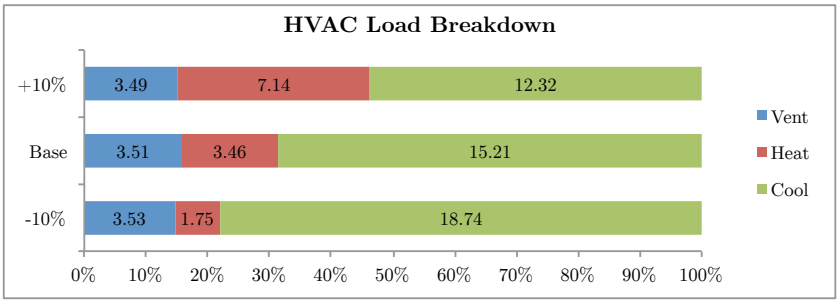

Figure 7.16: Breakdown on the HVAC sensitivities for the Reference case (DVI1, PV100)

decreasing the set point temperature the overall HVAC energy increases by 3.5% and 8.3%, respectively. This phenomenon can be explained by breaking down the energy consumption at the HVAC component level. Figure 7.16 shows the HVAC energy intensity (kWh/m^2) of the three primary components - cooling, heating, and ventilation. It turns out that the default set point temperature sits at the cusp between heating and cooling. As shown in the breakdown increasing the set point by 10% increases the annual heating load by approximately 3.7kWh/m^2 while reducing the cooling load by only 2.9%, a addition difference of 0.8kWh/m^2. Reducing the set point by the same degree, decreases the annual heat loading by 1.7kWh/m^2 while increasing the cooling load by 3.5kWh/m^2, or an additional difference of 1.8kWh/m^2. The Future low volume case exhibits the same phenomenon, however, is shifted with even lower internal heat (hence higher heating loading) due to the less heat intensive manufacturing processes.

Process & Machine Tool

The remaining sensitivity analysis focuses on the process, machine tool, and to some extent, the line scales of manufacturing. As a prime example, the analysis is based on the production of the BIP, and in particular, the molding/forming processes that were thoroughly detailed in Chapter 3. The objective of this analysis is to demonstrate the influence of design and design sensitivity to the process scale and thus to the all the scale of the SGM. Two design attributes were investigated, the thickness of the plate, or in the case of the metal BIP the stock thickness of the sheet metal, and the number of flow channels on the plate assuming that the dimensions of the channels remain constant. Both design attributes are particularly interesting where thinner plates lead to lower through-plane resistivity and lower mass (less required material with implications for reduced transportation emissions) while changing the number flow channels impacts the rate of reactants and products delivery and removal and is the primary attribute that determines the manufacturing process.

The results for the sensitivity of the two design attributes for compression and injection molding and stamping are tabulated in Table 7.3. The data results are listed by the process cycle time, machine tool size in U.S. tons, the theoretical process energy, the additional tool operation energy associated to the process, the baseline or idle energy consumption of the machine tool, and the total specific energy consumption of the the BIP (kWh per BIP). For the compression molding case, the variation in the plate thickness shows negligible effect on the energy consumption. The reason is simply due to the assumption that the molding operations is primarily during the formation of the channels. Hence, the variation of the number of channels influences the required pressing force due to the change in applied area. As the number of channels increase the tool size is increased from 840 tons to 930 tons. The consequence is the additional process energy to form the extra channels and the addition operation and baseline power to operate a larger machine. By the same measure, a reduction in channels reduces the size of the tool and thus the overall energy.

The influence of the plate design has a greater effect on the injection molding process. As the results show, changing the thickness of the plate influences the required molding pressure for injection. For larger thicknesses the pressure is reduce and thus a smaller sized machine tool (540 tons versus 670 tons) is sufficient. The change is highly non-linear where the reduction in thickness requires nearly an additional 200 tons of press force. The energy consumption as a result is greatly impacted where the overall energy consumption is increased by 34% or a sensitivity factor of $34\%/10\% = 3.4$. By the same token, varying the number of channels influences the mold pressure, and hence machine tools sizes, with pressures increasing with increased number of channels. Note that the overall energy consumption for injection molding is significant higher for a similar weighted compression molded BIP, partially due to the semi-automated operation of the machine tool whereas the compression molded plates require manual feeding and unloading. As a sanity check for the injection molding energy consumption, the values for the model were compared to that from the GaBi Software [248] for the injection molding unit process of polypropylene (PP) reinforced with 20-40% talc (recall the injection molded BIP is 30wt.% PP with 70wt.% filler). The

Table 7.3: Sensitivity results for the BIP molding/forming processes.

Process	Cycle-time (s/BIP)	Tool size (U.S. tons)	Process (kWh/BIP)	Operation (kWh/BIP)	Baseline (kWh/BIP)	Total (kWh/BIP)
Compression molding						
Base	38.003	840	0.05736	0.04754	0.4546	0.5594
+10% thick	38.003	840	0.05856	0.04754	0.4546	0.5607
-10% thin	38.003	840	0.05609	0.04754	0.4546	0.5582
+10% channels	38.483	930	0.06157	0.05217	0.4690	0.5827
-10% channels	37.546	760	0.05303	0.04339	0.4416	0.5380
Injection molding						
Base	27.879	670	0.719	0.1730	0.7052	1.597
+10% thick	27.739	540	0.5318	0.1211	0.5993	1.252
-10% thin	28.115	860	1.0282	0.2549	0.8520	2.135
+10% channels	27.926	710	0.7806	0.1897	0.7368	1.707
-10% channels	27.833	630	0.6592	0.1566	0.6731	1.489
Stamping (progressive die)						
Base	2.9647	400	0.0006798	0.006487	0.003416	0.01058
+10% thick	3.3427	430	0.0007487	0.007757	0.003749	0.01225
-10% thin	2.5264	360	0.0006110	0.005082	0.002593	0.008286
+10% channels	3.3427	430	0.0007469	0.007757	0.004166	0.01267
-10% channels	2.5264	360	0.0006127	0.0050816	0.002593	0.008288

output of the GaBi Software showed a specific energy consumption between 6.69kWh/kg to 12.97kWh/kg depending on mass while the SEC of the injection molded BIP from the model is 1.597kWh/BIP×1BIP/0.15kg = 10.6kWh/kg.

The stamping operation for sheet metal BIP is vastly more efficient in terms of BIP production. The cycle time for a stamped plate is on an order of magnitude smaller than the carbon molded plates and has significantly lower machine tool power consumption due to the lack of thermal processing. The design attributes show that a thicker sheet metal or increased number of channels require greater stamping and punching forces and thus leading to higher energy consumptions. On average, a -10% and +10% design change results in 23% lower and 16% high energy consumptions, respectfully.

The results of the process and machine tool sensitivities highlight a key characteristic of the SGM integration. The efficacy of the SGM is highly dependent on the quality of the unit processes and the robustness in linking one scale (e.g., energy flows) to the others. Figure 7.17 show the energy breakdown between the scales from theoretical process energy, to process operation, machine tool baseline consumption, and the loading to the HVAC from the release heat during operation. The most significant revelation is the relatively small fraction of process energy to the actual energy consumption required for processing. As summarized in Table 7.4, neglecting to include the facility scale effects reduces the accuracy of the results by approximately 20% for the compression molding case. Exclusion of the tool

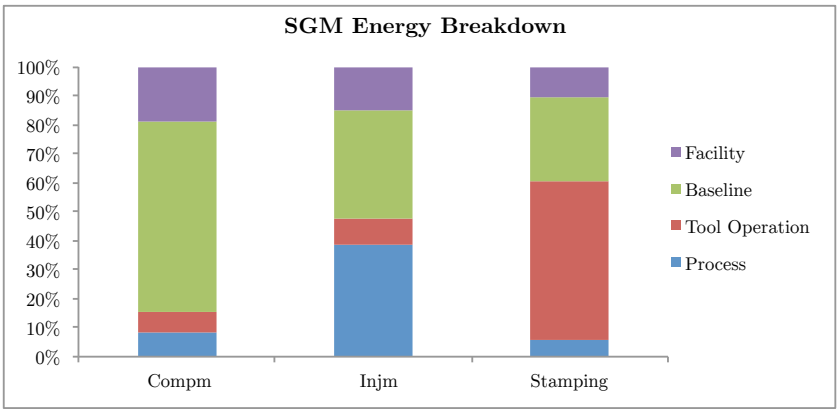

Figure 7.17: Breakdown of the energy consumption by scale.

Table 7.4: Reduction the total energy consumption accuracy by exclusion of the scales.

Process type	Facility (%)	+Baseline (%)	+Operation (%)
Compression molding	81.1	15.2	8.3
Injection molding	85.2	47.6	38.4
Stamping	89.6	60.7	5.8

baseline energy, which was empirical modeled, and the tool operation such as opening and closing the mold cavity, further reduces the accuracy by 65% and 7%, respectively. The end result, if only the theoretical process energy was taken into consideration, yields a staggering error magnitude of 12x, 2.5x, and 17x, for the compression molding, injection molding, and stamping, respectively!

7.5 End-of-Life

The final consideration of the assessment is the influence of the end-of-life phases to the GWP and cost of the fuel cell stack. A complete end-of-life scenario analysis was not conducted due to the high levels of uncertainty, and furthermore, a proper comprehensive assessment requires modeling of the SGM for the entire end-of-life value chain. As a reasonably sufficient simplification three case scenarios are considered: refurbishment of the stack, re-manufacturing of the materials back into the manufacturing process flows, and primary recycling of the materials. For re-manufacturing and recycling, it is assumed that the only materials that can be reclaimed are the platinum metal catalyst, stainless steel from the metal BIP (chromium coating is not recovered), and the composite injection molded BIP materials - polypropylene, graphite, and carbon black. It is also assumed that the stack hardware can be re-used or reprocessed, however, only the aluminum, copper, and steel can be recycled.

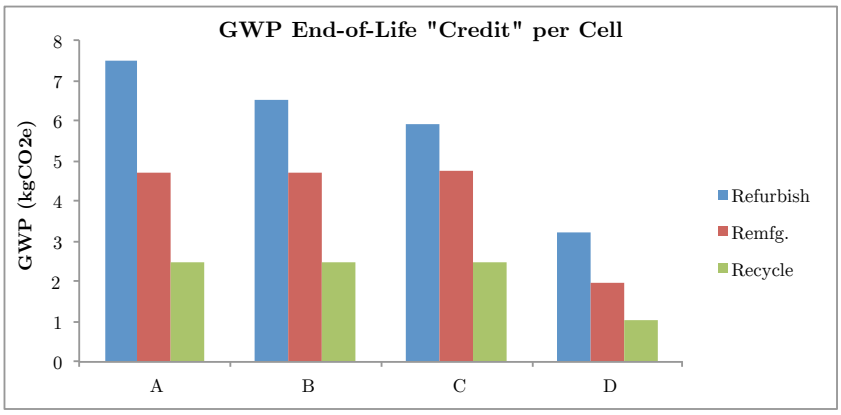

Figure 7.18: GWP end-of-life credit per cell for A: Reference (DVI1, PV100), B: Reference (DVI1, PV10000), C: Reference (DVI3, PV10000), D: Future (DVI3, PV10000)

The presented results focuses specifically on the GWP due to high uncertainty for the implications of costs. Four fuel cell stack scenarios were considered - A: Reference (DVI1, PV100), B: Reference (DVI1, PV10000), C: Reference (DVI3, PV10000), D: Future (DVI3, PV10000). The selection of scenarios was primarily due to the likelihood of being at the state of design and production during the first end-of-life stacks. Furthermore, the assumption is that the stacks are only reclaimed once. The results would change (favorably) if multiple end-of-life lifetimes were considered. The GWP end-of-life results per cell is shown in Figure 7.18. As clearly shown in the figure it is advantageous to refurbish the cell to the highest degree possible thereby avoiding additional added embodied energy to the cell. If refurbishing is not possible, re-use of the component materials back into the process stream is preferable thus reducing the amount of incoming virgin materials. The level of GWP "credit" varies for each stack scenario. Not surprisingly, for the stacks with larger GWP at the beginning-of-life have a greater influence at the end-of-life.

Despite being the most preferable, the refurbished end-of-life option may have certain limitations. For instance, if all of the cells in the stack need to be replaced, it may not be worth (GWP and cost) transporting the stack 8000km from Germany to Vancouver and back. To illustrate, Figure 7.19 plots the net GWP versus the number of refurbished cells. The plot shows in that general it is advantageous to refurbish the stack and at low refurbish cell counts the benefits are quite large. For instance, refurbishing a single cell (hence re-using the remaining cells) effectively lowers the GWP of the new stack by over 40% for all stack scenarios. As the number of required refurbish cells increase the benefits decrease accordingly until at some break even cell count where the refurbishment becomes detrimental due to the added transportation emissions. The results show that the break even cells for the scenarios A, B, C, and D are 264, 254, 251, and, 259, respectfully.

The net overall GWP can be further reduced by taking the secondary end-of-life option of re-manufacturing and recycling into account. Note that there can only be one secondary end-of-life option where re-manufacturing preferable occurs before recycling. Using scenario

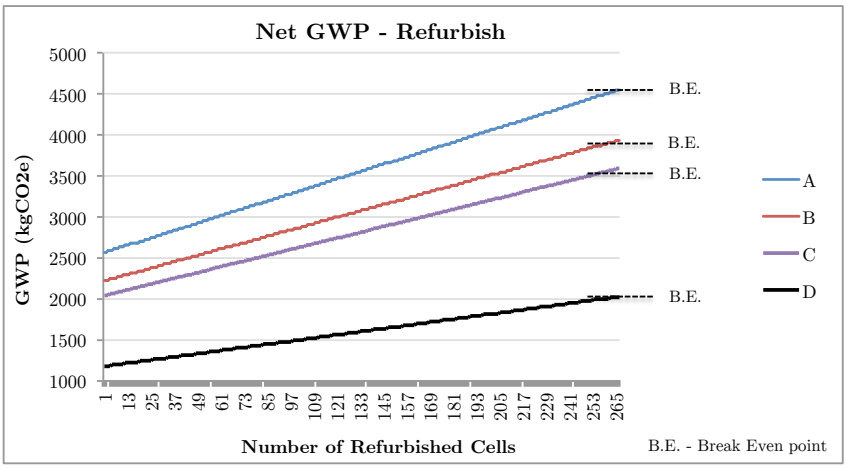

Figure 7.19: Net GWP for refurbish end-of-life as a function of replaced cells. A: Reference (DVI1, PV100), B: Reference (DVI1, PV10000), C: Reference (DVI3, PV10000), D: Future (DVI3, PV10000).

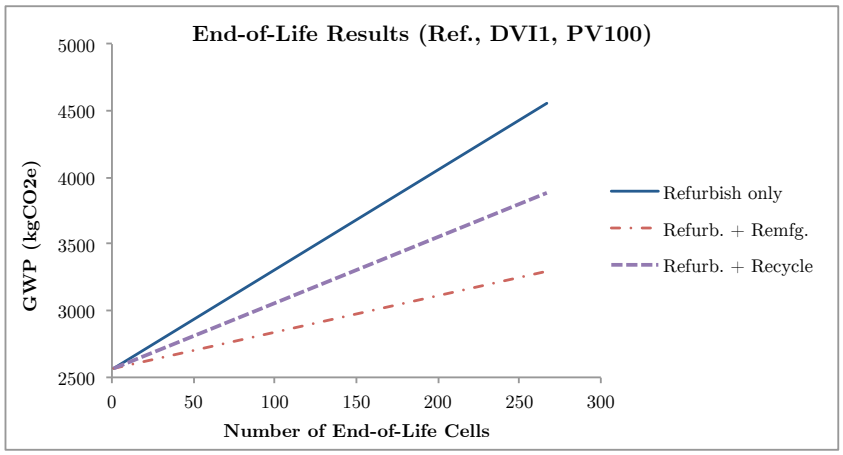

Figure 7.20: Effective overall GWP at various end-of-life option for the Reference case (DVI1, PV100).

A as an illustration, Figure 7.20 plots the best case end-of-life GWP as function of end-of-life cells. As shown in the figure, the GWP at the higher cell count lowers the original refurbish curve due to more cells accounting for the secondary end-of-life. At the low cell count the added benefit is not as pronounced due to lack of cells to be reprocessed. The most preferable option for the lowest effective GWP of the fuel cell stack is to include both refurbishment and remanufacture of the cells.

Chapter 8

Conclusion

The current state of the environmental economy and the predicted trajectory of "business-as-usual" shows alarming anthropogenic carbon emission levels that threaten our well-being, the ecosystem, and the opportunity for future generations to thrive. Numerous predicted trajectories have been represented by stabilization scenarios where the introduction of various technologies and socio-economic factors greatly influence the anthropogenic carbon emissions. Furthermore, these scenarios have been partitioned into the so called stabilization wedges where each wedge represents a solution on a global scale such as the introduction of a new technology or a change to an existing technology that aims to drastically reduced or eliminate carbon emissions. The implementation of the various wedge technologies are crucial in lowering the carbon emissions curve back to sustainable levels.

The proposed designs and implementation of these new technologies are an absolute necessity, however, they must be first assessed from a holistic perspective to verify their environmental efficacy. More specifically, designers require the tools and methodologies to incorporate, assess, and optimize the environmental performance in-situ as part of the design process. By doing so, the environmental efficacy can be maximized and deceptive designs, which may ultimately lead to adverse effects, can be avoided. Such a tool was proposed in this dissertation as the Integrated Sustainable Life Cycle Design (iSLCD) framework and methodology, which emphasizes the harmony between the three pillars of sustainability - environmental, economical, and social (also referred to as the Triple Bottom Line). The proposed framework incorporates a unique perspective of sustainable design with the integration two orthogonal dimensions - the temporal view represented by the Product Life Cycle Zodiac (PLCZ) and the spatial view represented by the Scales of Green Manufacturing (SGM).

The PLCZ expands on the traditional linear view of the cradle-to-grave product by incorporating the full circular 12 life cycle phases that includes: 1) material creation (i.e., Earth), 2) pre-manufacturing (i.e., material processing), 3) intermediate manufacturing, 4) final product manufacturing and assembly, 5) product distribution, 6) product use, 7) product re-use, 8) product redistribution, 9) refurbishment, 10) re-manufacture, 11) recycle, and lastly, 12) landfill back into the Earth. In addition, the PLCZ reallocates the dedicated design phase in attempt to emphasize the equal importance of design in all life cycle phases.

The design details of each phase can be described by integrating the SGM. The SGM defines five hierarchal levels of manufacturing - enterprise, facility, production line, machine tool and process level, which intimately couples energy, materials, and resource flows through the each of PLCZ phases. The enterprise scale defines the geographic location of the enterprise, which has implications for all three pillars of sustainability (e.g., supply chain network, local community, power generation emissions, and so on). The facility scale concerns with the energy and resources to run and maintain the overhead services such the HVAC and lighting. The design of the facility in terms of the layout, construction materials, and overhead equipment will play a large role in determining the overall energy consumption. The line scale narrows the focus to the specific collection of machine tools and ancillary equipment that make up a production line. How the line is constructed will influence the line utilization and thus the efficiency of energy and resources flows within the line and to the facility. Furthermore, the size of the line will play a large role in dictating the size of the facility. The machine tool scale looks at the inherent behavior and functionality of the tool irrespective of the process. Machine tools that perform the same process may have very different energy and resource requirements depending on the manufacturer, size of the tool, and how the tool is utilized. Lastly, process level concerns with the actual value-added processing such as molding and material removal/addition that defines the product. Furthermore, the process level carries the most leverage and the design of which will percolate through all the manufacturing scales. The integration of the all the scales enables the complete comprehensive and precise modeling of the holistic impacts of the product, which can ultimately be assessed and optimized by the designer.

An example of the implement and efficacy of the iSLCD framework was demonstrated by a case study on PEM fuel cells for automotive applications. Fuel cells pose as a potential emerging technology for at least one wedge stabilization from the transportation sector. Th case study was performed in collaboration with Daimler-Benz in attempts to assess the environmental impacts and economical factors for fuel cell production. The results shows substantial carbon emissions from the manufacturing of the fuel cell stack due to current low volume productions and energy intensive processes and a discrepancy between the impacts from the components and the costs. Generally speaking, the most beneficial factor in reducing both carbon emissions and costs is the natural scaling of volume, which is dependent on the adoption rate. Furthermore, it is advantageous to strategically layout the objective for the degree of vertical integration. To target high adoption, costs require to stay at a minimum, therefore, lower a DVI is required (e.g., DVI0,1). However, the results also showed that the break point transition in DVI can occur near the volume quantities of 1000-5000 for the future stack design, which signifies that in-house production is recommended after the initial start-up phase. The transition to the future design is very advantageous dude to high manufacturing utilization and lower required energy and materials for production, which have further implications on reduced transportation emissions. For future generation fuel cell stacks, if the enterprise level remains at the current DVI, the majority of the focus (e.g., R&D, process improvement) should be focused on the MEA, particularly the catalyst layers and membrane for cost. In addition, although not a strikingly large contribution to

the cost, efforts to improve the design and manufacturing of the GDL has large implications in reducing in the GWP, considering that over 95% of the GDL mass comes from highly energy intensive carbon fiber.

The model results also displayed unique sensitivity at all scales of manufacturing, which would not have been revealed if the scales of green manufacturing was not implemented. The sensitivity analysis showed how design could be leveraged to reduce the carbon emissions and cost by increasing the stack performance or simply by strategically locating an enterprise where the cost of energy and the emissions thereof are low. Even at the process and machine tool levels, as shown with the example of the bipolar plate, a change in design can propagate through all scales and the exclusion of any of the scales drastically decreases the accuracy and representativeness of the results. Assessment of such leverage from the design was made possible by the implementation of iSLCD framework with the SGM.

In concluding remarks, the list below highlights some of the recommendations to Daimler and the fuel cell industry as a whole.

- First and foremost, begin now to implement at the iSLCD framework with integrated SGM. The fuel cell technology and volumes are nascent enough such that design changes can be more easily made.
- Continue to stay at a DVI of 0 or 1 until the adoption rate begins to increase. However, at the same time start planning for the transition to a higher DVI, particularly in-house manufacturing of the CCM, MEA, frame, and bipolar pates.
- Transition to the future stack design as quickly as possible in a reasonable manner. The benefits of lower weight and less embodied material and energy intensive components have large implications in reducing the carbon footprint and costs.
- Strategically plan now the supply-chain network for reclaiming the fuel cell stack. Large implications in reducing emissions and costs for refurbishing the stack and reclaiming precious materials. It should be planned such that the re-manufacturing of the end-of-life materials can easily be incorporated back into the manufacturing process flow. Furthermore, there should be consideration to conduct local stack refurbishments to reduces the transportation emissions.
- At the very high volumes, Daimler should consider relocating their fuel cell production back to Germany or locally to where the fuel cells are being used. Doing so will further reduced the transportation emissions, which have a much larger contributions due to the decrease in contribution from manufacturing.
- Last, but not least, a complete assessment include the remaining aspects of the fuel cell vehicles over all life cycle phases (including use) should be preformed. The true environmental performance will depend on the remaining balance-of-plant, motors, controllers, batteries, the production of vehicle itself, and perhaps the greatest contributor, the production of the hydrogen fuel.

Bibliography

[1] Eberhard Abele et al. "Analyzing Energy Consumption of Machine Tool Spindle Units and Identification of Potential for Improvements of Efficiency". In: *Glocalized Solutions for Sustainability in Manufacturing - Proceedings of the 18th CIRP International Conference on Life Cycle Engineering*. Ed. by Jrgen Hesselbach and Christoph Herrmann. Springer Verlag, 2011, pp. 280–285. URL: http://tubiblio.ulb.tu-darmstadt.de/51886/.

[2] Ellsworth Adhesives. *Henkel Loctite 3526 Light Cure Adhesive 25 mL Syringe*. 2013. URL: http://www.ellsworth.com/henkel-loctite-3526-light-cure-adhesive-25ml-syringe/.Accessed:December19,2013.

[3] Orest Adrianowycz. "Next Generation Bipolar Plates for Automotive PEM Fuel Cells". In: *2009 DOE Hydrogen Program - Annual Merit Review*. GrafTech International, 2010.

[4] "Advancements in Carbon Fiber Processing, Research & Development". In: *Composites World*. Harper International, 2010.

[5] J. Akbari, K. Oyamada, and Y. Saito. "LCA of machine tools with regard to their secondary effects on quality of machined parts". In: *Environmentally Conscious Design and Inverse Manufacturing, 2001. Proceedings EcoDesign 2001: Second International Symposium on*. 2001, pp. 347–352. DOI: 10.1109/.2001.992379.

[6] Jamie Ally and Trevor Pryor. "Life-cycle assessment of diesel, natural gas and hydrogen fuel cell bus transportation systems". In: *Journal of Power Sources* 170.2 (2007), pp. 401–411. ISSN: 0378-7753. DOI: http://dx.doi.org/10.1016/j.jpowsour.2007.04.036. URL: http://www.sciencedirect.com/science/article/pii/S0378775307008117.

[7] AltusGroup. *2012 Property Tax Rate Analysis*. Report. Real Property Association of Canada, 2012.

[8] Paul T Anastas and Julie B Zimmerman. "Peer reviewed: design through the 12 principles of green engineering". In: *Environmental Science Technology* 37.5 (2003), 94A–101A. ISSN: 0013-936X.

[9] ANL. *GREET Model*. 2013. URL: http://greet.es.anl.gov.Accessed:December19,2013.

[10] Renato A. Antunes et al. "Corrosion of metal bipolar plates for PEM fuel cells: A review". In: *International Journal of Hydrogen Energy* 35.8 (2010), pp. 3632–3647. ISSN: 0360-3199. DOI: http://dx.doi.org/10.1016/j.ijhydene.2010.01.059. URL: http://www.sciencedirect.com/science/article/pii/S0360319910001308.

[11] S. Artibise R.H.; Farrington. "Membrane Electrode Assembly with Integrated Seal". United States Patent 7,070,876. 2006.

[12] Michael Ashby. *CES Selector 2012*. PC Software. Granta Design, 2012.

[13] ASHRAE. *2009 ASHRAE Handbook: Fundamentals*. SI Edition. American Society of Heating, Refrigerating and Air Conditioning Engineers, Incorporated, 2009. ISBN: 9781933742557. URL: http://books.google.com/books?id=D65XPgAACAAJ.

[14] B2PCO2. *Manufacturing Fuel Cell Manhattan Project*. U.S. Department of Defense, 2012.

[15] John E. Bacino. "Highly Air Permeable Expanded Polytetrafluoroethylene Membranes and Process for Making Them". United States Patent 4,902,423. 1990.

[16] Bamdad Bahar et al. "Ultra-Thin Integral Composite Membrane". United States Patent 5,547,551. 1996.

[17] Shoibal Banerjee and Dennis E. Curtin. "Nafion perfluorinated membranes in fuel cells". In: *Journal of Fluorine Chemistry* 125.8 (2004), pp. 1211–1216. ISSN: 0022-1139. DOI: http://dx.doi.org/10.1016/j.jfluchem.2004.05.018. URL: http://www.sciencedirect.com/science/article/pii/S0022113904001411.

[18] Kaj Barlund. *Sustainable development - concept and action*. 2005. URL: http://www.unece.org/oes/nutshell/2004-2005/focus_sustainable_development.html. Accessed: July 31, 2013.

[19] Paul Barringer. "A Life Cycle Cost Summary". In: *International Conference of Maintenance Societies*. Maintenance Engineering Society of Australia, 2003, p. 10.

[20] A. Barrio et al. "Influence of Manufacturing Parameters on MEA and PEMFC Performance". In: *International Journal of Chemical Reactor Engineering* 6.1 (2008). ISSN: 1542-6580.

[21] Joseph Beck et al. "Ultrasonic Bonding of Membrane Electrode Assemblies for Low Temperature Proton Exchange Membrane Fuel Cells". In: *Journal of Fuel Cell Science and Technology* 9.5 (2012). 10.1115/1.4007136, pp. 051005–051005. ISSN: 1550-624X. DOI: 10.1115/1.4007136. URL: http://dx.doi.org/10.1115/1.4007136.

[22] Thomas Becker. *Macroeconomic Analysis of EV Adoption - Projections to 2030*. PPT Presentation. UC Berkeley, 2009.

[23] Ryan Beene. *Hyundai's salvo may signal the start of a fuel cell fight*. 2013. URL: http://www.autonews.com/article/20131125/OEM05/311259930/hyundais-salvo-may-signal-the-start-of-a-fuel-cell-fight#axzz2lyZy7MQf. Accessed: December 19, 2013.

[24] C. Benoit. *Guidelines for social life cycle assessment of products*. UNEP/Earthprint, 2009. ISBN: 9280730215.

[25] Nico W van den Berg et al. "Quality assessment for LCA". In: *CML Report* 152 (1999).

[26] Ketill Berger. *Projected impact of climate change*. 2008. URL: http://www.grida.no/graphicslib/detail/projected-impact-of-climate-change_1011#.Accessed: 7/17/2013.

[27] M. Bischoff et al. "MCFC fuel cell systems". In: *Handbook of Fuel Cells*. John Wiley and Sons, Ltd, 2010. ISBN: 9780470974001. DOI: 10.1002/9780470974001.f312106. URL: http://dx.doi.org/10.1002/9780470974001.f312106.

[28] AnnaE Bjrklund. "Survey of approaches to improve reliability in lca". In: *The International Journal of Life Cycle Assessment* 7.2 (2002), pp. 64–72. ISSN: 0948-3349. DOI: 10.1007/bf02978849. URL: http://dx.doi.org/10.1007/BF02978849.

[29] John Blackwell. *Nafion*. Powerpoint Presentation. Case Western Reserve University, 2008. URL: gertrude-old.case.edu/276/projects/projectreports2008/Nafion.ppt.

[30] Felix Blank. "Design Requirements for Bipolar Plates and Stack Hardware for Durable Operation". In: *Polymer Electrolyte Fuel Cell Durability*. Ed. by FelixN Bchi, Minoru Inaba, and ThomasJ Schmidt. Springer New York, 2009. Chap. 21, pp. 419–430. ISBN: 978-0-387-85534-9. DOI: 10.1007/978-0-387-85536-3_21. URL: http://dx.doi.org/10.1007/978-0-387-85536-3_21.

[31] Kanda Boosothonsatit, Sami Kara, and Suphunnika Ibbotson. "A Generic Simulation Model for Green Supplier Selection". In: *Leveraging Technology for a Sustainable World*. Ed. by David A. Dornfeld and Barbara S. Linke. Springer Berlin Heidelberg, 2012. Chap. 99, pp. 587–592. ISBN: 978-3-642-29068-8. DOI: 10.1007/978-3-642-29069-5_99. URL: http://dx.doi.org/10.1007/978-3-642-29069-5_99.

[32] G. Boothroyd, P. Dewhurst, and W.A. Knight. *Product Design for Manufacture and Assembly, Third Edition*. 3rd. Boca Raton, FL: Taylor and Francis, 2011, p. 670. ISBN: 9781420089271. URL: http://books.google.com/books?id=W2FDCcVPBcAC.

[33] Michael P Brady et al. "Preferential thermal nitridation to form pin-hole free Cr-nitrides to protect proton exchange membrane fuel cell metallic bipolar plates". In: *Scripta Materialia* 50.7 (2004), pp. 1017–1022. ISSN: 1359-6462.

[34] S. Braun and U. Heisel. "Simulation and Prediction of Process-Oriented Energy Consumption of Machine Tools". In: *Leveraging Technology for a Sustainable World*. Ed. by David A. Dornfeld and Barbara S. Linke. Springer Berlin Heidelberg, 2012. Chap. 42, pp. 245–250. ISBN: 978-3-642-29068-8. DOI: 10.1007/978-3-642-29069-5_42. URL: http://dx.doi.org/10.1007/978-3-642-29069-5_42.

[35] Peter Broomes and David A. Dornfeld. "HVAC Modeling for Cost of Ownership Assessment in Biotechnology and Drugs Manufacturing". In: *Laboratory for Manufacturing and Sustainability, UC Berkeley* (2003). URL: http://www.escholarship.org/uc/item/4qm8r8zn.

[36] D. H. Brunk and D. Perti. "Unitized Membrane Electrode Assembly and Process for its Preparation". United States Patent 7,267,902. 2007.

[37] Colin Busby. "Manufacturing Low-Cost, Durable Membrane Electrode Assemblies Engineered for Rapid Conditioning". In: *DOE Hydrogen and Fuel Cells Program*. U.S. DOE, 2011.

[38] Rand California. *Annual Average Industry Wages in the U.S. States and Counties*. 2013. URL: http://ca.rand.org/stats/economics/avgwagenaicsUS.html. Accessed:November27,2013.

[39] James V. Camahan and Deborah L. Thurston. "Trade-off Modeling for Product and Manufacturing Process Design for the Environment". In: *Journal of Industrial Ecology* 2.1 (1998), pp. 79–92. ISSN: 1530-9290. DOI: 10.1162/jiec.1998.2.1.79. URL: http://dx.doi.org/10.1162/jiec.1998.2.1.79.

[40] Government of Canada. *Average hourly wages of employees by selected characteristics and occupation, unadjusted data, by province*. 2013. URL: http://www.statcan.gc.ca/tables-tableaux/sum-som/l01/cst01/labr69k-eng.htm. Accessed:December,19,2013.

[41] KellyG Canter et al. "Screening stochastic Life Cycle assessment inventory models". In: *The International Journal of Life Cycle Assessment* 7.1 (2002), pp. 18–26. ISSN: 0948-3349. DOI: 10.1007/bf02978906. URL: http://dx.doi.org/10.1007/BF02978906.

[42] EJ Carlson et al. *Cost Analysis of PEM Fuel Cell Systems for Transportation*. Report. 2005.

[43] NOAA National Climatic Data Center. *State of the Climate: Global Analysis for Annual 2012*. 2012. URL: http://www.ncdc.noaa.gov/sotc/global/2012/13. Accessed:7/25/2013.

[44] H.-L. Chang et al. "Method for fabricating a proton exchange membrane". European Patent EP1964874 (European). 2009.

[45] Ssuwei Chen. "Fabrication of PEM fuel cell bipolar plate by indirect selective laser sintering". Copyright - Copyright UMI - Dissertations Publishing 2006 Last updated - 2010-08-07 First page - n/a. Ph.D. 2006.

[46] T Chen et al. "Stamping and Springback of PEMFC Metal Bipolar Plate". In: *Advanced Materials Research* 215 (2011), pp. 1–4. ISSN: 303785071X.

[47] Marian R. Chertow. "The IPAT Equation and Its Variants". In: *Journal of Industrial Ecology* 4.4 (2000), pp. 13–29. ISSN: 1530-9290. DOI: 10.1162/10881980052541927. URL: http://dx.doi.org/10.1162/10881980052541927.

[48] Joshua M. Chien and David Dornfeld. "Semi-empirical Modeling of the Energy Consumed during the Injection Molding Process". In: *Re-engineering Manufacturing for Sustainability*. Ed. by Andrew Y. C. Nee, Bin Song, and Soh-Khim Ong. Springer Singapore, 2013. Chap. 49, pp. 297–302. ISBN: 978-981-4451-47-5. DOI: 10.1007/978-981-4451-48-2_49. URL: http://dx.doi.org/10.1007/978-981-4451-48-2_49.

[49] European Commission. *Analysis of existing Environmental Impact Assessment methodologies for use in Life Cycle Assessment*. Report. Institute for Environment and Sustainability, 2010.

[50] Joyce S. Cooper. "Design analysis of PEMFC bipolar plates considering stack manufacturing and environment impact". In: *Journal of Power Sources* 129.2 (2004), pp. 152–169. ISSN: 0378-7753. DOI: http://dx.doi.org/10.1016/j.jpowsour.2003.11.037. URL: http://www.sciencedirect.com/science/article/pii/S0378775303011303.

[51] L. Corcoran Samantha. "Energy Analysis of Manufacturing Equipment in a Production Setting". Thesis. 2010.

[52] United States Plastic Corporation. *.001x40" x100' Clear Polyester Film - Item Information*. 2013. URL: http://www.usplastic.com/catalog/item.aspx?sku=44092&gclid=CNS7yKH6nbsCFQqGfgodmiEAKg.Accessed:December19,2013.

[53] CPT. *TS Series - Toggle Injection Molding Machines*. 2012. URL: http://www.cinprotech.com/ts-series.html.Accessed:July,26,2012.

[54] J A Crabb, N Murdoch, and J M Penman. "A simplified thermal response model". In: *Building Services Engineering Research and Technology* 8.1 (1987), pp. 13–19. DOI: 10.1177/014362448700800104. URL: http://bse.sagepub.com/content/8/1/13.abstract.

[55] Robert H. Crawford. "Validation of a hybrid life-cycle inventory analysis method". In: *Journal of Environmental Management* 88.3 (2008), pp. 496–506. ISSN: 0301-4797. DOI: http://dx.doi.org/10.1016/j.jenvman.2007.03.024. URL: http://www.sciencedirect.com/science/article/pii/S0301479707001272.

[56] Drury B. Crawley et al. "Contrasting the capabilities of building energy performance simulation programs". In: *Building and Environment* 43.4 (2008), pp. 661–673. ISSN: 0360-1323. DOI: http://dx.doi.org/10.1016/j.buildenv.2006.10.027. URL: http://www.sciencedirect.com/science/article/pii/S0360132306003234.

[57] B. D. Cunningham, J. Huang, and D. G. Baird. "Review of materials and processing methods used in the production of bipolar plates for fuel cells". In: *International Materials Reviews* 52.1 (2007), pp. 1–13. DOI: 10.1179/174328006x102556. URL: http://www.ingentaconnect.com/content/maney/imr/2007/00000052/00000001/art00001http://dx.doi.org/10.1179/174328006X102556.

[58] Mary Ann Curran. *Life-cycle Assessment: Principles and Practice*. Report EPA/600/R-06/060. (SAIC). National Risk Management Research Laboratory, Office of Research and Development, US Environmental Protection Agency, 2006.

[59] Jeffrey Dahmus and Timothy Gutowski. "An environmental analysis of machining". In: *ASME International Mechanical Engineering Congress and RD and D Exposition, Anaheim, California, USA*. 2004.

[60] Steven J. Davis et al. "Rethinking wedges". In: *Environmental Research Letters* 8.1 (2013), p. 011001. ISSN: 1748-9326. URL: http://stacks.iop.org/1748-9326/8/i=1/a=011001.

[61] Emory S. De Castro et al. *Approaches for low cost components and MEAs for PEMFCs: current and future directions*. Report. De Nora Elettrodi, 2004.

[62] M. K. Debe. "Advanced Cathode Catalysts and Supports for PEM Fuel Cells". In: *2007 DOE Hydrogen Program - Annual Merit Review*. U.S. DOE, 2007.

[63] M. K. Debe. "Advanced MEAs for Enhanced Operating Conditions, Amenable to High Volume Manufacture". In: *2004 DOE Hydrogen, Fuel Cells & Infrastructure Technologies Review*. U.S. DOE, 2004.

[64] M. K. Debe. "Novel catalysts, catalysts support and catalysts coated membrane methods". In: *Handbook of Fuel Cells*. John Wiley and Sons, Ltd, 2010. ISBN: 9780470974001. DOI: 10.1002/9780470974001.f303050. URL: http://dx.doi.org/10.1002/9780470974001.f303050.

[65] M. K. Debe and R. J. Poirier. "Postdeposition growth of a uniquely nanostructured organic film by vacuum annealing". In: *Journal of Vacuum Science and Technology A: Vacuum, Surfaces, and Films* 12.4 (1994), pp. 2017–2022. ISSN: 0734-2101. DOI: 10.1116/1.578999.

[66] Mark K. Debe. "Electrocatalyst approaches and challenges for automotive fuel cells". In: *Nature* 486.7401 (2012). 10.1038/nature11115, pp. 43–51. ISSN: 0028-0836. URL: http://dx.doi.org/10.1038/nature11115.

[67] T. Derieth et al. "Development of highly filled graphite compounds as bipolar plate materials for low and high temperature PEM fuel cells". In: *Journal of New Materials for Electrochemical Systems* 11.1 (2008). Compilation and indexing terms, Copyright 2012 Elsevier Inc. 20082911376251 (+ mod 2N) operation (e ,3e) process Bipolar plate materials Bipolar plates Electrical conductivity Filling materials Filling particles Graphite flakes High temperature (HT) High temperature PEM Injection

moulding Low temperature (LTR) Material developments Plate materials, pp. 21–29. ISSN: 14802422.

[68] Tom Devoldere et al. "Improvement Potential for Energy Consumption in Discrete Part Production Machines". In: *Advances in Life Cycle Engineering for Sustainable Manufacturing Businesses*. Ed. by Shozo Takata and Yasushi Umeda. Springer London, 2007. Chap. 54, pp. 311–316. ISBN: 978-1-84628-934-7. DOI: 10.1007/978-1-84628-935-4_54. URL: http://dx.doi.org/10.1007/978-1-84628-935-4_54.

[69] N. Diaz et al. "Environmental analysis of milling machine tool use in various manufacturing environments". In: *Sustainable Systems and Technology (ISSST), 2010 IEEE International Symposium on*, pp. 1–6. DOI: 10.1109/issst.2010.5507763.

[70] Nancy Diaz, Moneer Helu, and David Dornfeld. "Design and Operation Strategies for Green Machine Tool Development". In: *Laboratory for Manufacturing and Sustainability, UC Berkeley* (2010). URL: http://www.escholarship.org/uc/item/613797g5.

[71] Nancy Diaz, Elena Redelsheimer, and David Dornfeld. "Energy Consumption Characterization and Reduction Strategies for Milling Machine Tool Use". In: *Glocalized Solutions for Sustainability in Manufacturing*. Ed. by Jrgen Hesselbach and Christoph Herrmann. Springer Berlin Heidelberg, 2011. Chap. 46, pp. 263–267. ISBN: 978-3-642-19691-1. DOI: 10.1007/978-3-642-19692-8_46. URL: http://dx.doi.org/10.1007/978-3-642-19692-8_46.

[72] Anton Dietmair and Alexander Verl. "A generic energy consumption model for decision making and energy efficiency optimisation in manufacturing". In: *International Journal of Sustainable Engineering* 2.2 (2009), pp. 123–133. ISSN: 1939-7038. DOI: 10.1080/19397030902947041. URL: http://dx.doi.org/10.1080/19397030902947041.

[73] Gilles Michel Marc Divoux. "Properties and Performance of Polymeric Materials Used in Fuel Cell Applications". Dissertation. 2012.

[74] U.S. DOE. *2011 Buildings Energy Data Book*. Report. U.S. Department of Energy, 2012. URL: http://buildingsdatabook.eere.energy.gov/.

[75] U.S. DOE. *Carbon Cycling and Climate*. 2011. URL: http://genomicscience.energy.gov.Accessed:July23,2013.

[76] U.S. DOE. "Technical Plan - Fuel Cells". In: *Fuel Cell Technologies Office : Multi-Year Research, Development and Demonstration Plan*. Energy Efficiency and Renewable Energy, 2012.

[77] David Dornfeld. *Sustainable Manufacturing Greening Processes, Systems and Products*. Conference Paper. 2010. URL: http://www.escholarship.org/uc/item/80x443hk.

[78] Berenice Dreux-Gerphagnon and Nizar Haoues. *Considering the social dimension in environmental design*. Conference Paper. 2011. DOI: 10.1007/978-3-642-19692-8_23,.

[79] LouiseCamilla Dreyer, AnneLouise Niemann, and MichaelZ Hauschild. "Comparison of Three Different LCIA Methods: EDIP97, CML2001 and Eco-indicator 99". In: *The International Journal of Life Cycle Assessment* 8.4 (2003), pp. 191–200. ISSN: 0948-3349. DOI: 10.1007/bf02978471. URL: http://dx.doi.org/10.1007/BF02978471.

[80] Joost R Duflou, Karel Kellens, and Wim Dewulf. "Environmental Performance of Sheet Metal Working Processes". In: *Key Engineering Materials* 473 (2011), pp. 21–26. ISSN: 3037850833.

[81] Joost R Duflou et al. "Critical comparison of methods to determine the energy input for discrete manufacturing processes". In: *CIRP Annals-Manufacturing Technology* (2012). ISSN: 0007-8506.

[82] DuPont. *About Our Products*. 2013. URL: http://www2.dupont.com/Fayetteville/en_US/products.html.Accessed:December19,2013.

[83] DuPont. *NR211 and NR212*. Report. E. I. du Pont, 2009.

[84] N. Duque Ciceri, T. G. Gutowski, and M. Garetti. "A tool to estimate materials and manufacturing energy for a product". In: *Sustainable Systems and Technology (ISSST), 2010 IEEE International Symposium on*. 2010, pp. 1–6. DOI: 10.1109/issst.2010.5507677.

[85] *Ecoinvent*. 2013. URL: www.ecoinvent.org.Accessed:August25,2013.

[86] Paul R Ehrlich and John P Holdren. "Impact of population growth". In: *Science* 171.3977 (1971), pp. 1212–1217. ISSN: 0036-8075.

[87] EIA. *Annual Energy Outlook 2013 - With Projections to 2040*. Report. U.S. DOE, 2013.

[88] EIA. *Electricity Prices for Industry for Selected Countries*. 2010. URL: http://www.eia.gov/countries/prices/electricity_industry.cfm.Accessed:December6,2013.

[89] EIA. *Table E6. Electricity Consumption (kWh) Intensities by End Use for Non-Mall Buildings, 2003*. 2008. URL: http://www.eia.gov/consumption/commercial/data/archive/cbecs/cbecs2003/detailed_tables_2003/2003set19/2003html/e06.html.Accessed:December14,2013.

[90] U.S. EIA. *Electric Power Monthly with Data for June 2013*. Report. U.S. Department of Energy, 2013.

[91] U.S. EIA. *United States Natural Gas Industrial Price*. 2013. URL: http://www.eia.gov/dnav/ng/hist/n3035us3m.htm.Accessed:September3,2013.

[92] Christian Eisele, Sebastian Schrems, and Eberhard Abele. "Energy-Efficient Machine Tools through Simulation in the Design Process". In: *Glocalized Solutions for Sustainability in Manufacturing*. Ed. by Jrgen Hesselbach and Christoph Herrmann. Springer Berlin Heidelberg, 2011. Chap. 45, pp. 258–262. ISBN: 978-3-642-19691-1. DOI: 10.1007/978-3-642-19692-8_45. URL: http://dx.doi.org/10.1007/978-3-642-19692-8_45.

[93] Per Ekdunge and Monika Rberg. "The fuel cell vehicle analysis of energy use, emissions and cost". In: *International Journal of Hydrogen Energy* 23.5 (1998), pp. 381–385. ISSN: 0360-3199. DOI: http://dx.doi.org/10.1016/S0360-3199(97)00062-1. URL: http://www.sciencedirect.com/science/article/pii/S0360319997000621.

[94] Tomas Ekvall and BoP Weidema. "System boundaries and input data in consequential life cycle inventory analysis". In: *The International Journal of Life Cycle Assessment* 9.3 (2004), pp. 161–171. ISSN: 0948-3349. DOI: 10.1007/bf02994190. URL: http://dx.doi.org/10.1007/BF02994190.

[95] Herbert Sousa Eleuterio and Robert Walter Meschke. "Fluorocarbon epoxides". United States Patent 3,358,003. 1967.

[96] Roger C. Emauelson, Warren L. Luoma, and William A. Taylor. "Separator Plate for Electrochemical Cells". United States Patent 4,301,222. 1981.

[97] Gary Emmett. *International construction cost survey 2012*. Report. 2012.

[98] Eurostat. *Electricity and natural gas price statistics*. 2013. URL: http://epp.eurostat.ec.europa.eu/statistics_explained/index.php/Electricity_and_natural_gas_price_statistics.Accessed:December6,2013.

[99] ExxonMobil. *Isopar K (EU): Isoparaffin Fluid*. Technical Document. ExxonMobil Chemical, 2011.

[100] *F-Cell World Drive - Successful Finish*. 2011. URL: http://technicity.daimler.com/en/fuelcellworlddrive/.Accessed:November28,2013.

[101] "Faces of the future". In: *The Economist* (2013).

[102] A. Fehske et al. "The global footprint of mobile communications: The ecological and economic perspective". In: *Communications Magazine, IEEE* 49.8 (2011), pp. 55–62. ISSN: 0163-6804. DOI: 10.1109/mcom.2011.5978416.

[103] *Fuel Cells*. Report. Energy Efficiency and Renewable Energy, 2012.

[104] FuelCellToday. *About Fuel Cells - History*. 2013. URL: http://www.fuelcelltoday.com/about-fuel-cells/history.Accessed:7/29/2013.

[105] FuelCellToday. *The Fuel Cell Industry Review 2012*. Report. 2012.

[106] R. L. Fuss. "Liquid cooled bipolar plate consisting of glued plates for PEM fuel cells". European Patent EP1009051 (European). 2000.

[107] GCP. *Carbon budget and trends 2012*. 2012. URL: www.globalcarbonproject.org/carbonbudget.Accessed:July16,2013.

[108] *GISS Surface Temperature Analysis (GISTEMP)*. 2013. URL: http://data.giss.nasa.gov/gistemp/.Accessed:December19,2013.

[109] *Global Apple iPhone sales from 3rd quarter 2007 to 2nd quarter 2013*. 2013. URL: http://www.statista.com/statistics/12743/worldwide-apple-iphone-sales-since-3rd-quarter-2007/.Accessed:7/17/2013.

[110] *Global Mobile Phone Subscribers to Reach 4.5 Billion by 2012*. 2008. URL: www.cellular-news.com/story/29824.php.Accessed:7/17/2013.

[111] *Global mobile statistics 2013 Part A: Mobile subscribers; handset market share; mobile operators*. 2013. URL: http://mobithinking.com/mobile-marketing-tools/latest-mobile-stats/a#subscribers.Accessed:7/17/2013.

[112] Mark Goedkoop et al. *Methods Library*. Report. PRe Consultants, 2008.

[113] Robert W. Gore. "Process for Producing Porous Products". United States Patent 3,953,566. 1976.

[114] D.Y. Goswami and J.F. Kreider. *Principles of Solar Engineering*. Taylor and Francis, 2000. ISBN: 9781560327141. URL: http://books.google.com/books?id=oaB4vzI-UdwC.

[115] Thomas Graedel and Jennifer Howard-Grenville. *Greening the industrial facility: Perspectives, approaches, and tools*. Springer, 2005. ISBN: 0387243062.

[116] Walter Grot. *Fluorinated Ionomers*. 2nd ed. William Andrew Pub, 2011, p. 312. ISBN: 1437744575.

[117] Walther G. Grot. "Perfluorinated ion exchange polymers and their use in research and industry". In: *Macromolecular Symposia* 82.1 (1994), pp. 161–172. ISSN: 1521-3900. DOI: 10.1002/masy.19940820117. URL: http://dx.doi.org/10.1002/masy.19940820117.

[118] Global Property Guide. *Effective rental income tax is low in Japan*. 2013. URL: http://www.globalpropertyguide.com/Asia/japan/Taxes-and-Costs.Accessed:February22,2013.

[119] Jeroen B. Guine et al. "Life Cycle Assessment: Past, Present, and Future". In: *Environmental Science and Technology* 45.1 (2010), pp. 90–96. ISSN: 0013-936X. DOI: 10.1021/es101316v. URL: http://dx.doi.org/10.1021/es101316v.

[120] T. Gutowski et al. "A Thermodynamic Characterization of Manufacturing Processes". In: *Electronics and the Environment, Proceedings of the 2007 IEEE International Symposium on*. 2007, pp. 137–142. ISBN: 1095-2020. DOI: 10.1109/isee.2007.369382.

[121] Timothy Gutowski, Jeffrey Dahmus, and Alex Thiriez. "Electrical energy requirements for manufacturing processes". In: *13th CIRP international conference on life cycle engineering, Leuven, Belgium*. Vol. 5. 2006, pp. 560–564.

[122] Timothy Gutowski et al. "Environmentally benign manufacturing: Observations from Japan, Europe and the United States". In: *Journal of Cleaner Production* 13.1 (2005), pp. 1–17. ISSN: 0959-6526. DOI: http://dx.doi.org/10.1016/j.jclepro.2003.10.004. URL: http://www.sciencedirect.com/science/article/pii/S0959652603001781.

[123] Timothy G. Gutowski et al. "Thermodynamic Analysis of Resources Used in Manufacturing Processes". In: *Environmental Science and Technology* 43.5 (2009), pp. 1584–1590. ISSN: 0013-936X. DOI: 10.1021/es8016655. URL: http://dx.doi.org/10.1021/es8016655.

[124] TimothyG Gutowski. "Manufacturing and the Science of Sustainability". In: *Glocalized Solutions for Sustainability in Manufacturing*. Ed. by Jrgen Hesselbach and Christoph Herrmann. Springer Berlin Heidelberg, 2011. Chap. 6, pp. 32–39. ISBN: 978-3-642-19691-1. DOI: 10.1007/978-3-642-19692-8_6. URL: http://dx.doi.org/10.1007/978-3-642-19692-8_6.

[125] Krisztina Gyorffy. *Germany Inflation Rate*. 2013. URL: http://www.tradingeconomics.com/germany/inflation-cpi.Accessed:December6,2013.

[126] Jeff S. Haberl. "Economic Calculations for ASHRAE handbook". In: *Energy Systems Laboratory Report EST-TR-93/04-07, College Station, TX: Texas AM University* (1994).

[127] Theo Hacking and Peter Guthrie. "A framework for clarifying the meaning of Triple Bottom-Line, Integrated, and Sustainability Assessment". In: *Environmental Impact Assessment Review* 28.23 (2008), pp. 73–89. ISSN: 0195-9255. DOI: http://dx.doi.org/10.1016/j.eiar.2007.03.002. URL: http://www.sciencedirect.com/science/article/pii/S0195925507000297.

[128] Helias A. Udo de Haes et al. "Three Strategies to Overcome the Limitations of Life-Cycle Assessment". In: *Journal of Industrial Ecology* 8.3 (2004), pp. 19–32. ISSN: 1530-9290. DOI: 10.1162/1088198042442351. URL: http://dx.doi.org/10.1162/1088198042442351.

[129] Forrest G. Hall et al. "Characterizing 3D vegetation structure from space: Mission requirements". In: *Remote Sensing of Environment* 115.11 (2011), pp. 2753–2775. ISSN: 0034-4257. DOI: http://dx.doi.org/10.1016/j.rse.2011.01.024. URL: http://www.sciencedirect.com/science/article/pii/S003442571100126X.

[130] Erica Hamilton. *British Columbia Hydro and Power Authority: Electric Tariff*. Report. BC Hydro, 2008.

[131] A. Hamnett. "Introduction to fuel-cell types". In: *Handbook of Fuel Cells*. John Wiley and Sons, Ltd, 2010. ISBN: 9780470974001. DOI: 10.1002/9780470974001.f101005m. URL: http://dx.doi.org/10.1002/9780470974001.f101005m.

[132] W. Hansen, K. Berger, and C. Wulff. *PK/PWT Fuel Cell Progress*. Internal Report. Daimler-Benz, 2009.

[133] Carla Heitner-Wirguin. "Recent advances in perfluorinated ionomer membranes: structure, properties and applications". In: *Journal of membrane science* 120.1 (1996), pp. 1–33. ISSN: 0376-7388. DOI: http://dx.doi.org/10.1016/0376-7388(96)00155-X.

[134] M. Helu, A. Vijayaraghavan, and D. Dornfeld. "Evaluating the relationship between use phase environmental impacts and manufacturing process precision". In: *CIRP Annals - Manufacturing Technology* 60.1 (2011), pp. 49–52. ISSN: 0007-8506. DOI: http://dx.doi.org/10.1016/j.cirp.2011.03.020. URL: http://www.sciencedirect.com/science/article/pii/S0007850611000217.

[135] Moneer Helu et al. "Evaluating Trade-Offs Between Sustainability, Performance, and Cost of Green Machining Technologies". In: *Glocalized Solutions for Sustainability in Manufacturing*. Ed. by Jrgen Hesselbach and Christoph Herrmann. Springer Berlin Heidelberg, 2011. Chap. 34, pp. 195–200. ISBN: 978-3-642-19691-1. DOI: 10.1007/978-3-642-19692-8_34. URL: http://dx.doi.org/10.1007/978-3-642-19692-8_34.

[136] Chris Hendrickson et al. "Peer Reviewed: Economic InputOutput Models for Environmental Life-Cycle Assessment". In: *Environmental Science Technology* 32.7 (1998), 184A–191A. ISSN: 0013-936X. DOI: 10.1021/es983471i. URL: http://dx.doi.org/10.1021/es983471i.

[137] Henkel. *Loctite 3526*. Product sheet. 2004.

[138] Henkel. *Loctite 5251*. Product sheet. 2008.

[139] C. Herrmann et al. "Energy oriented simulation of manufacturing systems Concept and application". In: *CIRP Annals - Manufacturing Technology* 60.1 (2011), pp. 45–48. ISSN: 0007-8506. DOI: http://dx.doi.org/10.1016/j.cirp.2011.03.127. URL: http://www.sciencedirect.com/science/article/pii/S0007850611001284.

[140] Christoph Herrmann et al. "Energy Efficiency in ManufacturingPerspectives from Australia and Europe". In: *CIRP International Conference on Life Cycle Engineering*. 2010, pp. 23–28.

[141] Steven Hoffenson, Andreas Dagman, and Rikard Sderberg. "A Multi-objective Tolerance Optimization Approach for Economic, Ecological, and Social Sustainability". In: *Re-engineering Manufacturing for Sustainability*. Ed. by Andrew Y. C. Nee, Bin Song, and Soh-Khim Ong. Springer Singapore, 2013. Chap. 119, pp. 729–734. ISBN: 978-981-4451-47-5. DOI: 10.1007/978-981-4451-48-2_119. URL: http://dx.doi.org/10.1007/978-981-4451-48-2_119.

[142] Martin I. Hoffert et al. "Advanced Technology Paths to Global Climate Stability: Energy for a Greenhouse Planet". In: *Science* 298.5595 (2002), pp. 981–987. DOI: 10.1126/science.1072357. URL: http://www.sciencemag.org/content/298/5595/981.abstract.

[143] Martin I. Hoffert et al. "Energy implications of future stabilization of atmospheric CO2 content". In: *Nature* 395.6705 (1998). 10.1038/27638, pp. 881–884. ISSN: 0028-0836. URL: http://dx.doi.org/10.1038/27638.

[144] J. Huang, D. Baird, and J. McGrath. "Highly Conductive Thermoplastic Composite for Rapid Production of Fuel Cell Bipolar Plates". United States Patent 2004/0229993. 2004.

[145] Jianhua Huang, Donald G. Baird, and James E. McGrath. "Development of fuel cell bipolar plates from graphite filled wet-lay thermoplastic composite materials". In: *Journal of Power Sources* 150.0 (2005), pp. 110–119. ISSN: 0378-7753. DOI: 10.1016/j.jpowsour.2005.02.074. URL: http://www.sciencedirect.com/science/article/pii/S037877530500248X.

[146] M. M. Hussain, I. Dincer, and X. Li. "A preliminary life cycle assessment of PEM fuel cell powered automobiles". In: *Applied Thermal Engineering* 27.13 (2007), pp. 2294–2299. ISSN: 1359-4311. DOI: http://dx.doi.org/10.1016/j.applthermaleng.2007.01.015. URL: http://www.sciencedirect.com/science/article/pii/S1359431107000506.

[147] Suphunnika Ibbotson et al. "Impact of Process Selection on Material and Energy Flow". In: *Re-engineering Manufacturing for Sustainability*. Ed. by Andrew Y. C. Nee, Bin Song, and Soh-Khim Ong. Springer Singapore, 2013. Chap. 26, pp. 159–163. ISBN: 978-981-4451-47-5. DOI: 10.1007/978-981-4451-48-2_26. URL: http://dx.doi.org/10.1007/978-981-4451-48-2_26.

[148] IEA. *CO2 Emissions From Fuel Combustion - Highlights*. Report. International Energy Agency, 2012.

[149] IEA. *Four energy policies can keep the 2C climate goal alive*. 2013. URL: http://www.iea.org/newsroomandevents/pressreleases/2013/june/name,38773,en.html.Accessed:7/23/2013.

[150] IKA. *Ika Pilots Brochure*. Report. IKA Works (Asia) Sdn Bhd, 2010.

[151] Frank P. Incropera et al. *Fundamentals of heat and mass transfer*. 6th. John Wiley and Sons, 2006. ISBN: 9780471457282.

[152] Rate Inflation. *Historical Inflation Rates for Japan (2003 to 2013)*. 2013. URL: http://www.rateinflation.com/inflation-rate/japan-historical-inflation-rate.Accessed:September3,2013.

[153] Carnegie Mellon University Green Design Institute. *Economic Input-Output Life Cycle Assessment (EIO-LCA)*. 2008. URL: http://www.eiolca.net.Accessed:December19,2013.

[154] IPCC. *Climate Change 2007: Mitigation of Climate Change*. Report. IPCC, 2007.

[155] IPCC. *Climate Change 2007: The Physical Science Basis*. Report. IPCC, 2007.

[156] IPCC. *Organization*. 2013. URL: http://www.ipcc.ch/organization/organization.shtml.Accessed:7/23/2013.

[157] IPCC. *Special Report on Emissions Scenarios*. Report. IPCC, 2000.

[158] ISO14040. *Environmental Management - Life Cycle Assessment - Principles and Framework*.

[159] Brian D James and Jeffrey A Kalinoski. *Mass Production Cost Estimation for Direct H2 PEM Fuel Cell Systems for Automotive Applications: 2007 Update*. Report. Directed Technologies, Inc., 2008.

[160] Brian D James, Jeffrey A Kalinoski, and Kevin N Baum. "Mass production cost estimation for direct H2 PEM fuel cell systems for automotive applications: 2010 update". In: *report to the DOE Fuel Cell Technologies Program* (2010).

[161] Brian D. James, Franklin D. Jr. Lomax, and C. E. Thomas. *Manufacturing Cost of Stationary Polymer Electrolyte Membrane (PEM) Fuel Cell Systems*. Report. NREL, 1999.

[162] Brian D James, Andrew B. Spisak, and Whitney G. Colella. *Manufacturing Cost Analysis of Stationary Fuel Cell Systems*. Report. Strategic Analysis Inc., 2012.

[163] *Japan Inflation Rate: Energy*. 2013. URL: http://ycharts.com/indicators/japan_inflation_rate_energy.Accessed:September3,2013.

[164] P. Johnson and M. Beverlin. *Beta Distriubtion*. 2013. URL: http://pj.freefaculty.org/guides/stat/Distributions/DistributionWriteups/Beta/Beta.pdf.Accessed:August1,2013.

[165] Babu Joseph and Vishu Shah. *Energy Efficient Injection Molding Operation*. Report. Southern California Edison Company, 2003.

[166] S. Junnila and A. Horvath. "Life-Cycle Environmental Effects of an Office Building". In: *Journal of Infrastructure Systems* 9.4 (2003), pp. 157–166. DOI: doi:10.1061/(ASCE)1076-0342(2003)9:4(157). URL: http://ascelibrary.org/doi/abs/10.1061/%28ASCE%291076-0342%282003%299%3A4%28157%29.

[167] Ludwig Jrissen et al. *Fuel Cell Concepts a Short Tutorial*. Tutorial. Zentrum fur Sonnenenergie- und Wasserstoff-Forschung, 2004.

[168] Andreas Jrgensen et al. "Methodologies for social life cycle assessment". In: *The International Journal of Life Cycle Assessment* 13.2 (2008), pp. 96–103. ISSN: 0948-3349. DOI: 10.1065/lca2007.11.367. URL: http://dx.doi.org/10.1065/lca2007.11.367.

[169] S. Kara, G. Bogdanski, and W. Li. "Electricity Metering and Monitoring in Manufacturing Systems". In: *Glocalized Solutions for Sustainability in Manufacturing*. Ed. by Jrgen Hesselbach and Christoph Herrmann. Springer Berlin Heidelberg, 2011. Chap. 1, pp. 1–10. ISBN: 978-3-642-19691-1. DOI: 10.1007/978-3-642-19692-8_1. URL: http://dx.doi.org/10.1007/978-3-642-19692-8_1.

[170] S. Kara and W. Li. "Unit process energy consumption models for material removal processes". In: *CIRP Annals - Manufacturing Technology* 60.1 (2011), pp. 37–40. ISSN: 0007-8506. DOI: http://dx.doi.org/10.1016/j.cirp.2011.03.018. URL: http://www.sciencedirect.com/science/article/pii/S0007850611000199.

[171] Karel Kellens et al. "Methodology for systematic analysis and improvement of manufacturing unit process life cycle inventory (UPLCI) CO2PE! initiative (cooperative effort on process emissions in manufacturing). Part 2: case studies". In: *The International Journal of Life Cycle Assessment* 17.2 (2012), pp. 242–251. ISSN: 0948-3349. DOI: 10.1007/s11367-011-0352-0. URL: http://dx.doi.org/10.1007/s11367-011-0352-0.

[172] Karel Kellens et al. "Methodology for systematic analysis and improvement of manufacturing unit process life-cycle inventory (UPLCI)CO2PE! initiative (cooperative effort on process emissions in manufacturing). Part 1: Methodology description". In: *The International Journal of Life Cycle Assessment* 17.1 (2012), pp. 69–78. ISSN: 0948-3349. DOI: 10.1007/s11367-011-0340-4. URL: http://dx.doi.org/10.1007/s11367-011-0340-4.

[173] DaleJ Kennedy, DouglasC Montgomery, and BethH Quay. "Data quality". In: *The International Journal of Life Cycle Assessment* 1.4 (1996), pp. 199–207. ISSN: 0948-3349. DOI: 10.1007/bf02978693. URL: http://dx.doi.org/10.1007/BF02978693.

[174] J. M. King and H. R. Kunz. "Phosphoric acid electrolyte fuel cells". In: *Handbook of Fuel Cells*. John Wiley and Sons, Ltd, 2010. ISBN: 9780470974001. DOI: 10.1002/9780470974001.f104015. URL: http://dx.doi.org/10.1002/9780470974001.f104015.

[175] J. H. Klug. "Process for Complex Shape Formation Using Flexible Graphite Sheets". United States Patent 6,663,807. 2003.

[176] Wolfram Knorr and Frank Dunnebeil. *Transport in China: Energy Consumption and Emissions of Different Transport Modes*. Report. Institute for Energy and Environmental Research, 2008.

[177] S. Kobayashi et al. "High Polymer Electrolyte Fuel Cell and Electrolyte Film-Gasket Assembly for the Fuel Cell". United States Patent 6,840,969. 2005.

[178] S. S. Kocha. "Principles of MEA preparation". In: *Handbook of Fuel Cells*. John Wiley and Sons, Ltd, 2010. ISBN: 9780470974001. DOI: 10.1002/9780470974001.f303047. URL: http://dx.doi.org/10.1002/9780470974001.f303047.

[179] K. Kohyama, H. Shinkai, and M. Tani. "Membrane Electrode Assembly for Polymer Electrolyte Fuel Cell". European Patent EP1480285 (European). 2004.

[180] Thomas Kolbusch. *New coating and laminating methods for MEAs*. Conference Paper. 2006.

[181] Jeffrey A Kolde et al. "Advanced composite polymer electrolyte fuel cell membranes". In: *Proc. Electrochem. Soc* 23 (1995), pp. 193–201.

[182] Daeyoung Kong et al. "Software-based tool path evaluation for environmental sustainability". In: *Journal of Manufacturing Systems* In Press (2011). URL: http://www.escholarship.org/uc/item/1387x8h9.

[183] David N Kordonowy. "A Power Assessment of Machining Tools". Bachelor Thesis. 2002.

[184] U.S. Department of Labor. *CPI Inflation Calculator*. 2013. URL: http://www.bls.gov/data/inflation_calculator.htm.Accessed:11/25/2013.

[185] Essential Wholesale and Labs. *Products: Di Propylene Glycol*. 2013. URL: http://www.essentialwholesale.com/product/1214/di-propylene-glycol.Accessed:December19,2013.

[186] Davis Langdon. "Life Cycle Costing (LCC) as a contribution to sustainable construction: a common methodology". In: *Final Report* (2007).

[187] James Larminie, Andrew Dicks, and Maurice S McDonald. *Fuel cell systems explained*. Vol. 2. Wiley Chichester, 2003.

[188] Christina Laskowski and Stephen Derby. "Fuel Cell ASAP: Two Iterations of an Automated Stack Assembly Process and Ramifications for Fuel Cell Design-for-Manufacture Considerations". In: *Journal of Fuel Cell Science and Technology* 8.3 (2011), p. 031004. URL: http://link.aip.org/link/?FCT/8/031004/1http://dx.doi.org/10.1115/1.4000684.

[189] R. J. Lawrance. "Low Cost Bipolar Current Collector-Separator for Electrochemical Cells". United States Patent 4,214,969. 1980.

[190] Shuo-Jen Lee, Yu-Pang Chen, and Ching-Han Huang. "Electroforming of metallic bipolar plates with micro-featured flow field". In: *Journal of Power Sources* 145.2 (2005), pp. 369–375. ISSN: 0378-7753. DOI: http://dx.doi.org/10.1016/j.jpowsour.2004.12.072. URL: http://www.sciencedirect.com/science/article/pii/S0378775305002867.

[191] Shuo-Jen Lee, Jian-Jang Lai, and Ching-Han Huang. "Stainless steel bipolar plates". In: *Journal of Power Sources* 145.2 (2005), pp. 362–368. ISSN: 0378-7753. DOI: 10.1016/j.jpowsour.2005.01.082. URL: http://www.sciencedirect.com/science/article/pii/S0378775305003198.

[192] Daniel Lenkeit. *Wage costs and anchillary wage costs in Germany*. Report. 2012.

[193] David Leonhardt. *State-by-State Property Tax*. 2007. URL: http://www.nytimes.com/2007/04/10/business/11leonhardt-avgproptaxrates.html. Accessed: February22,2013.

[194] Kurt J. Lesker. *Chromium (Cr) Sputtering Targets*. 2013. URL: http://www.lesker.com/newweb/deposition_materials/depositionmaterials_sputtertargets_1.cfm?pgid=cr1.Accessed:December19,2013.

[195] M. Li et al. "Design, Manufacturing, and Performance of PEM Fuel Cell Metallic Bipolar Plates". In: *Journal of Fuel Cell Science and Technology* 2008 (2009).

[196] Wen Li, Sami Kara, and Bernard Kornfeld. "Developing Unit Process Models for Predicting Energy Consumption in Industry: A Case of Extrusion Line". In: *Re-engineering Manufacturing for Sustainability*. Ed. by Andrew Y. C. Nee, Bin Song, and Soh-Khim Ong. Springer Singapore, 2013. Chap. 24, pp. 147–152. ISBN: 978-981-4451-47-5. DOI: 10.1007/978-981-4451-48-2_24. URL: http://dx.doi.org/10.1007/978-981-4451-48-2_24.

[197] Wen Li et al. "An Investigation into Fixed Energy Consumption of Machine Tools". In: *Glocalized Solutions for Sustainability in Manufacturing*. Ed. by Jrgen Hesselbach and Christoph Herrmann. Springer Berlin Heidelberg, 2011. Chap. 47, pp. 268–273. ISBN: 978-3-642-19691-1. DOI: 10.1007/978-3-642-19692-8_47. URL: http://dx.doi.org/10.1007/978-3-642-19692-8_47.

[198] Xianguo Li and Imran Sabir. "Review of bipolar plates in PEM fuel cells: Flow-field designs". In: *International Journal of Hydrogen Energy* 30.4 (2005), pp. 359–371. ISSN: 0360-3199. DOI: 10.1016/j.ijhydene.2004.09.019. URL: http://www.sciencedirect.com/science/article/pii/S0360319904003453.

[199] Xingong Li et al. "GIS analysis of global impacts from sea level rise". In: *Photogrammetric Engineering and Remote Sensing* 75.7 (2009), pp. 807–818.

[200] P.-C. Lin. "Estimating the Energy Demand of Industrial HVAC". Dissertation. 1999.

[201] Barbara Linke et al. "Combination of Speed Stroke Grinding and High Speed Grinding with Regard to Sustainability". In: *Laboratory for Manufacturing and Sustainability, UC Berkeley* (2011). URL: http://www.escholarship.org/uc/item/5qs5k8pv.

[202] Dongan Liu, Linfa Peng, and Xinmin Lai. "Effect of assembly error of bipolar plate on the contact pressure distribution and stress failure of membrane electrode assembly in proton exchange membrane fuel cell". In: *Journal of Power Sources* 195.13 (2010), pp. 4213–4221. ISSN: 0378-7753. DOI: http://dx.doi.org/10.1016/j.jpowsour.2009.12.113. URL: http://www.sciencedirect.com/science/article/pii/S0378775310000418.

[203] Yanxiong Liu and Lin Hua. "Fabrication of metallic bipolar plate for proton exchange membrane fuel cells by rubber pad forming". In: *Journal of Power Sources* 195.11 (2010), pp. 3529–3535. ISSN: 0378-7753. DOI: http://dx.doi.org/10.1016/j.jpowsour.2009.12.046. URL: http://www.sciencedirect.com/science/article/pii/S0378775309023088.

[204] Shannon M. Lloyd and Robert Ries. "Characterizing, Propagating, and Analyzing Uncertainty in Life-Cycle Assessment: A Survey of Quantitative Approaches". In: *Journal of Industrial Ecology* 11.1 (2007), pp. 161–179. ISSN: 1530-9290. DOI: 10.1162/jiec.2007.1136. URL: http://dx.doi.org/10.1162/jiec.2007.1136.

[205] B. Lu et al. "Systematic Lifecycle Design for Sustainable Product Development". In: *Concurrent Engineering* 19.4 (2011), pp. 307–324. DOI: 10.1177/1063293x11424513. URL: http://cer.sagepub.com/content/19/4/307.abstract.

[206] Nino Marchetti. *Worldwide Electric Vehicle Sales Slowly Inching Up*. 2013. URL: http://www.earthtechling.com/2013/04/worldwide-electric-vehicle-sales-slowly-inching-up/.Accessed:7/23/2013.

[207] M. F. Mathias et al. "Diffusion media materials and characterisation". In: *Handbook of Fuel Cells*. John Wiley and Sons, Ltd, 2010. ISBN: 9780470974001. DOI: 10.1002/9780470974001.f303046. URL: http://dx.doi.org/10.1002/9780470974001.f303046.

[208] S. Matsuo. "Honda fuel cell activities". In: *Handbook of Fuel Cells*. John Wiley and Sons, Ltd, 2010. ISBN: 9780470974001. DOI: 10.1002/9780470974001.f311099. URL: http://dx.doi.org/10.1002/9780470974001.f311099.

[209] J. Mattis et al. "A framework for analyzing energy efficient injection-molding die design". In: *Electronics and the Environment, 1996. ISEE-1996., Proceedings of the 1996 IEEE International Symposium on*. 1996, pp. 207–212. DOI: 10.1109/isee.1996.501879.

[210] Seward E. Matwick. "An Economic Evaluation of Sheet Hydroforming and Low Volume Stamping and the Effects of Manufacturing Systems Analysis". Thesis. 2003.

[211] Kenneth A Mauritz and Robert B Moore. "State of understanding of Nafion". In: *Chemical reviews* 104.10 (2004), pp. 4535–4585.

[212] Matt McGrath. *Arctic methane 'time bomb' could have huge economic costs*. 2013. URL: http://www.bbc.co.uk/news/science-environment-23432769.Accessed:7/25/2013.

[213] KatherineC McKinstry et al. "Decision Making Methodology to Reduce Energy in Automobile Manufacturing". In: *Leveraging Technology for a Sustainable World*. Ed. by David A. Dornfeld and Barbara S. Linke. Springer Berlin Heidelberg, 2012. Chap. 12, pp. 67–71. ISBN: 978-3-642-29068-8. DOI: 10.1007/978-3-642-29069-5_12. URL: http://dx.doi.org/10.1007/978-3-642-29069-5_12.

[214] Tim McMahon. *Current Inflation Rate*. 2013. URL: http://inflationdata.com/inflation/Inflation_Rate/CurrentInflation.asp. Accessed: September3, 2013.

[215] Viral Mehta. "Analysis of Design and Manufacturing of Proton Exchange Membrane Fuel Cells". Thesis. 2002.

[216] Viral Mehta and Joyce Smith Cooper. "Review and analysis of PEM fuel cell design and manufacturing". In: *Journal of Power Sources* 114.1 (2003), pp. 32–53. ISSN: 0378-7753. DOI: http://dx.doi.org/10.1016/S0378-7753(02)00542-6. URL: http://www.sciencedirect.com/science/article/pii/S0378775302005426.

[217] Methanex. *Methanol Regional Posted Contract Prices*. 2012. URL: http://www.methanex.com/products/methanolprice.html.Accessed:December19,2013.

[218] Methanex. *Technical Information and Safe Handling Guide for Methanol*. Report. Methanex Corporation, 2006.

[219] Joelle Michaels. *Update on the 2012 Commercial Building Energy Consumption Survey (CBECS)*. Report. U.S. EIA, 2012.

[220] Hans Millauer, Werner Schwertfeger, and Gnter Siegemund. "Hexafluoropropene Oxide A Key Compound in Organofluorine Chemistry". In: *Angewandte Chemie International Edition in English* 24.3 (1985), pp. 161–179. ISSN: 1521-3773. DOI: 10.1002/anie.198501611. URL: http://dx.doi.org/10.1002/anie.198501611.

[221] Tetsuo Mitani and Kenro Mitsuda. "Durability of Graphite Composite Bipolar Plates". In: *Polymer Electrolyte Fuel Cell Durability*. Ed. by FelixN Bchi, Minoru Inaba, and ThomasJ Schmidt. Springer New York, 2009. Chap. 12, pp. 257–268. ISBN: 978-0-387-85534-9. DOI: 10.1007/978-0-387-85536-3_12. URL: http://dx.doi.org/10.1007/978-0-387-85536-3_12.

[222] Mitsubishi. *Mitsubishi All-Electric Injection Molding Machine ME Series*. Brochure. MHI Injection Molding Machinery, Inc., 2012.

[223] Mitsubishi. *Mitsubishi All Electric Injection Molding Machine MEtIII Series*. Brochure. MHI Injection Molding Machinery, Inc., 2011.

[224] Jason Morgan. *Reduction in Fabrication Costs of Gas Diffusion Layers*. PPT Presentation. Ballard Material Products, 2011.

[225] Patrick John Morrisey. "Membrane moisture measurement". United States Patent 2003/0204323. 2003.

[226] W. R. Morrow et al. "Environmental aspects of laser-based and conventional tool and die manufacturing". In: *Journal of Cleaner Production* 15.10 (2007), pp. 932–943. ISSN: 0959-6526. DOI: 10.1016/j.jclepro.2005.11.030. URL: http://www.sciencedirect.com/science/article/pii/S0959652605002799.

[227] Richard H. Moss et al. "The next generation of scenarios for climate change research and assessment". In: *Nature* 463.7282 (2010). 10.1038/nature08823, pp. 747–756. ISSN: 0028-0836. DOI: http://www.nature.com/nature/journal/v463/n7282/suppinfo/nature08823_S1.html. URL: http://dx.doi.org/10.1038/nature08823.

[228] D. Mourtzis, K. Alexopoulos, and G. Chryssolouris. "Flexibility consideration in the design of manufacturing systems: An industrial case study". In: *CIRP Journal of Manufacturing Science and Technology* 5.4 (2012), pp. 276–283. ISSN: 1755-5817. DOI: http://dx.doi.org/10.1016/j.cirpj.2012.10.001. URL: http://www.sciencedirect.com/science/article/pii/S1755581712000673.

[229] Reimund Neugebauer et al. "Energy-Sensitive Production Control in Mixed Model Manufacturing Processes". In: *Leveraging Technology for a Sustainable World*. Ed. by David A. Dornfeld and Barbara S. Linke. Springer Berlin Heidelberg, 2012. Chap. 68, pp. 399–404. ISBN: 978-3-642-29068-8. DOI: 10.1007/978-3-642-29069-5_68. URL: http://dx.doi.org/10.1007/978-3-642-29069-5_68.

[230] Reimund Neugebauer et al. "Reducing Energy Demands of Printing Machines by Energy Reuse Options and Optimization". In: *Leveraging Technology for a Sustainable World*. Ed. by David A. Dornfeld and Barbara S. Linke. Springer Berlin Heidelberg, 2012. Chap. 19, pp. 107–112. ISBN: 978-3-642-29068-8. DOI: 10.1007/978-3-642-29069-5_19. URL: http://dx.doi.org/10.1007/978-3-642-29069-5_19.

[231] *New Brunswick Ultra-Low Temperature Freezers*. Report. 2012.

[232] Ruisheng Ng et al. "An Algorithmic Approach to Streamlining Product Carbon Footprint Quantification: A Case Study on Sheet Metal Parts". In: *Journal ref: International Journal of Automation Technology* 6.3 (2012), pp. 312–321.

[233] Tien Nguyen, Jake Ward, and Kristen Johnson. *Well-to-Wheel Greenhouse Gas Emissions and Petroleum Use for Mid-Size Light-Duty Vehicles*. Report. U.S. Department of Enegy, 2013.

[234] NHTSA. *Obama Administration Finalizes Historic 54.5 mpg Fuel Efficiency Standards*. 2012. URL: http://www.nhtsa.gov/About+NHTSA/Press+Releases/2012/Obama+Administration+Finalizes+Historic+54.5+mpg+Fuel+Efficiency+Standards.Accessed:July27,2013.

[235] Stephan Niggeschmidt et al. "Integrating Green and Sustainability Aspects into Life Cycle Performance Evaluation". In: *Laboratory for Manufacturing and Sustainability, UC Berkeley* (2010). URL: http://www.escholarship.org/uc/item/825308wk.

[236] Y. Nishi and K. Ishiguro. "Fuel Cell Separator and its Manufacturing Method". United States Patent 2005/0238941. 2005.

[237] Nissan. *The Strategic Cooperation Between Daimler and the Renault-Nissan Alliance Forms Agreement with Ford to Accerlate Commercialization of Fuel Cell Electric Vehicle Technology*. 2013. URL: http://www.nissan-global.com/EN/NEWS/2013/_STORY/130128-02-e.html.Accessed:November28,2013.

[238] David L. Nofziger. *Soil Temperature Variations With Time and Depth*. 2003. URL: http://soilphysics.okstate.edu/software/SoilTemperature/document.pdf. Accessed:January24,2013.

[239] NREL. *U.S. Life Cycle Inventory Database Roadmap*. Report. U.S. Department of Energy, 2009.

[240] NuCellSys. *History - NuCellSys - a future-oriented initiative*. 2013. URL: http://www.nucellsys.com/index.dhtml/045298220a38c433936m/-/enEN/-/CS/-/Unternehmen/Geschichte.Accessed:November28,2013.

[241] William George O'Brien. "Continuous Production of Catalyst Coated Membranes". United States Patent 7,316,794. 2008.

[242] G. J. Offer et al. "Comparative analysis of battery electric, hydrogen fuel cell and hybrid vehicles in a future sustainable road transport system". In: *Energy Policy* 38.1 (2010), pp. 24–29. ISSN: 0301-4215. DOI: http://dx.doi.org/10.1016/j.enpol.2009.08.040. URL: http://www.sciencedirect.com/science/article/pii/S0301421509006260.

[243] A. Ohma. "Electrolyte Membrane-Electrode Assembly and Method of Production Thereof". United States Patent 2009/0035634. 2009.

[244] Michael Overcash and Janet Twomey. "Unit Process Life Cycle Inventory (UPLCI) A Structured Framework to Complete Product Life Cycle Studies". In: *Leveraging Technology for a Sustainable World*. Ed. by David A. Dornfeld and Barbara S. Linke. Springer Berlin Heidelberg, 2012. Chap. 1, pp. 1–4. ISBN: 978-3-642-29068-8. DOI: 10.1007/978-3-642-29069-5_1. URL: http://dx.doi.org/10.1007/978-3-642-29069-5_1.

[245] Anil K Pabby, Syed SH Rizvi, and Ana Maria Sastre. *Handbook of membrane separations: Chemical, pharmaceutical, food, and biotechnological applications*. CRC press, 2008. ISBN: 0849395496.

[246] S. Pacala and R. Socolow. "Stabilization Wedges: Solving the Climate Problem for the Next 50 Years with Current Technologies". In: *Science* 305.5686 (2004), pp. 968–972. DOI: 10.1126/science.1100103. URL: http://www.sciencemag.org/content/305/5686/968.abstract.

[247] Sehkyu Park, Jong-Won Lee, and Branko N. Popov. "Effect of PTFE content in microporous layer on water management in PEM fuel cells". In: *Journal of Power Sources* 177.2 (2008), pp. 457–463. ISSN: 0378-7753. DOI: http://dx.doi.org/10.1016/j.jpowsour.2007.11.055. URL: http://www.sciencedirect.com/science/article/pii/S0378775307025657.

[248] PE-International. *GaBi Life Cycle Assessment Software*. PC Software. 2013.

[249] Martin Pehnt. "Life-cycle assessment of fuel cell stacks". In: *International Journal of Hydrogen Energy* 26.1 (2001), pp. 91–101. ISSN: 0360-3199. DOI: http://dx.doi.org/10.1016/S0360-3199(00)00053-7. URL: http://www.sciencedirect.com/science/article/pii/S0360319900000537.

[250] JL Pellegrino et al. "Energy Use, Loss and Opportunities Analysis: US Manufacturing Mining". In: *US Department of Energy* (2004).

[251] Linfa Peng et al. "Design, Optimization, and Fabrication of Slotted-Interdigitated Thin Metallic Bipolar Plates for PEM Fuel Cells". In: *Journal of Fuel Cell Science and Technology* 8.1 (2011), p. 011002. ISSN: 1550-624X.

[252] Linfa Peng et al. "Fabrication of Metallic Bipolar Plates for Proton Exchange Membrane Fuel Cell by Flexible Forming Process-Numerical Simulations and Experiments". In: *Journal of Fuel Cell Science and Technology* 7.3 (2010), p. 031009. URL: http://link.aip.org/link/?FCT/7/031009/1http://dx.doi.org/10.1115/1.3207870.

[253] Linfa Peng et al. "Flow channel shape optimum design for hydroformed metal bipolar plate in PEM fuel cell". In: *Journal of Power Sources* 178.1 (2008), pp. 223–230. ISSN: 0378-7753. DOI: http://dx.doi.org/10.1016/j.jpowsour.2007.12.037. URL: http://www.sciencedirect.com/science/article/pii/S0378775307026596.

[254] British Petroleum. *BP Statistical Review of World Energy; June 2013*. Excel File. 2013. URL: http://www.bp.com/statisticalreview.Accessed:7/23/2013.

[255] J. C. Phillips. *USA Energy Inflation Forecast*. 2013. URL: http://www.forecast-chart.com/inflation-usa-energy.html.Accessed:September3,2013.

[256] D. Pierpont et al. "Processing Methods and Systems for Assembling Fuel Cell Perimeter Gaskets". United States Patent 8,288,059. 2012.

[257] *Polymer Fuel Cells Cost reduction and market potential*. Report. The Carbon Trust, 2012.

[258] David N. Prugh and H. P. Tannenbaum. "Production of Catalyst Coated Membranes". United States Patent 2009/0169950. 2009.

[259] PTI. *German Property Tax Information*. 2008. URL: http://www.ptireturns.com/en/tax_info/de.php.Accessed:December6,2013.

[260] Robert E. Putnam and William D. Nicoll. "Fluorocarbon Ethers Containing Sulfonyl Groups". United States Patent 3,301,893. 1967.

[261] Farhan Qureshi et al. "Unit Process Energy Consumption Models for Material Addition Processes: A Case of the Injection Molding Process". In: *Leveraging Technology for a Sustainable World*. Ed. by David A. Dornfeld and Barbara S. Linke. Springer Berlin Heidelberg, 2012. Chap. 46, pp. 269–274. ISBN: 978-3-642-29068-8. DOI: 10.1007/978-3-642-29069-5_46. URL: http://dx.doi.org/10.1007/978-3-642-29069-5_46.

[262] V. Ramanathan. "Trace-Gas Greenhouse Effect and Global Warming: Underlying Principles and Outstanding Issues Volvo Environmental Prize Lecture-1997". In: *Ambio* 27.3 (1998), pp. 187–197. ISSN: 00447447. DOI: 10.2307/4314715. URL: http://www.jstor.org/stable/4314715.

[263] Karthik Ramani et al. "Integrated Sustainable Life Cycle Design: A Review". In: *Journal of Mechanical Design* 132.9 (2010). 10.1115/1.4002308, pp. 091004–091004. ISSN: 1050-0472. DOI: 10.1115/1.4002308. URL: http://dx.doi.org/10.1115/1.4002308.

[264] Kim J. R. Rasmussen. *Full-range Stress-strain Curves for Stainless Steel Alloys*. Report. The University of Sydney, 2001.

[265] G. Rebitzer et al. "Life cycle assessment: Part 1: Framework, goal and scope definition, inventory analysis, and applications". In: *Environment International* 30.5 (2004), pp. 701–720. ISSN: 0160-4120. DOI: http://dx.doi.org/10.1016/j.envint.2003.11.005. URL: http://www.sciencedirect.com/science/article/pii/S0160412003002459.

[266] Corinne Reich-Weiser, Athulan Vijayaraghavan, and David Dornfeld. "Appropriate use of green manufacturing frameworks". In: (2010).

[267] Corinne Reich-Weiser et al. "Development of the supply chain optimization and planning for the environment (SCOPE) tool-applied to solar energy". In: *Electronics and the Environment, 2008. ISEE 2008. IEEE International Symposium on*. IEEE, 2008, pp. 1–6. ISBN: 1424422728.

[268] Gunther Reinhart et al. "Comparison of the Resource Efficiency of Alternative Process Chains for Surface Hardening". In: *Glocalized Solutions for Sustainability in Manufacturing*. Ed. by Jrgen Hesselbach and Christoph Herrmann. Springer Berlin Heidelberg, 2011. Chap. 54, pp. 311–316. ISBN: 978-3-642-19691-1. DOI: 10.1007/978-3-642-19692-8_54. URL: http://dx.doi.org/10.1007/978-3-642-19692-8_54.

[269] Ins Ribeiro, Paulo Peas, and Elsa Henriques. "Assessment of Energy Consumption in Injection Moulding Process". In: *Leveraging Technology for a Sustainable World*. Ed. by David A. Dornfeld and Barbara S. Linke. Springer Berlin Heidelberg, 2012. Chap. 45, pp. 263–268. ISBN: 978-3-642-29068-8. DOI: 10.1007/978-3-642-29069-5_45. URL: http://dx.doi.org/10.1007/978-3-642-29069-5_45.

[270] A. Rodrigues, M. Fronk, and B. McCormick. "General motors/OPEL Fuel cell activities driving towards a successful future". In: *Handbook of Fuel Cells*. John Wiley and Sons, Ltd, 2010. ISBN: 9780470974001. DOI: 10.1002/9780470974001.f311098. URL: http://dx.doi.org/10.1002/9780470974001.f311098.

[271] Frances Romero. *A Brief History of The Electric Car*. 2009. URL: http://www.time.com/time/business/article/0,8599,1871282,00.html.Accessed:7/29/2013.

[272] Sergio Romero-Hernandez et al. "Supply Chain Life Cycle Implications of Shipping Goods from Mexico A Case on PV Solar Panels". In: *Leveraging Technology for a Sustainable World*. Ed. by David A. Dornfeld and Barbara S. Linke. Springer Berlin Heidelberg, 2012. Chap. 102, pp. 605–610. ISBN: 978-3-642-29068-8. DOI: 10.1007/978-3-642-29069-5_102. URL: http://dx.doi.org/10.1007/978-3-642-29069-5_102.

[273] D.V. Rosato, D.V. Rosato, and M.G. Rosato. *Injection Molding Handbook*. Kluwer Academic Publishers, 2000. ISBN: 9780792386193.

[274] D.V. Rosato, M.G. Rosato, and N. R. Schott. *Plastics technology handbook, Volume 1: introduction, properties, fabrication, processes*. New York, NY: Momentum Press, 2010, p. 1458. ISBN: 9781606500798.

[275] Yeetsorn Rungsima, W. Fowler Michael, and Tzoganakis Costas. "A Review of Thermoplastic Composites for Bipolar Plate Materials in PEM Fuel Cells". In: *Nanocomposites with Unique Properties and Applications in Medicine and Industry*. 2011.

[276] K. Saito and A. Hagiwara. "Separator for Fuel Cell, Process for Production Thereof, and Solid Polymer Type Fuel Cell Using Said Separator". United States Patent 6,881,512. 2005.

[277] K. Saito, A. Hagiwara, and A. Miyazawa. "Fuel Cell Separator, Process for Production Thereof, and Polymer Electrolyte Fuel Cell". United States Patent 6,939,638. 2005.

[278] G. Sandstede et al. "History of low temperature fuel cells". In: *Handbook of Fuel Cells*. John Wiley Sons, Ltd, 2010. ISBN: 9780470974001. DOI: 10.1002/9780470974001.f104011. URL: http://dx.doi.org/10.1002/9780470974001.f104011.

[279] Joo P. Santos et al. "Improving the environmental performance of machine-tools: influence of technology and throughput on the electrical energy consumption of a press-brake". In: *Journal of Cleaner Production* 19.4 (2011), pp. 356–364. ISSN: 0959-6526. DOI: http://dx.doi.org/10.1016/j.jclepro.2010.10.009. URL: http://www.sciencedirect.com/science/article/pii/S0959652610004002.

[280] Makiko Sato. *Forcings in GISS Climate Model*. 2012. URL: http://data.giss.nasa.gov/modelforce/.Accessed:7/17/2013.

[281] Alexander Schabert. "Life cycle assessment of fuel cell components bipolar plate and membrane electrode assembly". Thesis. 2010.

[282] Michael Schaffroth, Tanja Sprosser, and Benedikt Rode. *Zusammenfassung: 12th Ulm Electrochemical Talks*. Report. Daimler-Benz, 2010.

[283] R. Schlosser et al. "Assessment of Energy and Resource Consumption of Processes and Process Chains within the Automotive Sector". In: *Glocalized Solutions for Sustainability in Manufacturing*. Ed. by Jrgen Hesselbach and Christoph Herrmann. Springer Berlin Heidelberg, 2011. Chap. 8, pp. 45–50. ISBN: 978-3-642-19691-1. DOI: 10.1007/978-3-642-19692-8_8. URL: http://dx.doi.org/10.1007/978-3-642-19692-8_8.

[284] H. P. Schmid and J. Ebner. "DaimlerChrysler fuel cell activities". In: *Handbook of Fuel Cells*. John Wiley and Sons, Ltd, 2010. ISBN: 9780470974001. DOI: 10.1002/9780470974001.f310097. URL: http://dx.doi.org/10.1002/9780470974001.f310097.

[285] Brian Selinger. *Building Costs*. Report. Department of Commerce and Economic Opportunity, 2011.

[286] Serv-A-Pure. *Serv-A-Pure Ez-Bulk-220, 200 Gallon Tote of Deionzied Water*. 2013. URL: http://www.servapure.com/Serv-A-Pure-EZ-BULK-220-220-Gallon-Tote-of-Deionized-Water_p_4982.html.Accessed:December19,2013.

[287] J. H. Shane, R. J. Russell, and R. A. Bochan. "Flexible Graphite Material of Expanded Particles Compressed Together". United States Patent 3,404,061. 1968.

[288] J. Shang et al. "Commercialization of Fuel Cell Bipolar Plate Manufacturing by Electromagnetic Forming". In: *Third Frontier Fuel Cell Program* (2010).

[289] James R. Sheats. "Roll-to-roll manufacturing of thin film electronics". In: vol. 4688. 10.1117/12.472297. 2002, pp. 240–248. URL: http://dx.doi.org/10.1117/12.472297.

[290] CheeWaiPatrick Shi et al. "Identifying Carbon Footprint Reduction Opportunities through Energy Measurements in Sheet Metal Part Manufacturing". In: *Glocalized Solutions for Sustainability in Manufacturing*. Ed. by Jrgen Hesselbach and Christoph Herrmann. Springer Berlin Heidelberg, 2011. Chap. 67, pp. 389–394. ISBN: 978-3-642-19691-1. DOI: 10.1007/978-3-642-19692-8_67. URL: http://dx.doi.org/10.1007/978-3-642-19692-8_67.

[291] J. Shi, A. Zhamu, and B. Z. Jang. "Continious Production of Exfoliated Graphite Composite Compositions and Flow Field Plates". United States Patent 7,758,783. 2010.

[292] Sigma-Aldrich. *Triton X-100: labortory grade*. 2013. URL: http://www.sigmaaldrich.com/catalog/product/sial/x100?lang=en&region=US.Accessed:December19,2013.

[293] Jayanti Sinha and Yong Yang. *Direct Hydrogen PEMFC Manufacturing Cost Estimate for Automotive Applications*. Report. Tiax LLC, 2010.

[294] Jayanti Sinha et al. *Fuel Cell Tech Team Review*. Report. Tiax, LLC, 2008.

[295] Terry Sizemore. *Design for Stamping*. Report. University of Detroit-Mercy, 2007.

[296] Duane R. Smith. *Challenges of Web Handling and Winding*. 2010. URL: http://www.tappi.org/content/events/10EXTRU/papers/2.4a.pdf.Accessed:December19,2013.

[297] Payman Sobhanipour, Reza Cheraghi, and Alex A. Volinsky. "Thermoporometry study of coagulation bath temperature effect on polyacrylonitrile fibers morphology". In: *Thermochimica Acta* 518.12 (2011), pp. 101–106. ISSN: 0040-6031. DOI: http://dx.doi.org/10.1016/j.tca.2011.02.015. URL: http://www.sciencedirect.com/science/article/pii/S004060311100102X.

[298] Duarte R. Sousa. *PEM Stack Manufacturing: Industry Status*. PPT Presentation. Ballard Power Systems, 2011.

[299] John Sousanis. *World Vehicle Population Tops 1 Billion Units*. 2011. URL: http://wardsauto.com/ar/world_vehicle_population_110815.Accessed:7/29/2013.

[300] Anne M. Stark. *Sufficient wind energy available to meet global demand without damaging climate*. 2012. URL: https://www.llnl.gov/news/newsreleases/2012/Sep/NR-12-09-03.html.Accessed:7/23/2013.

[301] StatisticsBureau. *Chapter 16 Labour and Wages*.

[302] Matteo Strano and Paolo Albertelli. *Eco-Design of Forming Machines*. Report. Polytechnic University of Milan, 2012.

[303] JackC P. Su, Chih-Hsing Chu, and Yu-Te Wang. "A Framework to Integrate Product Design and Supply Chain Decisions to Minimize CO2 Emission". In: *Leveraging Technology for a Sustainable World*. Ed. by David A. Dornfeld and Barbara S. Linke. Springer Berlin Heidelberg, 2012. Chap. 104, pp. 617–622. ISBN: 978-3-642-29068-8. DOI: 10.1007/978-3-642-29069-5_104. URL: http://dx.doi.org/10.1007/978-3-642-29069-5_104.

[304] Sangwon Suh. "Functions, commodities and environmental impacts in an ecological-economic model". In: *Ecological Economics* 48.4 (2004), pp. 451–467. ISSN: 0921-8009. DOI: http://dx.doi.org/10.1016/j.ecolecon.2003.10.013. URL: http://www.sciencedirect.com/science/article/pii/S0921800904000229.

[305] Sangwon Suh. "Materials and energy flows in industry and ecosystem networks". In: *The International Journal of Life Cycle Assessment* 9.5 (2004), pp. 335–336. ISSN: 0948-3349. DOI: 10.1007/bf02979425. URL: http://dx.doi.org/10.1007/BF02979425.

[306] Graco Supply. *Eccobond 60L A/B Qt Kit 12oz part A/ 4oz part B*. 2013. URL: http://www.gracosupply.com/p-60065-eccobond-60l-ab-qt-kit-12oz-part-a-4oz-part-b.aspx.Accessed:December19,2013.

[307] *Sustainable Transportation Energy Pathways: A Research Summary for Decision Makers*. Report. UC Davis, Institute of Transportation Studies, 2011.

[308] Bent Srensen. "Total life-cycle assessment of PEM fuel cell car". In: *Paper 3-1189 in Proc. 15th World Hydrogen Energy Conf., Yokohama. CDROM, World Hydrogen Energy Association*. 2004.

[309] K. Tabata, F. Fujibayashi, and M. Aimu. "Membrane-Electrode-Assembly with Solid Polymer Electrolyte". United States Patent 6,723,464. 2004.

[310] Joana Taborda. *Canada Inlfation Rate*. 2013. URL: http://www.tradingeconomics.com/canada/inflation-cpi.Accessed:September3,2013.

[311] Z. Tadmor and C.G. Gogos. *Principles of Polymer Processing*. 2nd. Wiley, 2006. ISBN: 9780471792765.

[312] Raymond R. Tan, Alvin B. Culaba, and Michael R. I. Purvis. "Application of possibility theory in the life-cycle inventory assessment of biofuels". In: *International Journal of Energy Research* 26.8 (2002), pp. 737–745. ISSN: 1099-114X. DOI: 10.1002/er.812. URL: http://dx.doi.org/10.1002/er.812.

[313] RaymondR Tan. "Using fuzzy numbers to propagate uncertainty in matrix-based LCI". In: *The International Journal of Life Cycle Assessment* 13.7 (2008), pp. 585–592. ISSN: 0948-3349. DOI: 10.1007/s11367-008-0032-x. URL: http://dx.doi.org/10.1007/s11367-008-0032-x.

[314] F. Tanno. "Fuel Cell Separator and Method of Manufacture". United States Patent 2004/0005493. 2004.

[315] Oleksandr Tanskyi. "Analysis of Innovative HVAC System Technologies and Their Application for Office Buildings in Hot and Humid Climates". Thesis. 2010.

[316] C. S. Thakur. *Compresson Molding*. 2008. URL: http://aml883.wdfiles.com/local--files/misc-mat/CompressionMoulding.ppt.Accessed:September17,2012.

[317] Sebastian Thiede, Christoph Herrmann, and Sami Kara. "State of Research and an innovative Approach for simulating Energy Flows of Manufacturing Systems". In: *Glocalized Solutions for Sustainability in Manufacturing*. Ed. by Jrgen Hesselbach and Christoph Herrmann. Springer Berlin Heidelberg, 2011. Chap. 58, pp. 335–340. ISBN: 978-3-642-19691-1. DOI: 10.1007/978-3-642-19692-8_58. URL: http://dx.doi.org/10.1007/978-3-642-19692-8_58.

[318] A. Thiriez and T. Gutowski. "An Environmental Analysis of Injection Molding". In: *Electronics and the Environment, 2006. Proceedings of the 2006 IEEE International Symposium on*. 2006, pp. 195–200. ISBN: 1095-2020. DOI: 10.1109/isee.2006.1650060.

[319] C. E. Thomas. "Fuel cell and battery electric vehicles compared". In: *International Journal of Hydrogen Energy* 34.15 (2009), pp. 6005–6020. ISSN: 0360-3199. DOI: http://dx.doi.org/10.1016/j.ijhydene.2009.06.003. URL: http://www.sciencedirect.com/science/article/pii/S0360319909008696.

[320] Rachel Thomas and Hugo Deacon. *Mobile Phone Sales Will Hit 1.86 Billion in 2013 as Strong Smarthphone Growth Continues*. 2013. URL: http://www.ccsinsight.com/press/company-news/1655-mobile-phone-sales-will-hit-186-billion-in-2013-as-strong-smartphone-growth-continues.Accessed:7/17/2013.

[321] Deborah L Thurston. "Multi-attribute utility analysis of conflicting preferences". In: *Decision making in engineering design* (2006), pp. 125–133.

[322] U.S. Department of Transportation. *Table 3-21: Average Freight Revenue Per Ton-mile*. 2013. URL: http://www.rita.dot.gov/bts/sites/rita.dot.gov.bts/files/publications/national_transportation_statistics/html/table_03_21.html.Accessed:December19,2013.

[323] V. Trapp et al. "Bipolar Plates for Fuel Cell Stacks". United States Patent 6,706,437. 2004.

[324] Haruki Tsuchiya and Osamu Kobayashi. "Mass production cost of PEM fuel cell by learning curve". In: *International Journal of Hydrogen Energy* 29.10 (2004), pp. 985–990. ISSN: 0360-3199. DOI: http://dx.doi.org/10.1016/j.ijhydene.2003.10.011. URL: http://www.sciencedirect.com/science/article/pii/S0360319903003136.

[325] C. L. III Tucker. "Compression molding of polymers and composites". In: *Marcel Dekker, Inc., Injection and Compression Molding Fundamentals* (1987), pp. 481–565.

[326] T. Uemura and S. Murakami. "Method for Producing a Carbon Sheet and a Fuel Cell Separator". United States Patent 4,737,421. 1988.

[327] *Unit Manufacturing Processes:Issues and Opportunities in Research*. The National Academies Press, 1995. ISBN: 9780309051927. URL: http://www.nap.edu/openbook.php?record_id=4827.

[328] URI. *Sheet Metal Forming*. Report. University of Rhode Island, 2013.

[329] Alexander Verl et al. "Modular modeling of energy consumption for monitoring and control". In: *Glocalized Solutions for Sustainability in Manufacturing*. Springer, 2011, pp. 341–346. ISBN: 3642196918.

[330] S. E. Veyo et al. "SOFC fuel cell systems". In: *Handbook of Fuel Cells*. John Wiley and Sons, Ltd, 2010. ISBN: 9780470974001. DOI: 10.1002/9780470974001.f312107. URL: http://dx.doi.org/10.1002/9780470974001.f312107.

[331] W. Vielstich. "Ideal and effective efficiencies of cell reactions and comparison to carnot cycles". In: *Handbook of Fuel Cells*. John Wiley and Sons, Ltd, 2010. ISBN: 9780470974001. DOI: 10.1002/9780470974001.f101004. URL: http://dx.doi.org/10.1002/9780470974001.f101004.

[332] W. Vielstich, A. Lamm, and H. A. Gasteiger. *Volume 1: Fundamentals and Survey of Systems*. Handbook of Fuel Cells: Fundamentals, Technology, Applications. Wiley, 2003, p. 3826. ISBN: 0471499269.

[333] Wabash. *Vantage Series 50 to 1000 ton Press*. 2007. URL: www.wabashmpi.com/PDFs/207.pdf.Accessed:November8,2011.

[334] P. E. Waggoner and J. H. Ausubel. "A framework for sustainability science: A renovated IPAT identity". In: *Proceedings of the National Academy of Sciences* 99.12 (2002), pp. 7860–7865. DOI: 10.1073/pnas.122235999. URL: http://www.pnas.org/content/99/12/7860.abstract.

[335] Bill Walczak. *Novel Technology for Mass Production of Bipolar Plates*. Presentation. Cellimpact, 2008.

[336] Da-Yung Wang and Ko-Wei Weng. "Deposition of CrN coatings by current-modulating cathodic arc evaporation". In: *Surface and Coatings Technology* 137.1 (2001), pp. 31–37. ISSN: 0257-8972. DOI: http://dx.doi.org/10.1016/S0257-8972(00)01111-7. URL: http://www.sciencedirect.com/science/article/pii/S0257897200011117.

[337] Fenfen Wang et al. "Exergy Analysis of Atomic Layer Deposition for Al2O3 Nano-film Preparation". In: *Re-engineering Manufacturing for Sustainability*. Ed. by Andrew Y. C. Nee, Bin Song, and Soh-Khim Ong. Springer Singapore, 2013. Chap. 47, pp. 285–290. ISBN: 978-981-4451-47-5. DOI: 10.1007/978-981-4451-48-2_47. URL: http://dx.doi.org/10.1007/978-981-4451-48-2_47.

[338] Ling Wang and Li Lin. "A methodology to incorporate life cycle analysis and the triple bottom line mechanism for sustainable management of industrial enterprises". In: *Proc. of SPIE* 5262 (2004). 10.1117/12.516027, pp. 201–209. URL: http://dx.doi.org/10.1117/12.516027.

[339] Max Wei and Thoms McKone. "A Total Cost of Ownership Model for Design and Manufacturing Optimization of Fuel Cells in Stationary and Emerging Market Applications". In: *Hydrogen and Fuel Cells Program: 2013 Annual Merit Review*. U.S DOE, 2013.

[340] Bo Pedersen Weidema and Marianne Suhr Wesns. "Data quality management for life cycle inventoriesan example of using data quality indicators". In: *Journal of Cleaner Production* 4.34 (1996), pp. 167–174. ISSN: 0959-6526. DOI: http://dx.doi.org/10.1016/S0959-6526(96)00043-1. URL: http://www.sciencedirect.com/science/article/pii/S0959652696000431.

[341] Malcolm A Weiss et al. *Comparative assessment of fuel cell cars*. 2003.

[342] Alexander Weissman et al. "A systematic methodology for accurate design-stage estimation of energy consumption for injection molded parts". In: *Proceedings of the ASME 2010 International Design Engineering Technical Conferences and Computers and Information in Engineering Conference IDETC/CIE*. 2010.

[343] Norman Eugene West. "Process for Pyrolyzing Tetrafluoroethylene to Hexafluoropropylene". United States Patent 3,873,630. March 25, 1975.

[344] D. Wheeler and G. Sverdrup. *2007 Status of Manufacturing: Polymer Electrolyte Membrane (PEM) Fuel Cells*. Report. NREL, 2008.

[345] Darrell Whiteside. "Basics of Web Tension Control". In: *2007 PLACE Conference*. 2007.

[346] T. M. L. Wigley, R. Richels, and J. A. Edmonds. "Economic and environmental choices in the stabilization of atmospheric CO2 concentrations". In: *Nature* 379.6562 (1996). 10.1038/379240a0, pp. 240–243. URL: http://dx.doi.org/10.1038/379240a0.

[347] M. S. Wilson and S. Gottesfeld. "Thin-film catalyst layers for polymer electrolyte fuel cell electrodes". In: *Journal of applied electrochemistry* 22.1 (1992), pp. 1–7. ISSN: 0021-891X. DOI: 10.1007/bf01093004. URL: http://dx.doi.org/10.1007/BF01093004.

[348] M.S. Wilson and D. N. Busick. "Composite Bipolar Plate for Electrochemical Cells". United States Patent 6,248,467. 2001.

[349] J. Wind. "The case for and activities on hydrogen powered fuel cell vehicles". In: *Symposium Water electrolysis and hydrogen as part of the future Renewable Energy System*. Daimler-Benz, 2012.

[350] Boguslaw Wozniczka, Nicholas J. Fletcher, and Peter R. Gribb. "Electrochemical Fuel Cell Stack with Compression Bands". United States Patent 5,993,987. 1999.

[351] Christian Wulff. *Communications with Daimler AG*. Personal Communication. 2013.

[352] Christian Wulff. *Vorgenhen Industrialisierung Potenzialoffensive Welle 2*. Report. Daimler-Benz, 2010.

[353] Cong Xu. "Multi-scale modeling and optimization of PEM fuel cells: Analyses in operations, economics and materials". Copyright - Copyright UMI - Dissertations Publishing 2005 Last updated - 2013-05-09 First page - n/a. Ph.D. 2005.

[354] M. A. Yandrasits, D. A. Ylitalo, and D. W. Kado. "One-Step Method of Bonding and Sealing a Fuel Cell Membrane Electrode Assembly". United States Patent 2005/0263246. 2005.

[355] Dong-hao Ye and Zhi-gang Zhan. "A review on the sealing structures of membrane electrode assembly of proton exchange membrane fuel cells". In: *Journal of Power Sources* 231.0 (2013), pp. 285–292. ISSN: 0378-7753. DOI: http://dx.doi.org/10.1016/j.jpowsour.2013.01.009. URL: http://www.sciencedirect.com/science/article/pii/S0378775313000177.

[356] H. Yokokawa and N. Sakai. "History of high temperature fuel cell development". In: *Handbook of Fuel Cells*. John Wiley and Sons, Ltd, 2010. ISBN: 9780470974001. DOI: 10.1002/9780470974001.f104012. URL: http://dx.doi.org/10.1002/9780470974001.f104012.

[357] C. Yuan and D. Dornfeld. "Environmental performance characterization of atomic layer deposition". In: *Electronics and the Environment, 2008. ISEE 2008. IEEE International Symposium on*. 2008, pp. 1–6. DOI: 10.1109/isee.2008.4562943.

[358] Chris Yuan et al. "A Decision-Based Analysis of Compressed Air Usage Patterns in Automotive Manufacturing". In: *Laboratory for Manufacturing and Sustainability, UC Berkeley* (2006). URL: http://www.escholarship.org/uc/item/0330g886.

[359] Chris Y. Yuan and David A. Dornfeld. "Integrated Sustainability Analysis of Atomic Layer Deposition for Microelectronics Manufacturing". In: *Journal of Manufacturing Science and Engineering* 132.3 (2010). 10.1115/1.4001686, pp. 030918–030918. ISSN: 1087-1357. DOI: 10.1115/1.4001686. URL: http://dx.doi.org/10.1115/1.4001686.

[360] Dongming Zhang et al. "Preparation of Cr-based multilayer coating on stainless steel as bipolar plate for PEMFCs by magnetron sputtering". In: *International Journal of Hydrogen Energy* 36.3 (2011), pp. 2184–2189. ISSN: 0360-3199. DOI: http://dx.doi.org/10.1016/j.ijhydene.2010.10.085. URL: http://www.sciencedirect.com/science/article/pii/S0360319910021932.

[361] Hao Zhang and KarlR Haapala. "Integrating Sustainability Assessment into Manufacturing Decision Making". In: *Leveraging Technology for a Sustainable World*. Ed. by David A. Dornfeld and Barbara S. Linke. Springer Berlin Heidelberg, 2012. Chap. 93, pp. 551–556. ISBN: 978-3-642-29068-8. DOI: 10.1007/978-3-642-29069-5_93. URL: http://dx.doi.org/10.1007/978-3-642-29069-5_93.

[362] M. kermo and B. T. strm. "Modelling component cost in compression moulding of thermoplastic composite and sandwich components". In: *Composites Part A: Applied Science and Manufacturing* 31.4 (2000), pp. 319–333. ISSN: 1359-835X. DOI: http://dx.doi.org/10.1016/S1359-835X(99)00079-2. URL: http://www.sciencedirect.com/science/article/pii/S1359835X99000792.

Appendix A

Appendix

A.1 Chapter 1

No content.

A.2 Chapter 2

The DFMA cost calculation adopted from [114]:

$$
\begin{aligned}
C_c &= (C_{cap} - ITC)\, CRF\,(i', t) && \text{Initial capital investment} \\
C_r &= \left[\textstyle\sum_{k=1}^{t} R_k PWF\,(i', t_k)\right] CRF\,(i', t) && \text{Replacements} \\
C_u &= (C_e + C_{ng} + C_w)\, \tfrac{CRF(i',t)}{CRF(i'',t)} && \text{Utilities} \\
C_b &= C_{fs} CRF\,(i''', t) && \text{Facility floor space} \\
C_m &= M && \text{Maintenance} \\
C_I &= I && \text{Insurance} \\
C_{pt} &= T_{prop} C_{ass}\,(1 - T_{inc}) && \text{Effective property tax} \\
C_s &= -C_{salv} PWF\,(i', t)\, CRF\,(i', t) && \text{Salvage Value} \\
C_{ded} &= -T_{inc} \left[\textstyle\sum_k \tfrac{i_m P_k}{(1+i)^k}\right] CRF\,(i', t) && \text{Interest, tax deduction}
\end{aligned}
\tag{A.1}
$$

Where

C_{cap} = total equipment capital investment including sales tax
C_{salv} = equipment salvage value at end of life
C_{ass} = assess value of equipment
C_e = electricity cost
C_{ng} = natural gas cost
C_w = water cost
$i' = (i - j)/(1 + j)$ = effective equipment discount rate
$i'' = (i - j_e)/(1 + j_e)$ = effective electricity discount rate
$i''' = (i_b - j)/(1 + j)$ = effective facility discount rate
i = equipment discount rate
i_b = facility depreciation rate
M = maintenance ($\$/yr$)
j = general inflation rate
i_m = market mortgage rate
j_e = electricity inflation rate ($\$/\$ - yr$)
k = interval period at which replacements or repairs are made
I = insurance charge ($\$/yr$)
ITC = investment tax credit
R_k = replacement costs in year k in constant \$
P_k = outstanding principal of C_{cap} in year k
t = tool life expectancy
T_{prop} = property tax rate ($\$/\$_{assessed} - yr$)
T_{inc} = state tax rate + federal tax rate − state tax rate × federal tax rate

A.3 Chapter 3

Table A.1: Empirical injection molding data from meta-study.

Clamp Force (U.S. tons)	Baseline (kW)	Mold O/C (kW)	Mold Hold (kW)	Ref.
15	1.4	1.1	0.5	[261]
55	2.4	1.5	1.3	[223]
75	3.0	n.d.	n.d.	[165]
110	3.9	n.d.	3.2	[273]
210	5.8	4.5	6.7	[165]
220	7.0	6.0	6.9	[53]
337	9.0	11	10.5	[269]
495	13	27	n.d.	[222]
550	17	39	18	[318]

Table A.2: Empirical hydraulic press molding power data from meta study.

Motor Rating	Force (U.S. tons)	Baseline (kW)	Ref.
7.5	110	1.5	[279]
9.5	50	1.69	[68]
11	110	2.5	[279]
15	170	4.8	[279]

Table A.3: Wabash Vantage series hydraulic press molding specifications [333].

Compression Force (U.S. tons)	Motor Rating (kW)	Mold Stroke (cm)
50	3.73	20.32
75	n/a	20.32
100	5.60	30.48
150	7.46	30.48
400	n/a	40.64
500	14.92	40.64
600	14.92	45.72
700	18.65	45.72
800	n/a	50.80
1000	22.38	50.80

Table A.4: Empirical servo-electric stamping power data from meta study.

Force (U.S. tons)	Baseline (kW)	Drive (kW)	Ref.
100	0.7	3.0	[279]
200	2.0	4.9	[290]
320	3.2	6.5	[302]

Table A.5: Mechanical behavior for various stainless steels (aggregated data) [264].

Alloy	E_o (GPa)	$\sigma_{0.2}$ (MPa)	σ_u (MPa)	ϵ_u	e	n
UNS30400	189	404	672	0.46	0.0021	5.88
UNS30403	195	429	703	0.51	0.0022	5.51
UNS31603	190	400	616	0.51	0.0017	5.88
UNS31803	205	404	831	0.23	0.0031	7.70
UNS43000	200	320	622	0.48	0.0016	6.37

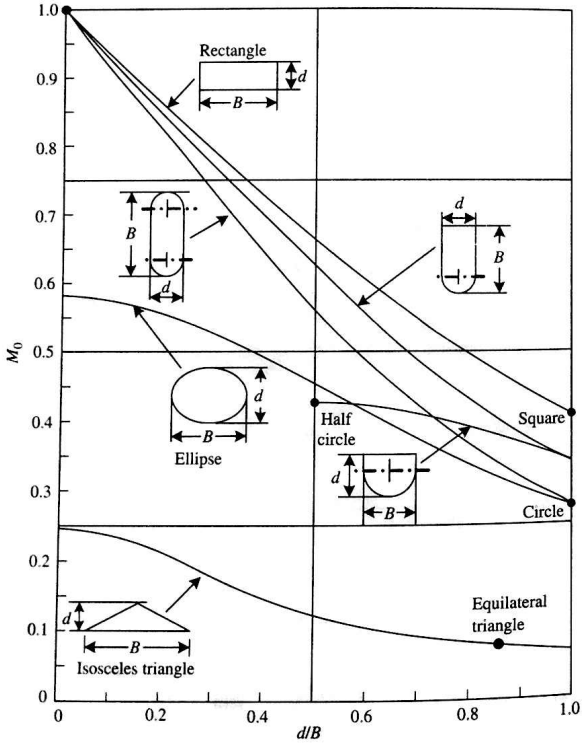

Figure A.1: Shape factors for various mold geometries [311].

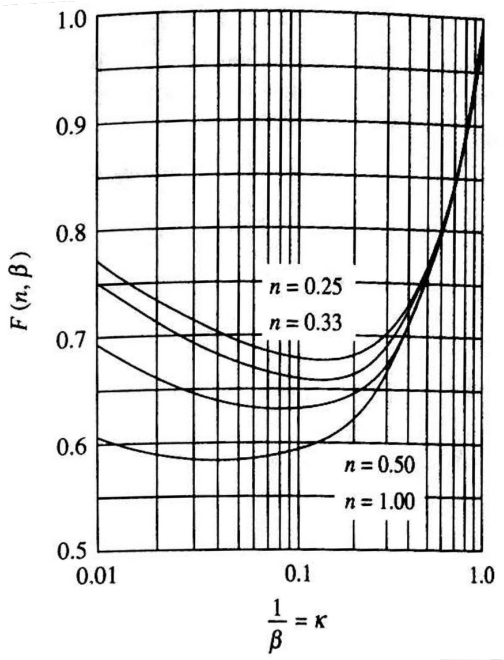

Figure A.2: Shear and geometry dependent shape function for annular shapes [311].

Table A.6: Typical metabolic heat generation rates for various activities [13].

Activity	W/m^2	met
Resting		
Sleeping	40	0.7
Reclining	45	0.8
Seated, quiet	60	1.0
Standing, relaxed	70	1.2
Walking (on level surface)		
3.2 km/h (0.9 m/s)	115	2.0
4.3 km/h (1.2 m/s)	150	2.6
6.4 km/h (1.8 m/s)	220	3.8
Office Activities		
Reading, seated	55	1.0
Writing	60	1.0
Typing	65	1.1
Filing, seated	70	1.2
Filing, standing	80	1.4
Walking about	100	1.7
Lifting/packing	120	2.1
Driving/Flying		
Car	60 to 115	1.0 to 2.0
Aircraft, routine	70	1.2
Aircraft, instrument landing	105	1.8
Aircraft, combat	140	2.4
Heavy vehicle	185	3.2
Miscellaneous Occupational Activities		
Cooking	95 to 115	1.6 to 2.0
Housecleaning	115 to 200	2.0 to 3.4
Seated, heavy limb movement	130	2.2
Machine work		
-sawing (table saw)	105	1.8
-light (electrical industry)	115 to 140	2.0 to 2.4
-heavy	235	4.0
Handling 50 kg bags	235	4.0
Pick and shovel work	235 to 280	4.0 to 4.8
Miscellaneous Leisure Activities		
Dancing, social	140 to 255	2.4 to 4.4
Calisthenics/exercise	175 to 235	3.0 to 4.0
Tennis, singles	210 to 270	3.6 to 4.0
Basketball	290 to 440	5.0 to 7.6
Wrestling, competitive	410 to 505	7.0 to 8.7

The minimum number of iteration for a Monte Carlo simulation is the number of iterations required to reach the maximum error bounds produced by the data and is determined by the standard deviation of the mean:

$$S_{\bar{x}} = \frac{S_x}{\sqrt{n}} \tag{A.2}$$

Where S_x is the standard deviation of the sample and n is the number of samples (i.e., iterations). Using a normal distribution as the reference probability density function with a z-score, z, the maximum error can therefore be defined as []:

$$error_{mas} = \frac{zS_x}{\sqrt{n}} \tag{A.3}$$

and in terms of the percent error (percent error deviation from the mean):

$$E = \frac{100zS_x}{\bar{x}\sqrt{n}} \tag{A.4}$$

Where E is the percent error and $\bar{x}$ is the sample mean. The maximum error, $error_{max}$, in the data can vary from ±50% to over +100%, however, the majority of the data, or the 95% confidence interval, is assumed to be bounded by the ±50%. Therefore, the above equation can be expressed as:

$$E = \frac{100 \times 0.5}{\sqrt{n}} \tag{A.5}$$

Where it has been defined the the 95% confidence interval (z=1.96) relative error, $(1.96S_x/\bar{x})$, is equal to 95% of the maximum data error, 50% (i.e., 0.5). Solve for n yields

$$n = \left[\frac{100 \times 0.5}{0.05}\right]^2 = 100 \tag{A.6}$$

Where the minimum percent error, or error of the highest quality data, is 5% (i.e, 5).

A.4 Chapter 4

No content.

A.5 Chapter 5

ePTFE

The manufacturing process flow of ePTFE for the reinforced membrane is shown in Figure A.3. The flow and process parameters are based on the DuPont patent U.S. 3,953,566 (see Table A.7).

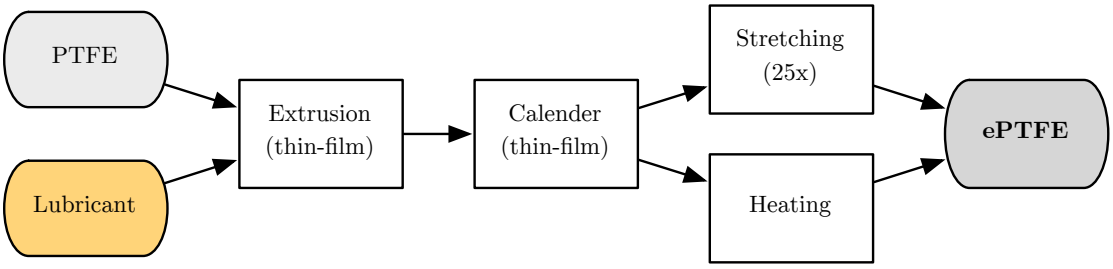

Figure A.3: Manufacturing process flow for ePTFE.

Table A.7: Parameters for ePTFE manufacturing.

Property	Value	Units	Reference
Materials			
ePTFE density	9.8	kg/m^3	[160]
ePTFE porosity	95	%	[160]
PTFE density	2.15	g/cc	[113]
PTFE scrap	2.4	%	[248]
Lubricant density	762	kg/m^3	[99] (Isopar-K[15])
Required lubricant	165.8	cc/lb	[113]
Stretching parameters			
Line speed	0.1524	m/s	[15]
Longitudinal stretch	24.97	n/a	[15]
Traverse stretch	17.76	n/a	[15]
Final width	1	m	assumption
Thickness	25.4	μm	membrane thickness
Original width	5.63	cm	final width/traverse stretch
First stretch width	0.135	m	[15] assuming 2.4 stretch
Final volume	6.34	cm^3	calculated
Final mass	6.21	grams	calculated
Stretching Energy			
Transverse energy	459	joules	calculated
Longitudinal energy	15.1	kJ	calculated
Net energy	15.6	kJ	assuming 20% efficiency loss
Specific energy	3.14	MJ/kg	calculated
Heating Energy			
Heat time	300	sec	[113]
Process temperature	370	°C	[113]
Ramp rate to temperature	30	sec	assumption
Required power	17.5	kW	specific heat of 1500J/kg-K (PTFE)
Specific energy	2.89	kWh/kg	assuming 30s at 100D.C, 50D.C. remaining

HFP analysis

The contribution of HFP to the production of Nafion® based on the U.S. patent 3,873,630. The masses calculations:

Table A.8: HFP material properties.

Property		US Patent 3873630 [343]	
Density, HCl (@ 25°C)	1.49 g/cm^3	TFE/CO_2 wt. ratio	16.2
[1]Density, CO_2 (@ 25°C)	1.81×10^{-3} g/cm^3	HCl flow rate	2.5 cm^3/min
[2]Density, TFE (@ 25°C)	0.904 g/cm^3	HFP yield	85%
[3]Mass (/kg HFP), TFE	1.00 kg	Heated volume	5 cm^3
[4]Mass (/kg HFP), TFE (waste)	0.176 kg	Residence time	1.75 sec
[5]Mass (/kg HFP), CO_2	7.26×10^{-2} kg	[6]TFE flow rate	0.292 kg/hr
[7]Mass (/kg HFP), HCl	0.900 kg		

[1]The reported density of CO_2 is 1.977g/cm^3 at STP, assuming ideal gas law conditions the density at 25°C is: $1.977\times[273/(273+25)] = 0.0018$.

[2]The density of TFE at 25°C can be obtained using the equation from [116]: 1.1325-0.0029*T-0.00025*T^2.

[3]It is assumed that the TFE can be continuously recycled per patent US3873630 to yield a utilization of 100%.

[4]Because the HFP yield is 85%, 15% of the total TFE mass is waste: $1\times(1\text{-}0.85)/0.85 =$ 0.176kg.

[5]The mass ratio of TFE:CO_2 is 16.2, therefore the mass of CO_2 is: $(1+0.176)/16.2 =$ 0.0726kg.

[6]The TFE flow rate: (volume/residence time)$\times[1/\text{Density}_{\text{TFE}}+1/(16.2\times\text{Density}_{\text{CO}_2})]^{-1}$

[7]The HCl mass is equal to HCl flow rate × TFE mass / TFE flow rate × HCl density

The processing energy calculations:

Table A.9: HFP processing energy.

Property	
Processing temperature	834°C [343]
Specific molar heat capacity, TFE	87 J/mol-K
Molecular weight, TFE	100.02 g/mol [116]
[1]Theoretical energy consumption, TFE	0.195 kWh/kg
[2]Energy consumption, HFP	0.460 kWh/kg

[1]Assume that the theoretical energy consumption is equal to the rate of heat loss due to mass flow, i.e. $Q = mC_p\Delta T$. For 1kg of TFE at 25°C: $87\times1000\times1/100.02\times(834\text{-}25) =$ 703690 joules = 0.195 kWh.

[2]Since there will be heat loss from the furnace (conduction, convection, radiation) and any ancillary equipment/electronics necessary for processing, will assuming a 100% energy markup factor: $2\times0.195\times1.176$kgTFE = 0.460 kWh per kg of HFP.

HFPO Analysis

The contribution of HFPO to the production of Nafion® from the U.S. patent 3,335,8003 example IV. The masses calculations:

Table A.10: HFPO material properties.

Property		US Patent 3358003 [95]	
Density, water (@ 25°C)	1.00 g/cm^3	Volume, water	150 cm^3
Density, methanol (@ 25°C)	0.792 g/cm^3	Volume, methanol	750 cm^3
Density, H_2O_2 (30%)	1.135 g/cm^3	Volume, H_2O_2	525 cm^3
[1]Density, HFP (@ -30°C)	1.578 g/cm^3	Volume, HFP	80 cm^3
[2]Process waste, HFP	5%	Mass, KOH	84 g
[3]Mass (/kg HFPO), HFP	0.904 kg	[5]Synthesized mixture	62.8 g
[4]Mass (/kg HFPO), HFP (waste)	4.76×10^{-2} kg	Conversion to HFPO	65%
[6]Mass (/kg HFPO), methanol	14.6 kg		
[7]Mass (/kg HFPO), KOH	2.06 kg		
[8]Mass (/kg HFPO), water	3.67 kg		
[9]Mass (/kg HFPO), H_2O_2 (30%)	14.6 kg		

[1]The reported density of HFP is 1.332 g/cm^3 at 20°C []. Assuming an inverse linear relationship with temperature: $1.332\times[1+(20-(-30))/273] = 1.58$.

[2]The process waste of 5% is a pure assumption based on the 35% of unreacted HFP post synthesis.

[3]The molecular weight of HFP and HFPO is 150 g/mol and 166 g/mol, respectively. Therefore, 1 kg of HFPO consumes 150/166 or 0.904 kg of HFP (note the remaining mass is made up by oxygen from the hydrogen peroxide).

[4]From the example, the synthesis results in a mixture of 62.8 g containing both unreacted HFP and HFPO.

[5]It is assumed that the HFP can be continuously recycled and the waste mass is determined only by the process waste rate (of 5%): $0.904\times0.05/(1-0.05) = 4.76\times10^{-2}$.

[6]The batch contains 750 ml of methanol to produce $62.8g\times0.65 = 40.82$ g of HFPO (assuming the methanol can not be recycled). Therefore, the mass of methanol per kg of HFPO: $(1000/40.82)\times750\times0.792 = 14550$ g or 14.6 kg.

[7]Assuming KOH requires replenishment after every batch: 84g KOH per 0.65×62.8 g HFPO = 2.06 kg KOH.

[8]Assuming water requires replenishment after every batch: 150ml water per 0.65×62.8 g HFPO = 3.67 kg water.

[9]Since hydrogen peroxide is the epoxidizing agent it requires replenishment after every batch: 525ml H_2O_2 per 0.65×62.8 g HFPO = 14.6 kg H_2O_2.

The processing energy calculations:

Table A.11: HFPO processing energy.

Property	
Processing temperature	-40°C [95]
Processing time	1.5 hours [95]
Specific heat capacity, methanol (@ 25°C)	2.53 J/g-K [218]
Specific heat capacity, water (@ 25°C)	4.19 J/g-K
Molecular weight, methanol	32.04 g/mol
[1]Theoretical energy consumption, HFPO	1.92 kWh/kg
[2]Energy consumption, HFPO	3.93 kWh/kg

[1]The theoretical energy consumption is equal to the energy required to cool the batch from room temperature, 25°C, down to -40°C. Using the equation, $Q = mC_p\Delta T$, and assuming the major components for specific heat are methanol and water (assume the 30% concentration hydrogen peroxide has the same specific heat as water), the energy consumed per batch: (750ml×0.792g/ml×2.53J/g-K+(150ml+525ml)×1g/ml×4.19J/g-K)×(25°C-(-40°C)) = 2.81×10^5 joules = 0.0782 kWh per batch. Since every batch produces 40.82 g of HFPO, the theoretical energy consumption for 1 kg of HFPO = 1.92 kWh.

[2] The actual energy consumption takes into account the additional energy post cool down when the synthesis continues to occur for the 1.5 hours. Due to lack of information of the actual process and equipment, the energy consumption will be modeled using an industrial freezer, Premium Chest Model C660, from New Brunswick. The freezer has a capacity of 660 L and is capable of freezing down to -85°C with a reported energy consumption of 15 kWh (empty) per day at -80°C [231]. The batch volume in the patent example to synthesize 40.82 g of HFPO is: 750ml + 150ml + 525 ml + 80ml (KOH volume assumed negligible) = 1.51 L. Therefore, at a freezer capacity of 660 L, the maximum HFPO production mass per batch (assuming 90% capacity) is: 660L×0.9×0.0408kg/1.51L = 16.1 kg of HFPO. The energy consumed during processing scaled from -80°C to -40°C is: 15kWh×1.5hr/24hr×(273-80)/(283-40) = 0.745 kWh, which translates to 0.745/16.1 = 0.0462 kWh per kg HFPO. Combining with the theoretical energy consumption and assuming an energy markup of 100% (for and ancillary electronics/equipment and electrical inefficiencies): 2×(1.92+0.0462) = 3.93 kWh.

Nafion®: sulfonate fluoride form

Table A.12: Properties for the formation of Nafion®

Property	Value	Units
Nafion®	1	mol
TFE	7	mol
SO_3	1	mol
HFPO	2	mol
Ha_2CO_3	1	mol
Polymerization energy	2.114	MJ/mol of Nafion® at 100% efficiency

Nafion®: PFSA form

Table A.13: Properties for the formation of PFSA Nafion®

Property	Value	Units
Nafion® PFSA	1028	kg/mol
Nafion® sulfonate	1046	kg/mol
KOH	53.633	kg
Water	255.4	kg
H_2SO_4	49	kg
dT process	60	°C, temperature change
Specific heat	4188	J/kg-K, assume mainly that of water
Nafion® bath energy	4.14[248]	kJ/m^2
Overall efficiency/utilization	95	%, assumption
Final PFSA GWP	38.2	$kgCO_2e/kg$

A.6 Chapter 6

This section lists all the model parameter using for the LCI and DFMA modeling.

Table A.14: LCI Methodology: CML2001 - November 2010 GWP 100 years [248] (not full list).

Flow	GWP ($kgCO_2e$)
Tetrafluoroethylene (TFE)	0.021
Hexafluoropropylene (HFP)	025
Carbon dioxide	1
Dichloromethane	8.7
Methane	25
Dichlorotrifluoroethane (R123)	77
Difluoroethane (R152a)	124
Nitrous oxide	298
Difluoromethane (R32)	675
Tetrafluoroethane (R134a)	1430
Chlorodifluoromethane (R22)	1810
Halon (1211)	1890
Trifluoroethane (R143a)	4470
Dichlorotetrafluoroethane (R114)	10000
Chlorotrifluoromethane (R13)	14400
Sulphur hexafluoride	22800

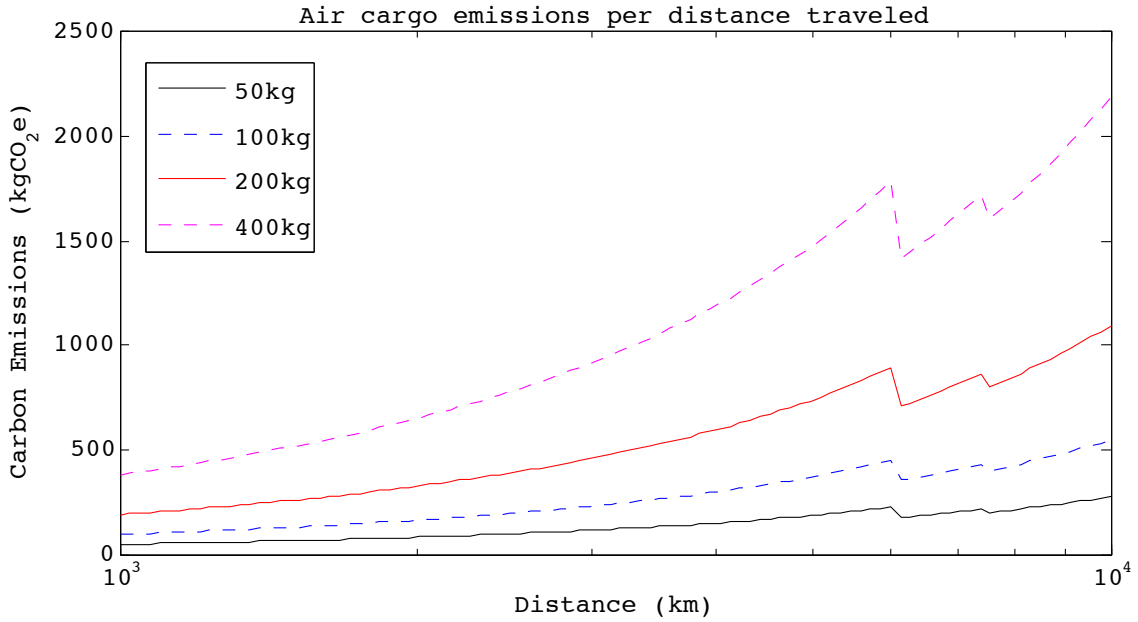

Figure A.4: Modeled air cargo emissions per distance from Gabi Software [248].

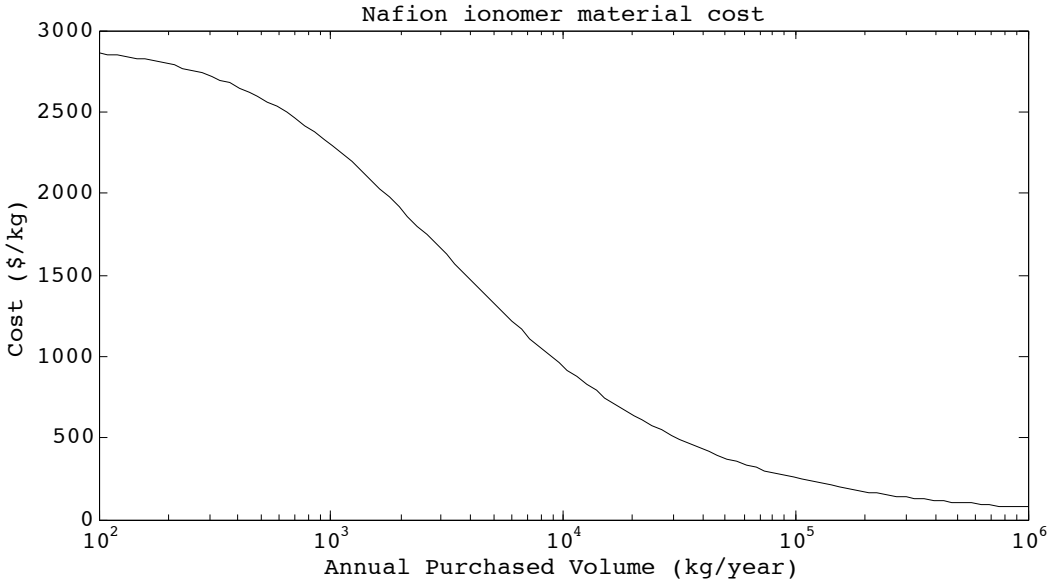

Figure A.5: Material cost of Nafion® ionomer extrapolated from [160].

Table A.15: List of all LCI data from the Gabi Software (unless otherwise specified) used in the modeling (all values in $kgCO_2e/kg$ or $kgCO_2e/2002USD$).

Material	Component(s)	Value	Comments
Polypropylene	Carbon BIP	1.93	
Epoxy	Carbon BIP	6.0	
Carbon black	Carbon BIP, GDL	2.4	
Distilled water	GDL	4.33×10^{-3}	
Argon(g)	CCM, metal BIP	0.311	
Silicone	MESA	7.46	silicone sealing compound
PEN	MEFA	8.85	Data from CES Selector [12]
PVA	GDL	8.8	Carbon fiber paper production
Carbon fiber	GDL	20	
PF resin	Carbon BIP, GDL	4.15	
Methanol	CCM, GDL	0.756	
Nitrogen	Metal BIP, GDL	0.0962	
PTFE	CCM, GDL	12	
Aluminum	Stack assy	10.5	
Graphite	Carbon BIP, GDL	7.1	Data from CES Selector [12]
Stainless steel 304	Metal BIP, Stack assy	4.7	
Chromium	Metal BIP	26.7	Ferro chrome mix
Surfactant	GDL	3.52	For Triton-X100, assume Tensides in Gabi
Platinum	CCM	18500	
De-ionized water	CCM	5.22×10^{-3}	
DPG	CCM	5.65	Dipropylene glycol
Polyimide	CCM	9.36	Kapton® film
Polyurethane	MEA	5.11	PUR sealing compound, for film adhesive
HDPE	MEA	1.89	HDPE film assumed for film adhesive base
PA6,6	Stack Assy	7.31	Used PA6 with 30wt.% glass fiber
Generic steel	Stack Assy	2.39	
Gasket	BIP	4.77	Flexible polyurethane
Naphtha	Membrane	6.2	Proxy for Isopar-K
Copper	Stack Assy	3.65	
Electrical adhesive	Carbon BIP	5.28	80wt.% epoxy, 20wt% carbon black
Film adhesive	MEA	3.5	50wt% HDPE, 50wt.% polyurethane
Tar	CCM	0.858	Production of Perylene Red-149
Perylene Red	CCM	18.97	1mol Rylene dye to 2mol naphthalene
Carbon dioxide	Nafion®	0.537	
HCl	Nafion®	1.47	
KOH	Nafion®	1.6	
Hydrogen peroxide	Nafion®	3.32	
SO^3	Nafion®	0.87	Sulfur trioxide
Na_2CO_3	Nafion®	1.05	
DMSO	Nafion®	1.3	
H_2SO_4	Nafion®	0.348	
TFE	Nafion®	14/21	direct/waste
Kerosene	Transportation	0.446	Air cargo
Diesel	Transportation	0.47	Land cargo
Machinery	Tools	0.571	eiolca.net, Sector:33329A [153]
Buildings	Facility	0.437	eiolca.net, Sector:230102 [153]

Table A.16: List of all material cost data in 2013USD per kg (unless otherwise stated).

Material	Component(s)	Value	Comments
Polypropylene	Carbon BIP	2.94	From [12]
Carbon black	Carbon BIP, GDL	6.80	From [160]
Silicone	MESA	48.77	Henkel Loctite LIM hydrocarbon [160]
PEN	MEFA	4	Per m^2, from [12]
PF resin	Carbon BIP, GDL	4.18	From [160]
Methanol	CCM, GDL	0.6	From [217]
PTFE	CCM, GDL	22.17	From [293]
ePTFE	CCM	5.36	Per m^2, from [160]
Aluminum	Stack assy	3.16	From [12]
Graphite	Carbon BIP, GDL	2.83	From [293]
Stainless steel 304	Metal BIP, Stack assy	11.78	From [293]
Chromium	Metal BIP	750	Sputter target, from [194]
Surfactant	GDL	39	For Triton-X100 [292]
Platinum	CCM	50000	Estimated, [160]
De-ionized water	CCM	0.4	From [286]
DPG	CCM	10	Dipropylene glycol [185]
Polyimide	CCM	45	Kapton® film on Alibaba.com
PA6,6	Stack Assy	4.28	Used PA6 with 50wt.% glass fiber [12]
Generic steel	Stack Assy	0.623	steel-1080 [12]
Gasket	BIP	22.60	Generic silicone [160]
Copper	Stack Assy	11.54	From [12]
Electrical adhesive	Carbon BIP	273.91	Eccobond 60L [306]
Film adhesive	MEA	22	Polyester film [52]
Liquid adhesive	MEA	1007.5	Loctite 3526 UV-curable [2]
Perylene Red	CCM	50	Various suppliers on Alibaba.com

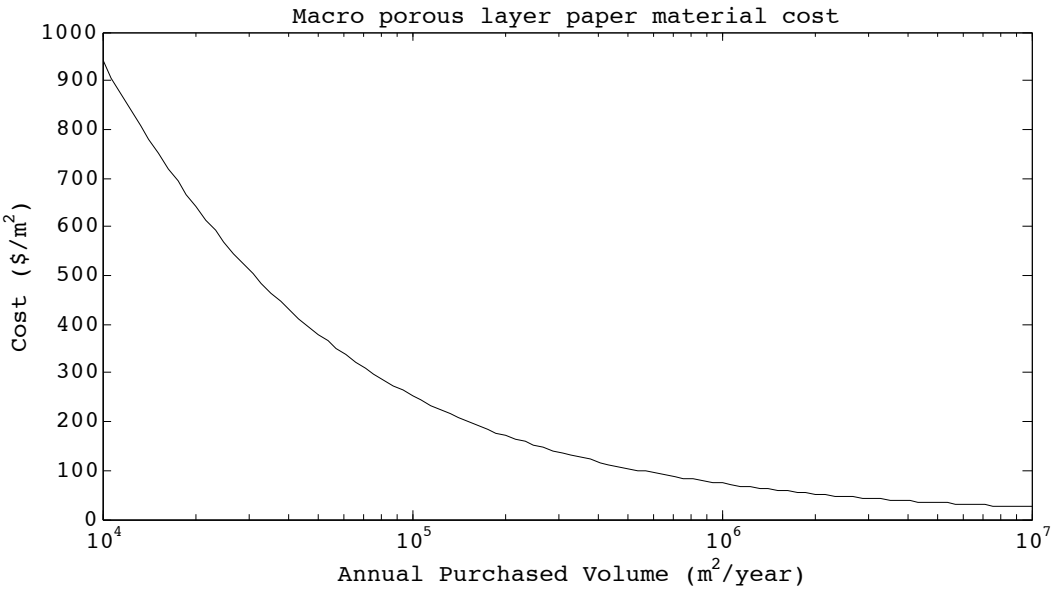

Figure A.6: Material cost of the macro porous layer carbon fiber paper for the GDL, extrapolated from [160].

Table A.17: Location parameters at the Enterprise scale.

Parameter	US East	Germany	Japan	Vancouver
Inflation rate, [%]	3[214]	1.5[125]	0.36[152]	1.7[310]
Energy inflation rate, [%]	5.6[255]	5.5[125]	4.04[163]	0.3[310]
Property tax, [%]	1.4[193]	4.3[259]	2.05[118]	1.75[7]
Electric tariff, $[cent/kWh]$	7.75[90]	18.59[98]	13.07[88]	BC Hydro model
Natural gas, $[/m^3]$	0.169[91]	0.174[98]	0.582[88]	0.213[88]
Floor space cost, $[/m^2]$	1311.3[285]	1986.3[97]	4280.9[97]	1262.1[97]
Labor rate, $[/hr]$	30.93[38]	32.64[192]	29.02[301]	21.15[40]
GWP natural gas, $[kgCO_2eq/kg]$[248]	0.634	0.479	0.839	0.523
GWP electricity, $[kgCO_2eq/kWh]$[248]	0.723	0.639	0.717	0.0456

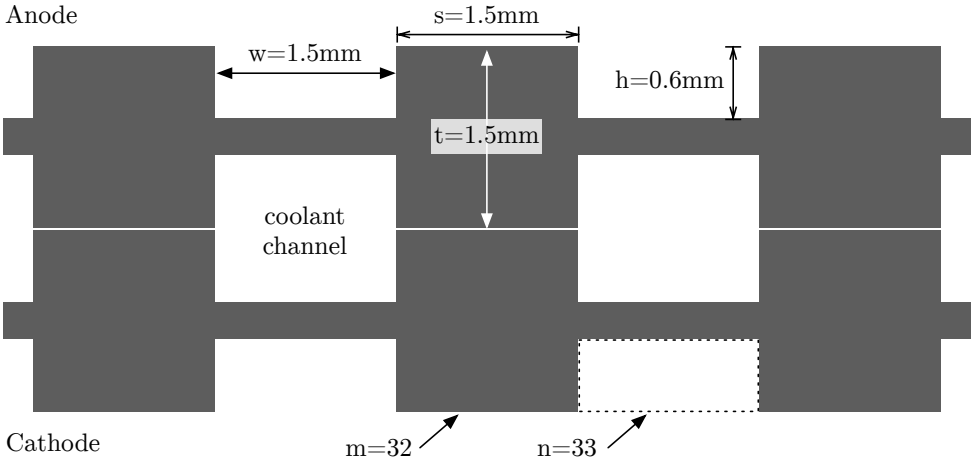

Figure A.7: Cross-sectional design of of carbon BIP.

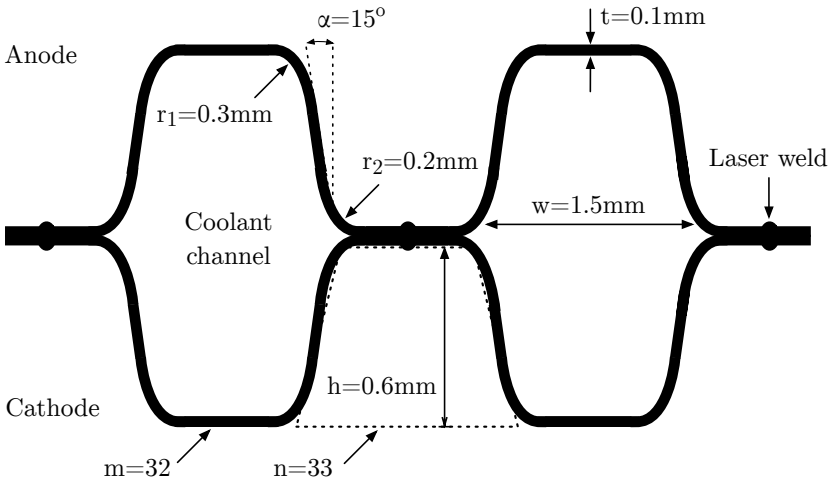

Figure A.8: Cross-sectional design of of metal BIP.

Table A.18: Slot-die tool parameters. Power data are estimated assumptions unless otherwise stated.

Component	Process Power (kW)	Baseline Power (kW)	Cost (2013USD)
Slot-die tool	60[180]	n.a.	84,450[159]
XRF Inspection	-	-	150,000
Motors	7	0.7	-
Blowers	8	0.8	-
Slot-die coater	5	2.5	-
Controls	5	4.5	-
Heater	35	14	-

Table A.19: NSTF tool parameters. Power data are estimated assumptions unless otherwise stated. Modeled power is dependent on the HVAC energy model.

Component	Process Power (kW)	Baseline Power (kW)	Cost (2013USD)
NSTF tool	727[160]	n.a.	1,255,127[160]
XRF Inspection	-	-	assumed built-in
Motors	6	0.6	-
Rough pump	5.5(4x)	1.375(4x)	-
Diffusion pump	72(3x)	3.6(4x)	-
PVD Sputter	modeled	modeled	-
PVD Sublimation	modeled	modeled	-
Controls	modeled	modeled	-
Heater	modeled	modeled	-

Table A.20: CCM assembly tool parameters. Power data are estimated assumptions unless otherwise stated.

Component	Process Power (kW)	Baseline Power (kW)	Cost (2013USD)
Lamination tool	10[160]	n.a.	107,100[160]
XRF Inspection	-	-	200,000
Motors	3	0.3	-
Heated roller	5	2.5	-
Controls	2	1.8	-

Table A.21: Application of the MPL onto the GDL tool parameters. Power data are estimated assumptions unless otherwise stated. Modeled power is dependent on the HVAC energy model.

Component	Process Power (kW)	Baseline Power (kW)	Cost (2013USD)
Dipper	5	0.25	87,660[160]
IR oven (small)	modeled(2x)	modeled(2x)	167,416(2x)[160]
IR oven (large)	modeled	modeled	502,247[160]
Ultrasonic mixer	1.5	0	28,322[160]
Sprayer	12.5	11	350,641[160]
Winders	74[4]	3.7	29220[160]
Inspection (manual)	-	-	20,000
Inspection (auto)	0.5	2	100,00
Controls	5	3.5	-

Table A.22: MEA tool parameters. Power data are estimated assumptions unless otherwise stated. Modeled power is dependent on the HVAC energy model.

Component	Process Power (kW)	Baseline Power (kW)	Cost (2013USD)
Hot press	modeled	modeled	160,650
CNC plotter	2	0.75	160,650
Roll cutter	0(3x)	0(3x)	26,775(3x)[160]
Misc.	0	0	26,775
Stamp punch	2	3	26,775
Robot	6(2x)	1(2x)	53,550(2x)
Screen printer	2.5	1	160,650[160]
UV-cure system	5.64	0.49	171,360[160]

Table A.23: Frame (MESA and MEFA) tool parameters. Power data are estimated assumptions unless otherwise stated. Modeled power is dependent on the HVAC energy model.

Component	Process Power (kW)	Baseline Power (kW)	Cost (2013USD)
Hot press (1cav)	modeled	modeled	160,650
Hot press (2cav)	modeled	modeled	227,193
LIM	modeled	modeled	500.47*tonnage+161,808
LIM aux	0	0	15% of LIM
Robot	3	1	160,650
Stamp punch	2	3	80,325
Mixer	modeled	modeled	n.a

Table A.24: Carbon BIP tool parameters. Power data are estimated assumptions unless otherwise stated. Modeled power is dependent on the HVAC energy model.

Component	Process Power (kW)	Baseline Power (kW)	Cost (2013USD)
Compression molder (2cav)	modeled	modeled	9395.3*tonnage$^{0.6612}$
Compression molder (4cav)	modeled	modeled	9395.3*tonnage$^{0.6612}$
Injection molder (1cav)	modeled	modeled	500.47*tonnage+161,808
Injection molder (2cav)	modeled	modeled	500.47*tonnage+161,808
Hot press (1cav)	modeled	modeled	160,650
Hot press (2cav)	modeled	modeled	227,193
Oven (small)	modeled	modeled	176,715
Oven (large)	modeled	modeled	353,430
CNC plotter	2	0.75	160,650
Clean & dry (small)	22.4	6.7	160,650
Clean & dry (large)	33.6	10	240,975
Shot-peening	5.5	2.75	160,650
Oven HT (small)	modeled	modeled	117,810[362]
Oven HT (large)	modeled	modeled	176,715
Screen printer (small)	2.5	1	160,650[160]
Screen printer (med.)	2.5	1	214,200[160]
Mixer	4	2	40,163[150]
Inspection (auto)	5	2.5	214,200

Table A.25: Metal BIP tool parameters. Power data are estimated assumptions unless otherwise stated. Modeled power is dependent on the HVAC energy model.

Component	Process Power (kW)	Baseline Power (kW)	Cost (2013USD)
Die stamper (2cav)	modeled	modeled	480,000
Clean & dry (small)	33.6	10	107,100
Clean & dry (large)	22.4	6.7	160,650
Welder	25	3	642,600
PVD (small)	modeled	modeled	1,64,2200
PVD (large)	modeled	modeled	2,463,300
Thermal (small)	modeled	modeled	1,392,300
Thermal (large)	modeled	modeled	2,088,450
Inspection (auto)	5	2.5	214,200

Table A.26: Stack assembly tool parameters. Power data are estimated assumptions unless otherwise stated.

Component	Process Power (kW)	Baseline Power (kW)	Cost (2013USD)
Stacker (manual)	0	0	10710
Stacker (semi-auto)	7[351]	5[351]	401,625
Compression band (semi-auto)	8	4	80,325
Compression band (auto)	10[351]	4[351]	160,650
Welder	50[351]	2[351]	n.a.
Misc.	0	0	26,775

A.7 Chapter 7

Table A.27: GWP results - DVI versus PV

Design	DVI	100	500	1000	5000	10000	50000
Reference	DVI1	4537.0	4187.7	4030.1	3885.4	3862.2	3481.3
	DVI3	5695.0	4400.8	4020.2	3564.4	3506.4	3038.4
Future	DVI1	3081.9	2498.2	2397.4	2248.9	2178.4	2125.5
	DVI3	4675.5	2671.1	2334.1	2039.9	2004.9	1806.5

Table A.28: Cost results - DVI versus PV

Design	DVI	100	500	1000	5000	10000	50000
Reference	DVI1	1624.1	637.1	503.7	356.9	316.3	208.1
	DVI3	2561.5	778.0	536.0	305.9	255.9	166.6
Future	DVI1	2369.8	803.3	599.0	377.9	308.1	170.4
	DVI3	3569.9	1010.4	671.7	353.6	277.0	138.6

Table A.29: GWP results - PV versus DVI

Design	PV	DVI0	DVI1	DVI2	DVI3	DVI4
Reference	100	4027.7	4537.0	5319.9	5695.0	5748.2
	10000	3525.5	3862.2	3805.1	3506.4	3483.1
Future	100	2293.3	3081.9	3743.9	4675.5	4731.5
	10000	1956.5	2178.4	1998.3	2004.9	1981.5

Table A.30: Cost results - PV versus DVI

Design	PV	DVI0	DVI1	DVI2	DVI3	DVI4
Reference	100	461.3	1624.1	2534.6	2561.5	2688.6
	10000	303.1	316.3	262.9	255.9	248.0
Future	100	470.8	2369.8	3502.0	3569.9	3697.9
	10000	297.7	308.1	279.6	277.0	269.2

Table A.31: Breakdown GWP results - Reference design, DVI1, PV100

Component	Membrane	CCM	GDL	MEA	Frame	BIP	Stack Assy.	Total
Material (direct)	31.70	756.64	507.19	0.15	20.80	304.43	99.39	1720.30
Material (scrap)	30.08	599.88	321.73	3.24	122.12	27.58	0.00	1104.63
Tool	19.62	4.01	3.66	184.39	74.81	70.76	34.55	391.79
Tool energy	9.29	41.68	57.59	100.67	39.05	364.06	25.96	638.31
Infrastructure	0.42	0.28	0.37	21.64	2.91	6.61	3.84	36.07
Infras. Energy	0.73	14.78	1.27	44.05	14.99	11.80	10.49	98.11
Transportation	4.34	7.06	11.63	2.72	53.77	186.38	281.92	547.82
Total	96.18	1424.34	903.44	356.85	328.45	971.62	456.14	4537.04

Table A.32: Breakdown Cost results - Reference design, DVI1, PV100

Component	Membrane	CCM	GDL	MEA	Frame	BIP	Stack Assy.	Total
Material (Direct)	410.44	2126.62	896.18	0.94	135.96	198.83	76.16	7551.06
Material (Scrap)	389.47	1685.91	347.75	20.34	798.42	17.96	0.00	5682.47
Labor	1504.68	233.48	167.99	307.35	654.79	261.95	24.17	5646.50
Capital	3486.25	694.48	367.41	34765.65	14106.18	494.18	222.11	60632.6
Operational	18392.61	137.08	220.90	4408.71	1743.43	100.12	28.34	48218.3
Infrastructure	1.32	43.51	37.18	21.79	894.44	41.95	32.21	1302.18
Markup	2.23	2.00	1.70	1.00	1.00	1.71	5.00	0.00
Transportation	5.23	8.51	19.66	3.27	64.84	316.82	475.11	893.44
Total	54053.09	9850.63	3480.88	39528.05	18398.07	2225.81	2390.05	129927

Table A.33: Breakdown GWP results - Reference design, DVI1, PV10000

Component	Membrane	CCM	GDL	MEA	Frame	BIP	Stack Assy.	Total
Material (direct)	31.70	756.64	507.53	0.15	20.80	304.43	99.39	1720.64
Material (scrap)	29.25	595.22	321.37	3.24	122.12	4.66	0.00	1075.85
Tool	12.28	2.42	2.04	3.69	0.93	58.78	3.45	83.61
Tool energy	8.98	53.82	27.64	2.22	0.62	308.03	0.98	402.29
Infrastructure	0.26	0.21	0.06	0.43	0.03	5.49	0.15	6.63
Infras. Energy	0.46	13.69	0.20	0.92	0.17	9.81	0.26	25.50
Transportation	4.28	7.04	11.63	2.72	53.77	186.38	281.92	547.73
Total	87.22	1429.03	870.47	13.36	198.44	877.58	386.15	3862.25

Table A.34: Breakdown Cost results - Reference design, DVI1, PV10000

Component	Membrane	CCM	GDL	MEA	Frame	BIP	Stack Assy.	Total
Material (Direct)	315.40	2120.14	784.70	0.94	135.96	198.83	76.16	6881.76
Material (Scrap)	291.03	1667.69	304.18	20.34	798.42	3.03	0.00	5283.69
Labor	942.03	171.31	44.06	277.18	405.21	183.70	8.75	3440.36
Capital	2182.61	418.66	205.30	695.31	176.06	410.54	22.21	7456.75
Operational	203.18	151.13	107.49	87.20	23.47	87.46	1.34	1159.88
Infrastructure	0.82	43.15	5.97	26.63	9.03	34.85	1.10	187.62
Markup	2.17	2.00	1.62	1.00	1.00	1.45	3.42	0.00
Transportation	5.16	8.48	19.64	3.27	64.84	316.82	475.11	893.32
Total	8560.77	9152.63	2369.59	1110.88	1612.99	1646.22	850.30	25303.38

Table A.35: Breakdown GWP results - Reference design, DVI3, PV100

Component	Membrane	CCM	GDL	MEA	Frame	BIP	Stack Assy.	Total
Material (direct)	31.70	756.64	507.19	0.15	20.80	304.43	99.39	1720.30
Material (scrap)	35.23	933.01	321.73	3.24	122.12	204.98	0.00	1620.31
Tool	19.62	381.66	3.66	184.39	74.81	388.95	34.55	1087.64
Tool energy	9.29	49.75	57.59	101.09	39.39	117.81	25.96	400.89
Infrastructure	0.42	19.08	0.37	21.85	2.91	9.78	3.84	58.25
Infras. Energy	0.73	43.45	1.27	49.75	8.14	23.40	5.65	132.39
Transportation	4.70	8.66	11.63	2.72	53.77	311.80	281.92	675.20
Total	101.69	2192.26	903.44	363.18	321.94	1361.16	451.30	5694.98

Table A.36: Breakdown Cost results - Reference design, DVI3, PV100

Component	Membrane	CCM	GDL	MEA	Frame	BIP	Stack Assy.	Total
Material (Direct)	391.89	2134.80	896.18	0.94	135.96	198.83	76.16	5249.58
Material (Scrap)	435.54	2631.37	347.75	20.34	798.42	133.52	0.00	5147.75
Labor	1504.68	1075.73	167.99	307.35	654.79	1095.29	24.17	6902.08
Capital	3486.25	71961.90	367.41	34765.65	14106.18	2500.75	222.11	132860
Operational	18392.61	4980.78	220.90	4150.52	1647.33	245.38	25.99	52632.9
Infrastructure	1.32	19.22	37.18	22.00	699.58	77.10	27.52	1021.59
Markup	2.23	1.00	1.70	1.00	1.00	1.00	5.00	0
Transportation	5.66	10.44	19.66	3.27	64.84	530.13	475.11	1109.12
Total	54115.04	82814.24	3480.88	39270.08	18107.11	4780.99	2354.84	204923

Table A.37: Breakdown GWP results - Reference design, DVI3, PV10000

Component	Membrane	CCM	GDL	MEA	Frame	BIP	Stack Assy.	Total
Material (direct)	31.70	756.64	507.53	0.15	20.80	304.43	99.39	1720.64
Material (scrap)	29.45	601.04	321.37	3.24	122.12	5.50	0.00	1082.71
Tool	12.28	4.44	2.04	3.69	0.93	55.83	3.45	82.68
Tool energy	8.98	1.12	27.64	2.22	0.63	19.63	0.98	61.19
Infrastructure	0.26	0.31	0.06	0.44	0.03	1.54	0.15	2.78
Infras. Energy	0.46	0.80	0.20	1.12	0.08	2.47	0.13	5.26
Transportation	4.29	7.07	11.63	2.72	53.77	189.75	281.92	551.14
Total	87.43	1371.42	870.47	13.57	198.36	579.15	386.02	3506.41

Table A.38: Breakdown Cost results - Reference design, DVI3, PV10000

Component	Membrane	CCM	GDL	MEA	Frame	BIP	Stack Assy.	Total
Material (Direct)	314.81	2127.43	784.70	0.94	135.96	198.83	76.16	4678.67
Material (Scrap)	292.44	1689.80	304.18	20.34	798.42	3.58	0.00	3640.34
Labor	942.03	123.54	44.06	277.18	405.21	136.76	8.75	3092.14
Capital	2182.61	838.04	205.30	695.31	176.06	358.99	22.21	7222.21
Operational	203.18	70.03	107.49	86.87	23.46	54.69	1.34	855.39
Infrastructure	0.82	20.23	5.97	28.48	7.11	11.17	1.00	81.85
Markup	2.17	1.00	1.62	1.00	1.00	1.00	3.42	0.00
Transportation	5.17	8.51	19.64	3.27	64.84	322.54	475.11	899.10
Total	8562.57	4877.59	2369.59	1112.40	1611.06	1086.55	849.94	20469.70

Table A.39: Breakdown GWP results - Future design, DVI1, PV100

Component	Membrane	CCM	GDL	MEA	Frame	BIP	Stack Assy.	Total
Material (direct)	15.33	234.32	507.19	0.34	10.20	92.29	99.39	959.06
Material (scrap)	13.98	185.72	321.73	1.12	37.04	68.28	0.00	627.87
Tool	41.20	4.98	3.66	266.04	117.77	61.77	34.55	529.96
Tool energy	4.89	210.23	57.59	105.05	24.67	103.01	25.96	531.39
Infrastructure	0.41	0.41	0.37	26.50	2.85	0.99	3.84	35.37
Infras. Energy	0.71	47.51	1.27	54.98	6.73	5.58	18.91	135.69
Transportation	2.14	6.51	11.63	0.80	14.99	74.56	151.94	262.57
Total	78.65	689.68	903.44	454.83	214.25	406.47	334.58	3081.91

Table A.40: Breakdown Cost results - Future design, DVI1, PV100

Component	Membrane	CCM	GDL	MEA	Frame	BIP	Stack Assy.	Total
Material (Direct)	344.64	658.53	896.18	67.41	16.94	365.00	76.16	4699.79
Material (Scrap)	320.73	521.83	347.75	220.60	61.56	188.53	0.00	2956.12
Labor	1504.68	163.09	167.99	239.05	293.38	69.10	24.17	4745.83
Capital	7321.66	862.96	367.41	50160.94	22204.75	364.76	222.11	92813.20
Operational	33058.58	548.58	220.90	5322.40	1808.31	77.69	28.16	82755.96
Infrastructure	1.27	105.09	37.18	26.77	673.97	6.36	39.34	1184.51
Markup	2.23	2.00	1.70	1.00	1.00	1.71	5.00	0.00
Transportation	2.57	7.84	19.66	0.97	18.07	126.73	255.43	431.27
Total	95096.39	5727.98	3480.88	56038.14	25076.98	1961.17	2205.14	189586.67

Table A.41: Breakdown GWP results - Future design, DVI1, PV10000

Component	Membrane	CCM	GDL	MEA	Frame	BIP	Stack Assy.	Total
Material (direct)	15.33	234.32	507.53	0.34	10.20	92.29	99.39	959.39
Material (scrap)	13.59	184.28	321.37	1.12	37.04	61.44	0.00	618.84
Tool	26.41	2.93	2.04	2.66	1.37	20.53	3.45	59.40
Tool energy	4.52	156.06	27.64	1.16	0.42	49.92	0.98	240.71
Infrastructure	0.25	0.28	0.06	0.27	0.03	0.33	0.15	1.36
Infras. Energy	0.44	32.80	0.20	0.57	0.05	1.86	0.32	36.24
Transportation	2.11	6.48	11.63	0.80	14.99	74.56	151.94	262.51
Total	62.66	617.15	870.47	6.92	64.11	300.92	256.22	2178.45

Table A.42: Breakdown Cost results - Future design, DVI1, PV10000

Component	Membrane	CCM	GDL	MEA	Frame	BIP	Stack Assy.	Total
Material (Direct)	276.89	658.53	784.70	67.41	16.94	365.00	76.16	4062.79
Material (Scrap)	251.23	517.78	304.18	220.60	61.56	161.05	0.00	2589.46
Labor	942.03	172.82	44.06	215.66	148.95	27.41	8.75	2899.35
Capital	4692.26	507.65	205.30	501.61	258.84	121.21	22.21	12561.48
Operational	346.87	400.04	107.49	54.14	23.82	53.61	1.38	1888.51
Infrastructure	0.80	85.23	5.97	16.58	6.25	2.11	1.16	211.72
Markup	2.17	2.00	1.62	1.00	1.00	1.45	3.42	0.00
Transportation	2.54	7.81	19.64	0.97	18.07	126.73	255.43	431.20
Total	14156.71	4691.92	2369.59	1076.96	534.43	1183.97	630.93	24644.51

Table A.43: Breakdown GWP results - Future design, DVI3, PV100

Component	Membrane	CCM	GDL	MEA	Frame	BIP	Stack Assy.	Total
Material (direct)	15.33	234.32	507.19	0.34	10.20	92.29	99.39	959.06
Material (scrap)	16.34	285.11	321.73	1.12	37.04	121.19	0.00	782.54
Tool	41.20	458.09	3.66	266.04	117.77	883.51	34.55	1804.81
Tool energy	4.89	125.14	57.59	104.07	24.63	47.76	25.96	390.04
Infrastructure	0.41	27.73	0.37	25.12	2.85	13.43	3.84	73.74
Infras. Energy	0.71	138.17	1.27	125.14	4.07	20.30	11.44	301.09
Transportation	2.31	7.97	11.63	0.80	14.99	174.52	151.94	364.16
Total	81.19	1276.53	903.44	522.63	211.55	1353.01	327.11	4675.46

Table A.44: Breakdown Cost results - Future design, DVI3, PV100

Component	Membrane	CCM	GDL	MEA	Frame	BIP	Stack Assy.	Total
Material (Direct)	332.09	658.53	896.18	67.41	16.94	365.00	76.16	3753.30
Material (Scrap)	361.95	800.61	347.75	220.60	61.56	401.20	0.00	2883.61
Labor	1504.68	1344.66	167.99	239.05	293.38	175.57	24.17	5821.58
Capital	7321.66	86371.28	367.41	50160.94	22204.75	5680.55	222.11	182515
Operational	33058.58	7393.48	220.90	4988.13	1734.02	532.14	25.53	89029.7
Infrastructure	1.27	37.74	37.18	34.18	595.09	96.36	31.78	988.28
Markup	2.23	1.00	1.70	1.00	1.00	1.00	5.00	0.00
Transportation	2.78	9.60	19.66	0.97	18.07	296.65	255.43	603.16
Total	95160.69	96615.91	3480.88	55711.28	24923.80	7547.48	2154.16	285594

Table A.45: Breakdown GWP results - Future design, DVI3, PV10000

Component	Membrane	CCM	GDL	MEA	Frame	BIP	Stack Assy.	Total
Material (direct)	15.33	234.32	507.53	0.34	10.20	92.29	99.39	959.39
Material (scrap)	13.68	186.08	321.37	1.12	37.04	61.69	0.00	620.98
Tool	26.41	5.21	2.04	2.66	1.37	24.37	3.45	65.52
Tool energy	4.52	1.36	27.64	1.16	0.42	2.03	0.98	38.11
Infrastructure	0.25	0.40	0.06	0.25	0.03	0.36	0.15	1.50
Infras. Energy	0.44	2.16	0.20	1.36	0.03	0.46	0.22	4.88
Transportation	2.11	6.51	11.63	0.80	14.99	126.59	151.94	314.57
Total	62.75	436.03	870.47	7.69	64.09	307.79	256.12	2004.94

Table A.46: Breakdown Cost results - Future design, DVI3, PV10000

Component	Membrane	CCM	GDL	MEA	Frame	BIP	Stack Assy.	Total
Material (Direct)	276.48	658.53	784.70	67.41	16.94	365.00	76.16	3240.04
Material (Scrap)	252.54	522.83	304.18	220.60	61.56	162.06	0.00	2008.50
Labor	942.03	121.48	44.06	215.66	148.95	18.94	8.75	2654.47
Capital	4692.26	982.14	205.30	501.61	258.84	156.69	22.21	12509.55
Operational	346.87	82.81	107.49	52.56	23.28	53.84	1.33	1145.23
Infrastructure	0.80	35.51	5.97	22.33	5.86	2.53	1.07	81.28
Markup	2.17	1.00	1.62	1.00	1.00	1.00	3.42	0.00
Transportation	2.55	7.85	19.64	0.97	18.07	215.17	255.43	519.67
Total	14158.67	2411.16	2369.59	1081.14	533.49	974.21	630.48	22158.74

Table A.47: Breakdown GWP results per stack - BIP Comparisons, DVI1, PV100

Component	Carbon-Compm	Carbon-Injm	Metal-PVD	Metal-Thermal
Material GWP (direct)	304.43	217.22	91.44	86.33
Material GWP (scrap)	30.61	119.10	74.61	73.86
Tool GWP	70.76	40.73	61.77	56.20
Tool energy GWP	364.06	501.66	103.01	86.64
Infrastructure GWP	6.61	6.72	0.99	0.84
Infras. Energy GWP	11.80	12.00	5.58	4.73
Transportation GWP	186.38	160.67	52.05	51.51
Total	974.66	1058.09	389.45	360.09

Table A.48: Breakdown Cost results per stack - BIP Comparisons, DVI1, PV100

Component	Carbon-Compm	Carbon-Injm	Metal-PVD	Metal-Thermal
Material (Direct)	198.83	174.27	360.98	216.19
Material (Scrap)	19.41	70.84	206.40	185.11
Labor	261.95	218.54	69.10	70.15
Capital	494.18	284.44	364.76	331.86
Operational	100.12	109.12	77.69	73.69
Infrastructure	41.95	42.65	6.36	5.39
Markup	1.71	1.71	1.71	1.71
Transportation	316.82	273.11	125.53	124.22
Total	2228.28	1813.79	1983.68	1634.98

Table A.49: Breakdown GWP results per stack - BIP Comparisons, DVI1, PV10000

Component	Carbon-Compm	Carbon-Injm	Metal-PVD	Metal-Thermal
Material GWP (direct)	304.43	217.22	91.44	86.33
Material GWP (scrap)	7.69	110.88	63.25	62.90
Tool GWP	58.78	27.07	20.53	18.67
Tool energy GWP	308.03	466.10	49.92	44.33
Infrastructure GWP	5.49	4.47	0.33	0.28
Infras. Energy GWP	9.81	7.98	1.86	1.57
Transportation GWP	186.38	160.67	52.05	51.51
Total	880.62	994.38	279.37	265.58

Table A.50: Breakdown Cost results per stack - BIP Comparisons, DVI1, PV10000

Component	Carbon-Compm	Carbon-Injm	Metal-PVD	Metal-Thermal
Material (Direct)	198.83	174.27	360.98	216.19
Material (Scrap)	4.48	62.27	167.59	157.66
Labor	183.70	154.22	27.41	27.82
Capital	410.54	189.04	121.21	110.28
Operational	87.46	98.84	53.61	52.27
Infrastructure	34.85	28.34	2.11	1.79
Markup	1.45	1.45	1.45	1.45
Transportation	316.82	273.11	125.53	124.22
Total	1648.31	1296.47	1186.41	943.51

Table A.51: Breakdown GWP results per stack - BIP Comparisons, DVI3, PV100

Component	Carbon-Compm	Carbon-Injm	Metal-PVD	Metal-Thermal
Material GWP (direct)	304.43	217.22	91.44	86.33
Material GWP (scrap)	208.01	222.92	162.53	158.67
Tool GWP	388.95	195.72	883.51	810.24
Tool energy GWP	122.49	79.69	55.05	48.78
Infrastructure GWP	9.78	9.46	13.43	12.02
Infras. Energy GWP	47.22	38.46	32.98	31.09
Transportation GWP	313.66	325.48	147.12	146.17
Total	1394.55	1088.95	1386.07	1293.29

Table A.52: Breakdown Cost results per stack - BIP Comparisons, DVI3, PV100

Component	Carbon-Compm	Carbon-Injm	Metal-PVD	Metal-Thermal
Material (Direct)	198.83	174.27	360.98	216.19
Material (Scrap)	19.41	70.84	206.40	185.11
Labor	261.95	218.54	69.10	70.15
Capital	494.18	284.44	364.76	331.86
Operational	100.12	109.12	77.69	73.69
Infrastructure	41.95	42.65	6.36	5.39
Markup	1.71	1.71	1.71	1.71
Transportation	316.82	273.11	125.53	124.22
Total	2228.28	1813.79	1983.68	1634.98

Table A.53: Breakdown GWP results per stack - BIP Comparisons, DVI3, PV10000

Component	Carbon-Compm	Carbon-Injm	Metal-PVD	Metal-Thermal
Material GWP (direct)	304.43	217.22	91.44	86.33
Material GWP (scrap)	8.53	111.18	63.67	63.30
Tool GWP	55.83	28.12	24.37	22.17
Tool energy GWP	19.63	20.61	2.12	1.91
Infrastructure GWP	1.54	1.37	0.36	0.31
Infras. Energy GWP	2.47	1.93	0.55	0.53
Transportation GWP	191.60	242.84	89.89	89.31
Total	584.04	623.27	272.40	263.85

Table A.54: Breakdown Cost results per stack - BIP Comparisons, DVI3, PV10000

Component	Carbon-Compm	Carbon-Injm	Metal-PVD	Metal-Thermal
Material (Direct)	198.83	174.27	360.98	216.19
Material (Scrap)	5.02	62.59	169.01	158.66
Labor	136.76	129.77	18.94	19.22
Capital	358.99	180.80	156.69	142.55
Operational	54.69	45.89	53.91	52.62
Infrastructure	11.17	9.73	2.59	2.25
Markup	1.00	1.00	1.00	1.00
Transportation	325.69	412.89	216.79	215.39
Total	1091.15	1015.94	979.91	806.88